

The search for lanthanide containing Single Molecule
Magnets with toroidal moments

Zur Erlangung des akademischen Grades eines
DOKTORS DER NATURWISSENSCHAFTEN

(Dr. rer. nat.)

von der KIT-Fakultät für Chemie- und Biowissenschaften

des Karlsruher Instituts für Technologie (KIT)

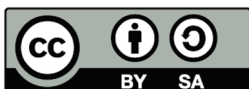
genehmigte

DISSERTATION

von

Thomas Ruppert

Dekan:	Prof. Dr. Manfred Wilhelm
Referent:	Prof. Dr. Annie K. Powell
Korreferent:	Prof. Dr. Karin Fink
Tag der mündlichen Prüfung:	20.07.2021



This document is licensed under a Creative Commons
Attribution ShareAlike 4.0 International Licence (CC BY-SA 4.0):
<https://creativecommons.org/licenses/by-sa/4.0/deed.en>

Note

The ions shown in the illustrations are not to scale. Organic hydrogen atoms are often not shown for a better overview. Atoms and ions are shown in the following colours in all illustrations:

Black: Carbon; blue: nitrogen; red: oxygen; green: chloride; yellow: fluoride; lavender: dysprosium; dark green: chromium; light yellow: aluminium; dark blue: cobalt; green: iron.

Numerical quantities such as bond lengths and angles are given with their standard uncertainties in round brackets after the respective values and refer to last digits. The lengths are given in Angstrom, where $1 \text{ \AA} = 1 \cdot 10^{-10} \text{ m}$.

This thesis was prepared from 1st of September 2017 to 9th of June 2021 at the Institute of Inorganic Chemistry, Faculty of Chemistry and Biosciences of the Karlsruhe Institute of Technology (KIT) under the supervision of Prof. Dr. Annie K. Powell.

Eidesstattliche Erklärung

Bei der vorliegenden Dissertation zu dem Thema

The search for lanthanide containing Single Molecule Magnets with toroidal moments

handelt es sich um meine eigenständig erbrachte Leistung.

Ich habe nur die angegebenen Quellen und Hilfsmittel benutzt und mich keiner unzulässigen Hilfe Dritter bedient. Insbesondere habe ich wörtlich oder sinngemäß aus anderen Werken übernommene Inhalte als solche kenntlich gemacht.

Die Arbeit oder Teile davon habe ich bislang nicht an einer Hochschule des In- oder Auslands als Bestandteil einer Prüfungs- oder Qualifikationsleistung vorgelegt.

Die Richtigkeit der vorstehenden Erklärungen bestätige ich.

Die Bedeutung der eidesstattlichen Versicherung und die strafrechtlichen Folgen einer unrichtigen oder unvollständigen eidesstattlichen Versicherung sind mir bekannt.

Ich versichere an Eides statt, dass ich nach bestem Wissen die reine Wahrheit erklärt und nichts verschwiegen habe.

Karlsruhe, 31.05.2021

.....

Ort und Datum

Kurzzusammenfassung

Diese Arbeit basiert auf der Suche nach molekularen Systemen, die einen toroidalen Grundzustand, d.h. eine vortex-ähnliche Anordnung der Spins, aufweisen, und gleichzeitig Single Molecule Magnet (SMM) Verhalten zeigen. Diese Moleküle werden Single Molecule Toroids genannt (SMTs).

Zu diesem Zweck wurden sowohl synthetisierte als auch aus der Literatur bekannte Komplexe auf ihre Magnetisierung und deren erste Ableitung untersucht. Ebenso wurden ausgewählte Systeme auf ihr SMM Verhalten getestet. Als Analysemethoden in dieser Arbeit kamen dabei das VSM (Vibrating Sample Magnetometer) für die Magnetisierungsmessungen, das SQUID (Superconducting Quantum Interference Device) für die Messung möglichen SMM Verhaltens und das micro-SQUID für die Messung zur Bestätigung des SMM Verhaltens und einem möglichen toroidalen Grundzustand zum Einsatz. Das Programm MAGELLAN wurde verwendet, um die Anisotropie Achsen der Dy(III) Ionen zu identifizieren.

Für die in Kapitel 3 synthetisierten $\{Ln_3\}$ -Dreiecke wurden zusätzlich *ab initio* Berechnungen durchgeführt und im Falle des Dysprosium Analog mit der vom Programm MAGELLAN berechneten Lage der Anisotropieachsen verglichen. Die Ergebnisse hinsichtlich der vortex-ähnlichen Anordnung der Anisotropieachsen bzw. Spins stimmen hier gut überein und der toroidale Grundzustand konnte in den Systemen $[Dy_3(3\text{-ethoxysalicyl})_3(\mu_3\text{-OH})_2(H_2O)_4Cl_2]Cl_2 \cdot 5H_2O \cdot 3MeOH$ (**1**) und $[Dy_3(3\text{-ethoxysalicyl})_3(\mu_3\text{-OH})_2(H_2O)_2(CH_3OH)Cl_3]Cl \cdot 2H_2O \cdot 2CH_3OH$ (**2**) durch Peaks in den Ableitungen der Magnetisierungskurve (M vs H -Plots) und durch micro-SQUID Messungen für (**1**) bestätigt werden. Auch SMM Verhalten wurde in den beiden Komplexen nachgewiesen.

Die in Kapitel 4 synthetisierten $\{M_2Dy_3\}$ -Systeme mit ($M = Cr, Al, Fe, Co$) ((**7**)-(**16**)) können als Sandwich-Komplexe von $\{Dy_3\}$ -Dreiecken betrachtet werden. Hier wurden verschiedene Benzoesäurederivate als Liganden für die Komplexe (**7**) bis (**12**) mit gleichem Metallion M und gleiche Liganden für (**12**) bis (**16**), aber unterschiedliche Metallionen Ionen M , verwendet. Die ersten Ableitungen (dM/dH) der niedrigsten gemessenen Temperaturmagnetisierung zeigten bei den untersuchten Systemen keine eindeutigen Peaks, was mit einem nicht-toroidalen Grundzustand in Verbindung gebracht werden kann, aber kein Ausschlusskriterium hinsichtlich einer möglichen Toroidizität bedeutet. Die mit MAGELLAN berechneten

Anisotropieachsen sind aber mit Vorsicht zu genießen, da nicht zwischen elektronenziehenden/elektronenschiebenden Gruppen an den Liganden unterschieden wird und die Einführung zusätzlicher Metallionen generell zu einer anderen elektrostatischen Verteilung der Ionen führt. Auch hier zeigten einige Systeme SMM-Verhalten.

In Kapitel 5 wurden die isostrukturellen co-planaren $\{Ln_4\}$ -Systeme (**17**) bis (**22**) unter Verwendung einer in-situ Schiff Base synthetisiert. Darüber hinaus wurden Dysprosium-basierte und auch $\{Dy_4\}$ co-planare Systeme aus der Literatur auf ihre Toroidizität getestet, indem die erste Ableitung der Magnetisierung bei den niedrigsten gemessenen Temperaturen verwendet wurde. Hier ließ sich der Übergang von einem nicht-magnetischen Grundzustand zu ersten angeregten Zuständen für einige Systeme mit Hilfe der ersten Ableitung der Magnetisierung finden. Das SMM-Verhalten bzw. der nicht magnetische Grundzustand von $Dy_4(OH)_2(NO_3)_2(DMF)_2(ehimp)_4$ (**18**) wurde mit frequenzabhängigen Suszeptibilitätsmessungen bzw. SQUID/micro-SQUID-Messungen nachgewiesen.

Dabei wurde gezeigt, dass generell kleinere Abstände der Dy(III)-Ionen zu einer Erhöhung der Toroidizität (Wert für das magnetische Feld H für den Übergang von nicht-magnetischem Grundzustand zu angeregtem Zustand) der $\{Dy_4\}$ -Systeme führen und dass dies indirekt auf die erhöhte Anzahl von μ_2O -Brückenliganden zurückzuführen ist. Ebenso verstärkt die Anzahl dieser Brückenliganden vermutlich die Wechselwirkungen zwischen den Dy(III) Ionen. Die Toroidizität scheint sich auch durch die Verwendung von Schiff Base Liganden und/oder negativ geladenen Liganden zu erhöhen.

Kapitel 6 beschäftigt sich mit ringförmigen $\{Dy_6\}$ -Komplexen, die teilweise aus der Literatur bekannt sind, aber für diese Arbeit resynthetisiert wurden, um an diesen micro-SQUID Messungen und MAGELLAN Rechnungen durchzuführen. Der Vergleich dieser Ergebnisse mit magnetischen Messungen am Bulk und *ab initio* Berechnungen aus der Literatur zeigte, dass all diese Systeme aufgrund ihrer hohen Symmetrie toroidale Grundzustände aufweisen.

Abstract

This work is based on the search for molecular systems that exhibit a toroidal ground state, *i.e.*, a vortex-like arrangement of spins, while exhibiting Single Molecule Magnet (SMM) behaviour. These molecules are called Single Molecule Toroids (SMTs).

For this purpose, synthesized complexes as well as those known from the literature were investigated for their magnetization and their first derivative. Selected systems were also tested for their SMM behaviour. The analysis methods used in this work were the VSM (Vibrating Sample Magnetometer) for the magnetization measurements, the SQUID (Superconducting Quantum Interference Device) for the measurement of possible SMM behaviour and the micro-SQUID for the measurement to confirm the SMM behaviour and a possible toroidal ground state.

For the $\{\text{Ln}_3\}$ triangles synthesized in Chapter 3, additional *ab initio* calculations were performed and compared with the position of the anisotropy axes of the dysprosium analogue calculated by the MAGELLAN program. The results with respect to the vortex-like arrangement of the anisotropy axes or spins, has a good agreement here and the toroidal ground state could be confirmed in the systems $[\text{Dy}_3(3\text{-ethoxysalicyl})_3(\mu_3\text{-OH})_2(\text{H}_2\text{O})_4\text{Cl}_2]\text{Cl}_2 \cdot 5\text{H}_2\text{O} \cdot 3\text{MeOH}$ (**1**) and $[\text{Dy}_3(3\text{-ethoxysalicyl})_3(\mu_3\text{-OH})_2(\text{H}_2\text{O})_2(\text{CH}_3\text{OH})\text{Cl}_3]\text{Cl} \cdot 2\text{H}_2\text{O} \cdot 2\text{CH}_3\text{OH}$ (**2**) by peaks in the derivatives of the magnetization curve (M vs H plots) and by micro-SQUID measurements for (**1**). SMM behaviour was also detected in the two complexes.

In chapter 4, $\{\text{M}_2\text{Dy}_3\}$ systems with ($\text{M} = \text{Cr}, \text{Al}, \text{Fe}, \text{Co}$) ((**7**)-(16)) were synthesized which can be regarded as sandwich complexes of $\{\text{Dy}_3\}$ triangles. Here, different benzoic acid derivatives were used as ligands for the complexes (**7**) to (**12**) with the same metal(III) ions M and the same ligands but different metal(III) ions M for (**12**) to (**16**). The first derivatives (dM/dH) of the lowest measured temperature magnetization did not show clear peaks for the investigated systems, which can be associated with a non-toroidal ground state but is not a criterion for exclusion with respect to a possible toroidicity. The anisotropy axes were calculated using MAGELLAN, but these should be treated with caution, as no distinction is made between electron-withdrawing/electron-pushing ligands and the introduction of additional metal ions generally results in a different electrostatic distribution. Again, some systems showed SMM behaviour.

In Chapter 5, the isostructural co-planar $\{\text{Ln}_4\}$ systems (**17**) to (**22**) were synthesized using an in-situ Schiff base ligand. In addition, $\{\text{Dy}_4\}$ co-planar systems from the

literature were tested for their toroidicity (value for the magnetic field H for the level-crossing from the non-magnetic ground state to excited state) by using the first derivative of the magnetization at the lowest measured temperatures. Some systems with a non-magnetic ground state could be found here. The SMM behaviour and the toroidal ground state of $\text{Dy}_4(\text{OH})_2(\text{NO}_3)_2(\text{DMF})_2(\text{ehimp})_4$ (**18**) was demonstrated with frequency-dependent susceptibility measurements and SQUID/micro-SQUID measurements, respectively.

Here, it was shown that generally smaller distances of the Dy(III) ions lead to an increase in the toroidicity of the $\{\text{Dy}_4\}$ systems and that this is indirectly due to the increased number of $\mu_2\text{-O}^-$ bridging ligands. Likewise, the number of these bridging ligands presumably enhances the interactions between the Dy(III) ions. Toroidicity is also enhanced using Schiff base ligands and/or negatively charged ligands.

Chapter 6 deals with $\{\text{Dy}_6\}$ wheel complexes partially known from literature but resynthesized for this work to perform micro-SQUID measurements and MAGELLAN calculations. The comparison of these results with bulk measurements and *ab initio* calculations from the literature showed, that they all exhibit toroidal ground states due to their symmetry.

Table of contents

1	Introduction and theory	1
1.1	Magnetism and magnetic properties in materials	3
1.2	Van-Vleck equation	8
1.3	Single Molecule Magnets (SMMs)	10
1.4	Anisotropy	16
1.5	Magnetic frustration	20
1.6	Toroidal moments	22
1.7	Single Molecule Toroids (SMTs)	27
1.8	Theoretical determination of anisotropy axes	34
2	Motivation	37
3	Triangular Ln₃ systems	39
3.1	Comparison with the Dy ₃ triangular systems (1) and (2)	42
3.1.1	Calculations on (1)	49
3.1.2	Calculations on (2)	52
3.1.3	Magnetic properties of (1) and (2)	55
3.1.4	Isostructural compounds of (2) with Eu (3), Tb (4), Ho (5) and Er (6)	63
3.2	Summary of triangular Ln ₃ systems	69
4	Heteronuclear M₂Dy₃ systems	72
4.1	Static magnetic properties of (7) to (12)	80
4.2	Magnetization of (7) to (12)	81
4.3	Dynamic magnetic properties of (7) and (9)	84
4.4	Static magnetic properties of (13), (14) and (15)	86
4.5	Magnetization of (13), (14) and (15)	87
4.6	Dynamic magnetic properties of (15)	89
4.7	Single crystal measurements of (15)	90
4.8	MAGELLAN calculations on (8) to (16)	91
4.9	Summary of heteronuclear M ₂ Dy ₃ systems	95
5	Tetranuclear Ln₄ systems	100
5.1	Molecular structure of isostructural Ln ₄ complexes (17)-(22)	102
5.2	Magnetic properties of (18) and (20)	106
5.3	Investigation of magnetization properties of planar Ln ₄ systems in the literature	111
5.4	Summary of tetranuclear Ln ₄ systems	121
6	Hexanuclear Ln₆ systems	124

6.1	Properties of $[\text{Dy}_6(\text{NO}_3)_6(\text{teaH})_6] \cdot 2\text{C}_2\text{H}_5\text{OH}$ (23)	128
6.2	Properties of $[\text{Dy}_6(\text{apadH}_2)_6(\text{NO}_3)_6]$ (24)	132
6.3	Properties of $[\text{Dy}_6(\text{NO}_3)_3(\text{pmide})_6]$ (Dy6-4)	136
6.4	Summary of hexanuclear Dy_6 systems	140
7	Overall summary and conclusion	142
8	Experimental section	151
8.1	General procedures	151
8.2	Synthesis	153
9	Crystallographic data	162
10	Literature	174
11	Acknowledgements	181
12	Appendix	182
12.1	Molecular structures, bond lengths, angles and distances of (1) and (2)	182
12.2	Molecular structure, bond lengths, angles and distances of (3) to (6)	186
12.3	Molecular structure, coordination spheres, bond lengths, angles, distances and packing of (7) to (16)	191
12.4	Molecular structure, bond lengths, angles and distances of (17) to (22)	225
12.5	List of abbreviations	231
12.6	List of complexes	232
12.7	List of tables	233
12.8	List of figures	235

1 Introduction and theory

Single Molecule Toroids (SMTs) are defined as bistable coordination clusters with a toroidal magnetic state, which arises from a “vortex-like” arrangement of the spins. This leads to an almost vanishing magnetic moment in the ground state but a non-zero toroidal moment.^[1] These kind of complexes have the possibility for next-generation ultra-high-density information storage, multiferroic materials with magnetoelectric effect and magnetic, electronic and optical switches.^[2,3] SMTs are also promising candidates for the use in quantum computation due to their relatively insensitivity against external magnetic fields and can therefore be packed more densely than for example Single Molecule Magnets (SMMs) or Single Ion Magnets (SIMs). In theory these systems can store one bit per molecule if the temperature is lower than the energy gap between the excited doublets and the ground state.^[4] Precisely because of their weak response to the environment, the detection of a toroidal moment and their spin arrangement is a difficult task and can be managed by the combination of different techniques such as magnetic measurements, cantilever torque measurements and *ab initio* calculations.^[5] The “unusual” magnetic behaviour of the first SMT, the {Dy₃} triangle in 2006^[6], soon become the benchmark for non-magnetic ground states and their toroidal explanation. The cyclic topology which is believed to be a basic feature of SMTs has been found in a range of homonuclear complexes such as other {Dy₃} triangles^[6-11], planar {Dy₄} squares^[12-14], {Dy₄} butterfly-shaped complexes^[15], {Dy₄} cubanes^[1], {Dy₆} hexagons^[11,16], {Dy₆} helicates^[17] and {Dy₈} wheels^[18]. Coupled {Dy₃} units lead to an enhanced toroidal moment as demonstrated in homonuclear {Dy₆} complexes.^[19] The coupling of {Dy₃} units can also be realised via a paramagnetic 3d-ion and this led to enhanced toroidal moment of zero due to strong exchange coupling between the {Dy₃} units and the 3d-ion. These kinds of complexes were realised in compounds such as heptanuclear {CrDy₆}^[20,21] complexes and {Cu^{II}Dy₃}_n 1D chains.^[22] Further heteronuclear complexes where strong exchange couplings between the metal centres are favourable for creating the toroidal arrangements of the spins are {Fe₈Dy₈}^[4], {Cu^{II}Ln₆}^[2] and {Fe₁₈Dy₆}^[23] cycles. The dipole and/or exchange interactions between the spin centres and the strong axuality of the ground state are key factors for the formation of a toroidal state. Due to the strong axuality of the anisotropic Dy(III)

ion, most of the SMTs are dysprosium-based.^[2,4] Nevertheless, a toroidal arrangement of spin centres could be found in Tb(III) and Ho(III) containing complexes such as {Tb₃} and {Ho₃}^[11], {Tb₆} and {Ho₆}^[24], {CrTb₆} and {CrHo₆}^[21] and {Tb₆Cu₆}^[2].

In the following, the basics of magnetism and the measurement of the magnetization *via* the susceptibility (chapter 1.1) and the quantum chemical description of the magnetization and susceptibility, respectively, using the Van-Vleck equation (chapter 1.2) is explained. The characteristics of Single Molecule Magnets and their determination are described in chapter 1.3, followed by a brief introduction of the anisotropy (chapter 1.4), magnetic frustration (chapter 1.5) and toroidal moments (chapter 1.6). Outstanding examples for SMTs are given in chapter 1.7. The theoretical determination of the anisotropy axes *via ab initio* calculation and MAGELLAN are given in chapter 1.8.

1.1 Magnetism and magnetic properties in materials

There are two different types of non-cooperative magnetism in materials: diamagnetism and paramagnetism. Diamagnetism is based on the property of paired electrons inducing an opposing magnetic field in the material which leads to a repulsion of the applied magnetic field lines. Diamagnetic materials have a total spin of zero. Every element in the periodic table - except hydrogen - has a diamagnetic component. Paramagnetism originates from unpaired electrons which, when an external magnetic field is applied, align in the same direction of the field. However, due to the thermal self-motion of the magnetic moments in the material and the resulting random arrangement of the magnetic moments, paramagnetic materials do not show spontaneous magnetization.

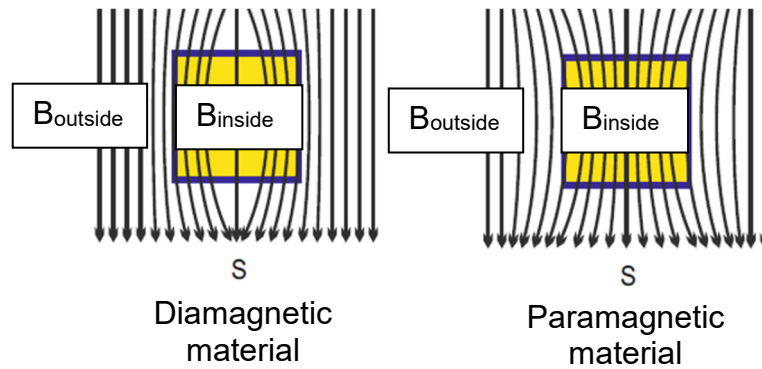


Figure 1-1 Magnetic flux course in a diamagnetic and paramagnetic material under an applied field. Adapted from reference^[25].

The strength of a magnetic field is described by the density of magnetic field lines, the magnetic flux density B . If a material is placed in a magnetic field H , the change in the magnetic flux density within the body is expressed as the magnetization M and lead to a new magnetic flux density B_{inside} as shown in Figure 1-1. This can be written with the magnetic permeability in vacuum μ_0 :

$$B_{inside} = B_{outside} + \mu_0 \cdot (H + M)$$

The magnetization M can be either negative (diamagnetism) or positive (paramagnetism). In material, the material-dependent magnetic permeability μ_r is added and this leads to:

$$B_{inside} = \mu_r \cdot B_{outside} = \mu_r \cdot \mu_0 \cdot (H)$$

The material-dependent permeability can also be written with the voluminal susceptibility χ_V as $\chi_V = \mu_r - 1$ and it is common to state the susceptibility as molar susceptibility with the unit cm^3/mol . The magnetic susceptibility χ is used to determine the absorption capacity of these magnetic field lines by the corresponding material and is linked to the magnetization M and the magnetic field H as follows:

$$\chi = \frac{M}{H}$$

The measured susceptibility consists of the paramagnetic χ^P and the diamagnetic part χ^D .

$$\chi = \chi^D + \chi^P$$

Therefore, the measured susceptibility must be corrected to obtain the susceptibility, arising only from paramagnetic centres. Either the diamagnetic susceptibility of the free ligand or the corresponding Na/K salt can be used for this. However, it is common to use Pascal's constants for the diamagnetic correction. These are based on the addition of the diamagnetic fractions of each atom and bond in the molecule. An approximation is given by the equation with the molecular weight M_{mol} and values for k between 0.4 and 0.5:

$$\chi^D = -k \cdot M_{mol} \cdot 10^{-6}$$

The interactions between neighbouring paramagnetic centres lead to collective magnetism and the spin alignment under a certain temperature is described in three main types of cooperative magnetism: Antiferromagnetism, ferromagnetism, and ferrimagnetism. The spin alignments for the different types are displayed in Figure 1-2.

Ferromagnetism: The regions of spin in a ferromagnetic material are called Weiss-domains. The existence of these domains is due to a reduction of the internal energy by splitting magnetic regions into smaller domains. These domains are in a statistical distribution and no spontaneous magnetization is observed. An external magnetic field aligns the spins within the domains parallel to the field. The induced magnetic field is maintained below a substance-specific temperature, the Curie temperature T_C . Above this temperature, the thermal component becomes too large,

and the arrangement of the spins is broken up, which leads to a random distribution of the magnetic moments. The material then acts as a paramagnet.

Antiferromagnetism: Antiferromagnetic materials form sublattices due to the overlapping of domains. Below a specific temperature, the Néel temperature T_N , the spins of these sublattices are arranged in opposite directions. The antiparallel arrangement of the spins leads to an extinction of the total magnetic moment and no spontaneous magnetization occurs. By exceeding this temperature, the antiparallel order of the spins breaks down and the material acts as a paramagnet.

Ferrimagnetism: The sublattices in ferrimagnetic materials have different magnitudes of spins which are arranged antiparallel. This is a special case of an antiferromagnetically coupled material. Below the Curie temperature T_C , these materials behave like ferromagnets. As the temperature increases, these revert to paramagnetic behaviour.

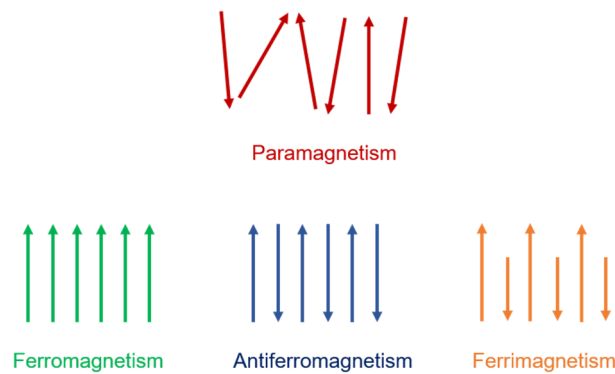


Figure 1-2 Spin alignment for the different types of magnetism.

The susceptibility is measured experimentally as a function of temperature and can be plotted as χ vs T , with ferro-, antiferro- and paramagnetism detectable in the graph (Figure 1-3, left). However, it is more common to plot the χT product against the temperature, χT vs T . With this plot, all four types of magnetism can be distinguished more easily (Figure 1-3, right). Another plot is that of the reciprocal of the susceptibility against temperature, $\frac{1}{\chi}$ vs T (Figure 1-4). Here the intersection with the abscissa is the Weiss constant θ and the slope corresponds to the reciprocal of the Curie constant, C^{-1} . Negative θ indicates antiparallel interactions between the spin centres (antiferromagnetism (blue line) and ferrimagnetism (yellow line)), positive θ indicates parallel interactions between the spin centres (ferromagnetism (green line)). A

paramagnet (red line) has the Weiss constant zero and the curve passes through the origin (Figure 1-4). The Curie-Weiss law is applied here:

$$\chi = \frac{C}{T - \theta}$$

and

$$\frac{1}{\chi} = \frac{T - \theta}{C}$$

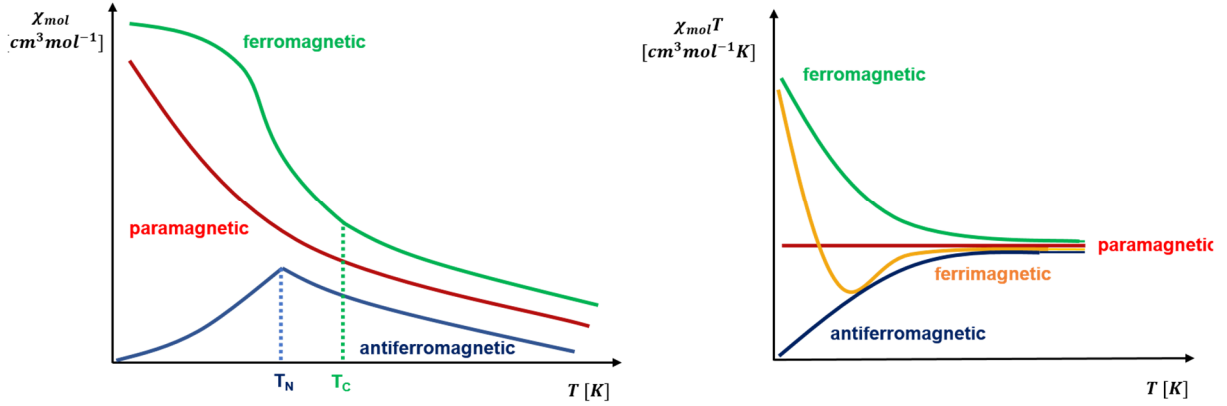


Figure 1-3 χ vs T and χT vs T plots.

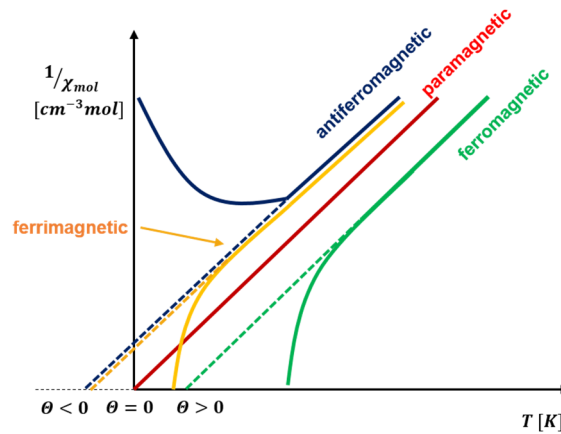


Figure 1-4 $1/\chi$ vs T plots with Weiss constant θ .

Characteristic for a ferromagnetic material is the formation of a hysteresis (Figure 1-5), where the material remains its magnetization (M_R), called remanence, even by switching off the external magnetic field H . The first time the material experiences an applied magnetic field, the domain walls are moving, and all magnetic moments are aligned parallel when the saturation of the magnetization (M_{sat}) is reached. This is illustrated by the so-called new curve in red. By reducing the field, the magnetization does not follow the red curve, but the blue one, it reaches the remaining magnetization, also known as remanence (M_R), at zero applied magnetic field. There

is a magnetic field in the other direction needed to reduce the magnetization to zero. This is named the coercivity with the corresponding coercive field $-H_c$. *Vice versa* the magnetization follows the direction of the applied field in the other direction to the saturated magnetization $-M_s$, the remaining magnetization $-M_R$ is reached for zero field H and a coercive field H_c is needed to get back to zero magnetization. A stronger field leads again to the saturated magnetization M_{sat} . Ferromagnetic materials with small coercivity are known as soft magnets and the change of the magnetization is therefore easier to accomplish. According to those materials with a high coercivity are known as hard magnets. To recover to the new curve, respectively to the origin, one can reduce the magnetic field in small steps so the magnetic moments can align in the field direction.^[26-29]

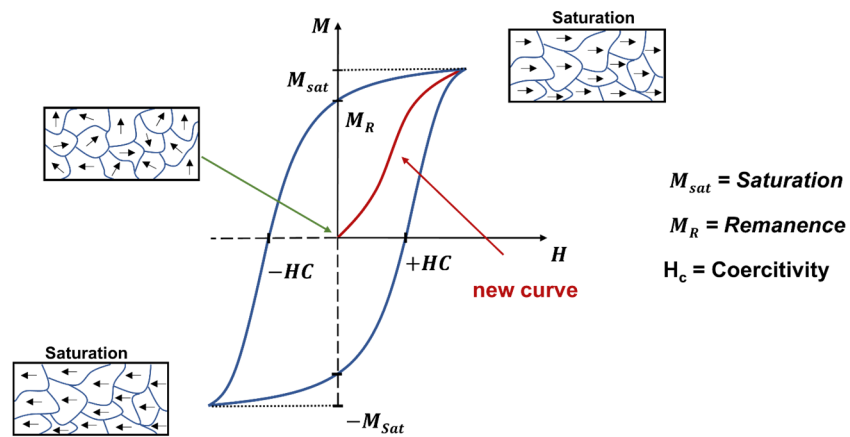


Figure 1-5 Hysteresis for a ferromagnet with the new curve (red), saturation of magnetization M_{sat} , remanence M_R and coercivity H_c . The black arrows in the boxes represent the magnetic moments within the domains.

1.2 Van-Vleck equation

Magnetism from a quantum chemical point of view can be described by the susceptibility of the energy states and is described by the Van-Vleck equation (1932).^[30,31] With no external magnetic field, neighbouring energy levels are degenerate. These energy levels have, as far as there is no coupling with excited states, the energies $2S + 1$ with the total angular momentum S . The application of a magnetic field cancels the degeneracy of the states and this is known as the first-order Zeeman effect. The splitting is thus proportional to the magnetic field H , $H \sim E_n$, and can be described with the Bohr magneton μ_B , the gyromagnetic constant g and the individual states m_s as:

$$E_n = \mu_B \cdot g \cdot H \cdot m_s$$

The mixing of the states, *i.e.* of ground state and excited states, is called the second-order Zeeman effect. The energy levels here are proportional to H^2 and the series expansion of the Van-Vleck equation is given as:

$$E_n = E_n^0 + E_n^1 H + E_n^2 H^2 + \dots$$

The first term is the energy of the states n without an applied field (E_n^0), the second term is the energy with an applied field which is the first-order Zeeman effect (E_n^1) and the third term takes the interactions of the ground and excited states into account which is the second-order Zeeman effect (E_n^2).

A microscopic moment μ_n can be assigned to each magnetic centre of a material when a magnetic field is applied. With the energy of the states E_n and the magnetic field H , this can be described as:

$$\mu_n = - \frac{dE_n}{dH}$$

The Boltzmann distribution describes the occupation of these states and with the Avogadro number N_A , the Boltzmann constant k and the temperature T , the macroscopic moment μ_M for one mole of substance is obtained with the equation:

$$\mu_M = N_A \frac{\sum_n (-\frac{dE_n}{dH}) \exp(-\frac{E_n}{kT})}{\sum_n \exp(-\frac{E_n}{kT})}$$

The terms E_n^1 and higher are relatively small compared to kT and with the following assumption

$$\exp\left(-\frac{E_n}{kT}\right) = \left(1 - \frac{E_n^1 H}{kT}\right) \exp\left(-\frac{E_n^0}{kT}\right)$$

the equation can be simplified as follows:

$$\mu_M = N_A \frac{\sum_n (-E_n^1 - 2E_n^2 H) \left(1 - \frac{E_n^1 H}{kT}\right) \exp\left(-\frac{E_n^0}{kT}\right)}{\sum_n \left(1 - \frac{E_n^1 H}{kT}\right) \exp\left(-\frac{E_n^0}{kT}\right)}$$

Another assumption is that the macroscopic magnetic moment μ_M is linear in H and together with $\mu_M = 0$ for $H = 0$ we obtain:

$$\mu_M = N_A \frac{H \sum_n \left[\frac{(E_n^1)^2}{kT} - 2E_n^2\right] \exp\left(-\frac{E_n^0}{kT}\right)}{\sum_n \exp\left(-\frac{E_n^0}{kT}\right)}$$

And for the molar susceptibility:

$$\chi_M = \frac{\mu_M}{H} = N_A \frac{\sum_n \left[\frac{(E_n^1)^2}{kT} - 2E_n^2\right] \exp\left(-\frac{E_n^0}{kT}\right)}{\sum_n \exp\left(-\frac{E_n^0}{kT}\right)}$$

This equation is valid if it is assumed that no long-range ordered ferro- or ferrimagnetic substances are present and weak fields or high temperatures prevail, *i.e.* $\frac{H}{kT} \ll 1$. If the Zeeman splitting, *i.e.* the first-order Zeeman effect, is applied, the following equation is obtained for a gyromagnetic factor $g = 2$, the ground spin S and the corresponding energy states $M_S = 2S + 1$:

$$\chi_M = N_A \frac{\frac{g^2 \mu_B^2}{kT} \sum_{M_S=-S}^{M_S=+S} M_S^2}{2S+1} = N_A \frac{g^2 \mu_B^2}{3kT} S(S+1)$$

This form practically approximates the following equation used to determine the χT product of the system at room temperature:

$$\chi T = \frac{g^2}{8} \cdot S(S+1)$$

At high values of $\frac{H}{kT}$, *i.e.* at high fields and/or low temperatures, the magnetic moments are aligned in the field direction and the saturation magnetization M_{sat} can be described as:

$$M_{sat} = N_A \cdot g \cdot \mu_B \cdot S$$

1.3 Single Molecule Magnets (SMMs)

Single Molecule Magnets^[32-37] are paramagnetic materials which exhibit slow relaxation of magnetization at their molecular level and can therefore retain their magnetization for a relatively long time in the absence of an applied magnetic field. This behaviour can be quantified using, e.g. hysteresis measurements, and the highest temperature up to which hysteresis can be observed is called the blocking temperature T_B . The hysteresis is temperature and sweep rate dependent. These molecular nanomagnets have the potential to be used as high-density information storage, molecular spintronic devices or magnetic qubits provide the prospect of significant miniaturisation.

The characteristic of an SMM is the bistability of the ground state, often depicted with a double well potential (Figure 1-6 (a)), separated by the energy barrier U_{eff} . This energy barrier is $U_{eff} = S^2|D|$ for systems with integer spins (non-Kramers' ion) and $U_{eff} = (S^2 - \frac{1}{4})|D|$ for half-integer spins (Kramers' ion), where S is the overall spin of the system and the parameter D the absolute value of the zero-field splitting (for SMMs D is negative). The unit of the energy barrier is stated either in K or cm^{-1} , the conversion is given by:

$$U_{eff}[K] \cdot \frac{k_B[J K^{-1}]}{hc[J cm]} = U_{eff}[cm^{-1}]; \text{ leads to } (1.44 \text{ K} \sim 1 \text{ cm}^{-1})$$

with

$hc = 1.986 \cdot 10^{-23} J cm$ (with Planck constant ($h = 6.626 \cdot 10^{-34} Js$) and speed of light ($c = 2,998 \cdot 10^{10} cm s^{-1}$) and $k_B =$ Boltzmann constant ($1.3806 \cdot 10^{-23} J K^{-1}$)).

The possibility of spin up or down in the ground state can be varied by the application of a magnetic field. Therefore, on application of a magnetic field the system will favour having all spins in the field direction which means that the degeneracy is lifted and energy states (M_S) with spins in field direction are favoured (Figure 1-6 (b)). If the field is now switched off, the ground state is degenerated again with a larger population of one spin direction in one of these degenerated states. To reach equilibrium of the spins again, spin reversal occurs ideally over the energy barrier (Figure 1-6 (c)).

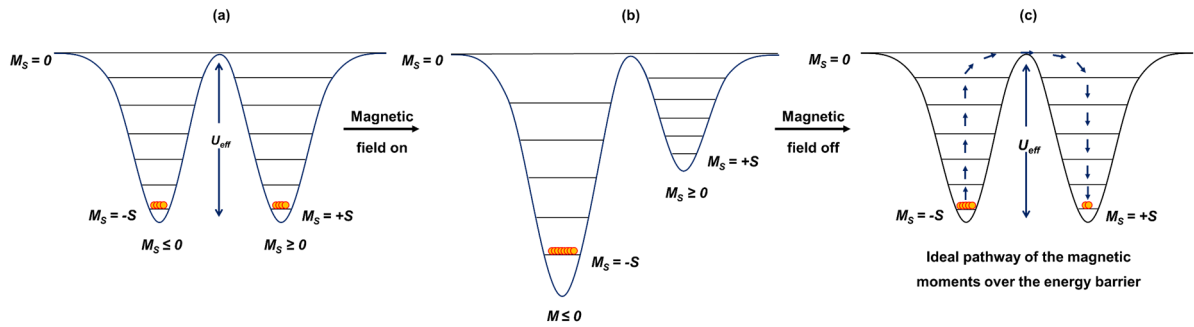


Figure 1-6 The bistability (a) is destroyed by applying a magnetic field and reduce the energy of the M_S states in field direction (b). By switching off the magnetic field (c), the relaxation of the spins is slowed down by an energy barrier U_{eff} . The yellow dots represent the spins.

This ideal pathway is known as the Orbach process. However, relaxation processes mediated by acoustic or optical phonons (lattice and molecule vibrations, respectively) in addition to the possibility of ground state quantum tunnelling (QTM) and thermal activated QTM (TA-QTM), will shortcut the **Orbach process** (red line in Figure 1-7, left) and reduce the energy barrier. Along with zero field quantum tunnelling these processes are the **Direct process** (green line in Figure 1-7, left) and the **Raman process** (blue line in Figure 1-7, left). The spins are also able to tunnel from energy states which are in resonance but with opposite spin directions. This is possible within the ground state and is known as quantum-tunnelling of the magnetization (**QTM**) (red dotted line in Figure 1-7, left). Also, thermally-assisted QTM (**TA-QTM**), is possible within one excited state (pink dotted line in Figure 1-7, left). The Direct process is a one phonon-process, and the Raman processes (1st and 2nd order) and the Orbach process are two-phonon processes (Figure 1-7, right).

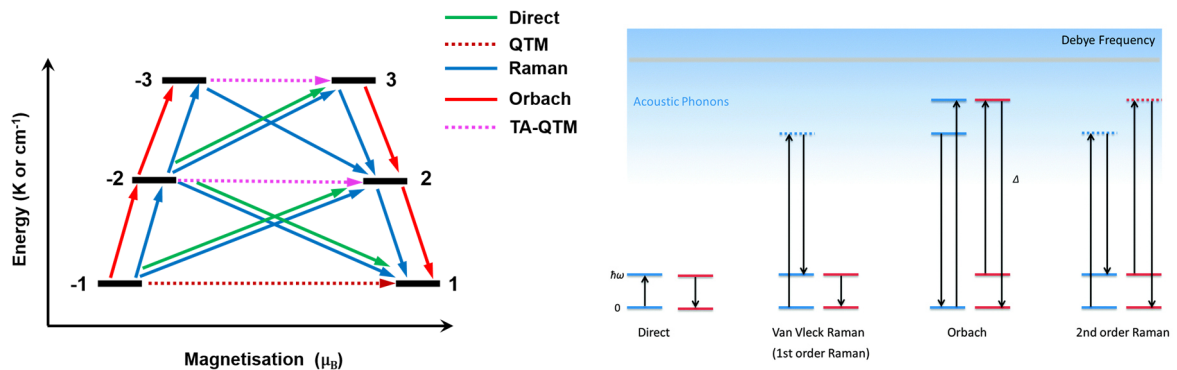


Figure 1-7 Left: The arrows show the mechanisms of relaxation of magnetization. An ideal SMM corresponds to the suppression of all relaxation mechanisms except the Orbach process (red arrows). Adapted from reference^[38]. Right: The blue lines indicate levels of the lattice and the red ones are crystal field levels of the lanthanide ion. The dotted lines are virtual states, involved only in the Raman processes. Reprinted with permission from reference^[39].

The following equation can be used to describe the various relaxation processes.

$$\tau^{-1} = \underbrace{AH^{n_1}T}_{\text{Direct}} + \underbrace{CT^{n_2}}_{\text{Raman}} + \underbrace{\tau_0^{-1} \exp\left(-\frac{U_{eff}}{k_B T}\right)}_{\text{Orbach}} + \underbrace{\frac{B_1}{1 + B_2 H^2}}_{\text{QTM}}$$

The parameters A, C and τ_0 contain the spin-phonon coupling. B includes the energy difference between states where transition occurs and system specific parameters. The values of the parameter n differ from 2-9.^[39] H is the applied magnetic field, therefore the part of the Direct process to the relaxation time is increased at higher fields. In contrary, the part of QTM is reduced at higher fields because the degeneracy of the sublevels is lifted.

The spin-lattice processes (Direct, Raman, Orbach) are predominant in the thermal regime. With smaller temperatures QTM and TA-QTM occur in the so-termed quantum-assisted thermal regime and all the processes contributing to the magnetic relaxation. At very low temperatures the spin relaxation is often entirely controlled by QTM.^[39,40]

The relaxation times can be examined by alternating current (AC) measurements out of the maxima from out-of-phase frequency-dependent susceptibility measurements at different temperatures. In-phase χ' and out-of-phase χ'' susceptibility measurements are illustrated in Figure 1-8 left and right. It is also possible to examine the relaxation times out of the temperature-dependent out-of-phase susceptibility measurements at different frequencies.

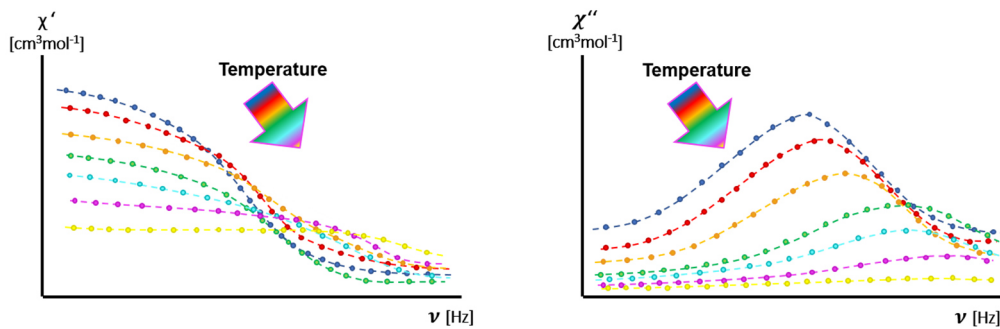


Figure 1-8 Frequency-dependent in-phase (left) and frequency-dependent out-of-phase measurements (right).

These maxima can then be plotted with the natural logarithm of the relaxation time τ versus the inverse temperature T , illustrating the relaxation processes (Figure 1-9).

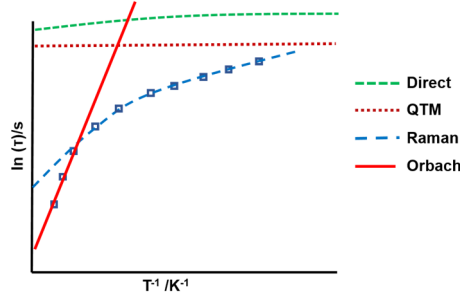


Figure 1-9 The different relaxation processes in a plot of $\ln t$ vs T^{-1} . Only the Orbach process follows the Arrhenius law in a straight line (red line).

The relaxation times for the Orbach process at high temperatures result in a straight line (red line in Figure 1-9) and the energy barrier U_{eff} is given by the slope of the Arrhenius law:

$$\tau = \tau_0 \cdot \exp\left(\frac{U_{eff}}{kT}\right)$$

The pre-exponential factor τ_0 , often referred to the relaxation time itself, is calculated from the intercept with the ordinate as follows:

$$\tau_0 = \exp -(intercept)$$

To establish the distribution of the relaxation processes, the Cole-Cole plot, based on the Debye model is used. The susceptibility $\chi(\omega)$ depends on the angular frequency ω of the applied alternating field (AC) and is composed of an isothermal χ_T and an adiabatic susceptibility χ_S . The thermal equilibrium requires a time τ to establish. The isothermal susceptibility χ_T is equal to the measured susceptibility χ , if the frequency ω of the ac field is low, $\omega \ll 1$. If $\omega \gg 1$, the system has no time to exchange energy with the external world and the adiabatic susceptibility χ_T is measured. The one-component Debye model is given with:

$$\chi(\omega) = \chi_S + \frac{\chi_T - \chi_S}{1 + (i\omega\tau)^{1-\alpha}}$$

The frequency dependence of χ' and χ'' can be split into:

$$\chi'(\omega) = \chi_S + \frac{(\chi_T - \chi_S)[1 + (\omega\tau)^{1-\alpha} \sin(\pi\alpha/2)]}{1 + 2(\omega\tau)^{1-\alpha} \sin(\pi\alpha/2) + ((\omega\tau)^{2-2\alpha}}$$

$$\chi''(\omega) = \chi_S + \frac{(\chi_T - \chi_S)[(\omega\tau)^{1-\alpha} \cos(\pi\alpha/2)]}{1 + 2(\omega\tau)^{1-\alpha} \sin(\pi\alpha/2) + ((\omega\tau)^{2-2\alpha}}$$

The Argand plot (Cole-Cole 1941) of $\chi'(\omega)$ vs $\chi''(\omega)$ ideally results in semicircles and the parameter α indicates the distribution of the relaxation processes (Figure 1-10). The larger the distribution, the larger α is. With increasing temperature, α usually decreases because of the smaller number of different relaxation processes on-going in the high temperature area.

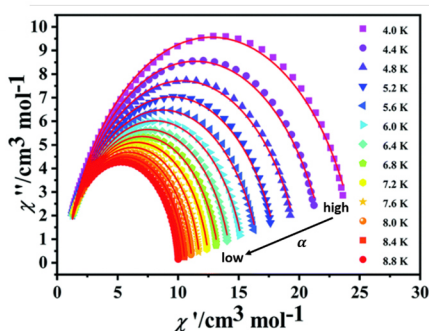


Figure 1-10 Cole-Cole plot at different temperatures with the distribution parameter α . Adapted with permission from reference^[41]. Copyright 2020 Royal Society of Chemistry.

Observed AC susceptibility behaviour may also result from intermolecular interactions of spin centres. Therefore, a micro-SQUID investigation of the hysteresis can go to low enough temperatures on single crystals to establish whether the magnetism is molecular based.^[42] Here, the magnetization is measured as a function of the magnetic field H at fixed sweep rates or as a function of temperature (Figure 1-11). Furthermore, the smaller steps that can be observed within the hysteresis are generated by quantum tunnelling of magnetization (QTM) and/or spin reversal. The hysteresis loops widen with higher sweep rates or lower temperatures.^[43] This makes it possible to monitor whether the relaxation becomes time and temperature-independent which is only possible for molecules. This is illustrated in Figure 1-12 with the M vs t plot for different temperatures where the slow relaxation of magnetization under 0.1 K is temperature-independent, seen by the overlapping curves for 0.1 and 0.04 K.^[44]

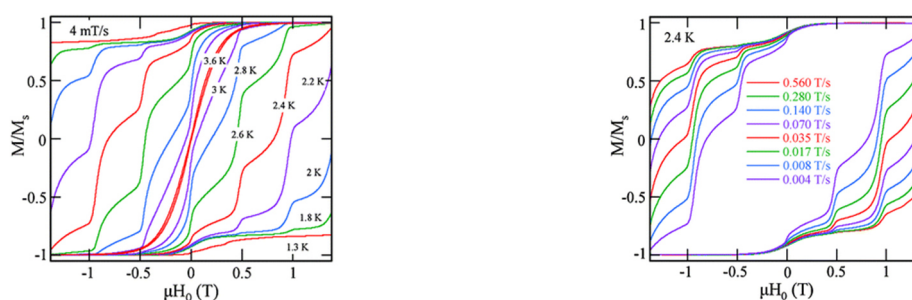


Figure 1-11 Hysteresis loops for a complex of the Mn₁₂ family. Adapted with permission from reference^[45]. Copyright 2005 American Chemical Society.

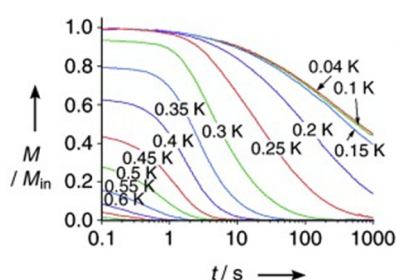


Figure 1-12 The M vs T plot shows time-independent slow relaxation of magnetization below 0.1 K. Adapted with permission from reference^[44]. Copyright 2005 Wiley-VCH.

1.4 Anisotropy

Nowadays, it is known that increasing the spin ground state S does not necessarily increase the energy barrier of SMMs. It is rather the case that high anisotropy, a directional dependence of the magnetization, has a strong positive influence on the height of the energy barrier. The anisotropy determines the preferred alignment of the magnetic moment along a specific direction which is either defined as the easy axis or the easy plane of the system. The lowest energy level defines the most favourable direction of magnetization. The energy levels are split through several effects and can be divided into:

- *Coulomb or interelectronic repulsion*, which describes the repulsion between electrons in the same atom and has the strongest influence on the degeneration of the energy levels.
- *Ligand or crystal field effects*, which describe the repulsion between the metal ions and the ligands which are considered as point charges.
- *Spin-orbit coupling*, which describes the interaction between the magnetic moment of the electron spin and the orbital angular momentum within the atom.

The influence of the individual interactions in 3d transition metals follows the order Coulomb repulsion > Ligand field > Spin-orbit coupling. The ligand field is stronger than the Spin-orbit coupling because the orbital angular momentum L is *quenched*. The quantum number M_S is used to describe the energy states. However, it is insufficient to use M_S to describe the energy states in lanthanides. In lanthanides, the f orbitals are "buried" and do not participate in bonds with the ligand, or only to a limited extent. Therefore, the interactions between the electron spins of the f-orbital and the orbital angular momentum are not negligible and stronger than the ligand field effects. Thus, the quantum number M_J is used to describe the energy states in lanthanides. The electronic interactions for lanthanide ions and the usual energy quantities are shown in Figure 1-13. The Zeeman effect refers to the further splitting of the multiplets by applying a magnetic field.

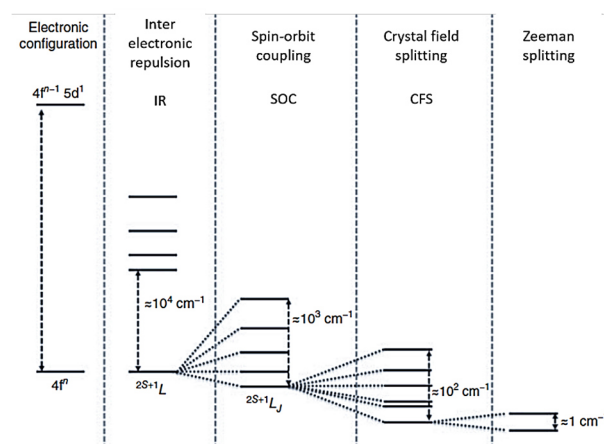


Figure 1-13 Electronic interactions for lanthanide ions and the usual energy quantities. Adapted with permission from reference^[46]. Copyright 2016, Wiley-VCH Verlag.

In this context, the group of lanthanides is highly interesting. Not only have they already shown interesting magnetic properties, including slow relaxation of the magnetization, but their high anisotropy compared to transition metals has also come to the fore. In this respect, Rinehart and Long^[47] developed a magneto-structural correlation between free lanthanide ions and their ligand field environment in 2011, based on the work of Sievers^[48]. This shows that the ground state of ions with oblate electron densities, such as is the case with Dy(III) or Tb(III), is stabilised by axial electron density in the ligand field (Figure 1-14, left). If we look at the reorientation of the spins (green arrow), the ions go from their oblate shape into a prolate shape within their different energy levels m_j (Figure 1-14, right). Ions which possess a prolate electron density in their ground state, such as Er(III) or Tm(III), are stabilised by an equatorial ligand field environment (Figure 1-15, left) and by reorientation of the spin, they change their shape from prolate to oblate (Figure 1-15, right) which is the energetically most unfavourable state. These insights into the electrostatic correlation between ligand field and lanthanide ions led to coordination compounds with blocking temperatures up to 80K and the possible handling of SMMs in the liquid nitrogen range.^[49] Although Tb(III) has similar properties in terms of electron density shape and even higher anisotropy than Dy(III), it is the systems with Dy(III) that often show the better SMM properties, as the bistability is not always given for non-Kramers' ions like Tb(III).

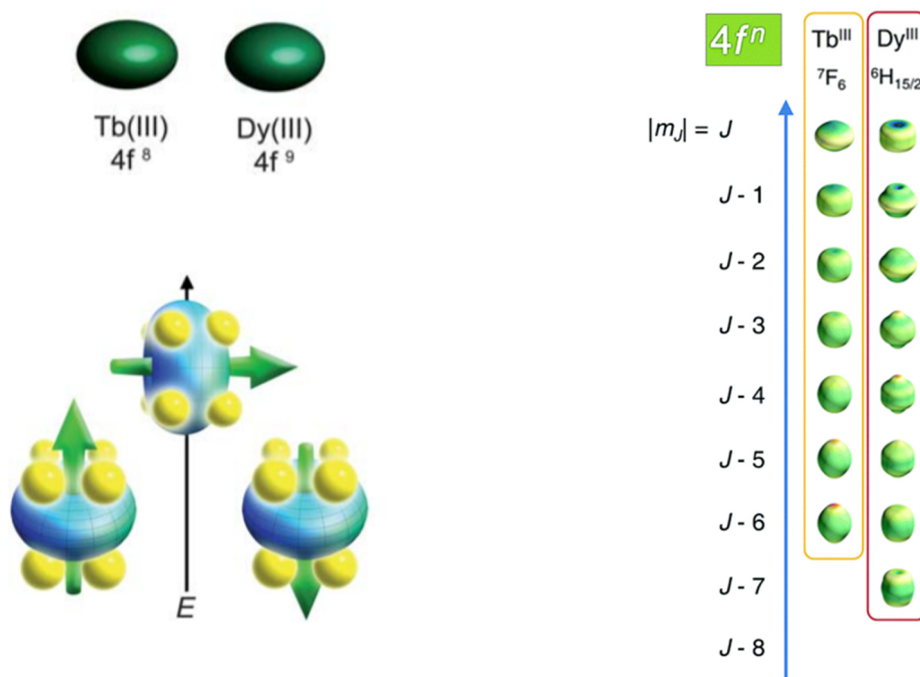


Figure 1-14 Left: The electron density for oblate ions (Dy(III), Tb(III)) in the ground state is stabilised by an axial ligand field (yellow dots). The shapes from oblate to prolate in the different energy states (right) with $J = 6$ for Tb(III) and $J = 15/2$ for Dy(III). Adapted with permission from references [47,50].

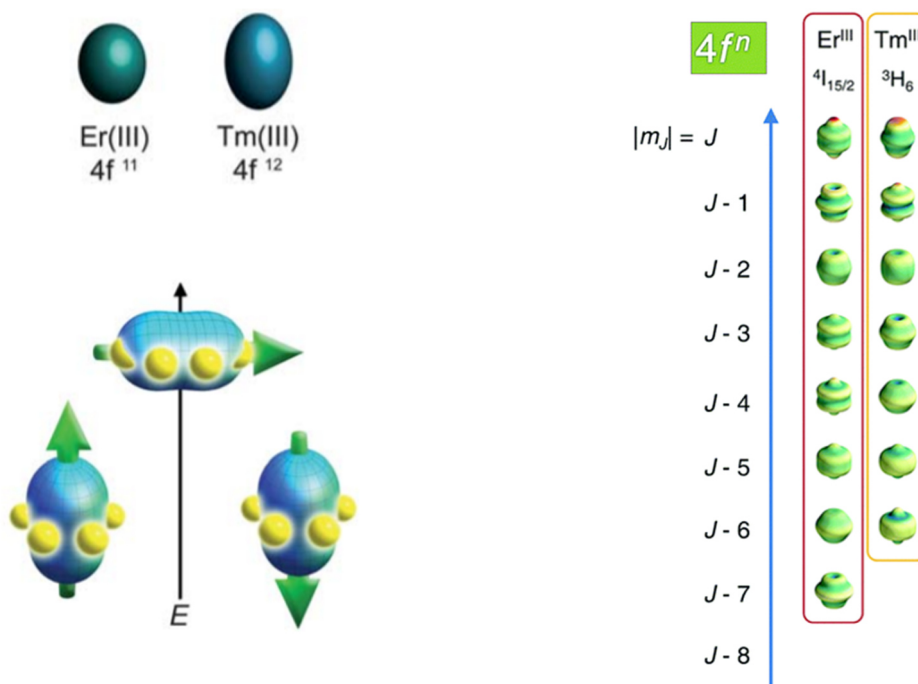


Figure 1-15 Left: The electron density for prolate ions (Er(III), Tm(III)) in the ground state is stabilised by an equatorial ligand field (yellow dots). The shapes from prolate to oblate in the different energy states (right) with $J = 15/2$ for Er(III) and $J = 6$ for Tm(III).^[47,50]

To obtain a system with good SMM properties (high energy barrier and/or blocking temperature), it is necessary to suppress the three processes (QTM, Raman process,

Direct process). This can be achieved by modulating the ligand field and/or a higher symmetry. Approaches are:

- (a) modulation of the ligand field can increase the axial anisotropy of the system, or lead to higher symmetry, which reduces the mixing of energy states and thus shifts the relaxation of the spins to higher excited states.
- (b) by applying a DC magnetic field, the degeneracy of the ground state energy is cancelled and thus QTM is suppressed.
- (c) the substance is "diluted" with diamagnetic species (magnetic dilution) to minimise dipolar interactions between the paramagnetic spin centres in the lattice and hyperfine interactions with the core.^[51]

1.5 Magnetic frustration

The collinear arrangement (parallel or antiparallel) of Ising spins (the spins exhibit one of the two states, spin up or spin down) in a molecule with multiple spin centres leads to either ferro- or antiferromagnetism as explained in chapter 1.1. The interactions can either be dipolar interactions (“through space” interactions between two magnetic dipoles, about 1 cm^{-1}) or exchange interactions (“through bond” interactions, about $1\text{--}200\text{ cm}^{-1}$).^[25] In an equilateral triangle, presuming that the interactions between the spins are all ferromagnetic, all spin states are energetically favourable states (Figure 1-16, left). In the same equilateral triangle, presuming that the spins have antiferromagnetic interactions between each other, all three spins cannot be simultaneously satisfied. This leads to spin frustration of the system and therefore to a manifold of ground states (Figure 1-16, right) rather than a single stable ground state configuration. The red cross indicates the unfavourable bond in the system, where the spins align parallel.^[52-54]

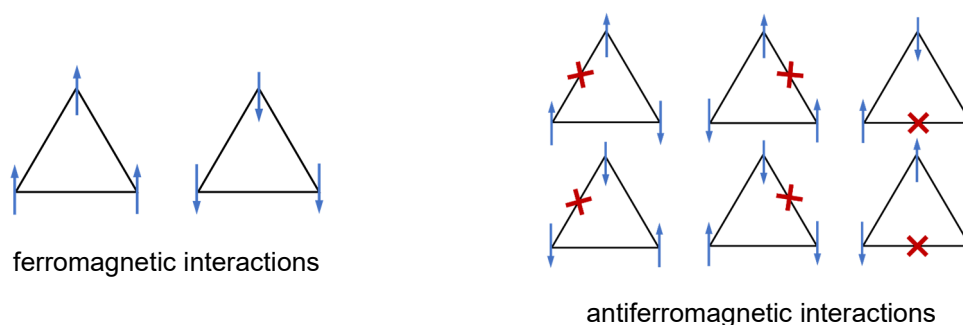


Figure 1-16 Ground state spin configuration of the co-linear Ising model on a triangle cluster. In the case of ferromagnetic interactions (left) between the spin centres (blue arrows), all interactions are favourable. With antiferromagnetic interactions between the spins (right), there is one bond (red cross) which is energetically unfavourable, and this leads to a manifold of degenerated ground states.

Similarly, rectangular/square geometries and tetrahedrons can appear as frustrated systems if the interactions between all spin centres have equal values (Figure 1-17).

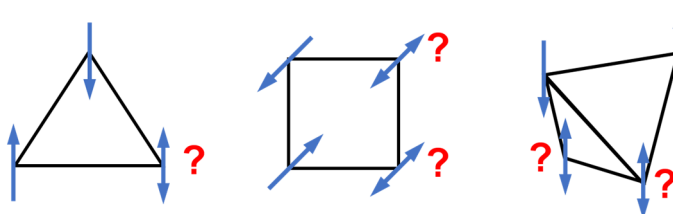


Figure 1-17 Magnetic frustration within systems with the same antiferromagnetic interactions between all spin carriers, forming a triangle (left), a square (middle) and a tetrahedron (right). There are two spins in each system (blue arrows) which align antiparallel, but the remaining spins are frustrated.

The spin alignments in 2-dimensional lattices with corner and edge sharing triangular units (Figure 1-18, left) and in the so-called Kagomé lattice with only vertex-sharing triangular units (Figure 1-18, middle), the spins are non-collinear and in a complicated order but also exhibit, especially in the Kagomé lattice, parts where the spins either all point inwards (red circle), all point outwards (green circle) or have a vortex-like arrangement (orange circle). The corner-sharing tetrahedrons form a 3-dimensional pyrochlore lattice as shown in Figure 1-18, right. The complicated arrangements of the spins lead to extraordinary materials such as spin glasses, spin ices and spin liquids, where the spin fluctuations persist at all temperatures.^[52]

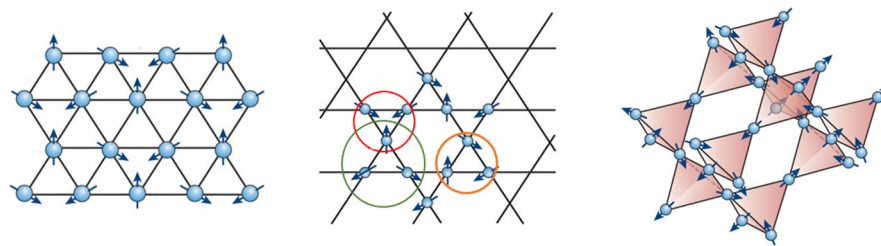


Figure 1-18 Frustrated 2D lattices with edge and corner-sharing triangular units (left) and Kagomé lattice (middle). The 3-D pyrochlore lattice are formed by corner-sharing tetrahedrons (right). The circles in the Kagomé lattice show the different spin arrangements within the lattice. Adapted from reference^[54]. Copyright 2010, Springer Nature.

1.6 Toroidal moments

Even though, these lattices do not refer to single molecules, the vortex-like arrangement of the spins, showed in the Kagomé lattice for some of them can also be observed in smaller systems. This arrangement is called toroidal and the spins (blue arrows in Figure 1-19) in either clockwise or anticlockwise direction lead, similar to the case of spin frustration, to degenerated ground states. This is shown in triangle systems (Figure 1-19, top left), square/rectangular systems (Figure 1-19, top right) and hexagonal systems (Figure 1-19, bottom) which can be seen as the superposition of two triangles in one system.^[2,20]

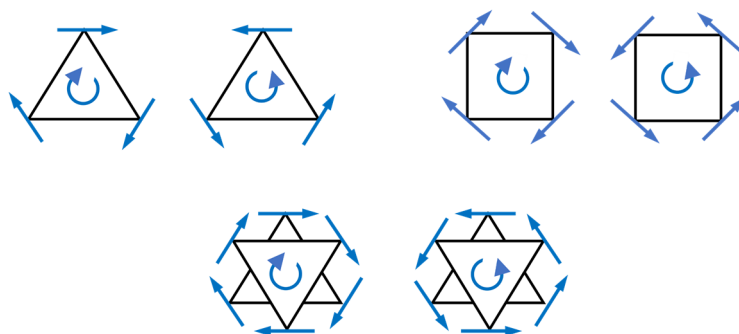


Figure 1-19 Degenerated ground states with the vortex-like arrangement of non-collinear spins (blue) in a triangle (top left), in a square (top right) and in a hexagon (bottom) with spins arranged either all clockwise or all anticlockwise.

The theoretical consideration of the existence of toroidal moments by Zel'dovic et al. dates back to 1957^[55] but the term “toroidal” was first introduced by Dubovik et al. a decade later.^[56] Up to now these kind of moments did not lose their attraction to researchers, mainly in the area of solid-state physics and electrodynamics.

In general, the toroidal moment can be displayed by orbital currents around a torus as shown in Figure 1-20 (left): The arrangement of circular currents I on the surface of a torus induce an enclosed magnetic field m within the torus and this field in turn create the toroidal magnetic dipole moment T . By considering the magnetic field as an array of local moments, one can also display the toroidal moment within a molecule arising from a vortex-like arrangement of spins S , like in the head-to-tail arrangement of spins shown in Figure 1-20 (right).

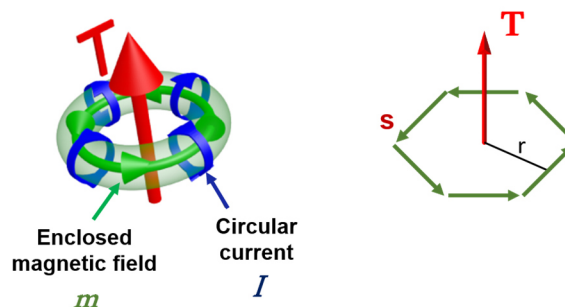


Figure 1-20 The illustration of a toroidal moment T created by an enclosed magnetic field m which are induced by circular currents I on the surface of a torus (left). The toroidal moment T can also be described as the head-to-tail arrangement of Spins S with the radius r from the origin of the molecule (right). Adapted from reference^[57].

Therefore the toroidal moment T is the sum of the cross product of the spins s_i on the site i and the radius r_i from the origin of the molecule^[58]:

$$T = \sum_{i=1}^N r_i \times s_i$$

for $N \geq 2$ spins per unit cell

The toroidal moment is often equalized with an anapole moment, which consists of an electric dipole moment and a toroidal moment. Due to the fact that a magnetization induces an electric field, makes these two properties non-distinguishable as shown in Figure 1-21 (left) schematically. The radiation of the electric dipole and the toroidal magnetic dipole cancel each other out by destructive interference and so there is no direct interaction neither with external electric nor magnetic fields. This makes a perfect anapole moment impossible to detect and is therefore a hot candidate for dark matter in the universe.^[59] If the anapole moment is slightly off-balanced and the electric dipole emission does not cancel out the toroidal dipole radiation, one can measure the electromagnetic anapole via microwave metamaterial. The smallest known existence of an anapole moment is displayed in Figure 1-21 (right) in an atomic nuclei, experimentally first shown in 1997 within a ^{133}Cs atom – by optical spectroscopy using an interference technique.^[60]

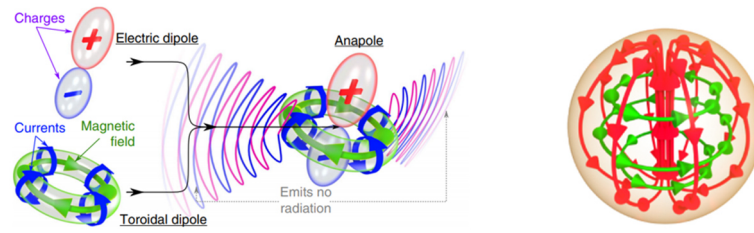


Figure 1-21 The combination of a toroidal magnetic dipole and an electric dipole leads to an anapole moment. The anapole moment does not emit any radiation because the radiation of the two dipoles cancel each other out (left).^[61] The smallest known anapole moment in an atomic nuclei (right). The nuclear currents (red) enclose a closed loop of magnetic field (green).^[57]

The toroidal moment is regarded as the third kind of multipoles next to electric and magnetic multipoles.^[62] There exist two types of toroidal moments: the polar magnetic toroidal moment T and the axial electric toroidal moment G . The latter arises from vortex-like configurations of electric dipoles but is not considered in this work. The term of the toroidal moment in this work is only referred to the polar magnetic toroidal moment T . The three types of multipoles have different transformation properties under space and under time inversion (Figure 1-22):

An electric dipole P is produced by a spatial ordering of different charges that is static in time.^[63] The inversion of this configuration (by applying an electric field in the opposite direction) also reverses the direction of the electric dipole moment, this is called space inversion. By convention, the electric dipole is not changing sign under time inversion which generally means that the current would change direction. Therefore, the electric dipole is antisymmetric under space inversion (-1) – in other words it breaks inversion symmetry – but not under time inversion (+1).

The magnetic dipole moment M is produced by the spin and orbital angular momenta and is demonstrated by a classical current loop where the corresponding magnetic moment is perpendicular to the plane in which the current flows. By inversion of the current direction, thus time inversion, the direction of the magnetic dipole moment is also reversed. There is no change for space inversion since the inversion of the spatial coordinates and of the current direction compensate each other. The magnetic dipole moment is considered as antisymmetric under time inversion (-1) but not under space inversion (+1).

The vortex-like arrangement of magnetic moments and spins, respectively, (green arrows) are defined by the orientation of the magnetic moments and their spatial arrangement in the crystal lattice. For both, time inversion (change of the direction of

the current I) and space inversion (change of the spatial coordinates), the toroidal dipole moment T is reversed. Hence, T is antisymmetric under time (-1) and under space inversion (-1). The electric toroidal moment with its axial moment G is not antisymmetric under time nor under space inversion (+1/+1).

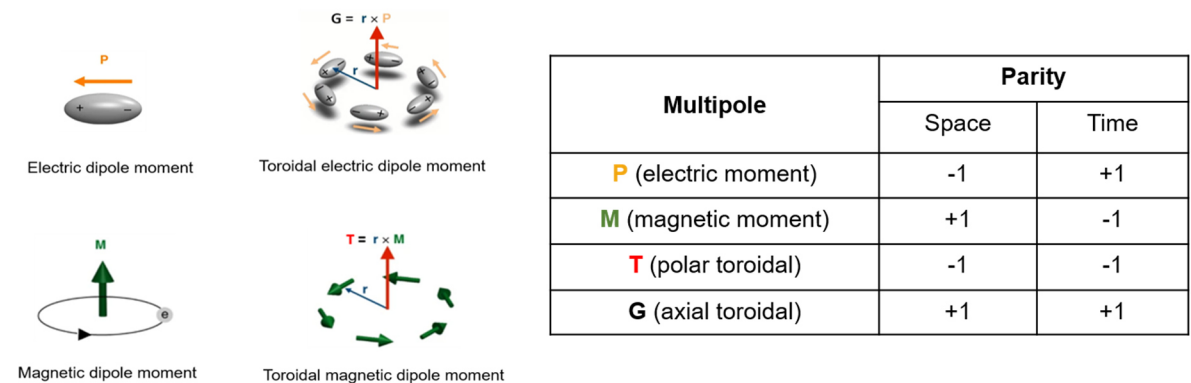


Figure 1-22 The demonstration of the three multipoles: Electric dipole moment P , magnetic dipole moment M and the toroidal moment which can be divided into the polar magnetic toroidal dipole moment T and the axial electric toroidal moment G . Images adapted by permission from reference^[64]. Copyright 2019, Springer Nature. The table implies the transformation properties of the multipoles under time and space inversion with inversion (-1) and no inversion (+1).

The spontaneous alignment of toroidal moments in a long-range order within a material can result in a ferrotoroidal ordered phase. Ferrotoroidictiy is considered as the fourth ferroic order next to ferromagnetism (spontaneous magnetization) with time inversion, ferroelectricity (spontaneous polarization) with space inversion and ferroelasticity (spontaneous strain) with neither time nor space inversion.¹ The four ferroic orders are displayed in Figure 1-23.

¹ The prefix *ferro-* does not refer to any parallel arrangement of spins, but to the historical fact that permanent magnetization was first discovered in metallic iron (*lat. ferrum*).

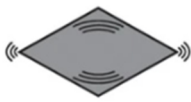
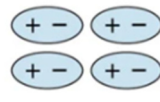
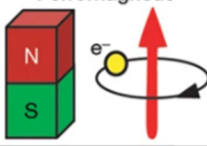
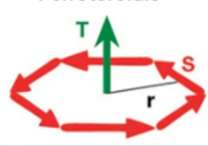
Time \ Space	Space	
	Invariant	Change
Invariant	Ferroelastic 	Ferroelectric 
Change	Ferromagnetic 	Ferrotoroidic 

Figure 1-23 The ferroic orders under the parity of space and time. Adapted with permission from reference^[65]. Copyright 2007 Nature Publishing Group.

The combined feature of ferroelectricity (space inversion) and ferromagnetism (time inversion) relates ferrotoroidics to multiferroic materials with magnetic and electrical phase control. A magnetization M by an electric field E ($M \propto E$) or a polarisation P by a magnetic field H ($H \propto P$) can be induced. This property is termed the magnetoelectric effect (ME).^[66,67] The first time, ferrotoroidic domains were observed, was in 2017 in the solid state material LiCoPO_4 ^[65]. Molecule-based multiferroic/ferrotoroidic materials can be achieved by the coupling between two toroidal moments leading to an enhancement of the collective toroidal moment.^[20,68]

1.7 Single Molecule Toroids (SMTs)

With the observation of toroidal moments in single molecules in a $\{\text{Dy}_3\}$ ^[6] triangle for the first time in 2006, the idea of **Single Molecule Toroids** (SMTs) was developed. Single Molecule Toroids are coordination clusters with a toroidal ground state in this state, these molecules show little to no magnetization, depending on how pronounced the toroidal moment is, *i.e.* depending how perfectly the anisotropy axes are aligned to each other. Accordingly, SMTs do not interact with external homogeneous fields and are thus better protected from the environment than conventional SMMs. Together with the fact that the magnetic field produced by the SMTs decays much faster with distance than the ones in SMMs,^[15] this makes it theoretically possible to attach these molecules more densely to a surface, leading to the possibility of high-density information storage and of quantum bits.

The toroidal ground state of a molecule, which can be equated with a non-magnetic ground state, is difficult to detect and often only *via* a combination of analytical methods such as high-frequency electron paramagnetic resonance (HF-EPR), far-infrared spectroscopy (FIR), cantilever torque magnetometry (CTM) and *ab initio* calculations.^[5] Nevertheless, for many SMTs, a possible toroidal ground state can experimentally be determined by magnetization measurements. In the case of a large gap between the (nearly) non-magnetic ground state and the excited magnetic state, the level-crossing is indicated by a strong increase in magnetization, if measured in the direction of the easy axes or easy plane, respectively. This is visible at low temperatures in the M vs H plot as an S-shaped curve and the crossover from the toroidal ground state can easily be extracted from the first derivative (dM/dH) (Figure 1-24, top). In the best cases, this level-crossing is confirmed with high-level *ab initio* calculations (Figure 1-24, bottom left). The transition from the toroidal ground state to the excited state can be measured more precisely with the micro-SQUID (Figure 1-24, bottom right), which can reach very low temperatures (~30 mK).

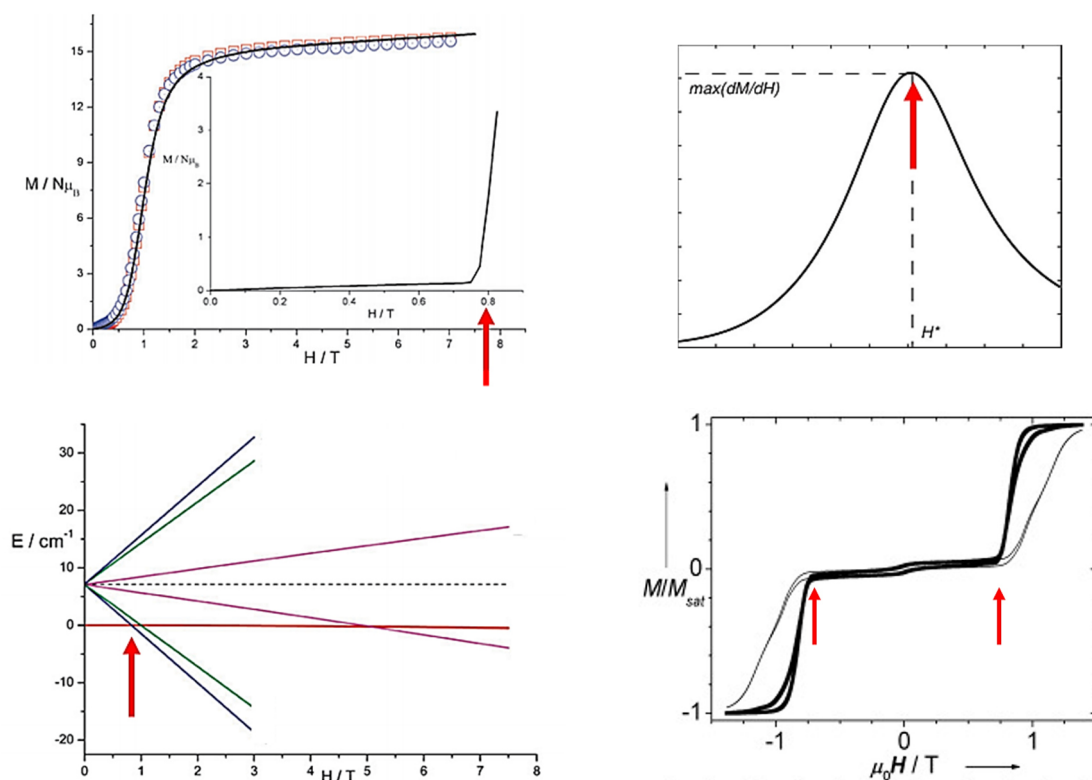


Figure 1-24 The often-observed S-shaped curve of the magnetization in a toroidal system at low temperatures, here at 1.8 K (top left). The graphical determination of the magnetic field where the steep rise of magnetization occurs in the dM/dH plot (top right). The determination of level-crossing from the toroidal (nearly non-magnetic) ground state and the first excited state, supported by *ab initio* calculations. (bottom left). The lines represent the energies of the system with different spin directions. Single crystal micro-SQUID measurements at very low temperatures (down to 30 mK) for a better determination of the desired magnetic field (bottom right). Adapted from reference^[69] and reference^[70]. Copyright 2009 Royal Society of Chemistry.

The wheel shaped topology where the spin centres are coupled *via* dipole and/or exchange interactions and the strong axuality of the anisotropy axes of the ground state are key factors for the formation of a toroidal state. Due to the strongly axial nature of the Dy(III) ions, most of the SMTs are dysprosium-based.^[2,4] In the following, some examples of SMTs with their anisotropy axes and magnetization measurements from the literature are presented.

In 2012, a $\{\text{Dy}_3\}$ complex with a N,N,N',N' -tetrakis(2-hydroxyethyl)-ethylene-diamine ligand was reported, showing a toroidal ground state.^[9] The corresponding susceptibility indicate antiferromagnetic interactions between the spin centres. Bulk and single crystal magnetization measurements show with the S-shaped M vs H plot and the steps in the hysteresis typical behaviour for a toroidal arrangement (Figure 1-25).

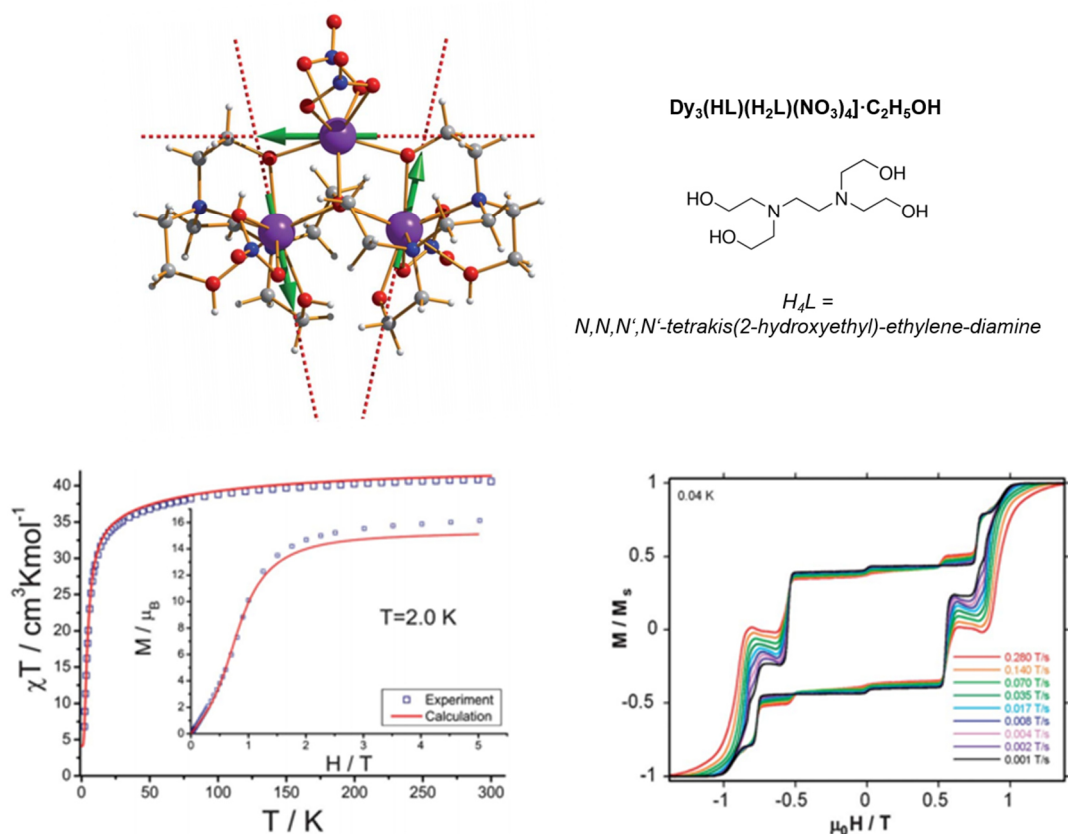


Figure 1-25 Toroidal arrangement in a $\{\text{Dy}_3\}$ -triangle and corresponding ligand (top) with antiferromagnetic interactions (bottom left) between the spin centres, typical S-shaped curve of the magnetization (inset) and steps in the hysteresis (bottom right). Adapted with permission from reference^[9]. Copyright 2012 Royal Society of Chemistry.

The $\{Dy_6\}$ complex by Zhang et al. in 2012 consists out of two $\{Dy_3\}$ units linked by a strong coupling *via* a μ_4-O^{2-} ion where the toroidal moments of both triangles have similar vortex-like arrangement and lead to an enhanced toroidal moment. Weak antiferromagnetic coupling between the dysprosium ions in the toroidal ground state are present but an applied field can overcome these interactions as shown in the χT vs T graph where the susceptibility increases for low temperatures by applying a moderate field (Figure 1-26).

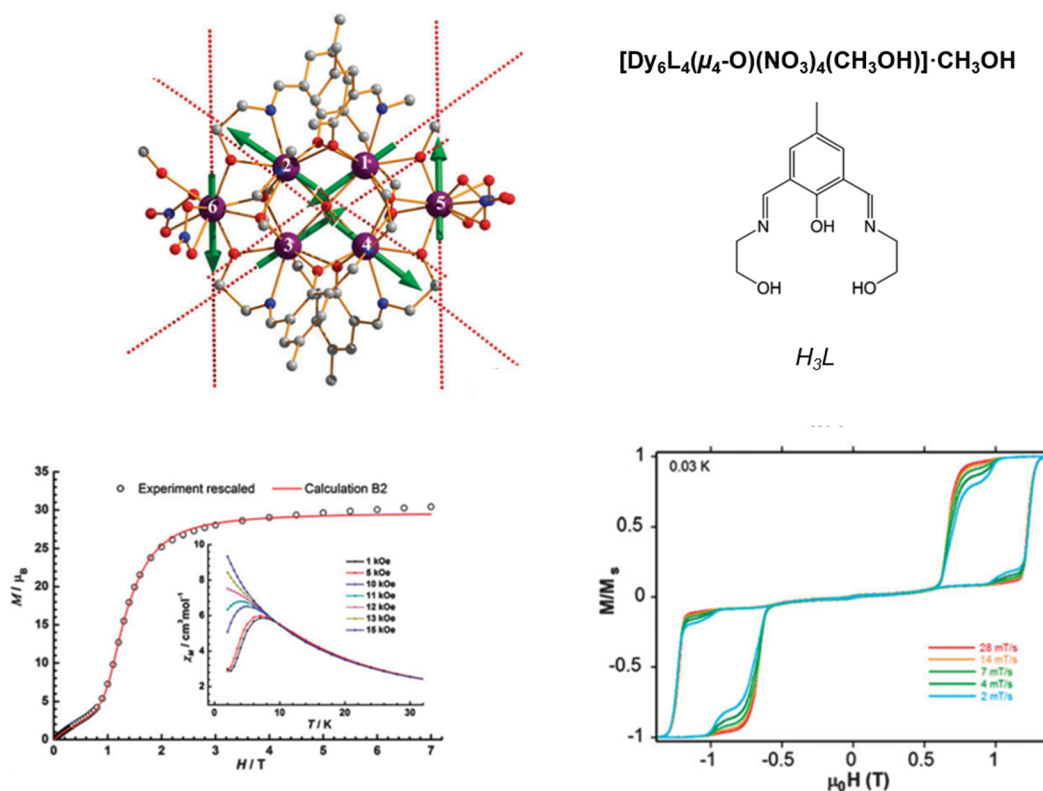


Figure 1-26 Toroidal arrangement in two coupled $\{Dy_3\}$ -triangles and corresponding ligand (top) with dominant antiferromagnetic interactions (bottom left inset) in the system which can overcome by an applied magnetic field and leads to ferromagnetic alignment of the magnetic moments. The pronounced S-shaped curve of the magnetization (bottom left) and steps in the hysteresis (bottom right) show the toroidal moment in the ground state. Adapted with permission from reference^[19]. Copyright 2012 John Wiley & Sons Ltd.

Another example for an enhanced toroidal moment is the heptanuclear complex $\{\text{Cr}^{\text{III}}\text{Dy}^{\text{III}}\}_6$. In 2017 Murray et al. realized the coupling of two $\{\text{Dy}_3\}$ triangles via a $\text{Cr}(\text{III})$ ion which led to a con-rotation of the toroidal magnetic moment between the two triangles (Figure 1-27).^[20] The analogues of this complex with terbium and holmium, $\{\text{CrTb}_6\}$ and $\{\text{CrHo}_6\}$, show a toroidal characteristic hysteresis loop at low temperatures. With *ab initio* calculations a ferrotoroidal behaviour (where the spins of both triangles follow the same direction) was predicted for the two complexes. Up to date these are the first non-dysprosium complexes with a toroidal behaviour.^[21] It was just recently reported, that it is possible to exchange the $\text{Cr}(\text{III})$ in this system with different metals without the “deletion” of the toroidicity.^[68]

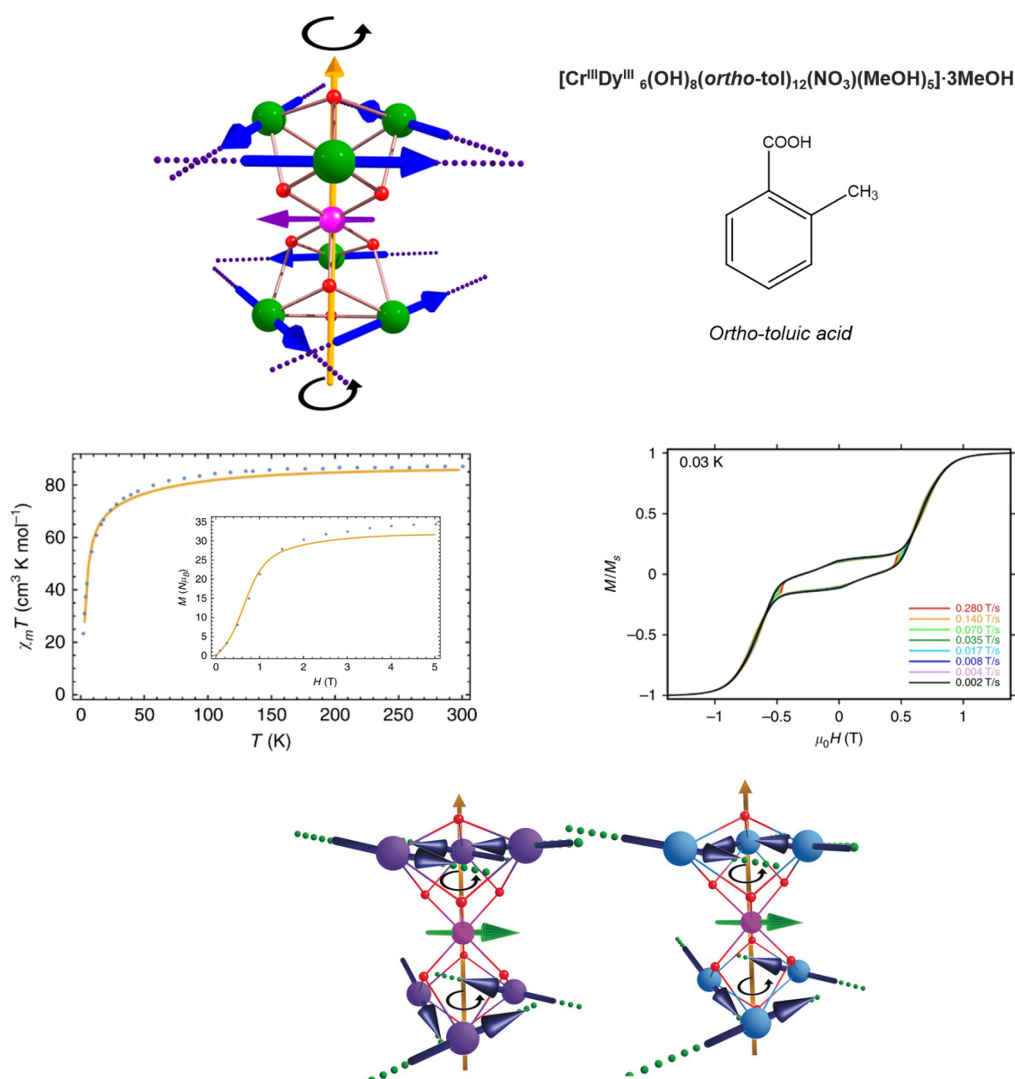


Figure 1-27 Toroidal arrangement in a $\{\text{Cr}^{\text{III}}\text{Dy}^{\text{III}}\}_6$ system and corresponding ligand (top) with dominant antiferromagnetic interactions (middle left), typical S-shaped curve of the magnetization (inset) and steps in the hysteresis (middle right). The anisotropy axes of the analogues, $\{\text{Cr}^{\text{III}}\text{Tb}^{\text{III}}\}_6$ and $\{\text{Cr}^{\text{III}}\text{Er}^{\text{III}}\}_6$ also suggest a toroidal moment in the ground state (bottom). Adapted with permission from reference^[20] and reference^[21]. Copyright 2017 Nature Publishing Group and 2018 Wiley-VCH.

Recently, in 2020 by Zheng et al., a 16-membered heterometallic cluster $\{\text{Fe}_8\text{Dy}_8\}$ with a net toroidal moment was reported, showing the typical S-shaped in the M vs H plot (Figure 1-28, bottom left). The ferromagnetic exchange interaction between the Fe(III) and Dy(III) ions might be responsible for the stability of the toroidal moment. This system exhibits the largest number of dysprosium ions found in a toroidal arrangement to date.^[4]

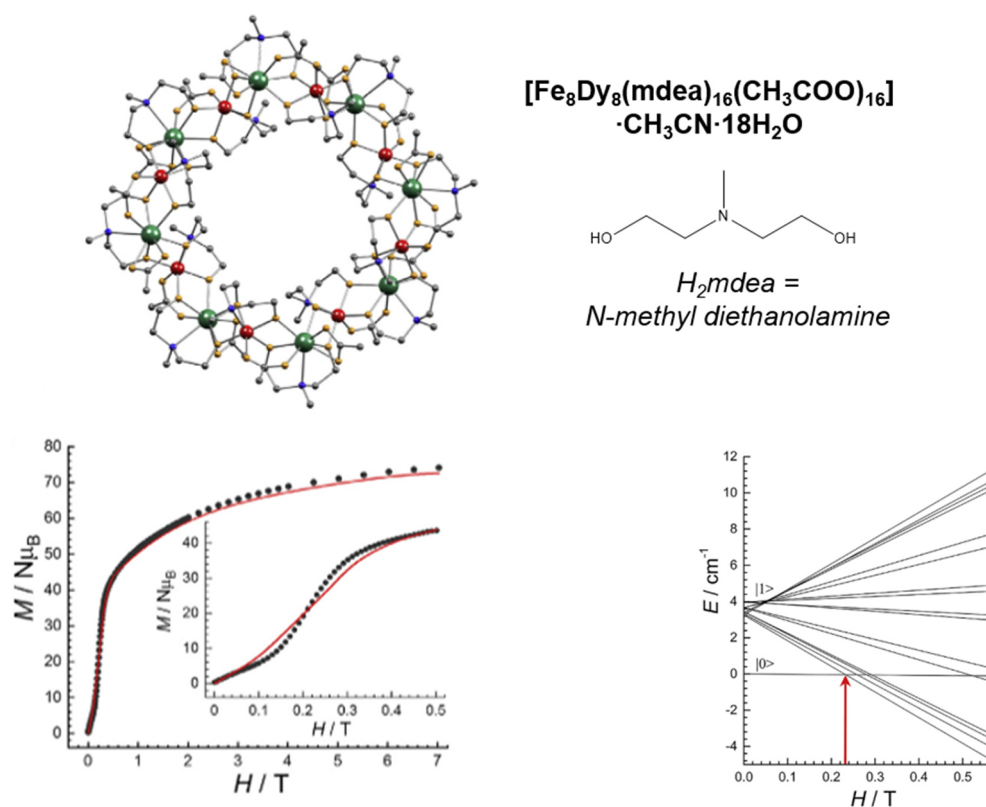


Figure 1-28 The structure of $\{\text{Fe}_8\text{Dy}_8\}$ with a toroidal arrangement and corresponding ligand (top), The typical S-shaped curve is seen in the M vs H plot (bottom left). *Ab initio* calculations (bottom right) with lines representing the energies of the system with different spin directions. The red arrow indicates the level-crossing from the toroidal ground state to the excited state. Adapted with permission from reference^[4]. Copyright 2020 Elsevier Inc.

The biggest molecular based toroidal arrangement so far has been realised with the complex $\{\text{Fe}_{18}\text{Dy}_6\}$ which is also the largest 3d-4f Single Molecule Magnet to date. Synthesized recently, in 2020 by Powell et al., the structure can be explained by the cyclization of six $\{\text{Fe}_3\text{Dy}\}^+$ units.^[23] Two giant $\{\text{Dy}_3\}$ triangles sandwich the strongly antiferromagnetically coupled $\{\text{Fe}_{18}\}$ ring. Quantum Monte-Carlo calculations confirm the presence of a toroidal arrangement of the spin centres, even though not a clear S-shaped curve in the M vs H plot is visible. Bulk and single crystal magnetic measurements are shown in Figure 1-29.

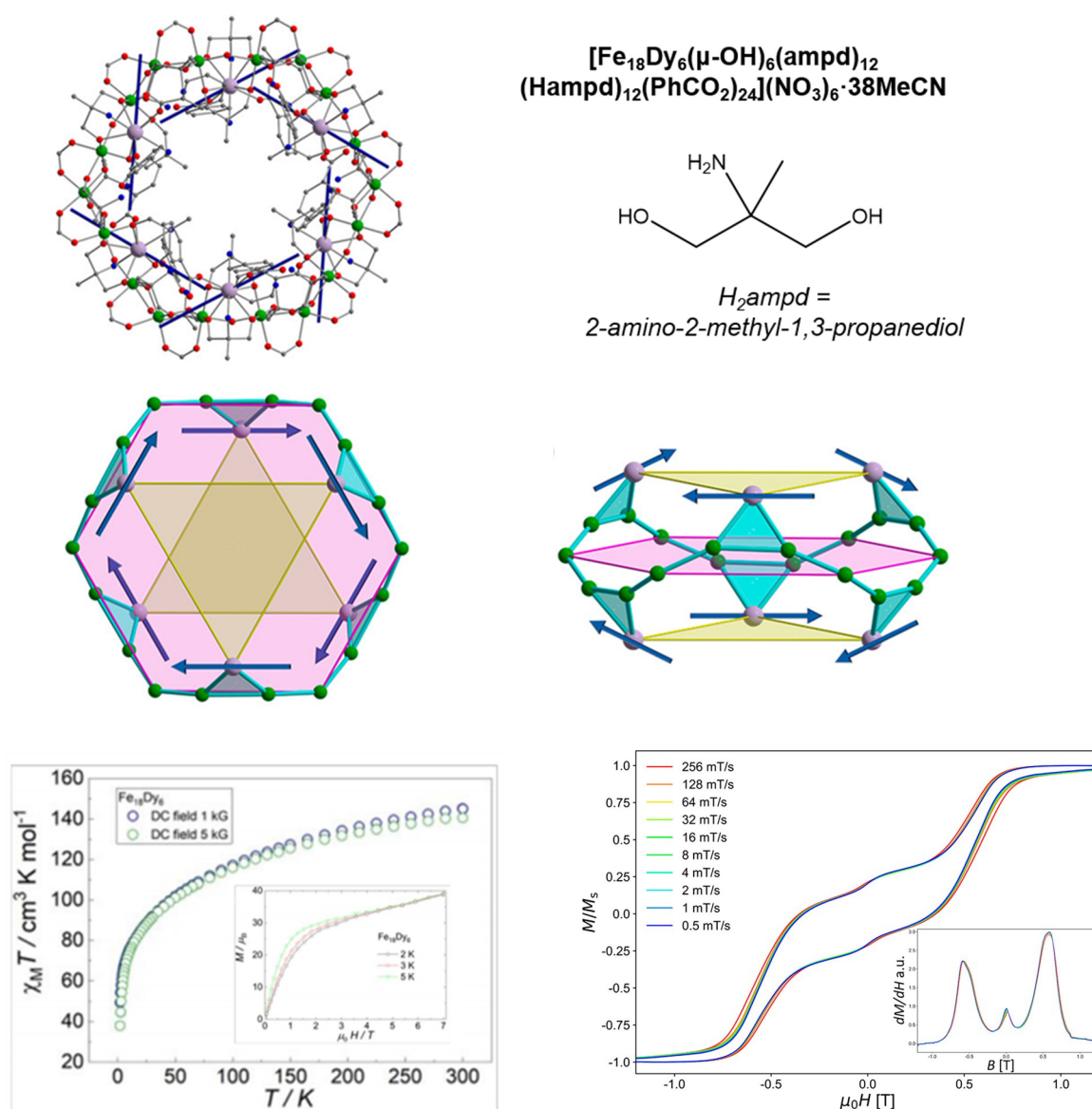


Figure 1-29 The structure of a $\{\text{Fe}_{18}\text{Dy}_6\}$ SMT with corresponding ligand (top), the anisotropy axes forming a wheel (middle), susceptibility (bottom left), bulk magnetization (inset) and single crystal micro-SQUID measurements (bottom right). Adapted with permission from reference^[23]. Copyright 2020 American Chemical Society.

1.8 Theoretical determination of anisotropy axes

In addition to various experimental possibilities, such as angular-resolved^[71] or cantilever torque magnetometry,^[72] to determine the anisotropy axes, there are theoretical approaches such as *ab initio* calculations, that only require the coordinates of the crystal structure.

Due to their unquenched orbital angular momentum, 4f systems have more attractive magnetic properties than 3d or 5f systems. Coulomb interaction (interelectronic repulsion) and subsequent spin-orbit coupling (SOC) lead to $^{2S+1}L_J$ multiplets, which are further split by ligand-field effects (the crystal field CF) into sublevels, also called Stark levels. The CF Hamiltonian for 4f ions can be denoted as follows:

$$\hat{H} = \sum_{i,k,q} B_k^q O_k^q(\theta_i, \varphi_i)$$

In this equation B_k^q represents the CF parameters for the ranks = 2, 4, 6. The number of electrons is described with i and q ranges from $-k$ to k . $O_k^q(\theta_i, \varphi_i)$ describes the Stevens operator which relies on the angular coordinates (θ_i, φ_i) .^[71]

Together with the weak lanthanide-ligand interactions, this leads to high magnetic anisotropy. *Ab initio* calculations are computer processes, which calculate the energies of these multiplets and are used for the estimation of the orientation of the anisotropy axes. First, the basis sets of the lanthanides are generated, whereby relativistic effects are considered. The possible excitations of the boundary orbitals, *i.e.* the orbitals which are partially occupied, are determined with the complete active space self-consistent field (CASSCF) method and spin-free eigenstates are generated. Spin-orbit couplings are then considered.

With the help of these results, the anisotropy axes of the metal atom can be determined. Theorists have powerful programs at their disposal for these calculations. One of these is the program MOLCAS, which was developed by Chibotaru and co-workers in 2006. A second option is to directly diagonalize a Hamiltonian that includes spin orbit coupling. The starting point is a set of inactive (doubly occupied) and active orbitals which is either determined in Turbomole^[71,73-75] calculations - programmed in the 1980' s and continuously developed in Karlsruhe

(KIT) - or by a state average CASSCF-calculation. All Slater determinants with the correct number of electrons in the active space, for 4f compounds usually the 4f orbitals, are considered.^[76]

It is common practice to theory calculations to reduce the molecule to one paramagnetic centre only and determine the energies for this centre. To do this, the remaining paramagnetic centres are replaced with diamagnetic centres, commonly used La(III), Lu(III) or Y(III). The calculation of several paramagnetic centres at the same time would quickly bring today's computers to their capacity limits.

These *ab initio* calculations are complex and time-consuming computational processes. Chilton et al. developed the program MAGELLAN,^[77] which uses a simple electrostatic distribution of the ligands around the Dy(III) ion to predict the anisotropy axes. These calculations agree remarkably well with high-level *ab initio* for low-symmetry Dy(III) complexes. The considerations are based on the aspherical electron distribution of the lanthanide ions, found by Sievers,^[48] and the concept of anisotropy in the lanthanide ions developed by Rinehart and Long as mentioned in chapter 1.4. The ground Kramer's doublets of the Dy(III) ion are strongly axial and are described by the state $M_J = \pm 15/2$ in the atomic multiplet $^6H_{15/2}$. In this state the g values, characterizing the magnitude and anisotropy of the magnetic moment, are $g_x = g_y = 0$ for the transversal direction and $g_z = 20$ for the axial direction. The approach of MAGELLAN is based on the solution of a classical energy minimisation problem. The determination of the angles α and β in the atomic wave function $\psi_{\pm}(\alpha, \beta)$, give the results for the full g -tensor (g_x, g_y, g_z) of the ground Kramer's doublet for the Dy(III) ion. This many-electron wave function $\psi_{\pm}(\alpha, \beta)$ can also be described by an electron density distribution $\rho_{\pm\frac{15}{2}}^{(\alpha, \beta)}(\theta, \varphi)$. The angles θ and φ , defined in the reference frame of the crystal field V_{CF} , are polar angles and express the angular dependence of the axially symmetric aspherical electron density. An electrostatic energy integral can be established, which is caused by the interactions between the electric potential due to the crystal field $V_{CF}(\theta, \varphi)$ and the charge density $\rho_{\pm\frac{15}{2}}^{(\alpha, \beta)}(\theta, \varphi)$ of the f-electrons of the Dy(III) ion:

$$E_{\pm\frac{15}{2}}(\alpha, \beta) = \int_{\theta=0}^{\pi} \int_{\varphi=0}^{2\pi} V_{CF}(\theta, \varphi) \rho_{\pm\frac{15}{2}}^{(\alpha, \beta)}(\theta, \varphi) \sin(\theta) d\theta d\varphi$$

It is now necessary to calculate the minimum energy of this system. To do this, the crystal field V_{CF} must be determined as precisely as possible. Charged ligands have the strongest effect on the electrostatic potential of the Dy(III) ion and their charge are determined using the minimum valence bond model (VB). For this purpose, the charge is delocalised and distributed as a resonance hybrid over the entire Lewis structure, resulting in a simple fractional charge distribution for the ligands. Metal ions are assigned with their corresponding positive charge (Dy(III) and Cr(III) gets the charge 3+ for example), negative ligands such as chlorides and bridging $\mu_3\text{-OH}^-$ and $\mu_2\text{-O}^{2-}$ units are assigned the charge -1 and -2, respectively. Most of the atoms in the ligand will remain neutral in this model. The ligands which are used in this thesis to calculate anisotropy axes, from literature and this work, are shown in Figure 1-30.

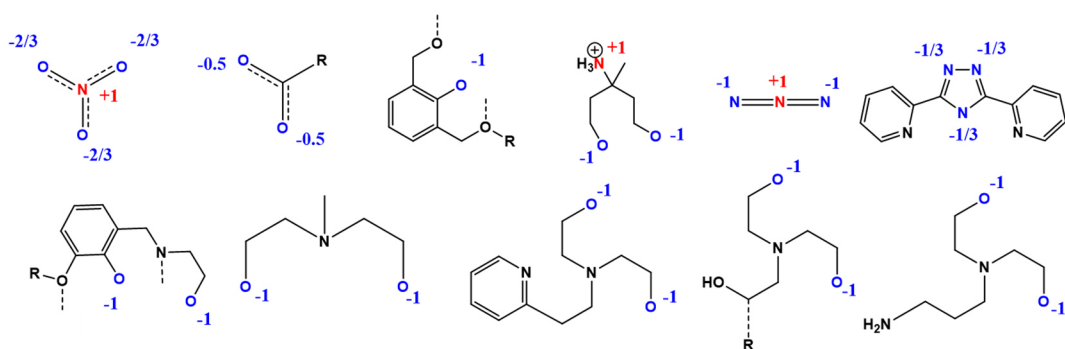


Figure 1-30 Partial charges assigned to the formally charged ligands in this thesis.

The minimum reversal energy is also given by MAGELLAN and is explained as the smallest peak energy, relative to the optimised electrostatic minimum, that it takes to flip the $\pm 15/2$ density by 180° . The electron density, *i.e.* the shape, of the Dy(III) ion is considered unchanged, what it is not the case for the density of the ions in a SMM as shown in Chapter 1.4.

2 Motivation

The ambition of this work was to find lanthanide-based coordination clusters with exotic magnetic properties, such as slow relaxation of magnetization, characteristic for SMMs, and/or (almost) non-magnetic ground states, so-called toroidal ground states, characteristic for SMTs. The toroidal ground state is mostly indicated by a vortex-like arrangement of the anisotropy axes and spins, respectively. It should be investigated whether the coordination environment of the Dy(III) ions has an influence on the toroidicity (toroidicity = value of the magnetic field H at which the level-crossing from the ground state to excited state occur). For this purpose, different dysprosium based molecular systems should be synthesized and investigated for their position of the anisotropy axes by theoretical *ab initio* and MAGELLAN calculations. To verify whether MAGELLAN can be used to find a vortex-like anisotropy axis of the Dy(III) ions, the results are compared to *ab initio* calculations if available. The experimental determination of possible toroidal states and possible SMM behaviour should be determined with magnetic measurements by using SQUID and/or micro-SQUID and VSM instrumentation and should be compared with the MAGELLAN/*ab initio* calculations in regard of a possible toroidicity.

The greatest motivation is the aspect, that SMMs can be used as ultra-high density storage and that especially SMTs are hot candidates for the use of elementary building blocks in quantum computation due to their insensitivity of external magnetic fields. Based on bits in classical computers, the molecular counterpart is named qubit.^[78,79]

The initial idea for this work arises from the well-known {Dy₃} compound which is the first molecule where this exotic behaviour of an almost non-magnetic ground state and the vortex-like arrangement of the anisotropy axes was detected.^[6] The idea was to search for similar compounds using slightly altered ligands compared with the *ortho*-vanillin ligand of the original {Dy₃} compound *via* the substitution of the methoxy group with an ethoxy group (Chapter 3). The outlook for this compound was to compare them with the literature known {Dy₃} compound and in the best scenario improve the toroidicity of the molecule.

Even though, dysprosium-based compounds seem to be the best choice for constructing a toroidal ground state, lanthanide analogues using terbium, holmium, erbium and europium were synthesized and the anisotropy axes were calculated

using *ab initio* methods for all apart from europium. The aim was to compare these structures with the results on the dysprosium compounds.

The search for toroidal ground states in 3d-4f-compounds in Chapter 4 was driven by the ambitious work of Murray et al. where chromium and lanthanides were combined to form a heptanuclear compound. Here the 3d metal ion is sandwiched between two lanthanide triangles and the toroidal ground state for the dysprosium, terbium and holmium analogues and even slow relaxation of magnetization for the dysprosium one was observed.^[20] The use of toluate as ligand in their work led to the idea in the present work of using substituted benzoates.

Also, literature known compounds with a tetranuclear core of lanthanides are promising candidates for toroidal ground states within the molecule.^[1,12,15] For this reason, tetranuclear compounds were synthesized and investigated regarding SMM and SMT behaviour (Chapter 5). A further idea was to investigate compounds with the Schiff base ligand form between 3-ethoxysalicyl aldehyde and 2-amino phenol due to their ability to capture several lanthanides in the ligand's oxygen-nitrogen pockets.^[80,81]

Since in the literature $\{\text{Dy}_6\}$ wheel complexes are known^[82,83] to exhibit toroidal behaviour and in some cases also SMM behaviour, $\{\text{Dy}_6\}$ complexes should be resynthesized in Chapter 6 and additional micro-SQUID data should be acquired to compare the toroidicity and SMM behaviour with either the results of *ab initio* calculations from the literature or magnetization data (SQUID and or micro-SQUID).

3 Triangular Ln₃ systems

The region of Single Molecule Toroids began with two reported {Dy₃} complexes [Dy₃(μ₃-OH)₂L₃Cl₂(H₂O)₄][Dy₃(μ₃-OH)₂L₃Cl(H₂O)₅]Cl₅·19 H₂O (**Dy3-1**) and [Dy₃(μ₃-OH)₂L₃Cl(H₂O)₅]Cl₃·4 H₂O·2 MeOH·0.7 MeCN (**Dy3-2**) with HL = *ortho*-vanillin, first synthesized by Powell et al. in 2006.^[6] These molecules consist of triangles of dysprosium centres capped by two μ₃-OH⁻ units one above and one below the dysprosium plane. Additionally, three μ₂-OR phenoxo groups from deprotonated *ortho*-vanillin ligands hold the core together. These ligands bridge two Dy(III) ions along each side of the triangle. Aldehyde and methoxy oxygens also coordinate to the dysprosium centre. The main structural difference between the triangular units is that one Dy-site (Dy(3)) was chosen here is coordinated by one chloride above and in a 50:50 disorder by one water and one chloride below the Dy₃ plane in **Dy3-1** (Figure 3-1, left) and in **Dy3-2** (Figure 3-1, right). The core is highlighted in orange bonds.

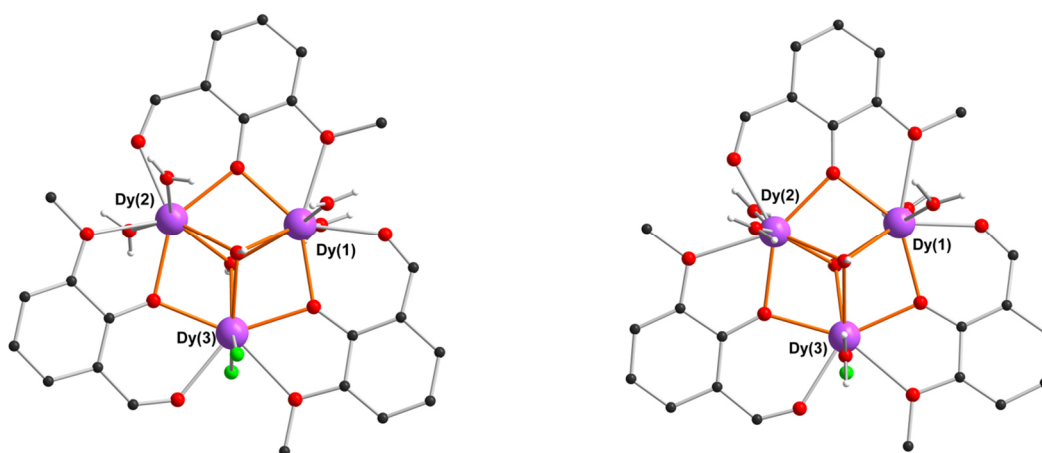


Figure 3-1 Molecular structure of **Dy3-1** with two chlorides on the Dy(3) site (left) and molecular structure of **Dy3-2** with a 50:50 disorder of chloride and water on the Dy(3) site (right). For the disorder, water is chosen to be illustrated.

The molecules have almost identical magnetic behaviour and antiferromagnetic interactions resulting in a non-magnetic ground state as shown by the χT product being almost zero.^[6] This found to be the result of a toroidal arrangement of the spins and is set as a benchmark for toroidicity with a level-crossing from the ground state to first excited states at $H = 0.95$ T. This was measured *via* micro-SQUID techniques. A narrow hysteresis was also observed and indicated slow relaxation of magnetization. The energy barrier for the Orbach process in the high temperature

regime was estimated with $U_{eff} = 61.7\text{ K}$ and the preexponential factor $\tau_0 = 9.14 \cdot 10^{-4}\text{ s}$. *Ab initio* calculations in 2006 for the complex with the Dy(3) site coordinated by two chlorides for **Dy3-1**, could prove that the gap between the ground state and the first excited state is relatively large with values of 234 cm^{-1} , 217 cm^{-1} , and 150 cm^{-1} for the single dysprosium ions.^[84] Later on, in 2016, *ab initio* calculations using an updated method for **Dy3-2** revealed first excited doublets with energies of 142.90 , 186.13 and 187.26 cm^{-1} .^[5] The structure of the molecule **Dy3-1** with two chlorides on Dy(3) together with the calculated anisotropy axes is shown in Figure 3-2.

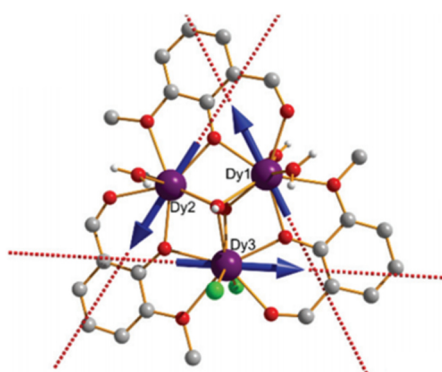
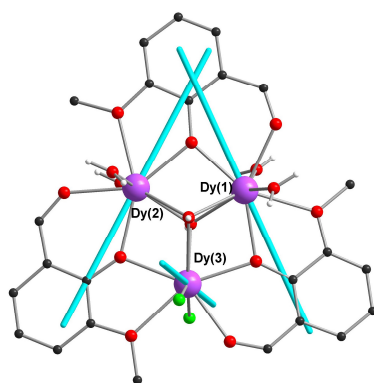


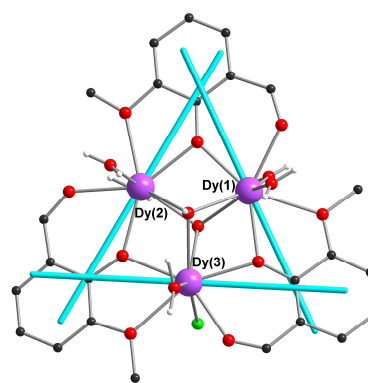
Figure 3-2 Molecular structure of the very first SMT (**Dy3-1**) with anisotropy axes represented by the dashed lines and the direction of the magnetic moments (blue arrows). Reprinted with permission from^[3] and^[84]. Copyright 2009 and 2019 Royal Society of Chemistry.

It is noteworthy, that even though the additional chloride coordinated at the Dy(3) site does not change the magnetic properties of the systems, and obviously also not the direction of the anisotropy axes, this looks different for MAGELLAN calculations. Here, the calculation on **Dy3-1** with two chlorides on the Dy(3) site gives two anisotropy axes lying almost in the Dy_3 plane whereas the anisotropy axis in Dy(3) is forced by the two negatively charged chlorides to lie almost perpendicular to the Dy_3 plane and the other two anisotropy axes, respectively (Figure 3-3, left). The almost perpendicular axis of Dy(3) remains for MAGELLAN calculations, even by taking the counterions (chlorides) into account. If the chloride is exchanged by a water molecule (and is therefore treated in MAGELLAN calculations as neutral), the anisotropy axis of Dy(3) is no longer perpendicular to the Dy_3 plane but lies in it and forms a nearly perfect triangle with the other two axes (Figure 3-3, right). The anisotropy axes of the Dy(III) ions for **Dy3-2** (Figure 3-3, bottom) are as a result of their similarity, almost congruent with the ones in **Dy3-1** with one chloride.

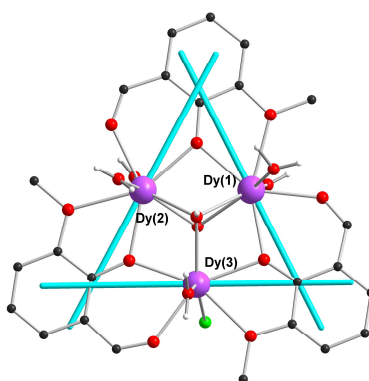
This reveals a drawback with the use of MAGELLAN to evaluate the anisotropy axes when charged but rather soft ligands such as chloride are present.



Dy3-1 with two chlorides



Dy3-1 with one chloride



Dy3-2

Figure 3-3 Anisotropy axes calculated using MAGELLAN for **Dy3-1** with two chlorides at the Dy(3) site (left) and one water and one chloride at the Dy(3) site (right). As comparison the anisotropy axes of the Dy(III) ions for **Dy3-2** are shown at the bottom.

3.1 Comparison with the Dy₃ triangular systems (1) and (2)

In this work, two similar {Dy₃} complexes to the literature known **Dy3-1** and **Dy3-2** could be obtained by using the ligand 3-ethoxysalicylaldehyde which differs from *ortho*-vanillin only in an additional methylene group, compared to the ligand used for **Dy3-1** and **Dy3-2** in the literature (Figure 3-4).

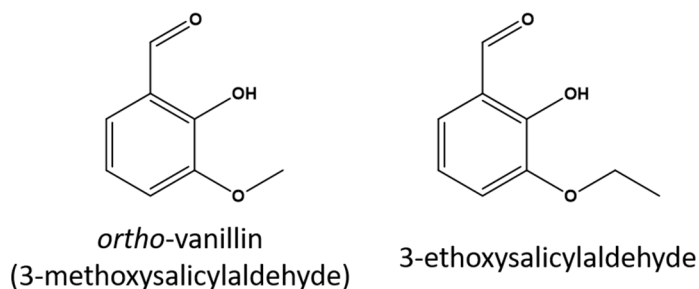


Figure 3-4 The ligand *ortho*-vanillin which was used for the originals {Dy₃} compounds (**Dy3-1** and **Dy3-2**) and the ligand 3-ethoxysalicylaldehyde used in this work for (1) and (2).

Dy(III)-chloride, 3-ethoxysalicylaldehyde, ethanolamine and triethylamine were dissolved in a mixture of methanol and dichloromethane. This led to crystals with the formula [Dy₃(L)₃(μ₃-OH)₂(H₂O)₄Cl₂]Cl₂·5H₂O·3MeOH (1)

with HL = 3-ethoxysalicylaldehyde, crystal structure measured at 293 K. A similar approach with slow ether diffusion into a methanolic solution of Dy(III)-chloride, 3-ethoxysalicylaldehyde, ethanolamine and triethylamine led to crystals with the formula [Dy₃(L)₃(μ₃-OH)₂(H₂O)₂(CH₃OH)Cl₃]Cl·2H₂O·2CH₃OH (2)

with HL = 3-ethoxysalicylaldehyde, crystal structure measured at 150 K. In both cases, ethanolamine acts as a base and is not in the crystal structure as observed for **Dy3-1** and **Dy3-2**.

The molecular structures of (1) and (2) (are shown in Figure 3-5 and differ from the literature known {Dy₃} complexes (**Dy3-1** and **Dy3-2**) in the organic ligand but have the same core structure, highlighted with orange bonds.

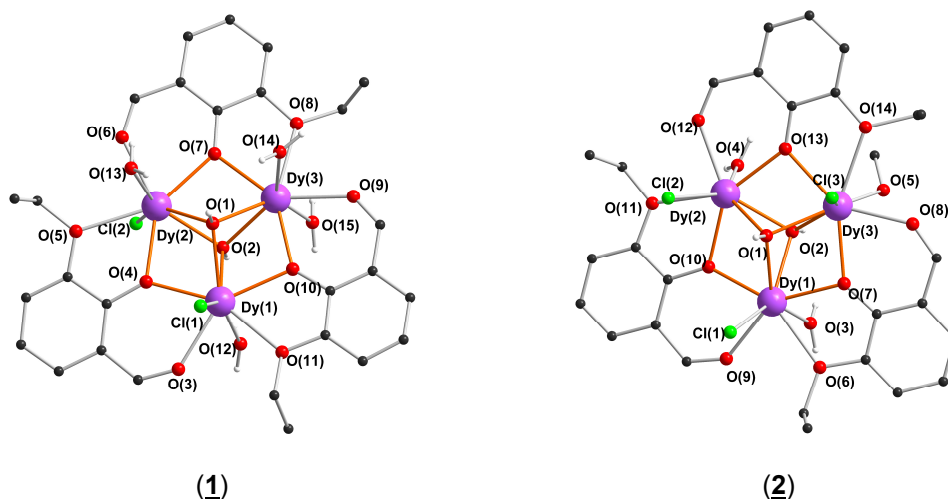


Figure 3-5 The molecular structures of $[\text{Dy}_3(\text{L})_3(\mu_3\text{-OH})_2(\text{H}_2\text{O})_4\text{Cl}_2]\text{Cl}_2$ (**1**) (left) and $[\text{Dy}_3(\text{L})_3(\mu_3\text{-OH})_2(\text{H}_2\text{O})_2(\text{CH}_3\text{OH})\text{Cl}_3]\text{Cl}$ (**2**) (right).

The complexes crystallize in the monoclinic crystal system, and the space groups are $I2/a$ for (**1**), $P2_1/c$ for (**2**), whereas **Dy3-1** and **Dy3-2** crystallize in $C2/c$.² The binding mode for the ligands in all four structures is $\eta^1:\eta^2:\eta^1:\mu_2$ as shown in Figure 3-6.

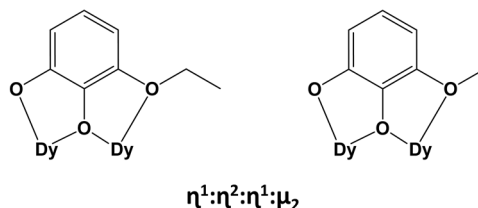


Figure 3-6 Binding mode of the organic ligands in (**1**), (**2**) (left) and **Dy3-1** and **Dy3-2** (right).

The Dy-Dy distances are 3.5492(3), 3.5491(4) and 3.5679(3) Å in (**1**) and 3.5129(5), 3.5463(5) and 3.5370(6) Å in (**2**), in both cases shorter than in **Dy3-1** (3.5026(6), 3.5231(4) and 3.5491(4) Å) and **Dy3-2** (3.5135(3), 3.5135(3) and 3.5400(3) Å). The Dy-Dy-Dy angles are in (**1**) and (**2**) close to 60°: 59.82(1), 59.83(1) and 60.348(7)° in (**1**) and 59.461(10), 60.403(10) and 60.138(11)° in (**2**). The differences to the angles in **Dy3-1** and **Dy3-2** are negligible. The Dy-OH-Dy angles vary from 96.48(12) to 97.52(12)° in (**1**) and from 95.2(2) to 97.52(12)° in (**2**). These angles are in a similar range to those in **Dy3-1** and in **Dy3-2** (Table 3-1). Selected angles and distances of (**1**) and (**2**) can be found in the appendix 12.1.

² The space group $I2/a$ is often wrongly avoided in crystallographic studies, being a non-standard setting of the space group $C2/c$. $I2/a$ is conventional when it gives a smaller angle β .^[85]

Table 3-1 Comparison of distances and angles of **Dy3-1**, **Dy3-2**, **(1)** and **(2)**.

complex & space group	Dy··Dy [Å]	Dy-Dy-Dy [°]	Dy-OH-Dy [°]
Dy3-1 C2/c	3.5026(6) 3.5231(4) 3.5272(4)	59.577(9) 60.153(9) 60.270(9)	95.85(15) to 97.32(16)
Dy3-2 C2/c	3.5135(3) 3.5185(3) 3.5400(3)	59.704(5) 59.843(7) 60.453(5)	95.85(8) to 98.28(8)
[Dy ₃ (L) ₃ (μ ₃ -OH) ₂ (H ₂ O) ₄ Cl ₂]Cl ₂ (1) I2/a	3.5491(4) 3.5492(3) 3.5679(3)	59.82(1) 59.83(1) 60.348(7)	96.48(12) to 97.52(12)
[Dy ₃ (L) ₃ (μ ₃ -OH) ₂ (H ₂ O) ₂ (CH ₃ OH)Cl ₃]Cl (2) P2 ₁ /c	3.5219(5) 3.5370(6) 3.5463(5)	59.461(10) 60.403(10) 60.138(11)	95.2(2) to 97.52(12)

The coordination spheres of Dy(1) for **(1)** and **(2)** are described in detail: In addition to the two μ₃-OH⁻, O(1) and O(2), the coordination sphere of Dy(1) in common with Dy(2) and Dy(3) has four oxygens from two different 3-ethoxysalicylaldehyde ligands: The deprotonated phenol oxygen, O(4), which also bridges to a neighbouring Dy(III) ion, e.g. O(4) links Dy(1) and Dy(2), thereby providing the third oxygen. The fourth oxygen is provided by an aldehyde group, O(3), from the same ligand. The fifth and the sixth oxygens, coming from a different ligand, are provided by the ethoxy oxygen, O(11) and by the phenyl oxygen, O(10), which is also bridged to a neighbouring Dy(III) ion, e.g. O(10) links Dy(1) and Dy(3). The coordination sphere for Dy(1) is completed by one water molecule and one chloride, O(12) and Cl(1). The environment for Dy(2) and Dy(3) is equal to the environment of Dy(1) in **(2)**. In **(1)**, the chloride and the water on Dy(2) are interchanged compared to Dy(1). For Dy3, two water are coordinated, O(14) and O(15). The Dy-Cl distances are 2.6802(15) and 2.686(2) Å in **(1)** and 2.676(2), 2.6957(19) and 2.710(2) Å in **(2)**. The Dy-O distances vary from 2.325(4) to 2.513(4) Å in **(1)** and from 2.310(5) to 2.507(7) Å in **(2)**.

In Figure 3-7, the geometries of perfect coordination spheres for a donor set around the Dy(III) ions are illustrated, here as an example for O₈ donor sets. These are

square antiprismatic (SAPR), triangular dodecahedral (TDD), biaugmented trigonal prismatic (BTPR) and snub disphenoid J84 (JSD).

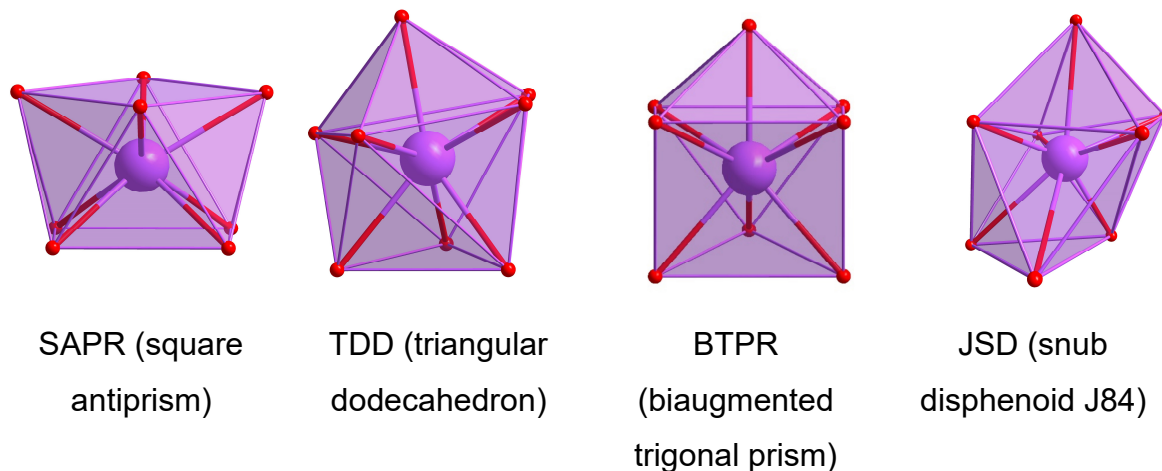


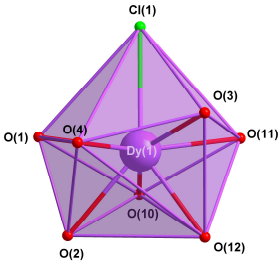
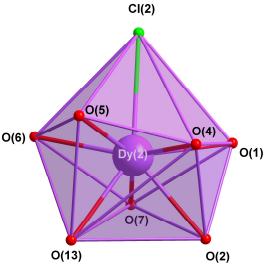
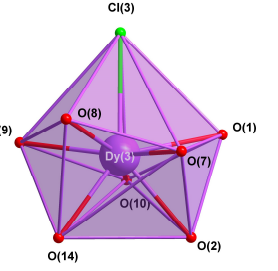
Figure 3-7 The perfect geometries of the coordination spheres for a donor set with eight atoms, here with an example of an O₈ donor set.

The coordination spheres of the Dy(III) ions in all structures can best be described as triangular dodecahedral with the exception of Dy(2) in **Dy3-1** best described as square antiprismatic. The coordination spheres of the Dy(III) ions together with their donor sets and the deviations of the corresponding geometries (in %) and closest geometries nearby are displayed in Table 3-2. The coordination spheres of the Dy(III) ions in the molecule are shown in Figure 3-8, here for the Dy(III) ions in (**1**) as a representative.

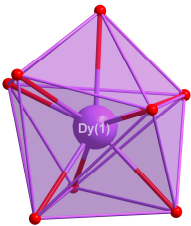
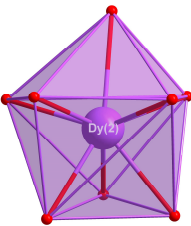
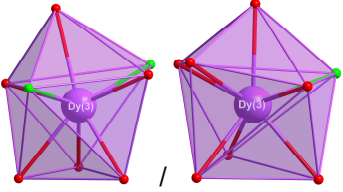
Table 3-2 Coordination spheres, donor sets and deviations from the perfect geometry (in %) for the Dy₃ complexes(**1**),(**2**), **Dy3-1** and **Dy3-2**.

Coordination spheres of the Dy(III) ions of [Dy ₃ (L) ₃ (μ ₃ -OH) ₂ (H ₂ O) ₄ Cl ₂]Cl ₂ ·5H ₂ O·3MeOH (1)								
O ₇ Cl			O ₇ Cl			O ₈		
2.353	1.048	2.496	2.751	0.884	2.681	1.565	1.076	1.740
SAPR	TDD	BTPR	SAPR	TDD	BTPR	SAPR	TDD	BTPR

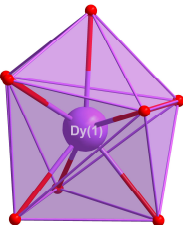
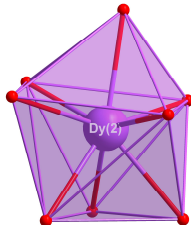
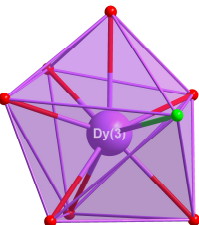
Coordination spheres of the Dy(III) ions of $[\text{Dy}_3(\text{L})_3(\mu_3\text{-OH})_2(\text{H}_2\text{O})_2(\text{CH}_3\text{OH})\text{Cl}_3]\text{Cl}$ (**2**)

								
O ₇ Cl			O ₇ Cl			O ₇ Cl		
2.144	1.127	2.283	1.982	1.261	1.957	3.397	0.803	3.223
SAPR	TDD	BTPR	SAPR	TDD	BTPR	SAPR	TDD	BTPR-8

Coordination spheres of the Dy(III) ions of **Dy3-1**

								
O ₈			O ₈			O ₆ Cl ₂ /O ₇ Cl		
2.686	0.621	2.494	1.056	1.445	2.002	3.106/2.967	0.988/0.827	2.864/2.923
JSD	TDD	BTPR	SAPR	TDD	BTP	SAPR	TDD	BTPR

Coordination spheres of the Dy(III) ions of **Dy3-2**

								
O ₈			O ₈			O ₇ Cl		
2.686	0.621	2.494	1.881	0.969	1.992	2.728	0.956	2.830
JSD	TDD	BTPR	SAPR	TDD	BTPR	SAPR	TDD	BTPR

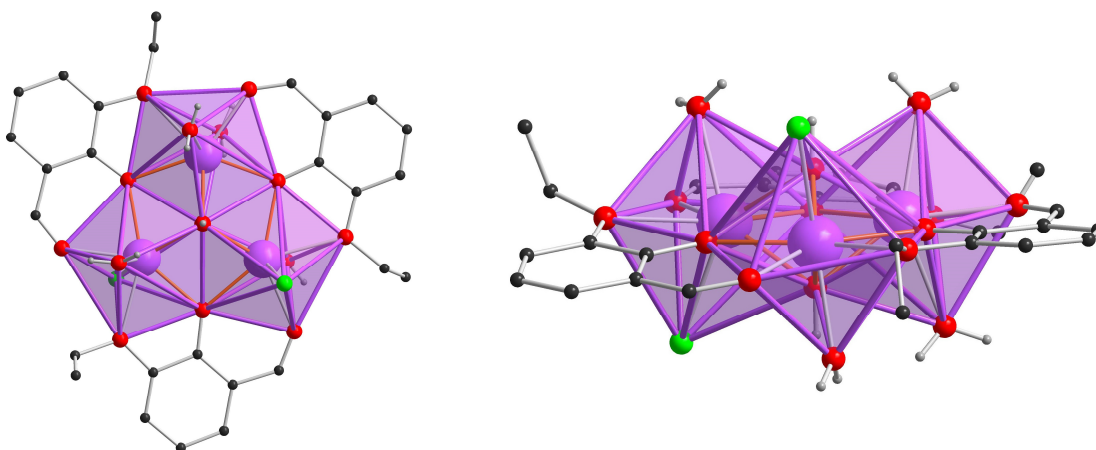
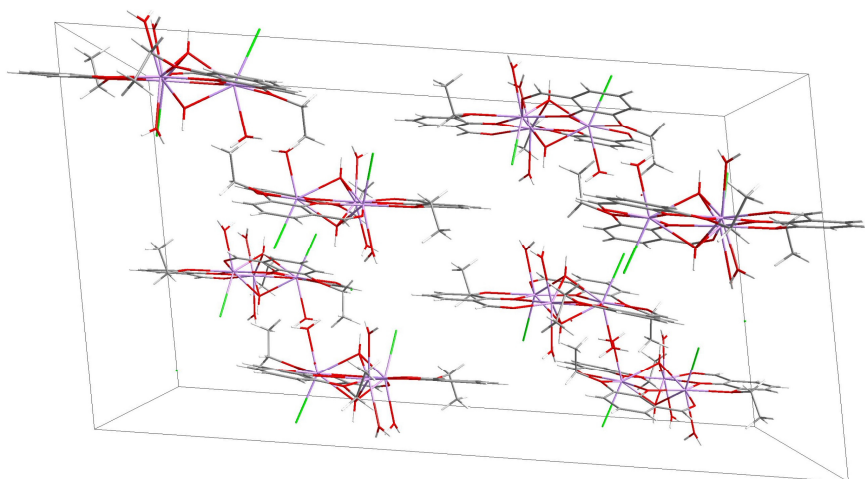


Figure 3-8 Coordination spheres of the Dy(III) ions in the molecule. Here as representative, complex (**1**) is chosen.

The packing of the molecules of $[\text{Dy}_3(\text{L})_3(\mu_3\text{-OH})_2(\text{H}_2\text{O})_4\text{Cl}_2]\text{Cl}_2 \cdot 5\text{H}_2\text{O} \cdot 3\text{MeOH}$ (**1**) (Figure 3-9) and $[\text{Dy}_3(\text{L})_3(\mu_3\text{-OH})_2(\text{H}_2\text{O})_2(\text{CH}_3\text{OH})\text{Cl}_3]\text{Cl} \cdot 2\text{H}_2\text{O} \cdot 2\text{CH}_3\text{OH}$ (**2**) (Figure 3-10) are stabilized by hydrogen bonding between solvent molecules (water/methanol) and chloride/water/ $\mu_3\text{-OH}^-$ units. Two triangle units are linked via two lattice chlorides by hydrogen bonding with distances between 2.246 and 2.347 Å in (**1**) and 2.250 and 2.267 Å in (**2**). The triangle planes are tilted to each other at an angle of 7.6° in (**1**) and 9.9° in (**2**), respectively. The shortest inter-triangle Dy-Dy distance is 8.88 Å in (**1**) and 7.05 Å in (**2**). In **Dy3-1** the shortest inter-triangle Dy-Dy distance is reported as 7.48 Å and in **Dy3-2** as 6.80 Å.^[6]



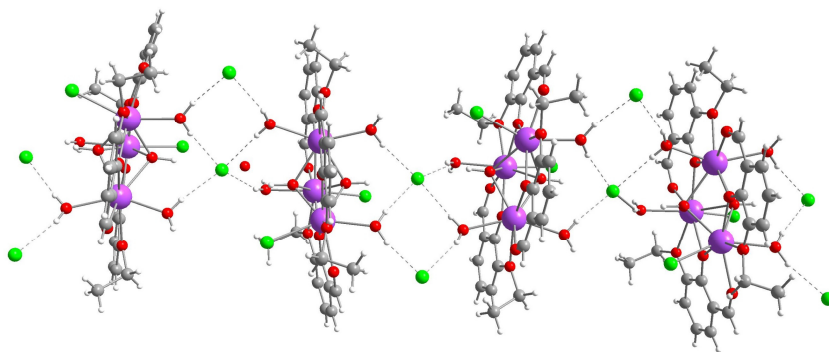


Figure 3-9 Packing of (**1**) and the chain of $\{\text{Dy}_3\}$ -triangles linked via lattice chlorides. The dashed lines represent hydrogen bonding.

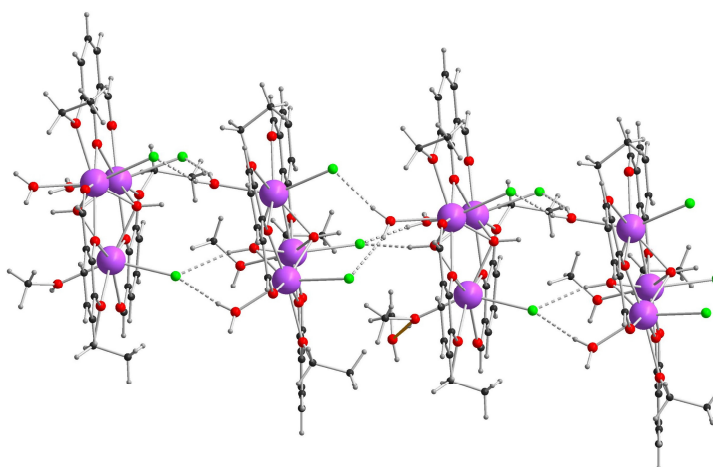
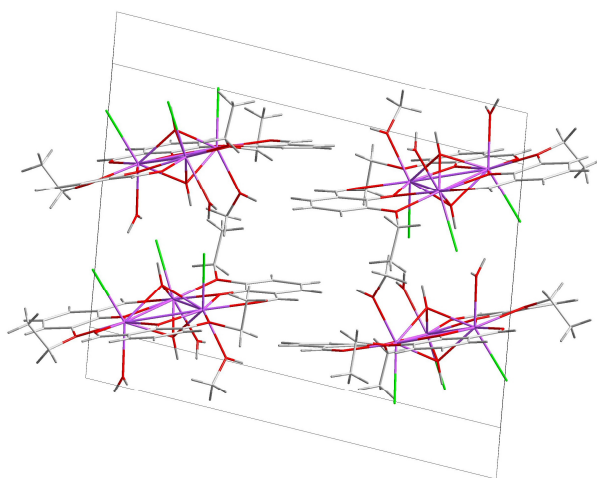


Figure 3-10 Packing of (**2**) and the chain of $\{\text{Dy}_3\}$ -triangles linked via coordinated chlorides. The dashed lines represent hydrogen bonding.

3.1.1 Calculations on (1)

Ab initio calculations on $[\text{Dy}_3(\text{L})_3(\mu_3\text{-OH})_2(\text{H}_2\text{O})_4\text{Cl}_2]\text{Cl}_2$ (**1**) and $[\text{Dy}_3(\text{L})_3(\mu_3\text{-OH})_2(\text{H}_2\text{O})_2(\text{CH}_3\text{OH})\text{Cl}_3]\text{Cl}$ (**2**) were performed by collaborators (Dr. Marko Damjanovic, former group member of Prof. Wolfgang Wernsdorfer and Yadav Twinkle, group member of apl. Prof. Karin Fink) and reveal the anisotropy axes of the Dy(III) ions. For calculation purposes, two Ln(III) ions are replaced either by Lu(III) ions in (**1**) or Y(III) ions in (**2**) to reduce the complex to one paramagnetic centre only. Each centre was studied individually. The program MOLCAS 8.2 with the following basis sets for Dy(III) (ANO-RCC-VTZP), for Lu(III), oxygens and chlorides (ANO-RCC-VDZP) and for the neutral carbon and hydrogen atoms (ANO-RCC-VDZ) were used for (**1**). The program TURBOMOLE with the basis sets x2c-TZVPall for Dy(III), x2c-SV(P)all for Y(III) and def-SV(P) for the rest of the atoms were applied for (**2**). The calculations were performed on structures with optimized hydrogen atoms. Additionally, MAGELLAN calculations were performed to compare the results for the orientation of the anisotropy axes with those of the *ab initio* calculations.

The dark blue and turquoise lines, respectively represent the anisotropy axes calculated by *ab initio* and MAGELLAN. The tilting angle θ of the anisotropy axes with the tangential direction (red line in Figure 3-11, left) and the tilting angle φ of the anisotropy axes out of the Dy_3 plane, the out-of-plane angle, (Figure 3-11, right), are the comparison factors of the anisotropy axes of the different molecules.^[5] The X indicates the centre of the molecule.

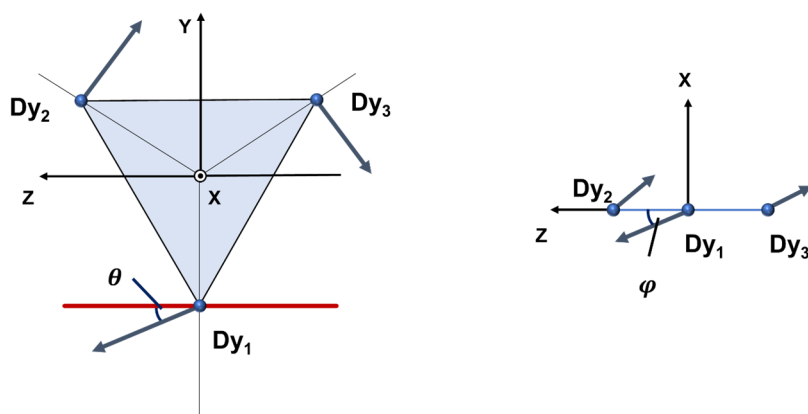
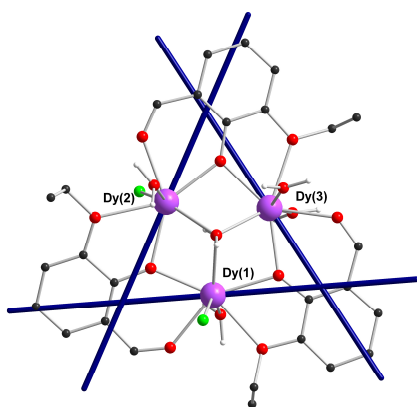


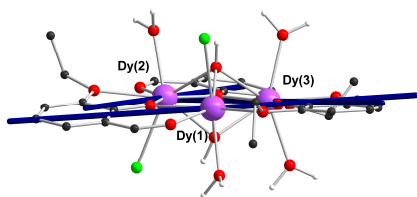
Figure 3-11 The comparison factors of the anisotropy axes of the Dy(III) ions are the tilting angle θ of the anisotropy axes with the tangential direction (red line) (left). The tilting angle of the anisotropy axes out of the Dy_3 plane, the out-of-plane angle, is identified by φ (right).

As shown in Figure 3-12, the anisotropy axes lie for both calculations almost in the Dy_3 plane with small φ angles of 1.65, 5.09 and 5.38° for the *ab initio* calculations and $\varphi = -6.25, 0.21$ and 4.68° for the MAGELLAN calculations. Viewed from the top of the molecule, the anisotropy axes form an almost perfect triangle. The tilting angles θ with 0.22, 2.12 and -2.75° are smaller for the MAGELLAN calculations than in the *ab initio* calculations with angles of 6.45, 7.45 and 9.75° but are overall in good agreement and lead to the suggestion that there is a toroidal moment in the ground state.

Ab initio calculations on
[Dy₃(L)₃(μ₃-OH)₂(H₂O)₄Cl₂]Cl₂ (**1**)

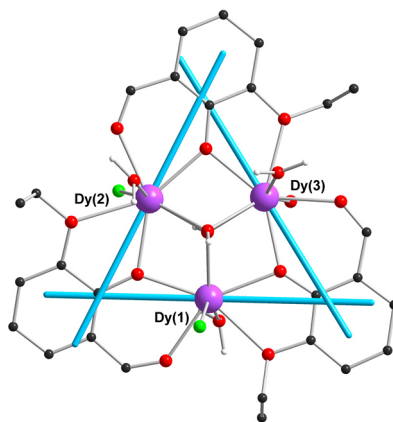


$$\begin{aligned}\theta &= 7.45^\circ (Dy1) \\ \theta &= 9.75^\circ (Dy2) \\ \theta &= 6.45^\circ (Dy3)\end{aligned}$$

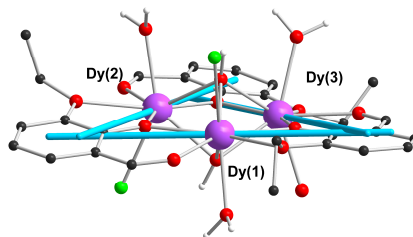


$$\begin{aligned}\varphi &= 5.09^\circ (Dy1) \\ \varphi &= 1.65^\circ (Dy2) \\ \varphi &= 5.38^\circ (Dy3)\end{aligned}$$

MAGELLAN calculations on
[Dy₃(L)₃(μ₃-OH)₂(H₂O)₄Cl₂]Cl₂ (**1**)



$$\begin{aligned}\theta &= -2.75^\circ (Dy1) \\ \theta &= 2.12^\circ (Dy2) \\ \theta &= 0.22^\circ (Dy3)\end{aligned}$$



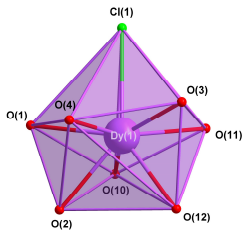
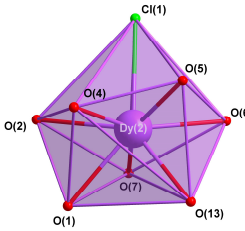
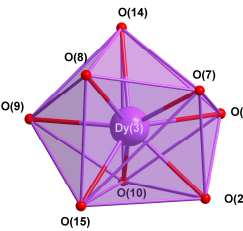
$$\begin{aligned}\varphi &= 4.68^\circ (Dy1) \\ \varphi &= -0.21^\circ (Dy2) \\ \varphi &= -6.25^\circ (Dy3)\end{aligned}$$

Figure 3-12 Anisotropy axes and angles of (**1**) from *ab initio* calculations (left) and MAGELLAN calculations (right), viewed from the top and the side.

The *ab initio* calculations provide information about the energy values of the individual Dy(III) ions (Table 3-2). The energies for the ground Kramers' doublets (KD1) are zero, as expected for Kramers' ions.^[47] The energy values of the individual Dy(III) ions for the first excited Kramers' doublets (KD2) are similar in size with values of

117.14 for Dy(1), 166.46 for Dy(2) and 139.87 cm^{-1} for Dy(3). The g -values indicate that the anisotropy axes are strongly axial with values in the z -direction (g_z) close to 20 (19.692 for Dy(1); 19.592 for Dy(2) and 19.693 for Dy(3)) and low transverse components (g_x, g_y). Dy(2), whose coordination sphere most closely resembles the triangular dodecahedron, has slightly higher values in the transverse direction of the anisotropy compared to Dy(1) and Dy(3). This is the case in the ground Kramers' doublets (KD1), and bigger in the first excited Kramers' doublets (KD2). It is noteworthy that the energies of the first Kramers' doublets of Dy(2) are also higher than those for Dy(1) and Dy(3). The minimum reversal energies (MRE) for the single-ion anisotropy axes are calculated by MAGELLAN but no obvious correlation to other energy values can be established.

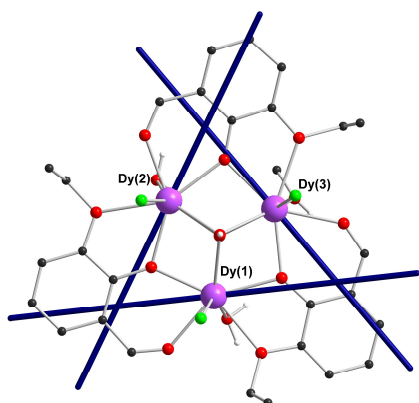
Table 3-2 Energies and g -values of the ground and first excited Kramers' doublets (KD1 and KD2) for (**1**), calculated by *ab initio*. The minimum reversal energy is calculated by MAGELLAN.

	 O ₇ Cl	 O ₇ Cl	 O ₈
	1.048 TDD-8	0.884 TDD-8	1.076 TDD-8
KD1 E [cm^{-1}]	0.00	0.00	0.00
g_x	0.000	0.037	0.005
g_y	0.0019	0.070	0.0107
g_z	19.692	19.592	19.693
KD 2 E [cm^{-1}]	117.141	166.459	139.874
g_x	0.101	1.392	0.902
g_y	0.113	3.314	1.672
g_z	16.669	15.614	16.156
Minimum reversal energy	342.0 cm^{-1}	319.1 cm^{-1}	844.7 cm^{-1}

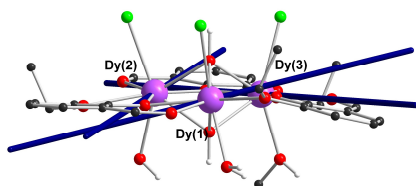
3.1.2 Calculations on (**2**)

Ab initio and MAGELLAN calculations for $[\text{Dy}_3(\text{L})_3(\mu_3\text{-OH})_2(\text{H}_2\text{O})_2(\text{CH}_3\text{OH})\text{Cl}_3]\text{Cl}$ (**2**) and the resulting anisotropy axes are shown in Figure 3-13. The anisotropy axes found for the *ab initio* calculations lie almost perfectly in the metal plane but with higher φ angles than in (**1**) of 13.90, -8.65 and -0.24°. The MAGELLAN calculation suggests smaller out-of-plane angles of 4.38, 1.81 and -1.53°. From the top view, the anisotropy axes of triangles in both calculations look similar but for the MAGELLAN calculations it is nearly perfect with very small θ angles of 1.37°, -2.36° and -1.11 compared to the *ab initio* calculations which give θ angles of 10.78, 8.45 and 14.92°. The vortex-like arrangement of the anisotropy axes gives, as in (**1**), the suggestion of a toroidal ground state.

Ab initio calculations on
 $[\text{Dy}_3(\text{L})_3(\mu_3\text{-OH})_2(\text{H}_2\text{O})_2(\text{CH}_3\text{OH})\text{Cl}_3]\text{Cl}$
 (**2**)

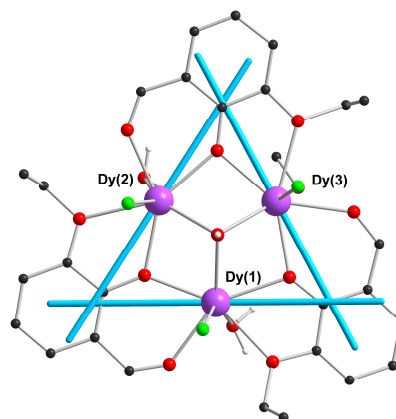


$$\begin{aligned}\theta &= 10.78^\circ (\text{Dy1}) \\ \theta &= 8.45^\circ (\text{Dy2}) \\ \theta &= 14.92^\circ (\text{Dy3})\end{aligned}$$

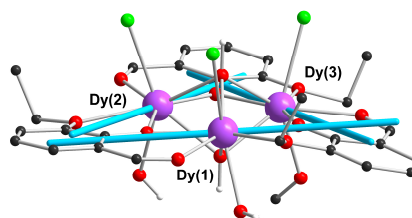


$$\begin{aligned}\varphi &= 13.90^\circ (\text{Dy1}) \\ \varphi &= -8.65^\circ (\text{Dy2}) \\ \varphi &= -0.24^\circ (\text{Dy3})\end{aligned}$$

Ab initio calculations on
 $[\text{Dy}_3(\text{L})_3(\mu_3\text{-OH})_2(\text{H}_2\text{O})_2(\text{CH}_3\text{OH})\text{Cl}_3]\text{Cl}$
 (**2**)



$$\begin{aligned}\theta &= 1.37^\circ (\text{Dy1}) \\ \theta &= -2.36^\circ (\text{Dy2}) \\ \theta &= -1.11^\circ (\text{Dy3})\end{aligned}$$

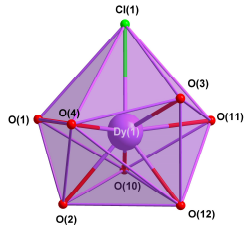
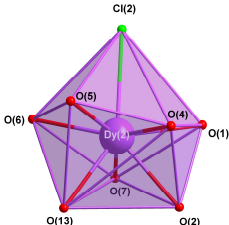
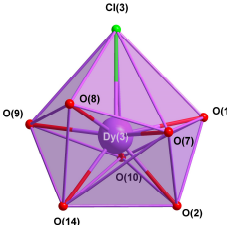


$$\begin{aligned}\varphi &= 4.38^\circ (\text{Dy1}) \\ \varphi &= 1.81^\circ (\text{Dy2}) \\ \varphi &= -1.53^\circ (\text{Dy3})\end{aligned}$$

Figure 3-13 Anisotropy axes and angles of (**2**) from *ab initio* calculations (left) and MAGELLAN calculations (right), viewing from the top and the side.

The energies calculated in Table 3-3 by *ab initio* for the ground Kramers' doublets (KD1) are zero, as expected for Kramers' ions. The energy values of the individual Dy(III) ions for the first excited Kramers' doublets (KD2) of Dy(1) and Dy(2) are similar with values of 224.39 and 253.85 cm⁻¹ and more than two times higher than the energy of Dy(3) with 100.98 cm⁻¹. The axially of the anisotropy axes are less pronounced than in (**1**) with g -values in z -direction (g_z) of 19.123 for Dy(1), 19.341 for Dy(2) and only 18.264 for Dy(3). As in (**1**) for Dy(2), the transverse components of the anisotropy (g_x, g_y) are highest for Dy(3), the dysprosium ion whose coordination sphere is closest to triangular dodecahedral. It is noteworthy that the reverse effect in the first excited Kramers' doublets (KD2) occur and the g_z value is with 17.163 much larger than the ones for Dy(1) with 11.802 and for Dy(2) with 14.182. The minimum reversal energies for the single-ion anisotropy axes are calculated by MAGELLAN and the values seemed to be approximately twice as high as the energies of the first excited Kramers' doublets (KD2) for Dy(2) and for Dy(3) but not for Dy(2) where the minimal reversal energy is closer to the energies of the first excited Kramers' doublets.

Table 3-3 Energies and g -values of the ground and first excited Kramers' doublets (KD1 and KD2) for (**2**), calculated by *ab initio*. The minimum reversal energy is calculated by MAGELLAN.

	 O ₇ Cl	 O ₇ Cl	 O ₇ Cl
	1.127 TDD-8	1.261 TDD-8	0.803 TDD-8
KD 1 E [cm ⁻¹]	0.00	0.00	0.00
g_x	0.179	0.112	0.772
g_y	0.105	0.100	0.105
g_z	19.123	19.341	18.264
KD 2 E [cm ⁻¹]	224.39	253.85	100.98
g_x	5.693	2.924	1.674
g_y	3.974	2.312	0.072

g _z	11.802	14.182	17.163
Min. reversal energy	261.9 cm⁻¹	521.6 cm⁻¹	209.2 cm⁻¹

3.1.3 Magnetic properties of (1) and (2)

The static magnetic susceptibility of the compounds $[\text{Dy}_3(3\text{-ethoxysalicylaldehyde})_3(\mu_3\text{-OH})_2(\text{H}_2\text{O})_4\text{Cl}_2]\text{Cl}_2 \cdot 5\text{H}_2\text{O} \cdot 3\text{MeOH}$ (**1**) and $[\text{Dy}_3(3\text{-ethoxysalicylaldehyde})_3(\mu_3\text{-OH})_2(\text{H}_2\text{O})_2(\text{CH}_3\text{OH})\text{Cl}_3]\text{Cl} \cdot 2\text{H}_2\text{O} \cdot 2\text{CH}_3\text{OH}$ (**2**) were measured under a DC field of 0.1 T over the temperature range 2-300 K. The χT vs T plots together with those from **Dy3-1** and **Dy3-2** for comparison, are shown in Figure 3-14.

The value of the χT products at 300 K is 41.67 for (**1**) and 40.65 $\text{cm}^3\text{mol}^{-1}\text{K}$ for (**2**). These values are largely in agreement with the theoretical value of 42.51 $\text{cm}^3\text{mol}^{-1}\text{K}$, expected for three non-interacting Dy(III) ions ($S = \frac{5}{2}$, $g = \frac{4}{3}$, $C = 14.17 \text{ cm}^3\text{mol}^{-1}\text{K}$). In both systems the value of the χT product decreases slightly on cooling, to 34.73 $\text{cm}^3\text{mol}^{-1}\text{K}$ for (**1**) and to 33.36 $\text{cm}^3\text{mol}^{-1}\text{K}$ for (**2**) at 30 K. These slight decreases result from depopulation of excited m_j states. On cooling below these temperatures to 2 K, the curves both decrease more sharply, to 6.61 $\text{cm}^3\text{mol}^{-1}\text{K}$ for (**1**) and to 1.61 $\text{cm}^3\text{mol}^{-1}\text{K}$ for (**2**). This is probably the result of further depopulation of excited m_j states and antiferromagnetic interactions between the metal centres. These decreases to almost zero susceptibility indicate non-magnetic ground states for the two systems. The observation of the course of the χT vs T plots coincide with those for **Dy3-1** and **Dy3-2**, where the values were reported for the χT product as 40.05 $\text{cm}^3\text{mol}^{-1}\text{K}$ at 300 K and the drop to almost zero at 2 K.^[6] The magnetization plots (M vs H) for **Dy3-1** and **Dy3-2** from the literature and the measured magnetization under variable fields from 1-7 T at different temperatures of (**1**) and (**2**) are shown in Figure 3-15. The highest values are 15.06 for (**1**) and 15.38 μ_B for (**2**), which are almost equal to the value for **Dy3-1** and **Dy3-2** with 15.6 μ_B . The saturation of magnetization is not reached, and this suggests strong anisotropy in the system and/or low-lying excited states. The insets in Figure 3-15 show expansions of the magnetization curves at 2 K for (**1**) and (**2**) to make the S-shaped curve visible, which indicate the level-crossing of the ground and paramagnetic states and is usually a signature of toroidal systems. The first derivatives of the magnetization curves at 2 K for (**1**) and (**2**) give peaks at 0.9 T for both complexes, where the level-crossings from the ground states to the first excited states occur (Figure 3-16). The values for **Dy3-1** and **Dy3-2**, respectively, were found to be 0.95 T using the micro-SQUID technique.

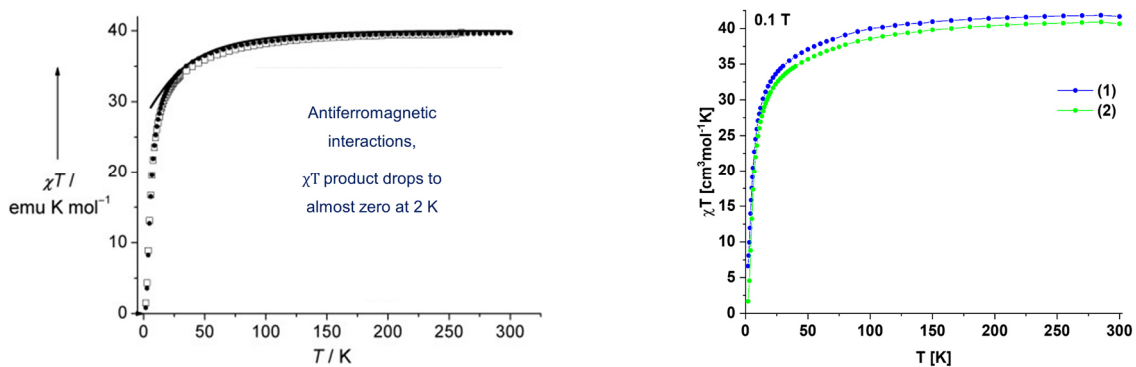


Figure 3-14 Plots of χT vs T for **Dy3-1** (\square) and **Dy3-2** (\bullet) (left). The solid line represents the calculated value for three uncorrelated Dy(III) ions. Adapted from reference^[6]. Plots of χT vs T for **(1)** (right, blue) and **(2)** (right, green).

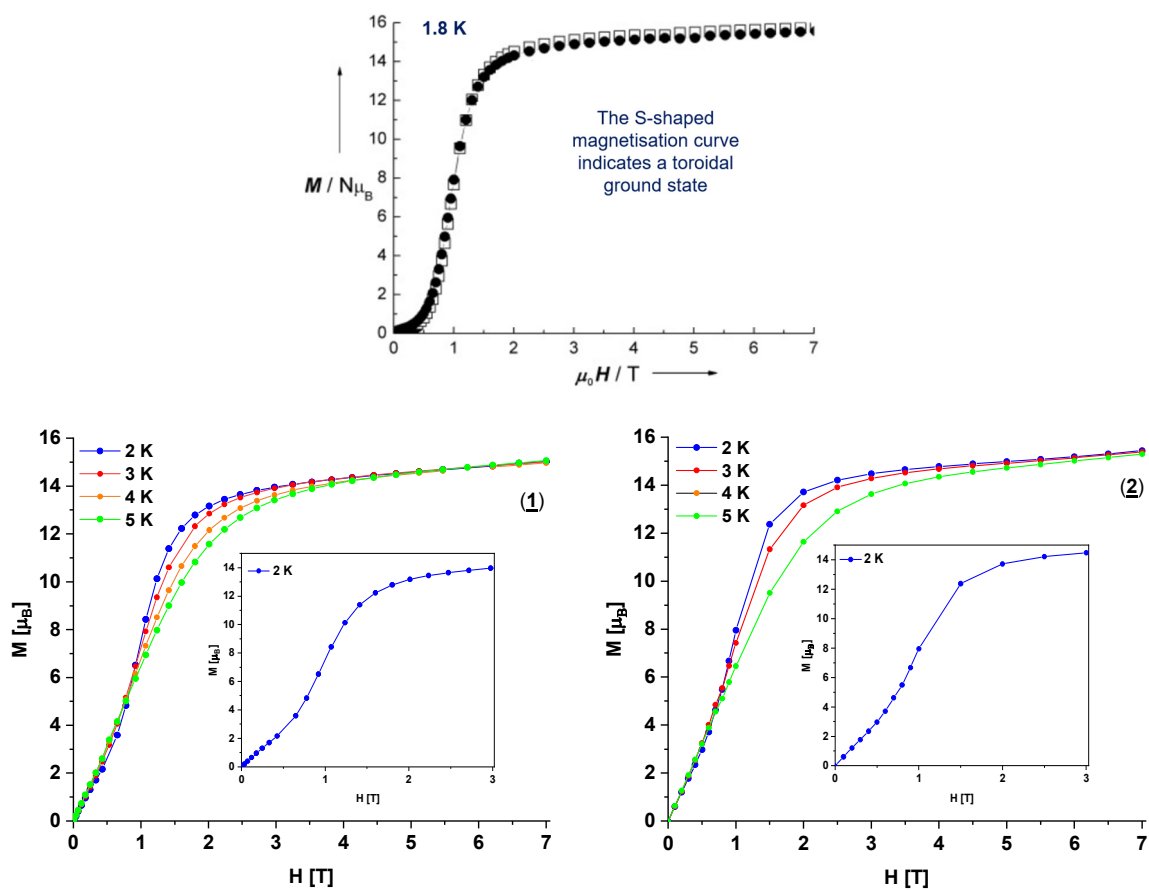


Figure 3-15 Plots of M vs H of **Dy3-1** (\square) and **Dy3-2** (\bullet) (top) at 1.8 K and the complexes **(1)** (bottom left) and **(2)** (bottom right) at different temperatures. The insets show the enlarged magnetization for 2 K to make the S-shaped curve visible.

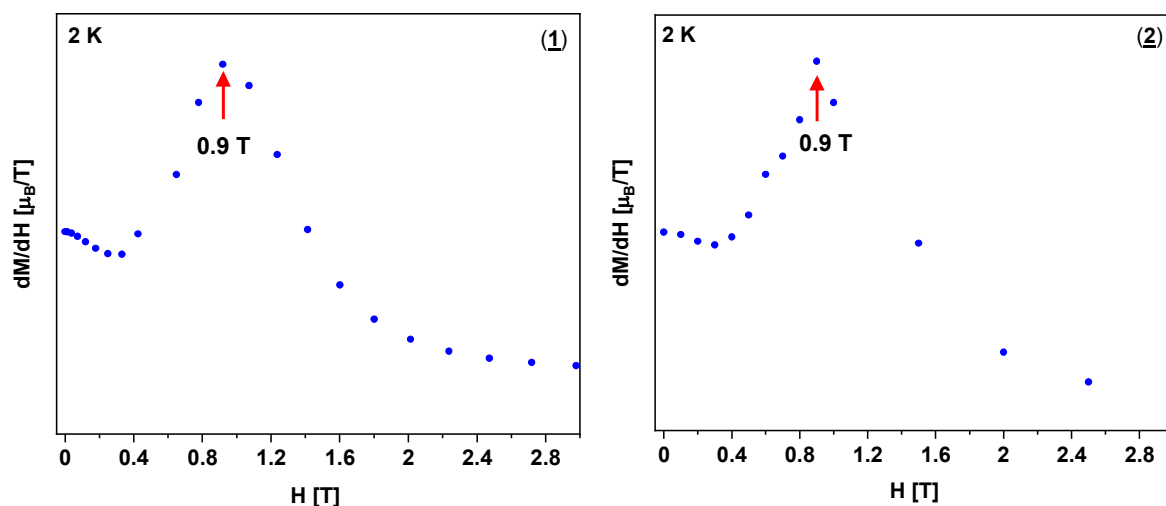


Figure 3-16 The first derivatives of the magnetizations at 2 K show peaks at 0.9 T for both complexes **(1)** (left) and **(2)** (right).

To investigate the SMM behaviour, alternating current (AC) magnetic susceptibility studies were performed in a range from 1-1500 Hz at different temperatures. The measurements for **(1)** under different static fields at 2 K shows the optimal field at 0.5 T (Figure 3-17). For a better comparison of the two systems, susceptibility measurements were carried out at the same DC field (0.5 T). Frequency dependent out-of-phase signals are observed up to 10 K for **(1)** and up to 14.5 K for **(2)** (Figure 3-18).

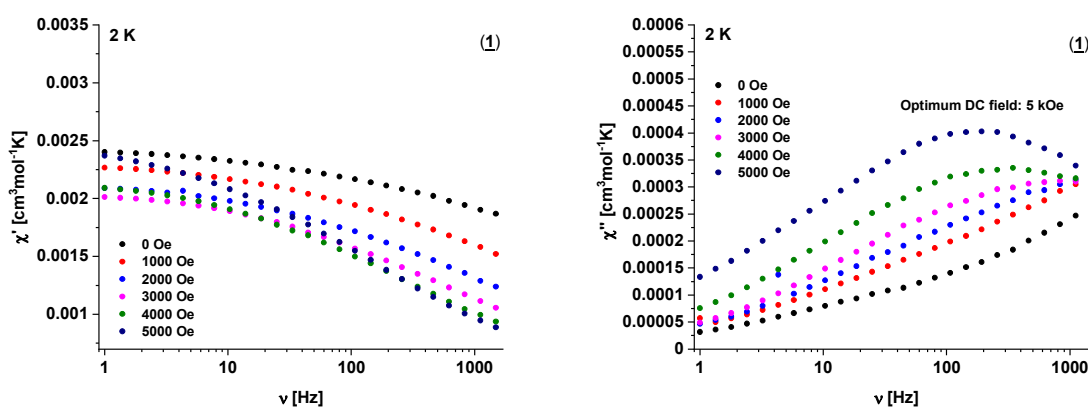


Figure 3-17 Frequency dependent in-phase (left) and out-of-phase (right) measurements on **(1)** at 2 K under different DC fields.

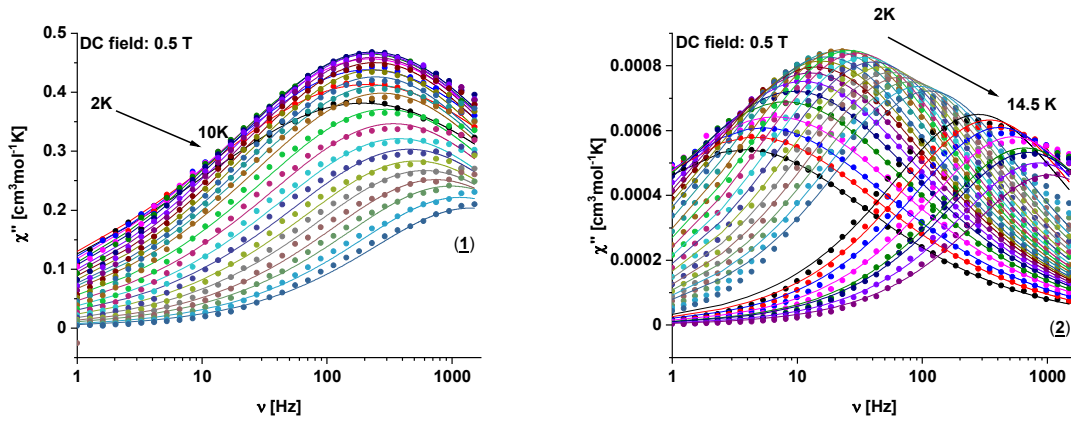


Figure 3-18 Frequency dependent out-of-phase measurements on **(1)** (left) and on **(2)** (right) under an applied field of 0.5 T.

For **Dy3-1** (\square) and **Dy3-2** (\bullet), the log plot of the relaxation time versus the inverse temperature (τ vs $1/T$) is given in the literature and follows the Arrhenius law in the high temperature region (Figure 3-19).

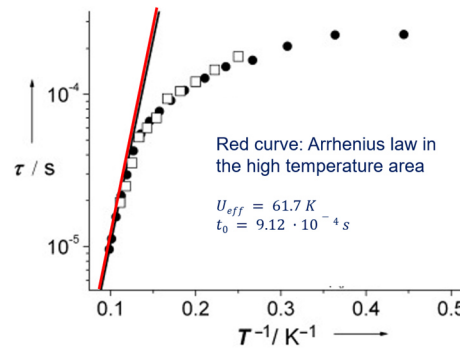


Figure 3-19 Relaxation time of the magnetization versus inverse temperature for **Dy3-1** (\square) and **Dy3-2** (\bullet). Adapted from reference^[6].

Since τ was plotted logarithmically here, plotting $\ln \tau$ vs $1/T$ gives the same results. This leads to energy barriers and relaxation times in the high temperature region $U_{eff} = 33.63 K$, $\tau_0 = 3.9 \cdot 10^{-6} s$ for **(1)** and $U_{eff} = 38.58 K$, $\tau_0 = 8.46 \cdot 10^{-6} s$ for **(2)**, fitting the Arrhenius law (Figure 3-20). These values are smaller than for **Dy3-1** and **Dy3-2**, respectively, where an energy barrier of $U_{eff} = 61.7 K$ and a preexponential factor of $\tau_0 = 9.12 \cdot 10^{-4} s$ was found. It is also noteworthy, that the measurement for **Dy3-1** and **Dy3-2**, respectively, to obtain the energy barriers and the relaxation times, were done at zero applied field, but the measurements for **(1)** and **(2)** under an applied field of 0.5 T.

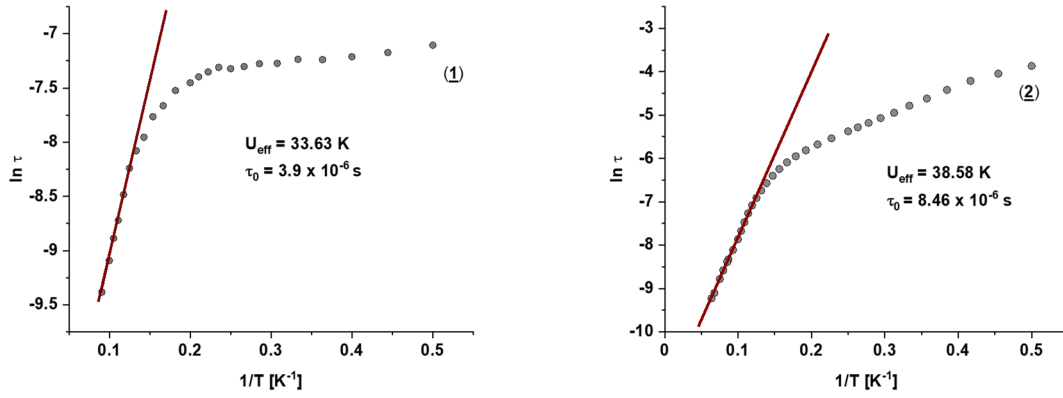


Figure 3-20 The relaxation times are following the Arrhenius law in the high temperature region (red curve) for **(1)** (left) and **(2)** (right).

Using the simplified form for all relaxation processes with the parameters A (Direct process), B (QTM) and C (Raman process):

$$\tau^{-1} = AT + B + CT^n + \tau_0^{-1} * \exp\left(-\frac{U_{eff}}{k_B T}\right)$$

and taking out the Raman process for **(1)**, leads to $A = 105.7 \text{ s}^{-1} \text{ K}^{-1}$ and $B = 1074 \text{ s}^{-1}$ which suggests a high proportion of Direct processes and severe QTM (Figure 3-21). The energy barrier of $U_{eff} = 44.73 \text{ K}$ is a bit higher than for the Orbach process. There was no satisfying fit for the relaxation processes in **(2)**.

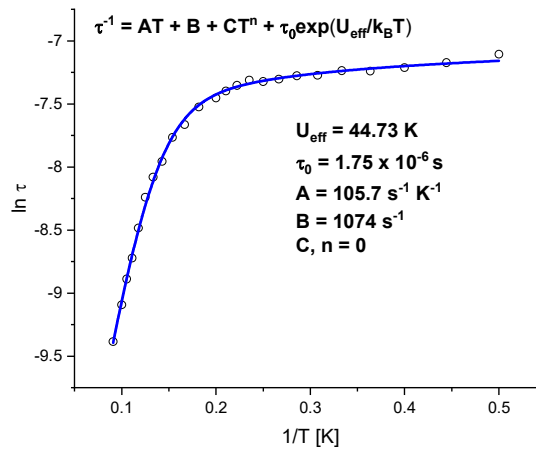


Figure 3-21 Parameters of the relaxation processes of **(1)**, indicating additional Direct processes (Parameter A) and QTM (Parameter B).

In the Cole-Cole plots (Figure 3-22) the distribution factor α is between 0.35 and 0.58 for **(1)** and between 0.16 and 0.45 for **(2)** which indicate a significant distribution of different relaxation processes (Figure 3-22).

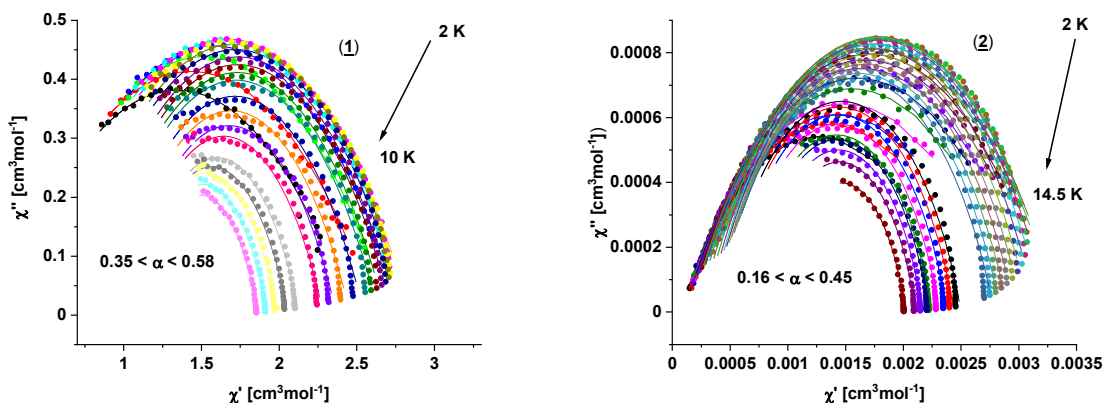


Figure 3-22 Arrhenius and Cole-Cole plots of **(1)** (left) and of **(2)** (right).

The single crystal measurements on a micro-SQUID at 0.1 K at a sweep rate of 28 mT/s are reported for **Dy3-2** in the literature (Figure 3-23, top), showing level-crossing from the ground to the first excited state at 0.95 T. For **(1)**, single crystal measurements were carried out in a range from 33 mK to 2 K with a field-sweep rate of 8 mT/s (Figure 3-23, middle left) and for different field sweep rates at 30 mK (Figure 3-23, middle right). The lowest temperature magnetization measurement (30 mK and 33 mK, respectively, blue curve) reveals two steps in each direction of the field with slow magnetic relaxation that results in hysteresis in the range from -0.8 T to 0.8 T. The steps indicate a magnetization change in a small interval of applied magnetic field, seen clearly in the first derivative of the magnetization (Figure 3-23, bottom). The steps at 0.73 T and 0.8 T indicate the spin flipping and the level-crossing of toroidal and paramagnetic states.^[86,87]

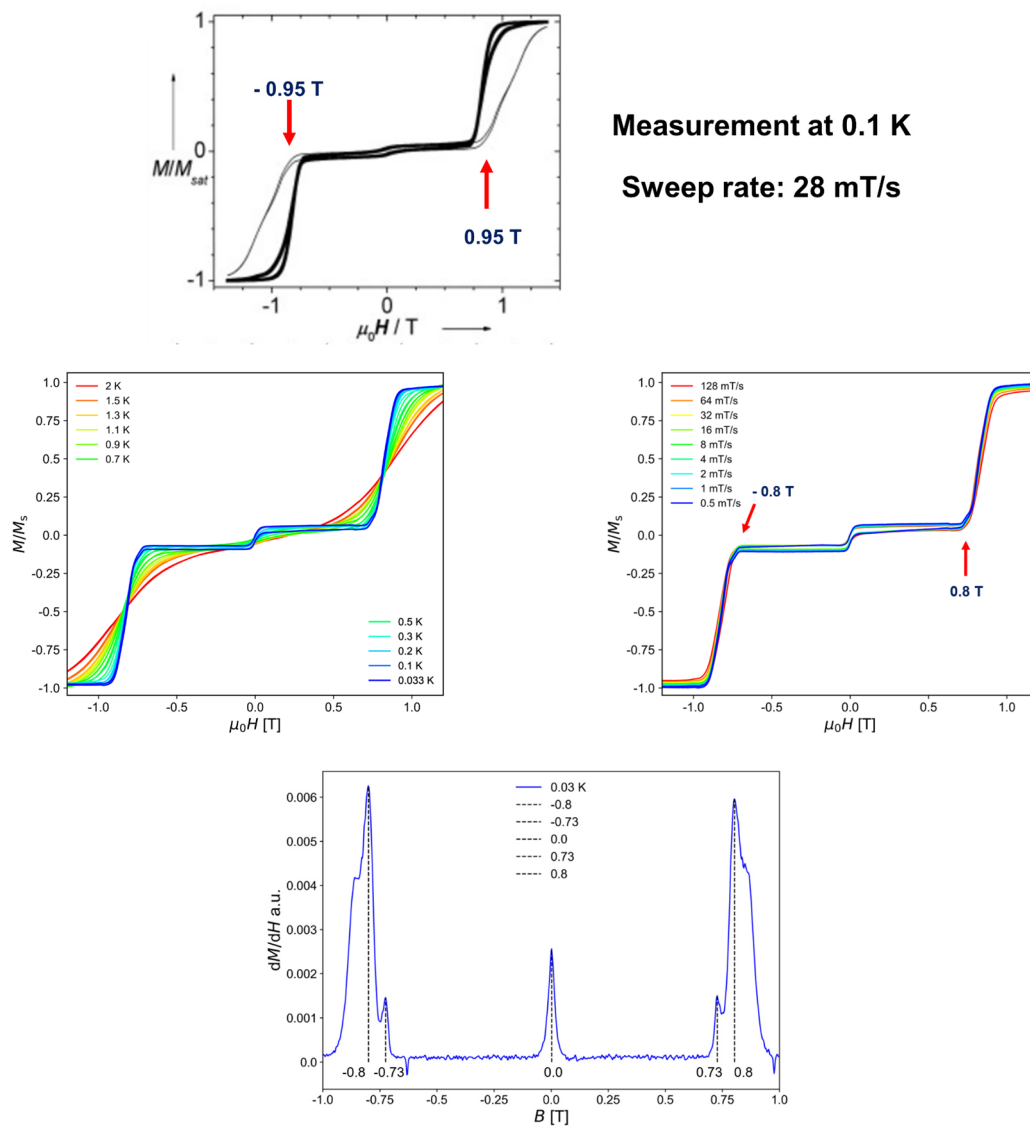


Figure 3-23 Single crystal measurements on **Dy3-2** with applied field in the plane (light) and perpendicular to the plane (bold) of the Dy(III) ions (top). Adapted from reference^[6]. Single crystal measurements on (**1**) (middle). The first derivative shows a steep rise of magnetization at ± 0.73 and ± 0.8 T and zero field (bottom).

In the case of the triangular system, the spins are all tangential to the Dy₃ plane. By applying a magnetic field H parallel to this plane (easy plane), one spin flips at a certain value. Due to the low symmetry of the structure, the Dy(III) ions are all different, and flip at different magnetic fields ($H = 0.73, 0.80$). Figure 3-24 shows the spin flip schematically for two different Dy(III) ions at different fields.

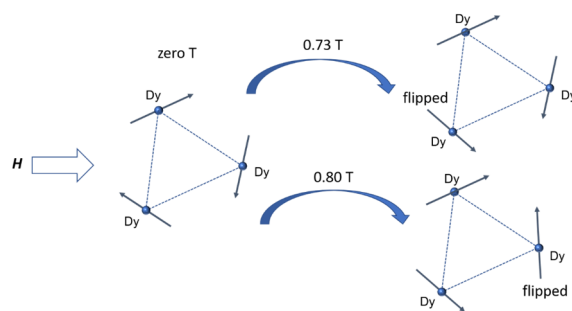


Figure 3-24 At zero applied field, the toroidal arrangement is intact. Due to the different Dy(III) ions, the values of H where one of the spin flips is different.

3.1.4 Isostructural compounds of (2) with Eu (3), Tb (4), Ho (5) and Er (6)

Identical crystal structures of $[\text{Dy}_3(\text{L})_3(\mu_3\text{-OH})_2(\text{H}_2\text{O})_2(\text{CH}_3\text{OH})\text{Cl}_3]\text{Cl}$ (2) were synthesized with different lanthanides, leading to the complexes

$[\text{Eu}_3(\text{L})_3(\mu_3\text{-OH})_2(\text{H}_2\text{O})_2(\text{CH}_3\text{OH})\text{Cl}_3]\text{Cl} \cdot 2\text{CH}_3\text{OH} \cdot 2\text{H}_2\text{O}$ (3),

$[\text{Tb}_3(\text{L})_3(\mu_3\text{-OH})_2(\text{H}_2\text{O})_2(\text{CH}_3\text{OH})\text{Cl}_3]\text{Cl} \cdot 3\text{CH}_3\text{OH}$ (4),

$[\text{Ho}_3(\text{L})_3(\mu_3\text{-OH})_2(\text{H}_2\text{O})_2(\text{CH}_3\text{OH})\text{Cl}_3]\text{Cl} \cdot 3\text{CH}_3\text{OH}$ (5),

$[\text{Er}_3(\text{L})_3(\mu_3\text{-OH})_2(\text{H}_2\text{O})_2(\text{CH}_3\text{OH})\text{Cl}_3]\text{Cl} \cdot \text{H}_2\text{O} \cdot 2\text{CH}_3\text{OH}$ (6)

with HL = 3-ethoxysalicylaldehyde. They all crystallize in the monoclinic space group $P2_1/c$, as for (2). Europium was chosen because, according to the literature, it has no magnetization in the ground state. Terbium sometimes shows better SMM performance (in high symmetry compounds) than dysprosium and together with holmium it is a non-Kramers' ion. Erbium was chosen because it has a prolate electron density in the ground state, unlike the oblate density for Tb(III) and Dy(III).^[47] In the crystal structures the Ln··Ln distances decrease with increasing Z in line with the lanthanide contraction from Eu to Er.^[88] The angles between the Ln(III) ions are approximately 60° in all structures. Likewise, the Ln-OH-Ln angles are similar for all structures (94.9-97.9°). These distances and angles, also the distance of the $\mu_3\text{-OH}^-$ units from the metal plane are shown in Table 3-4. Selected distances and angles and the molecular structure are given in the appendix 12.2.

Table 3-4 Comparison of selected angles and lengths for (3) to (6).

	Eu (3)	Tb (4)	Ho (5)	Er (6)
Ln··Ln [Å]	3.5782(9)	3.5386(3)	3.4969(4)	3.4824(8)
	3.6061(11)	3.5558(4)	3.5234(4)	3.5073(9)
	3.6167(9)	3.5771(3)	3.5321(4)	3.5182(8)
Ln-Ln-Ln [°]	59.39(2)	59.49(1)	59.42(1)	59.43(2)
	60.16(2)	59.95(1)	60.17(1)	60.13(2)
	60.45(2)	60.56(1)	60.41(1)	60.44(2)
Ln-OH-Ln [°]	96.4(3)- 97.9(3)	95.44(12)- 97.96(12)	95.15(13)- 98.41(13)	94.9(3)- 97.8(3)
OH··Ln ₃ plane [Å]	1.1920-1.2031	1.1566-1.2041	1.1490-1.2025	1.1569-1.2002

Ab initio calculations for the systems with Tb (4), Ho (5) and Er (6) were performed in collaboration with the group of apl. Prof. Karin Fink, using the program TURBOMOLE

as it was the case for the dysprosium analogue (**2**). The calculations were performed on structures with optimized hydrogen atoms. The anisotropy axes with the tilting angles θ of the anisotropy axes with the tangential direction and the out-of-plane angles φ for Tb (**4**) are given in Figure 3-25. Although no longer lying in the plane of the triangle, the arrangement of the anisotropy axes with θ angles of 32.90, 29.80 and 21.79°, still suggests a vortex-like arrangement of the spins from the top view, but the anisotropy axes protrude significantly out of the Tb₃ plane with φ angles of 6.66, 26.14 and 35.86°.

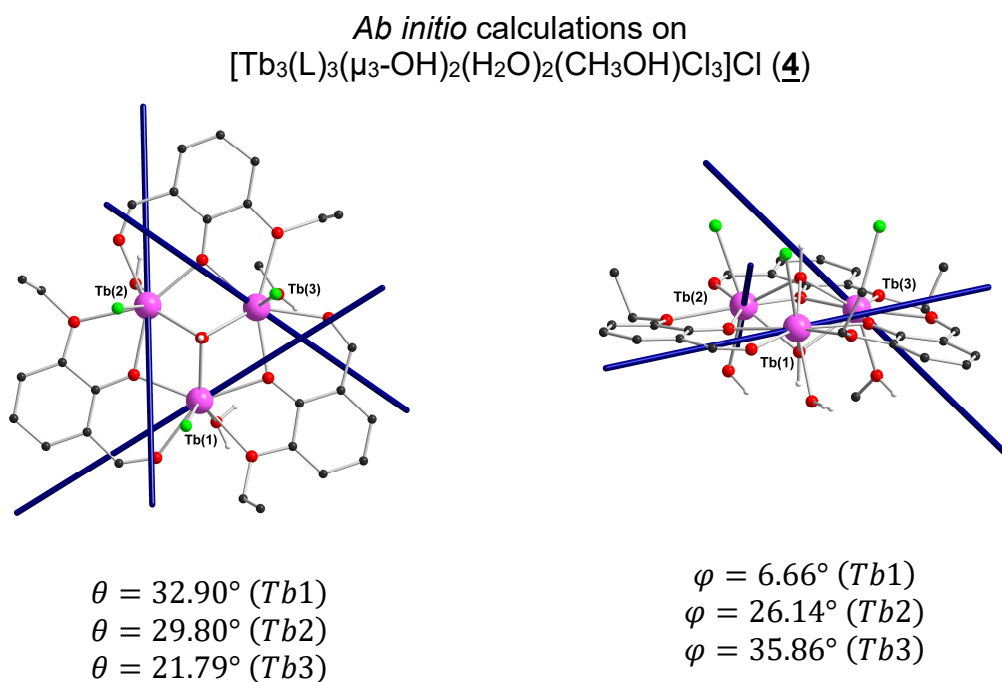


Figure 3-25 Anisotropy axes and tilting angles θ and φ of (**4**) from *ab initio* calculations.

The resulting energies of the ground and first excited doublets and g -values are given in Table 3-5. As expected for non-Kramers' ions, the energies within the ground state, as well as in the first excited state, are not degenerate.^[47,89] The energies for the ground states are zero and close to zero though (0.00 and 1.22 for Tb(1), 0.00 and 0.26 for Tb(2) and 0.00 and 0.66 for Tb(3)). The g values in z -direction (g_z) for the single Tb(III) ions with 16.35, 17.02 and 16.33 are smaller than for the dysprosium analogue (**2**). There is no transversal anisotropy in x - and y -direction ($g_x = g_y = 0$) because of the pure nature of Ising spin for non-Kramers' ion, e.g. there are only two discrete spin states (± 1).

Table 3-5 Energies and g -values of the ground and first excited doublets for (**4**).

	Tb(1)	Tb(2)	Tb(3)
Ground Doublets	0.00	0.00	0.00
E [cm ⁻¹]	1.22	0.26	0.66
g_x	0	0	0
g_y	0	0	0
g_z	16.35	17.02	16.33
1 st excited Doublets	30.71	65.19	50.91
E [cm ⁻¹]	34.22	73.18	55.90
g_x	0	0	0
g_y	0	0	0
g_z	13.63	11.73	15.55

Ab initio calculations for Ho (**5**) lead to the anisotropy axes and angles which are shown in Figure 3-26. The anisotropy axes, viewed from the top of the molecule, with θ angles of 40.56, 30.39 and 55.65° are not forming an equilateral triangle and the axes with out-of-plane angles φ of 16.42, -1.22 and 50.80° also protrude significantly out of the Ho₃ plane, as was the case in (**4**) with the Tb₃ plane.

Ab initio calculations on
 $[\text{Ho}_3(\text{L})_3(\mu_3\text{-OH})_2(\text{H}_2\text{O})_2(\text{CH}_3\text{OH})\text{Cl}_3]\text{Cl}$ (**5**)

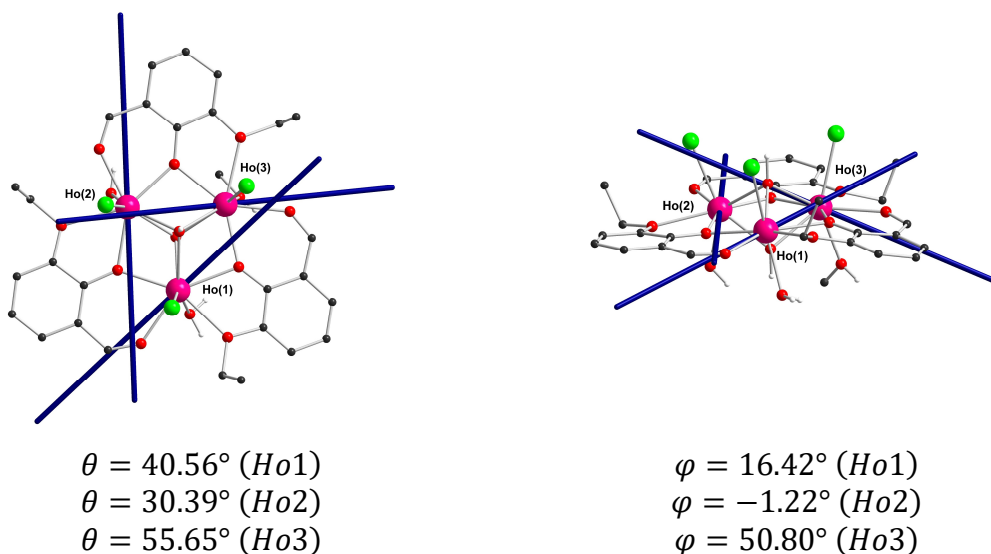


Figure 3-26 Anisotropy axes and tilting angles θ and φ of (**5**) from *ab initio* calculations.

The resulting energies of the ground and first excited doublets and g -values are given in Table 3-6. As expected for non-Kramers' ions, the ground state as well as the excited state is not degenerate as it is the case in (**4**). The splittings of the ground doublets are 4.94, 4.91 and 0.70 cm^{-1} for Ho(1), Ho(2) and Ho(3), respectively, which are slightly higher than the splitting for the terbium analogue (**4**). The g -values in z -direction (g_z) are about 17 for all Ho(III) ions, and slightly higher than for (**4**), with values of 16.33 to 17.02. The transverse components (g_x, g_y) of the anisotropy are zero for spins with pure Ising nature, as before.

Table 3-6 Energies and g -values of the ground and first excited doublets for (**5**).

	Ho(1)	Ho(2)	Ho(3)
Ground Doublets E	0.00	0.00	0.00
[cm^{-1}]	4.94	4.91	0.70
g_x	0	0	0
g_y	0	0	0
g_z	17.07	17.26	17.32
1 st excited Doublets	40.74	31.37	32.61
E [cm^{-1}]	50.77	39.56	35.73
g_x	0	0	0
g_y	0	0	0
g_z	12.24	11.66	16.91

The anisotropy axes of Er (**6**), resulting from *ab initio* calculations, are shown in Figure 3-27. From the top view, the axes do not form a triangle at all and the θ angles have values of -51.19° , 5.12° and 48.78° . Also the out-of-plane angles φ are rather large with values of 31.66° , -46.06° and 58.91° .

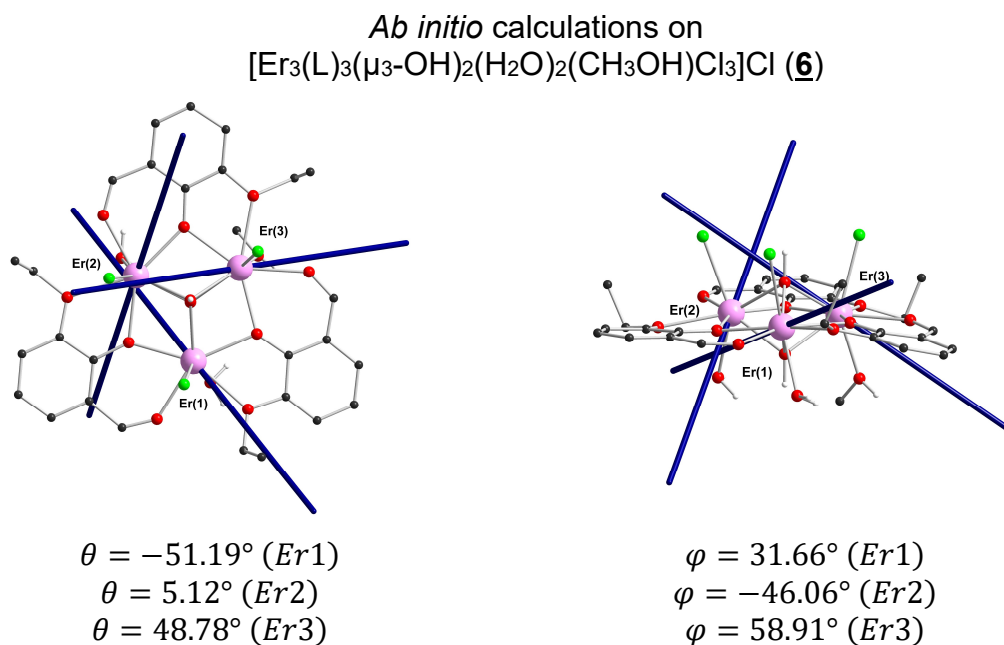


Figure 3-27 Anisotropy axes and tilting angles θ and φ of (**6**) from *ab initio* calculations.

The resulting energies of the ground and first excited doublets and g -values are given in Table 3-7. The ground Kramers' doublets (KD1) are zero and degenerate as expected for a Kramers' ion. The values for the first excited states are 97.7 , 117.9 , and 90.0 cm^{-1} , significantly larger than for the terbium (**4**) and holmium (**5**) analogues, but still lower than for the dysprosium analogue (**2**) with all values $> 100 \text{ cm}^{-1}$. The axially of the anisotropy with g -values in z -direction (g_z) of 14.54 , 15.17 and 14.83 is less pronounced compared to the discussed systems with dysprosium (**2**), terbium (**4**) and holmium (**5**). Also, the transversal components (g_x, g_y) have higher values than in (**2**).

Table 3-7 Energies and g -values of the Ground Kramers' doublets (KD1) and first excited Kramers' doublets (KD2) for (**6**).

	Er(1)	Er(2)	Er(3)
KD1 E [cm ⁻¹]	0.00	0.00	0.00
g_x	1.697	0.533	0.649
g_y	0.914	0.231	0.138
g_z	14.54	15.17	14.83
KD2 E [cm ⁻¹]	97.70	117.89	90.00
g_x	4.396	3.547	2.679
g_y	3.258	2.245	1.881
g_z	9.616	11.598	12.761

3.2 Summary of triangular Ln₃ systems

In this chapter, lanthanide triangles were synthesized, and their crystal structures were determined by X-ray diffraction. The magnetic properties of the dysprosium complexes [Dy₃(L)₃(μ₃-OH)₂(H₂O)₄Cl₂]Cl₂·5H₂O·3MeOH (**1**) and [Dy₃(L)₃(μ₃-OH)₂(H₂O)₂(CH₃OH)Cl₃]Cl·2H₂O·2CH₃OH (**2**), with HL = 3-ethoxysalicylaldehyde, for which the only difference is an extra chloride on the third Dy(III) ion, were studied.

Antiferromagnetic interactions were found to be dominant in both Dy systems, (**1**) and (**2**). The level-crossing between almost non-magnetic (toroidal) ground states and first excited states is experimentally shown for both complexes by the magnetization measurements with a typical S-shaped curve in the *M* vs *H* plot. The first derivatives of the magnetization lead to values of *H* with 0.90 T. Furthermore, the almost non-magnetic ground state is substantiated by the *χT* products at low temperatures reaching almost zero (6.61 cm³mol⁻¹K for (**1**) and 1.61 cm³mol⁻¹K for (**2**)). Both complexes are SMMs, observed from AC susceptibility measurements at applied DC field of 0.5 T with energy barriers and relaxation times of *U_{eff}* = 33.63 K, *τ*₀ = 3.9 · 10⁻⁶ s for (**1**) and *U_{eff}* = 38.58 K, *τ*₀ = 8.46 · 10⁻⁶ s for (**2**). Single crystal measurements of (**1**) with a micro-SQUID showed a narrow hysteresis and a strong increase in magnetization at about 0.73 and 0.80 T, respectively, for two different spins, which confirms the level-crossing between the toroidal ground state and the first excited state, seen in the first derivative of the bulk magnetization measurements. These results are compared to the literature-known complexes **Dy3-1** and **Dy3-2** which show practically identical magnetic properties amongst each other^[6]. A higher value of *H* = 0.95 T for the level-crossing were determined by micro-SQUID measurements and SMM behaviour were already observed in zero field but with a higher energy barrier and a similar relaxation time of *U_{eff}* = 61.7 K and *τ*₀ = 9.14 · 10⁻⁴ s.^[6]

From *ab initio* calculations for the complexes (**1**) and (**2**), a vortex-like arrangement of the anisotropy axes and spins, respectively was predicted. These calculations are in fairly close agreement with the much less computationally intensive MAGELLAN calculations. The *ab initio* determined anisotropy axes of isostructural compounds of (**2**) with the lanthanides Tb (**4**), Ho(**5**), and Er (**6**), showed no evidence of toroidal arrangement of the anisotropy axes and significantly less axiality. Similarly, the

energy and simultaneously the gap between ground state and first excited state for both dysprosium complexes (117.41 cm⁻¹ for Dy(1), 166.46 cm⁻¹ for Dy(2) and 139.87 cm⁻¹ for Dy(3)) for complex **(1)** and 224.39 cm⁻¹ for Dy(1), 253.85 cm⁻¹ for Dy(2) and 100.98 cm⁻¹ for Dy(3)) for complex **(2)** are much larger than for the Tb analogue **(4)** and the Ho analogue **(5)** (30.71/34.22 cm⁻¹ for Tb(1), 65.19/73.18 cm⁻¹ for Tb(2) and 50.91/55.90 cm⁻¹ for Tb(3)); (40.74/50.77 cm⁻¹ for Ho(1), 31.37/39.56 cm⁻¹ for Ho(2) and 32.61/35.73 cm⁻¹ for Ho(3)). Higher energy values than for **(4)** and **(5)** are present in the Er analogue **(6)** (97.70 cm⁻¹ for Er(1), 117.89 cm⁻¹ for Er(2) and 90.00 cm⁻¹ for Er(3)). The coordination spheres around the Ln(III) ions are all the same with O₇Cl donor sets. This suggests that it is not the coordination sphere but the nature of the Ln(III) ions which matter in regard of the finding of toroidal moments.

Kramers' (Dy(III)) versus non-Kramers' (Tb(III), Ho(III)) and electron density distribution (prolate for Er(III)) seems to be the crucial factor determining the anisotropy and the axiality of the system. *Ab initio* calculations for the literature known **Dy3-1** and **Dy3-2** were performed for the first time in 2008^[84] and 2016^[5], respectively. Even though these two systems have the same properties in regard of susceptibility and magnetization, the calculations revealed a discrepancy between the calculated energy values of the individual Kramers' doublets. The calculation on **Dy3-1** gave values of 150.2, 217.8, and 234.2 cm⁻¹ of the first excited Kramers' doublets for the individual Dy(III) ions. In this approach, the program MOLCAS-7.0 which treats each Dy(III) spin in isolation was used for the calculation. The calculation on **Dy3-2** took interactions between the spins into account, giving energies of 142.9, 186.13 and 187.26 cm⁻¹ for the first excited Kramers' doublets. This has little effect on the relative position of the anisotropy axes within the two complexes, but it shows that the improvements to *ab initio* calculations bring fresh insights into such systems.

The Dy···Dy distances show a clear correlation for the strength of the toroidicity (Table 3-8). The small distances between the Dy(III) ions in **Dy3-1** and **Dy3-2** in contrast to **(1)** and **(2)**, allow stronger Dy-Dy dipolar interactions which favour a stronger toroidal moment. The Dy-OH-Dy and Dy-Dy-Dy angles are similar and have no discernible effect on the toroidicity.

Table 3-8 Comparison of selected angles and lengths for **Dy3-1**, **Dy3-2**, (**1**) and (**2**).

complex & space group	Dy··Dy [Å]	Dy-Dy-Dy [°]	Dy-OH-Dy [°]	OH··Dy ₃ plane [Å]	Toroidicity	SMM behaviour
Dy3-1 C2/c	3.5026(6) 3.5231(4) 3.5272(4)	59.577(9) 60.153(9) 60.270(9)	95.85(15) to 97.32(16)	1.176 1.201	0.95 T (Micro-SQUID)	at zero field
Dy3-2 C2/c	3.5135(3) 3.5185(3) 3.5400(3)	59.704(5) 59.843(7) 60.453(5)	95.85(8) to 98.28(8)	1.184 1.205	0.95 T (Micro-SQUID)	at zero field
[Dy ₃ (L) ₃ (μ ₃ - OH) ₂ (H ₂ O) ₄ Cl ₂]Cl ₂ (1) I2/a	3.5491(4) 3.5492(3) 3.5679(3)	59.82(1) 59.83(1) 60.348(7)	96.48(12) to 97.52(12)	1.193 1.206	0.80/0.90 T (Micro-SQUID/bulk)	at 0.5 T
[Dy ₃ (L) ₃ (μ ₃ - OH) ₂ (H ₂ O) ₂ (CH ₃ OH)Cl ₃]Cl (2) P2 ₁ /c	3.5219(5) 3.5370(6) 3.5463(5)	59.461(10) 60.403(10) 60.138(11)	95.2(2) to 97.52(12)	1.168 1.204	0.90 T (bulk)	at 0.5 T

4 Heteronuclear M_2Dy_3 systems

To investigate the effect of additional metal ions in $\{Dy_3\}$ systems, pentanuclear systems were synthesized. The reaction of Dy(III) salts with the various metal salts and various benzoic derivatives as ligands in different solvents led to 10 different products. For the deprotonation of the organic ligands, triethylamine was used. In these systems, the Dy(III) ions form a triangle. This is sandwiched between two homo-metal ions M (M = Cr, Al, Fe, Co), forming a trigonal bipyramid with the M(III) ions at the axial sites. Each μ_3-OH^- unit hold two Dy(III) ions and one M(III) ion together over each of the six faces of the trigonal bipyramid forming a $[M_2(\mu_3-OH)_6Dy_3]$ core with the two M(III), three Dy(III) and the six μ_3-OH^- units. This core is further ligated by six benzoate derivate ligands, bridging neighbouring Dy(III) and Cr(III) ions in a syn-syn mode (Figure 4-1).

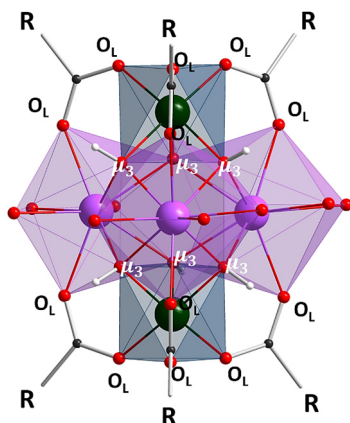


Figure 4-1 The general scheme of the M_2Dy_3 systems with the Dy (lavender), forming a plane and the metal ions M (green) in the axial positions. The μ_3-OH^- bridges in white and the additional bridging oxygens from the benzoate ligands (O_L). R stands for the different rest of the used ligands displayed below.

The M(III) ions exhibit an O_6 donor set, close to an octahedron and the oxygens are provided by three different bridging benzoate ligands (O_L) and three μ_3-OH^- units. The Dy(III) ions have either an O_9 donor set close to a muffin shape (MFF) and capped square antiprismatic (CSAPR) or an O_8 donor set close to a square antiprism (SAPR) (Figure 4-2). For each Dy(III) ion, the following scheme applies: Four oxygens are provided by four μ_3-OH^- units. The fifth and sixth oxygens are provided by two oxygens of two different bridging ligands (O_L). The remaining oxygens are provided by either charged or neutral ligands. These ligands are isopropanol (iPrOH), water

(H₂O), dimethyl formamide (DMF), mono- or bidentate nitrates (NO₃⁻) and/or mono- or bidentate benzoate derivatives (RCO₂⁻). The coordination spheres of the M(III) ions (M = Cr, Al, Fe, Co) have in all cases an almost perfect octahedral geometry with an O₆ donor set (Figure 4-2).

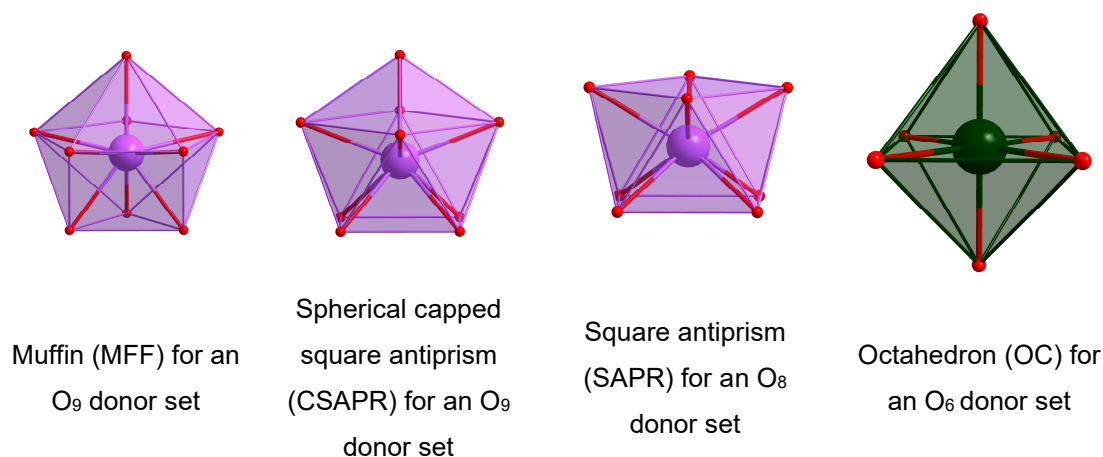
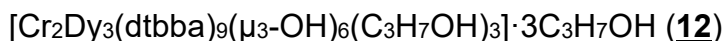
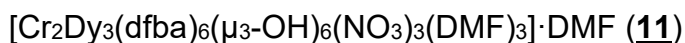
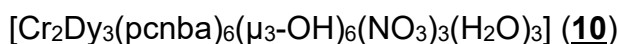
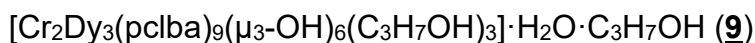
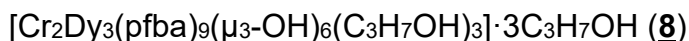
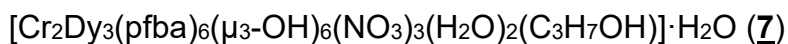
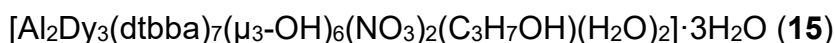
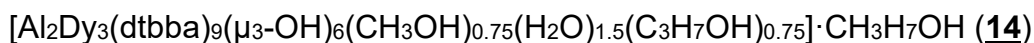
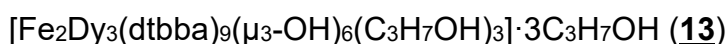


Figure 4-2 Coordination spheres with their perfect geometry around the metal ions for an O₉ and O₈ donor set for Dy(III) ions (lavender) and with an O₆ donor set for the M(III) ions (green).

The obtained systems are divided into two series. The complexes (**7**) to (**12**) are systems with a pentanuclear core of the form {Cr₂(μ₃-OH)₆Dy₃}, consisting of three Dy(III) ions and two Cr(III) ions and forming the first series of compounds (**series-1**). The organic ligands used here are different benzoic acid derivatives and are six and nine and resulted in the following complexes:



The second series (**series-2**) of compounds (**13**) to (**16**) possess the same ligand as in (**12**) – which is part of both series – but have the Cr(III) ions in the core replaced by Fe(III) in (**13**), by Al(III) in (**14**) and in (**15**) and by Co(III) in (**16**). The number of benzoate derivate ligands is either nine or seven:



$[\text{Co}_2\text{Dy}_3(\text{dtbba})_7(\mu_3\text{-OH})_6(\text{NO}_3)_2(\text{C}_3\text{H}_7\text{OH})_3] \cdot 3\text{C}_3\text{H}_7\text{OH} \cdot 3\text{CH}_3\text{CN}$ (**16**).

The different benzoic acid derivatives used as ligands are shown in Figure 4-3. The molecular structures of (**7**) to (**16**) with their coordination spheres around the metal ions, packing and selected distances, bond lengths and angles are given in the appendix 12.3.

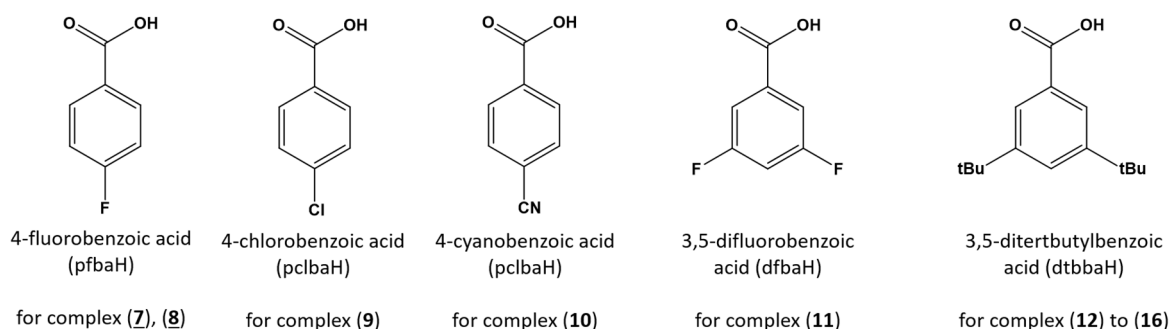


Figure 4-3 The different benzoic acid derivatives, used for (**7**) to (**16**).

The DC susceptibility data for **series-1**, (**7**) to (**12**) which all contain the $\{\text{Cr}_2\text{Dy}_3\}$ core but different organic ligands, are summarised based on their similarity. Likewise, the DC susceptibility data for complexes (**13**), (**14**) and (**15**), which contain the same ligand but different homometallic ions in the $\{\text{M}_2\text{Dy}_3\}$ core, are plotted together. For all complexes of **series-1** and **series-2**, except of (**16**), the magnetization data are plotted to examine a possible peak and therefore a level crossing between ground and excited states in the first derivative. The complexes are investigated for their possible SMM properties using AC susceptibility measurements. MAGELLAN calculations are then carried out on the complexes discussed. At the end of this section, a summary of angles, distances, lengths and magnetic properties are given. As an example for the complexes with six, seven and nine ligands, the molecular structures of $[\text{Cr}_2\text{Dy}_3(\text{pcnba})_6(\mu_3\text{-OH})_6(\text{NO}_3)_3(\text{H}_2\text{O})_3]$ (**10**), $[\text{Al}_2\text{Dy}_3(\text{dtbba})_7(\mu_3\text{-OH})_6(\text{NO}_3)_2(\text{C}_3\text{H}_7\text{OH})(\text{H}_2\text{O})_2]$ (**15**) and $[\text{Cr}_2\text{Dy}_3(\text{pfba})_9(\mu_3\text{-OH})_6(\text{C}_3\text{H}_7\text{OH})_3]$ (**8**) are illustrated in Figure 4-4.

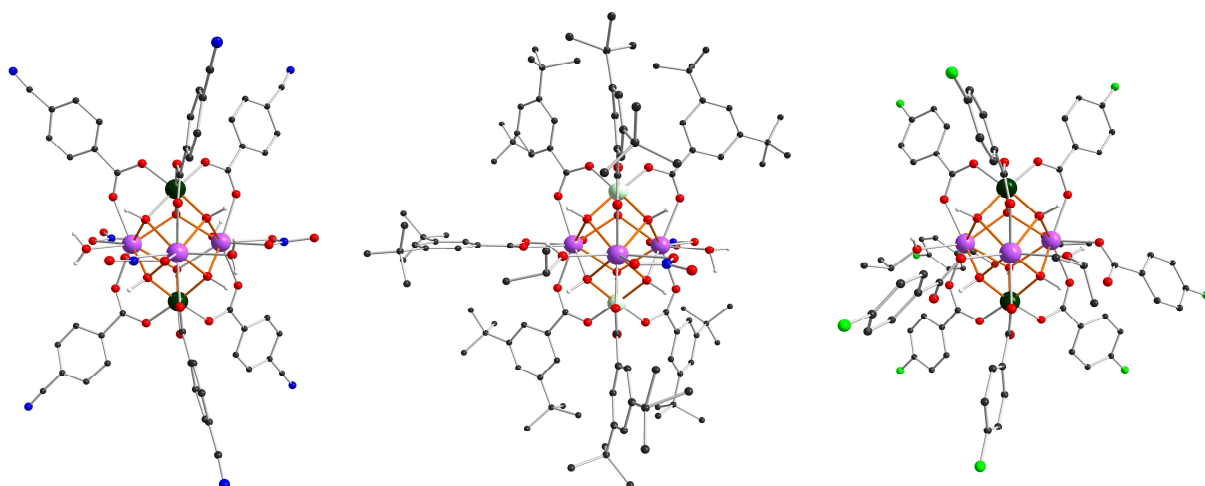
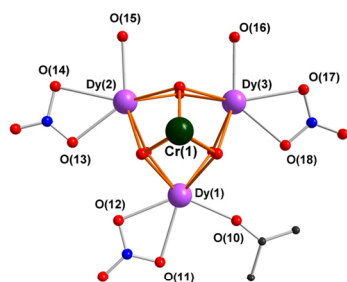
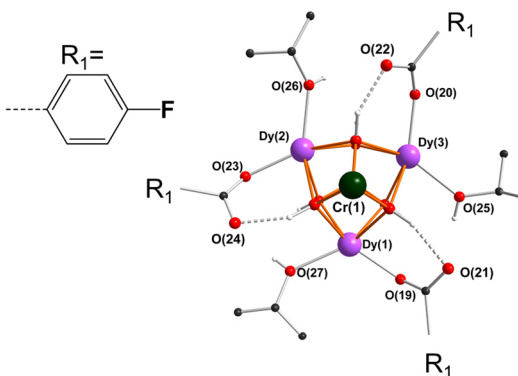


Figure 4-4 Structures with six (left), seven (middle) and nine (right) benzoate derivatives as ligands. Cr(III) in dark green, Al(III) in light yellow.

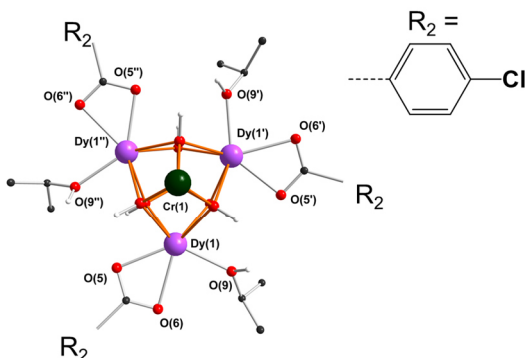
The biggest difference among the complexes (**7**) to (**12**), beside the different benzoate derivatives, lies in the variable coordination environment of the Dy(III) ions. For this purpose, the structures viewed along the pseudo 3-fold axes are shown in Figure 4-5. In common, there are four $\mu_3\text{-OH}^-$ units and the two oxygens from two different bridging ligands (the bridging ligands are omitted). The $\{\text{Cr}_2(\mu_3\text{-OH})_6\text{Dy}_3\}$ cores are highlighted by orange bonds.



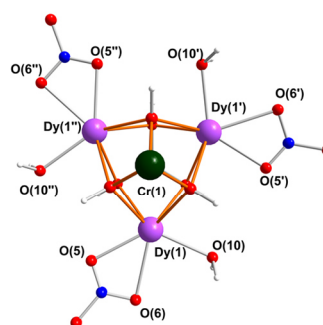
$[\text{Cr}_2\text{Dy}_3(\text{pfba})_6(\mu_3\text{-OH})_6(\text{NO}_3)_3(\text{H}_2\text{O})_2(\text{C}_3\text{H}_7\text{OH})]$ (**7**)



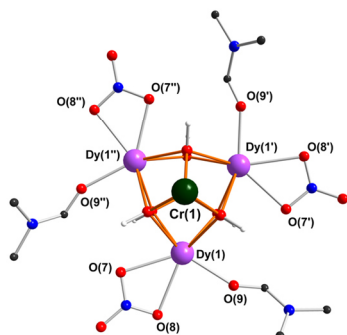
$[\text{Cr}_2\text{Dy}_3(\text{pfba})_9(\mu_3\text{-OH})_6(\text{C}_3\text{H}_7\text{OH})_3]$ (**8**)



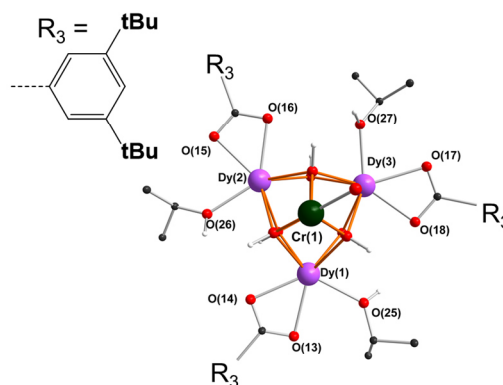
$[\text{Cr}_2\text{Dy}_3(\text{pclba})_9(\mu_3\text{-OH})_6(\text{C}_3\text{H}_7\text{OH})_3]$ (**9**)



$[\text{Cr}_2\text{Dy}_3(\text{pcnba})_6(\mu_3\text{-OH})_6(\text{NO}_3)_3(\text{H}_2\text{O})_3]$ (**10**)



$[\text{Cr}_2\text{Dy}_3(\text{dfba})_6(\mu_3\text{-OH})_6(\text{NO}_3)_3(\text{DMF})_3]$ (**11**)



$[\text{Cr}_2\text{Dy}_3(\text{dtbba})_9(\mu_3\text{-OH})_6(\text{C}_3\text{H}_7\text{OH})_3]$ (**12**)

Figure 4-5 The additional coordinated ligands on the Dy(III) ions of (**7**) to (**12**). The $\{\text{Cr}_2(\mu_3\text{-OH})_6\text{Dy}_3\}$ core is highlighted with orange bonds. The bridging benzoate derivatives are omitted for clarity. In (**7**) hydrogen atoms are omitted.

The coordination spheres of Dy(2) and Dy(3) in (**7**) are each completed by one water, O(15) and O(16) and one bidentate nitrate O(13) and O(14) for Dy(2) and O(17) and O(18) for Dy(3). For Dy(1), one bidentate nitrate is coordinated, O(11) and O(12). The water is exchanged by one isopropanol (O10) (hydrogens are omitted). This results in an O_9 donor sets and in coordination spheres which can be described as muffin

(MFF) with deviations of 0.312 % for Dy(1), 0.406 % for Dy(2) and 0.308 % for Dy(3) from the perfect geometry.

In (**8**), the coordination spheres of the Dy(III) ions are completed by one oxygen from a protonated isopropanol, O(27) for Dy(1), O(26) for Dy(2) and O(25) for Dy(3) and by one oxygen from one monodentate 4-fluorobenzoate, O(19) for Dy(1), O(23) for Dy(2) and O(20) for Dy(3). This results in an O₈ donor set and the coordination spheres can be described as square antiprismatic (SAPR) with deviations of 0.556 % for Dy(1), 0.531 % for Dy(2) and 0.633 % for Dy(3) from the perfect geometry.

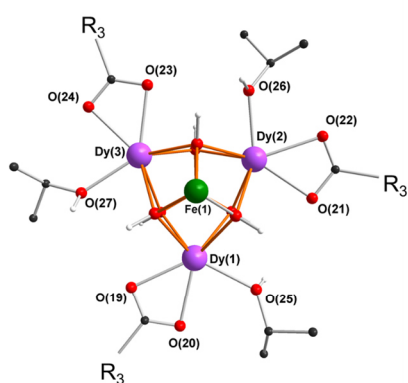
Instead of the monodentate 4-fluorobenzoate in (**8**), a bidentate 4-chlorobenzoate in (**9**), O(5) and O(6) and symmetry related, is coordinated to each Dy(III) ion. Together with one oxygen from one isopropanol, O(9) and symmetry related, this results in an O₉ donor set with the coordination spheres around the Dy(III) ions, best described as muffin with deviations of 0.322 % from the perfect geometry.

The O₉ donor sets around the Dy(III) ions in (**10**) are completed by one bidentate nitrate, O(5) and O(6) and symmetry related, and by one oxygen, coming from one water, O(10) and symmetry related. The coordination spheres can also be described as muffin with deviations of 0.513 % from the perfect geometry.

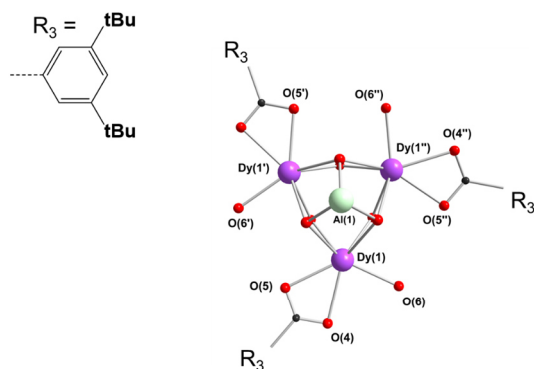
The coordination spheres around the Dy(III) ions in (**11**) are completed by one bidentate nitrate, O(7) and O(8) and symmetry related, and by one oxygen from a DMF molecule, O(9) and symmetry related. The O₉ donor set around the Dy(III) ions can be described as muffin with deviations of 0.274 %.

In (**12**), the O₉ donor sets of the Dy(III) ions are completed by two oxygens from one bidentate 3,5-ditertbutylbenzoate, O(13) and O(14) for Dy(1), O(15) and O(16) for Dy(2) and O(17) and O(18) for Dy(3) and by one oxygen from one isopropanol, O(25) for Dy(1), O(26) for Dy(2) and O(27) for Dy(3). The coordination spheres can be described as muffins with deviations of 0.433 % for Dy(1), 0.411 % for Dy(2) and 0.473 % for Dy(3).

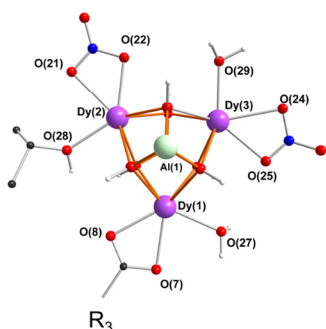
Series-2, which contains of the complexes with the {M₂Dy₃} core and the same ligand as in (**12**), differ in the used metal ions M and also in the variable coordination environment of the Dy(III) ions. The structures from the view down of the pseudo 3-fold axis are shown in Figure 4-6. In common, there are four μ_3 -OH⁻ units and the two oxygens from two different bridging ligands (the bridging ligands are omitted). The {M₂(μ_3 -OH)₆Dy₃} core is highlighted again by orange bonds.



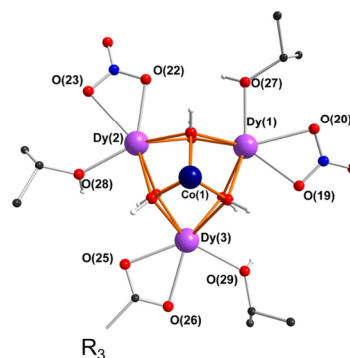
[Fe₂Dy₃(dtbba)₉(μ₃-OH)₆(C₃H₇OH)₃] (**13**)



[Al₂Dy₃(dtbba)₉(μ₃-OH)₆(CH₃OH)_{0.75}(H₂O)_{1.5}(C₃H₇OH)_{0.75}] (**14**)



[Al₂Dy₃(dtbba)₇(μ₃-OH)₆(NO₃)₂(C₃H₇OH)(H₂O)₂] (**15**)



[Co₂Dy₃(dtbba)₇(μ₃-OH)₆(NO₃)₂(C₃H₇OH)₃] (**16**)

Figure 4-6 The additional coordinated ligands on the Dy(III) ions of (**13**) to (**16**). The {M₂(μ₃-OH)₆Dy₃} core is highlighted with orange bonds. The bridging benzoate derivatives are omitted for clarity. In (**14**) for the disorder on Dy(1), water is chosen to be displayed, and hydrogen atoms are omitted.

The coordination spheres of each Dy(III) ion is completed in (**13**) by the oxygen from one protonated isopropanol, O(25) for Dy(1), O(26) for Dy(2) and O(27) for Dy(3), and two oxygens from one bidentate dtbba⁻ ligand, O(19) and O(20) for Dy(1), O(21) and O(22) for Dy(2) and O(23) and O(24) for Dy(3). This results in an O₉ donor sets and in coordination spheres which can be described as muffin (MFF) with deviations of 0.519 % for Dy(1), 0.536 % for Dy(2) and 0.413 % for Dy(3) from the perfect geometry.

In (**14**), a disorder of a terminal ligand on one of the Dy(III) ions occurs with methanol/water/isopropanol in a ratio of 50:25:25. Water is shown here as the majority ligand (hydrogen atoms are omitted). Same as in (**13**), additionally, two oxygens from one bidentate dtbba⁻ ligand, (O4) and O(5) and symmetry related, are

coordinated to the Dy(III) ions. The O₉ donor sets around the Dy(III) ions can best be described as muffin (MFF) with deviations of 0.281 %.

The coordination spheres around the Dy(III) ions in **(15)** is completed for Dy(1) with one oxygen from one water, O(27), and from two oxygens from one bidentate dtbba⁻ ligand, O(7) and O(8). For Dy(2), two oxygens are provided from one bidentate nitrate, O(21) and O(22), and one oxygen from one isopropanol, O(28). The coordination sphere of Dy(3) is completed by one oxygen from one water, O(28), and two oxygens from one bidentate nitrate, O(24) and O(25). The geometry for the O₉ donor sets of the coordination spheres of the Dy(III) ions can best be described as capped-square antiprismatic for Dy(1) (deviation of 0.522 %) and as muffin for Dy(2) and Dy(3) with deviations of 0.368 and 0.258 %.

All waters from **(15)** are exchanged by isopropanol and result in O₉ donor sets with the coordination sphere close to a muffin with deviations of 0.467 % for Dy(1), 0.453 % for Dy(2) and 0.358 % for Dy(3).

4.1 Static magnetic properties of (7) to (12)

The static magnetic susceptibilities of the compounds (7) to (12), which all possess the same {Cr₂Dy₃} core but different organic ligands, are measured under a DC field of 0.1 T over the temperature range 2-300 K. The χT vs T plots from 0-50 K and from 0-300 K are shown in Figure 4-7.

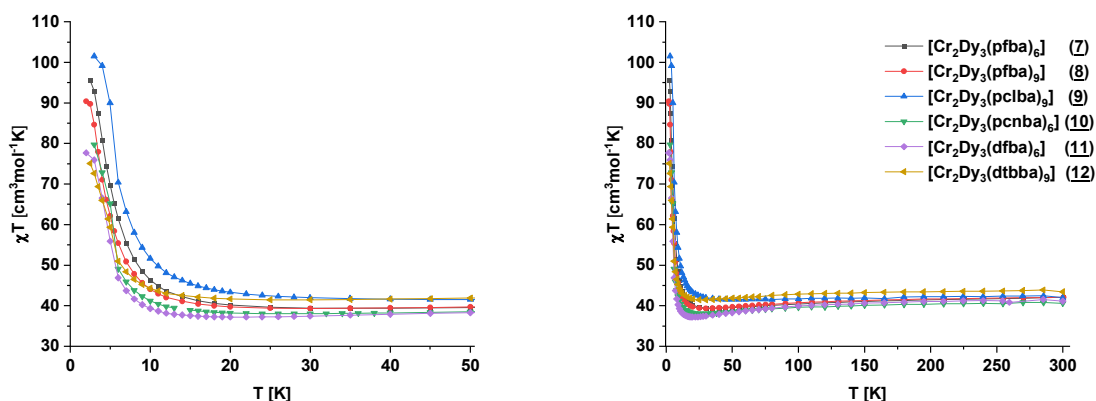


Figure 4-7 χT vs T plots from 0-50 K (left) and from 0-300 K (right) for the complexes (7)-(12) with the same {Cr₂Dy₃} core but different organic ligands at 0.1 T.

The values of the χT products at 300 K are 42.08 for (7), 42.09 for (8), 41.95 for (9), 40.59 for (10), 41.12 for (11) and 43.42 cm³mol⁻¹K for (12). These values are smaller than the calculated values of 46.26 cm³mol⁻¹K expected for three noninteracting Dy(III) ions ($S = \frac{5}{2}$, $g = \frac{4}{3}$, $C = 14.17 \text{ cm}^3 \text{mol}^{-1} \text{K}$) and two noninteracting Cr(III) ions ($S = \frac{3}{2}$, $g = 2$, $C = 1.875 \text{ cm}^3 \text{mol}^{-1} \text{K}$) but in good agreement with similar {Cr₂Dy₃} compounds in the literature. The smaller values result maybe from spin-orbit coupling of lanthanide-ions.^[90]

The χT products of all complexes decrease slightly on cooling, to minimum values of 39.33 cm³mol⁻¹K for (7) and (8) at 30 K, to 41.63 cm³mol⁻¹K for (9) at 40 K, 38.00 cm³mol⁻¹K for (10) at 26 K, 37.20 cm³mol⁻¹K for (11) at 22 K and 41.48 cm³mol⁻¹K for (12) at 30 K. These slight decreases result from depopulation of excited m_j states. On cooling below these temperatures to 2 K, the curves increase sharply, to 92.76 for (7), 90.41 for (8), 91.12 for (9), 79.70 for (10), 77.70 for (11) and 74.50 cm³mol⁻¹K for (12). This results from dominant ferromagnetic interactions between the metal centres.

4.2 Magnetization of (7) to (12)

The magnetization was measured for different temperatures in a field range from 0 to 7 T. The M vs H plots and the first derivatives of the lowest temperature measurement for the complexes (7) to (12) are shown below. The magnetizations for 2 K increase faster than the magnetization at higher temperatures. The maximum values at 7 T are 20.42 for (7), 22.60 for (8), 22.47 for (9), 20.35 for (10), 23.66 for (11) and 22.02 μ_B for (12). The saturation of magnetization in all of the complexes is not reached at 7 T. That indicates strong anisotropy of the compound and/or low-lying energy states. For the displayed compounds, no peaks in the first derivatives in the temperature area could be observed. The M vs H plots and the first derivatives at 2 K are shown in Figure 4-8 to Figure 4-13.

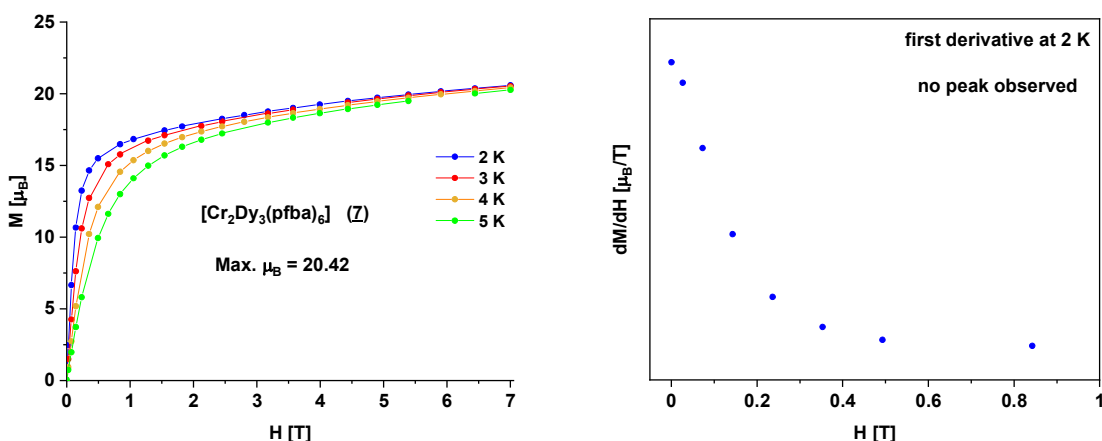


Figure 4-8 M vs H plots (left) and the first derivative at 2 K (right) of (7).

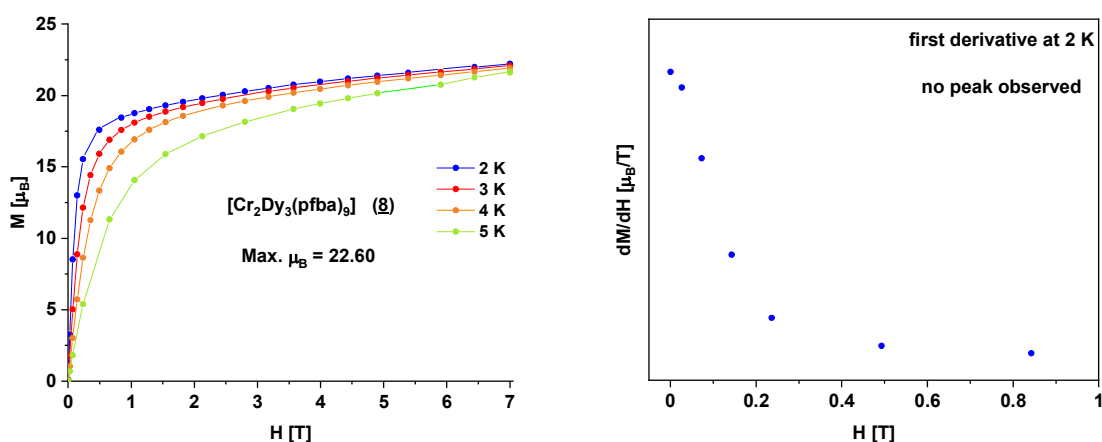


Figure 4-9 M vs H plots (left) and the first derivative at 2 K (right) of (8).

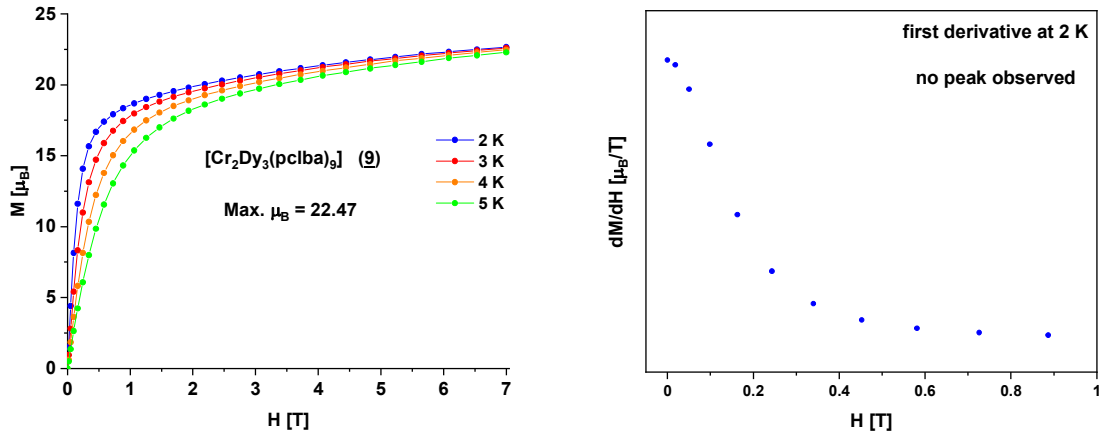


Figure 4-10 M vs H plots (left) and the first derivative at 2 K (right) of (9).

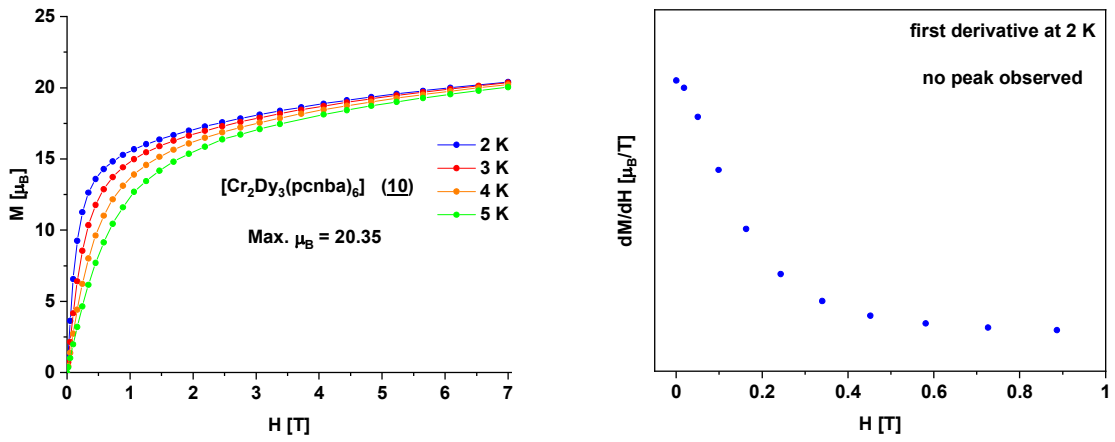


Figure 4-11 M vs H plots (left) and the first derivative at 2 K (right) of (10).

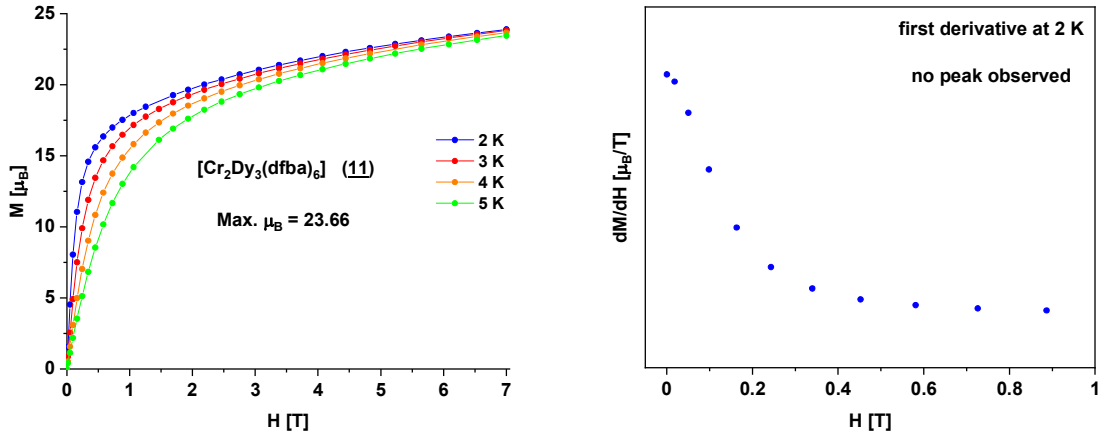


Figure 4-12 M vs H plots (left) and the first derivative at 2 K (right) of (11).

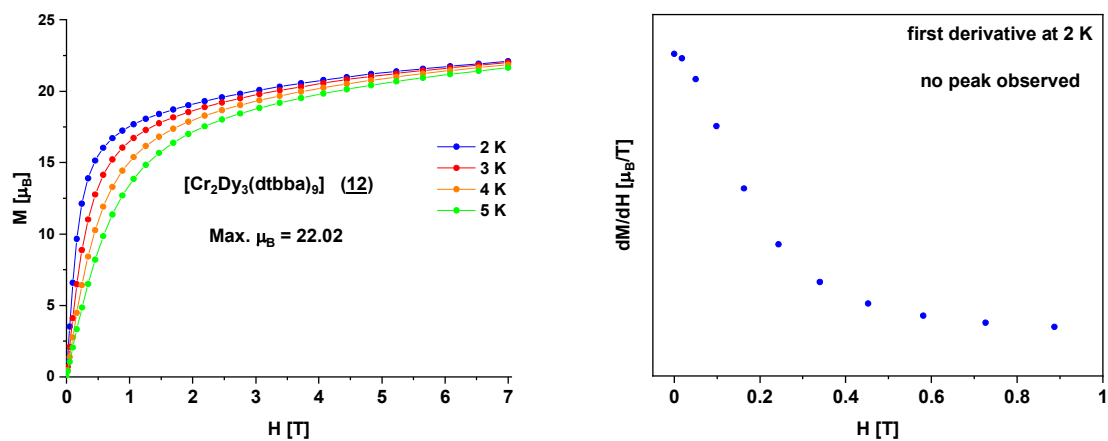


Figure 4-13 M vs H plots (left) and the first derivative at 2 K (right) of (12).

4.3 Dynamic magnetic properties of (7) and (9)

Dynamic (AC) susceptibility measurements were performed in a range from 1-1500 Hz at different temperatures. Susceptibility out-of-phase (χ'') maxima were observed for the complexes $[\text{Cr}_2\text{Dy}_3(\text{pfba})_6(\mu_3\text{-OH})_6(\text{NO}_3)_3(\text{H}_2\text{O})_2(\text{C}_3\text{H}_7\text{OH})]\cdot\text{H}_2\text{O}$ (**7**) in a range from 2 to 2.9 K and for $[\text{Cr}_2\text{Dy}_3(\text{pclba})_9(\mu_3\text{-OH})_6(\text{C}_3\text{H}_7\text{OH})_3]\cdot\text{H}_2\text{O}\cdot\text{C}_3\text{H}_7\text{OH}$ (**9**) in a range from 2 to 3 K. The relaxation times follow the Arrhenius law and energy barriers and preexponential factors could be estimated out of this with $U_{\text{eff}} = 17.31 \text{ K}, \tau_0 = 6.8 \cdot 10^{-8} \text{ s}$ for (**7**) and $U_{\text{eff}} = 23.31 \text{ K}, \tau_0 = 1.96 \cdot 10^{-8} \text{ s}$ for (**9**). The Cole-Cole plots indicate small distribution of relaxation times from 0.03 to 0.22 for (**7**) and from 0.06 to 0.18 for (**9**) with decreasing temperature. The out-of-phase measurements, together with the Arrhenius plots and the Cole-Cole plots for (**7**) are shown in Figure 4-14 and for (**9**) in Figure 4-15.

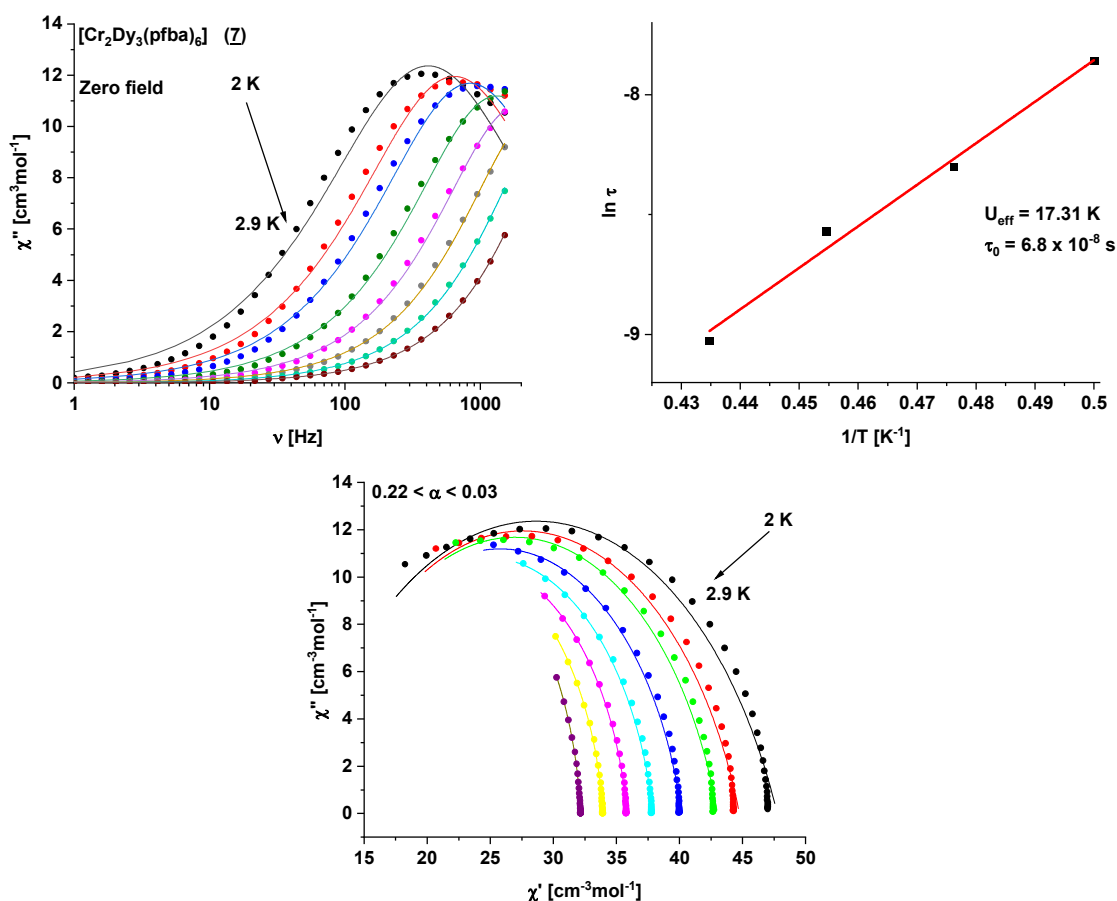


Figure 4-14 Out-of-phase susceptibility measurements (top left), Arrhenius plot (top right) and Cole-Cole plot (bottom) of (**7**).

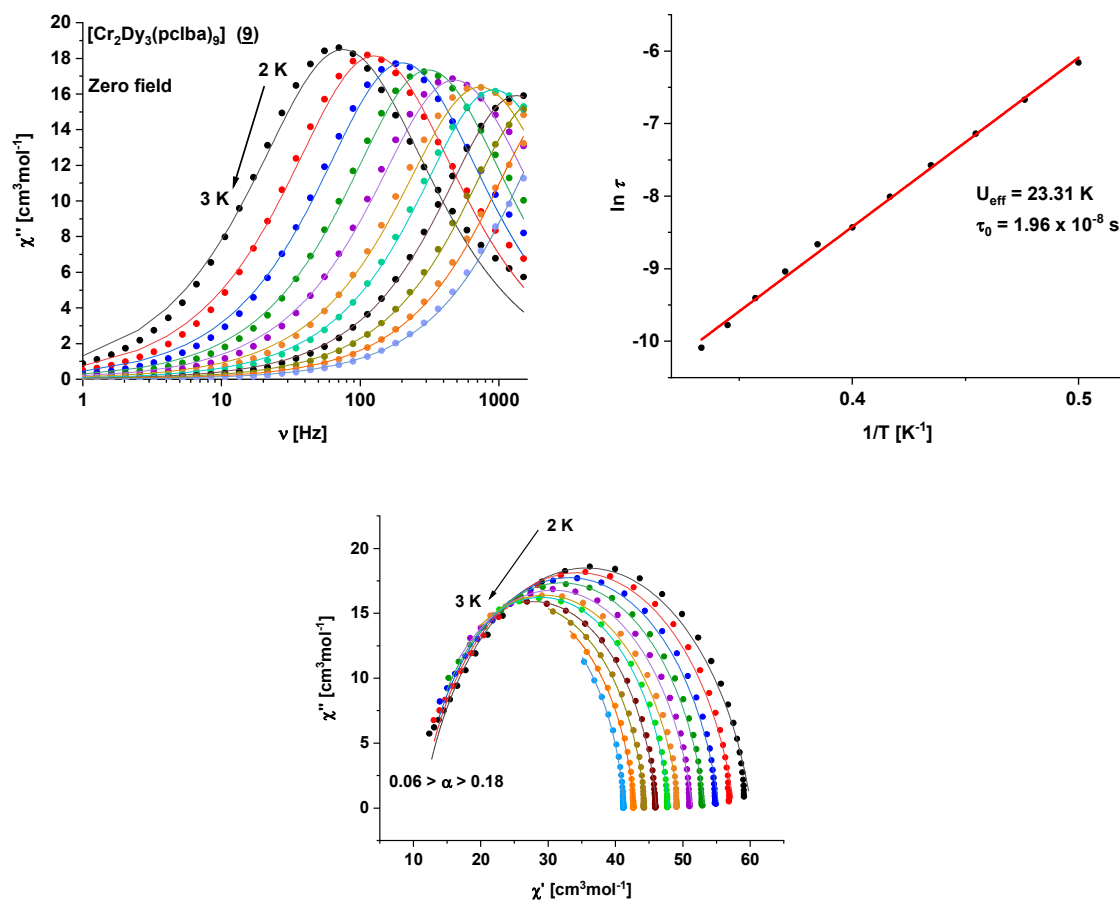


Figure 4-15 Out-of-phase susceptibility measurements (top left), Arrhenius plot (top right) and Cole-Cole plot (bottom) of **(9)**.

4.4 Static magnetic properties of (13), (14) and (15)

The static magnetic susceptibilities of the compounds (13), (14) and (15) which all possess the same ligand (dtbbaH) but differ in the metal ions M, forming the M_2Dy_3 core, are measured under a DC field of 0.1 T over the temperature range 2-300 K. The χT vs T plots are shown in Figure 4-16.

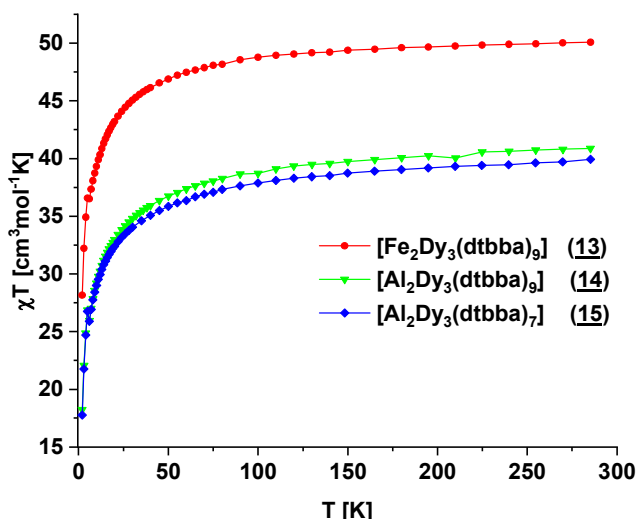


Figure 4-16 χT vs T plots at 0.1 T for the complexes (13), (14) and (15) with the same ligand but with different metal ions M in the $\{M_2Dy_3\}$ core.

The values of the χT products at 300 K are 50.08 for (13), 40.49 for (14) and 39.93 $cm^3mol^{-1}K$ for (15). The values are in good agreement with 51.26 $cm^3mol^{-1}K$ and 42.51 $cm^3mol^{-1}K$, calculated for three noninteracting Dy(III) ions ($S = \frac{5}{2}$, $g = \frac{4}{3}$, $C = 14.17 cm^3mol^{-1}K$) for (14) and (15) and for three noninteracting Dy(III) ions and two noninteracting high-spin Fe(III) ions ($S = \frac{5}{2}$, $g = 2$, $C = 4.375 cm^3mol^{-1}K$) for (13).

In all systems, the value of the χT product decreases slightly on cooling, to 46.15 for (13), 35.92 for (14) and 35.08 $cm^3mol^{-1}K$ for (15). These slight decreases result from depopulation of excited m_j states. On cooling below these temperatures to 2 K, the curves decrease sharply, to 28.15 for (13), 18.25 for (14) and 17.77 $cm^3mol^{-1}K$ for (15). This results from antiferromagnetic interactions between the metal centres.

4.5 Magnetization of (13), (14) and (15)

The magnetization was measured for different temperatures in a field range from 0 to 7 T and 9 T, respectively. The M vs H plots and the first derivatives of the lowest temperature measurement (2 K) for the complexes (13), (14) and (15) are shown in Figure 4-17, in Figure 4-18 and in Figure 4-19. The magnetizations for 2 K increase faster than the magnetization at higher temperatures. The values at 7 T are 22.98 for (13), 15.02 for (14) and 15.71 μ_B for (15). The maximum value of (13) at 9 T is 24.95 μ_B . The saturation of magnetization is not reached in any of the complexes. That indicates strong anisotropy of the dysprosium ions and/or low-lying energy states. For the displayed compounds, no peaks in the first derivatives in the temperature area could be observed.

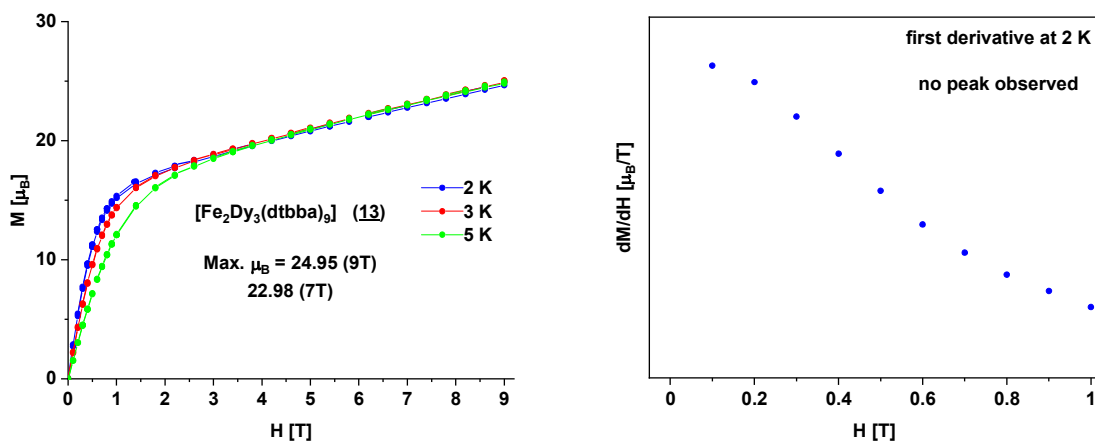


Figure 4-17 M vs H plots (left) and the first derivative at 2 K (right) of (13).

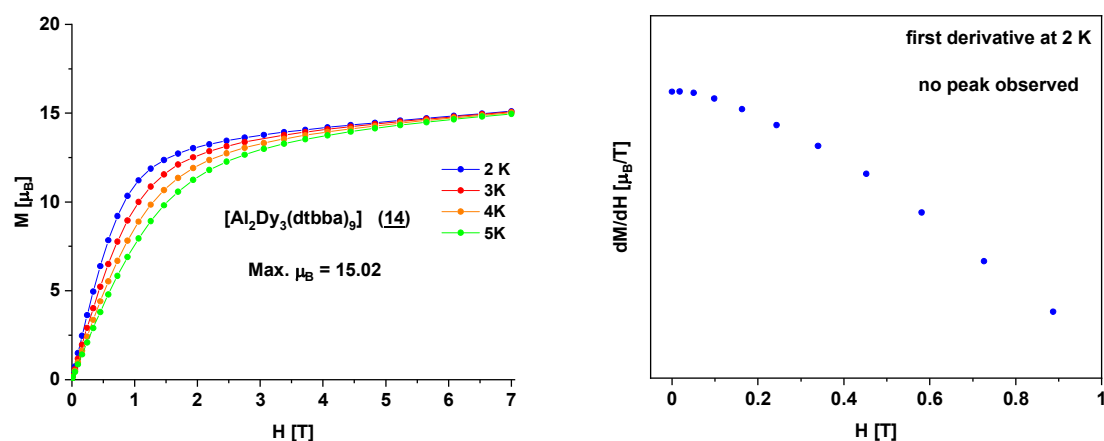


Figure 4-18 M vs H plots (left) and the first derivative at 2 K (right) of (14).

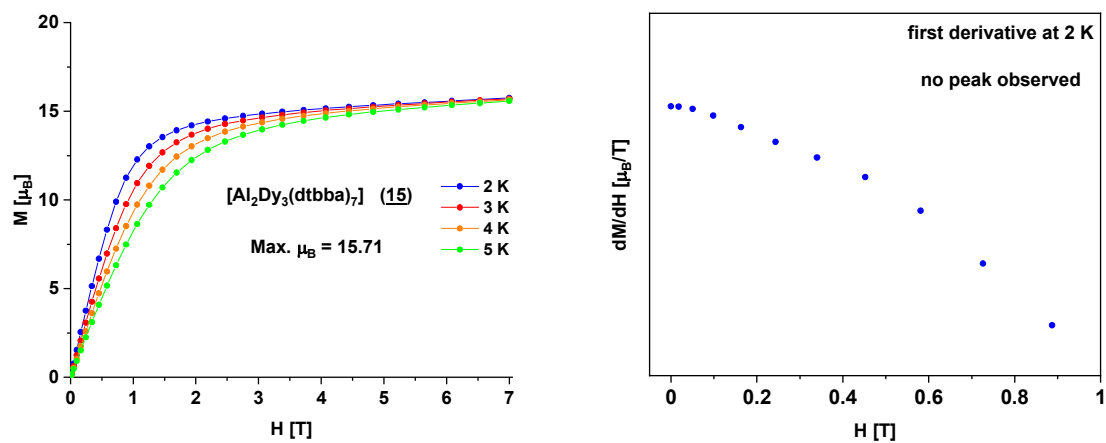


Figure 4-19 M vs H plots (left) and the first derivative at 2 K (right) of (15).

4.6 Dynamic magnetic properties of **(15)**

Dynamic (AC) susceptibility measurements were performed in a range from 1-1500 Hz at different temperatures. Susceptibility out-of-phase (χ'') maxima were observed for $[\text{Al}_2\text{Dy}_3(\text{dtbba})_7(\mu_3\text{-OH})_6(\text{NO}_3)_2(\text{C}_3\text{H}_7\text{OH})(\text{H}_2\text{O})_2]\cdot 3\text{H}_2\text{O}$ (**15**) in a range from 2 to 7.6 K. The relaxation times follow the Arrhenius law and energy barrier and preexponential factor could be estimated out of this with $U_{\text{eff}} = 19.50 \text{ K}$, $\tau_0 = 1.04 \cdot 10^{-5} \text{ s}$. The Cole-Cole plot indicate distribution of relaxation times from 0.26 to 0.41 with decreasing temperature. The out-of-phase measurements, together with the Arrhenius plots and the Cole-Cole plots are shown in Figure 4-20.

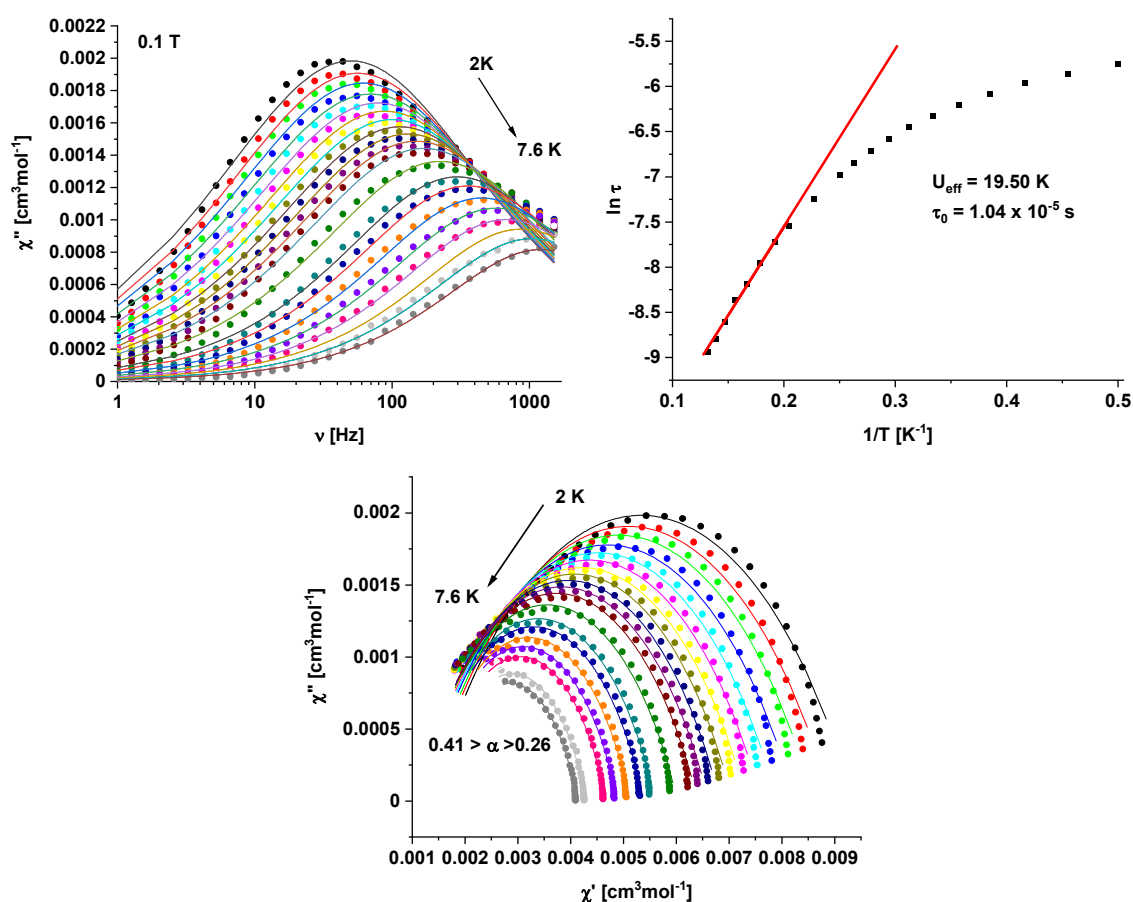


Figure 4-20 Out-of-phase susceptibility measurements (top left), Arrhenius plot (top right) and Cole-Cole plot (bottom) of **(15)**.

4.7 Single crystal measurements of (15)

Single crystal measurements were performed with the micro-SQUID technique at 30 mK for different sweep rates (Figure 4-21, top left) and at the sweep rate of 0.5 mT/s under different temperatures (Figure 4-21, top right). The broadening of the hysteresis loops which are usually occur with faster sweep rates^[19], is negligible. Very small hysteresis loops are observed for temperatures up to 1 K. With higher temperatures, the hysteresis loops vanish. The peaks in the corresponding derivatives are likely to show level crossings and/or QTM. The peaks occur at fields of ± 0.1 , ± 0.27 and ± 0.33 T (Figure 4-21, bottom).

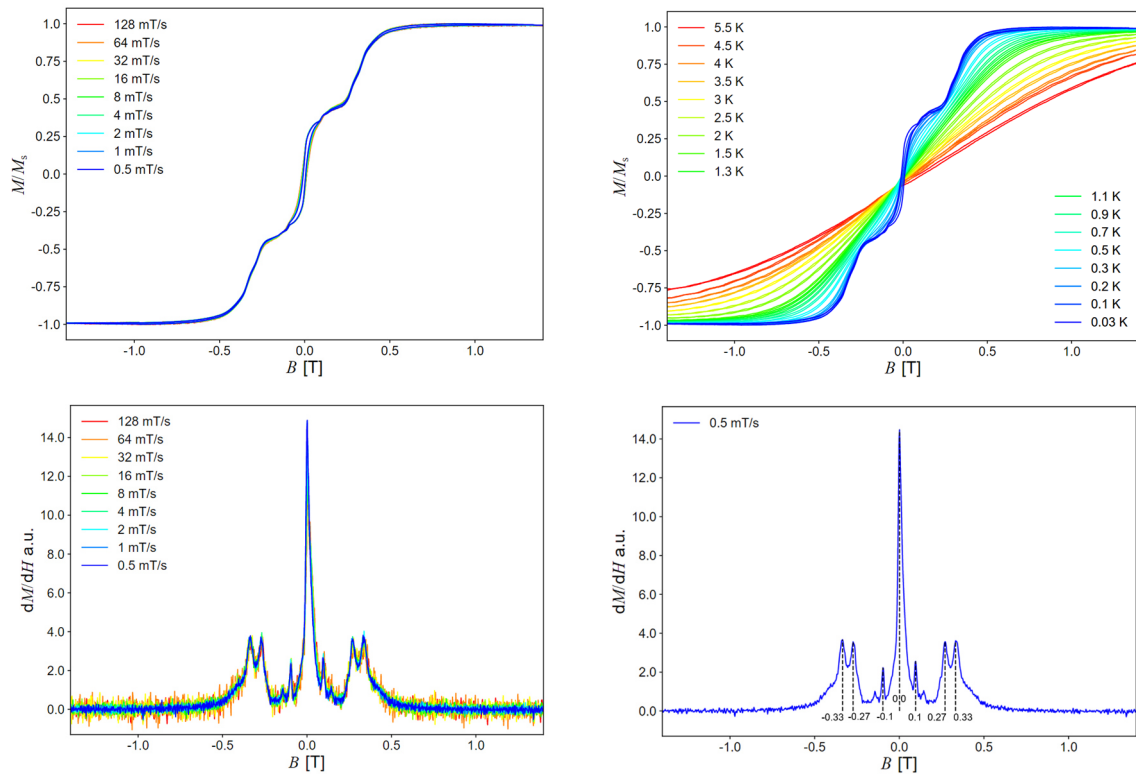


Figure 4-21 Single crystal measurements of (15) (top) and the derivative of the magnetization (bottom). The peaks in the derivatives indicate possible QTM and/or level-crossing.

4.8 MAGELLAN calculations on (8) to (16).

MAGELLAN calculations were performed on (8) to (16) to investigate the single-anisotropy axes of the Dy(III) ions. Due to disorder and twinning in the crystal structure of (7), the anisotropy axes are unmeaningful and are not shown here. For the comparison of the anisotropy axes, the tilting angle θ of the anisotropy axes with the tangential direction (red line) and the tilting angle φ of the anisotropy axes out of the Dy_3 plane, the out-of-plane angle, are used as for the $\{Ln_3\}$ systems in chapter 3 (Figure 4-22).

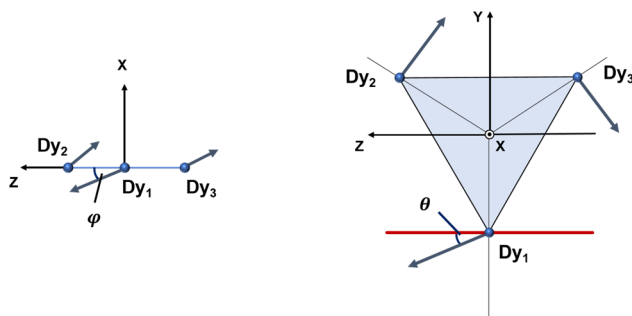


Figure 4-22 The deviation of the anisotropy axes out of the plane is identified by the angle φ (left). The tilting of the anisotropy axes from the tangential direction (red line) is identified by the angle θ (right).

The axes of $[Cr_2Dy_3(pfba)_9(\mu_3-OH)_6(C_3H_7OH)_3]$ (8) suggest a vortex-like arrangement of the axes with out-of-plane angles φ of -6.74° for $Dy(1)$, -11.67° for $Dy(2)$ and 11.78° for $Dy(3)$ (Figure 4-23, left). The axes form a triangle and the θ angles are -18.57° for $Dy(1)$, 18.72° for $Dy(2)$ and -19.18° for $Dy(3)$ (Figure 4-23, right).

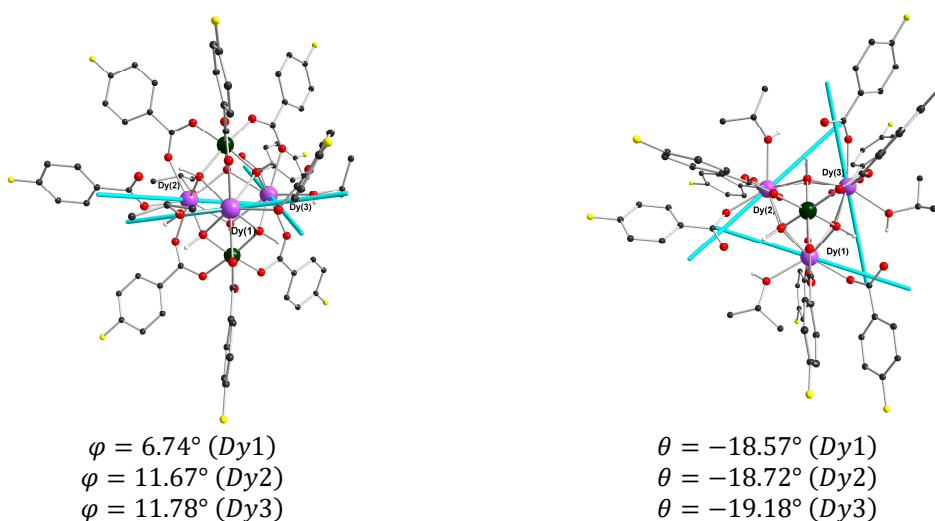


Figure 4-23 MAGELLAN calculations of the anisotropy axes from the side view (left) and down the pseudo 3-fold axis (right) of (8) with corresponding out-of-plane angles (φ) and deviation θ of the tangential direction.

The anisotropy axes of the crystallographic identical Dy(III) ions in $[\text{Cr}_2\text{Dy}_3(\text{pclba})_9(\mu_3\text{-OH})_6(\text{C}_3\text{H}_7\text{OH})_3]$ (**9**) lie almost perfectly in the Dy_3 plane with small out-of-plane angles $\varphi = 6.74^\circ$ (Figure 4-24, left). The anisotropy axes form a triangle with θ angles of 29.73° (Figure 4-24, right).

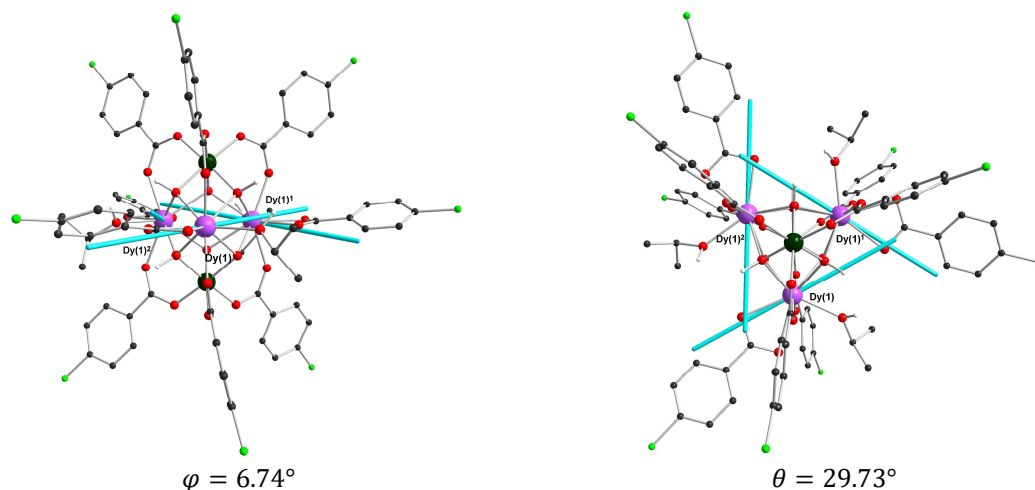


Figure 4-24 MAGELLAN calculations of the anisotropy axes from the side view (left) and down the pseudo 3-fold axis (right) of **9** with corresponding out-of-plane angles (φ) and deviation θ of the tangential direction.

The crystallographic identical Dy(III) ion in $[\text{Cr}_2\text{Dy}_3(\text{pcnba})_6(\mu_3\text{-OH})_6(\text{NO}_3)_3(\text{H}_2\text{O})_3]$ (**10**) and in $[\text{Cr}_2\text{Dy}_3(\text{dfba})_6(\mu_3\text{-OH})_6(\text{NO}_3)_3(\text{DMF})_3]$ (**11**) have anisotropy axes with out-of-plane angles of $\varphi = 24.40^\circ$ in (**10**) (Figure 4-25, left) and $\varphi = -26.53^\circ$ in (**11**) (Figure 4-25, right).

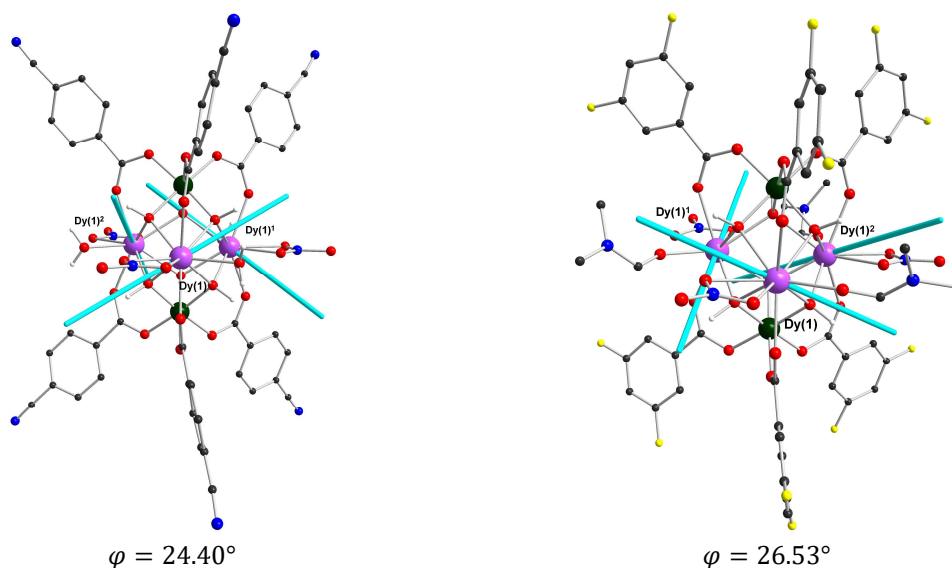


Figure 4-25 MAGELLAN calculations of the anisotropy axes from the side view of **10** (left) and of **11** (right) with corresponding out-of-plane angles (φ).

The arrangement of the anisotropy axes in $[\text{Cr}_2\text{Dy}_3(\text{dtbba})_9(\mu_3\text{-OH})_6(\text{C}_3\text{H}_7\text{OH})_3]$ (**12**) (Figure 4-26), $[\text{Fe}_2\text{Dy}_3(\text{dtbba})_9(\mu_3\text{-OH})_6(\text{C}_3\text{H}_7\text{OH})_3]$ (**13**) (Figure 4-27) and $[\text{Al}_2\text{Dy}_3(\text{dtbba})_9(\mu_3\text{-OH})_6(\text{CH}_3\text{OH})_{0.75}(\text{H}_2\text{O})_{1.5}(\text{C}_3\text{H}_7\text{OH})_{0.75}]$ (**14**) (Figure 4-28) suggest a vortex-like arrangement with small out-of-plane angles φ of 0.98° , -0.04° and -2.14° for (**12**), 0.61° , -3.69° and -1.04° for (**13**) and even 0.00° for (**14**). The deviation θ of the tangential direction are almost equal with 33.06° , 33.09° and 32.42° for (**12**), with -33.07° , -32.27° and -32.29° for (**13**) and with -30.15° for (**14**).

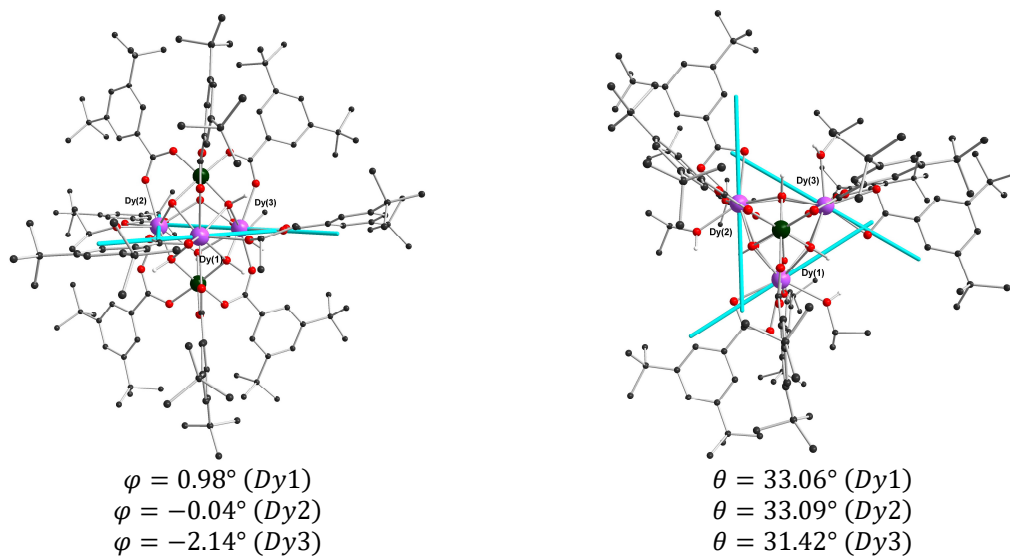


Figure 4-26 MAGELLAN calculations of the anisotropy axes from the side view (left) and down the pseudo 3-fold axis (right) of (**12**) with corresponding out-of-plane angles (φ) and deviation θ of the tangential direction.

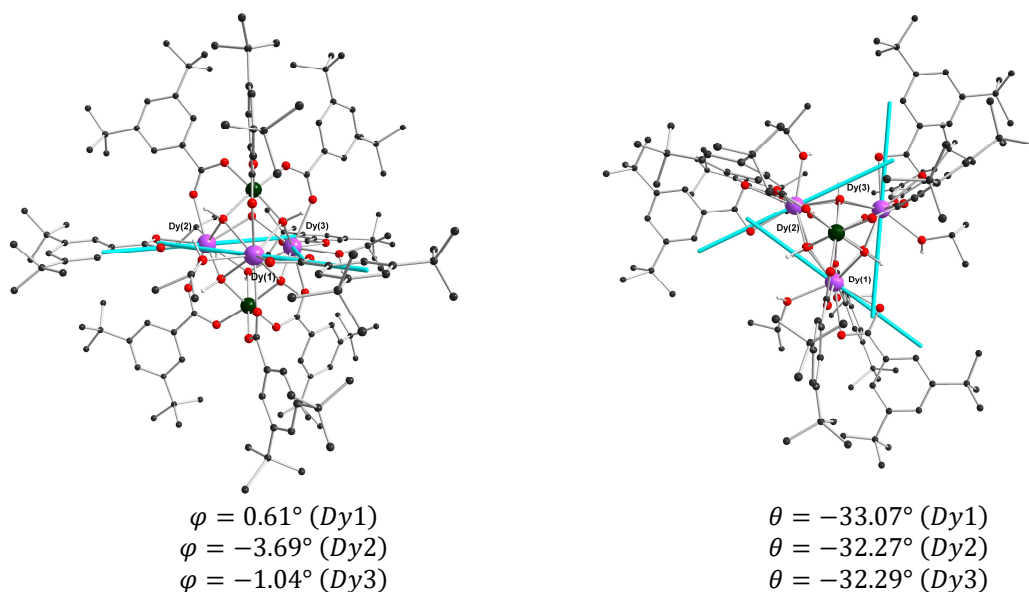


Figure 4-27 MAGELLAN calculations of the anisotropy axes from the side view (left) and down the pseudo 3-fold axis (right) of (**13**) with corresponding out-of-plane angles (φ) and deviation θ of the tangential direction.

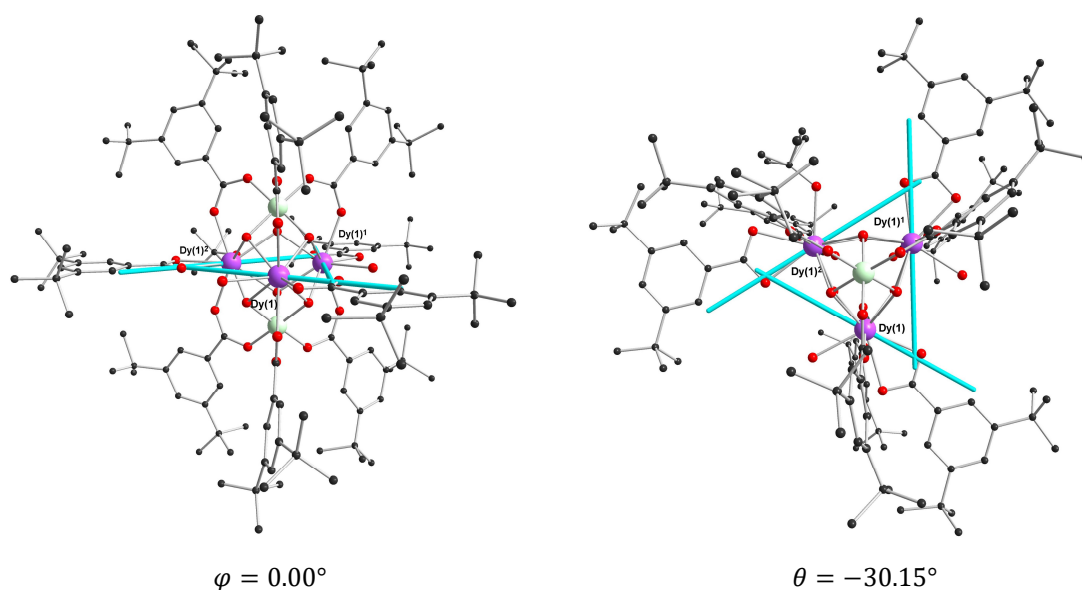


Figure 4-28 MAGELLAN calculations of the anisotropy axes from the side view (left) and down the pseudo 3-fold axis (right) of **(14)** with corresponding out-of-plane angles (φ) and deviation θ of the tangential direction.

The anisotropy axes in $[\text{Al}_2\text{Dy}_3(\text{dtbba})_7(\mu_3\text{-OH})_6(\text{NO}_3)_2(\text{C}_3\text{H}_7\text{OH})(\text{H}_2\text{O})_2]$ **(15)** have out-of-plane angles of 6.76° for Dy(1), 76.52° for Dy(2) and -65.42° for Dy(3) (Figure 4-29, left). In $[\text{Co}_2\text{Dy}_3(\text{dtbba})_7(\mu_3\text{-OH})_6(\text{NO}_3)_2(\text{C}_3\text{H}_7\text{OH})_3]$ **(16)** (Figure 4-29, right), the anisotropy axes have out-of-plane angles of -39.23° for Dy(1), -65.39° for Dy(2) and 10.32° for Dy(3).

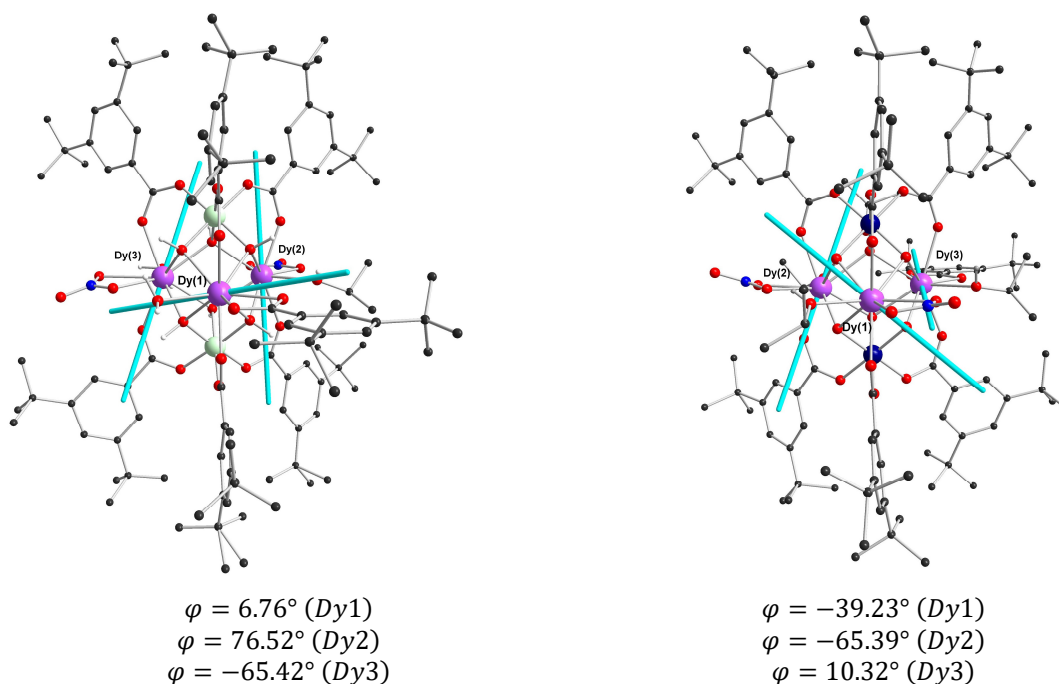


Figure 4-29 MAGELLAN calculations of the anisotropy axes from the side view of **(15)** (left) and of **(16)** (right) with corresponding out-of-plane angles (φ) and deviation θ of the tangential direction.

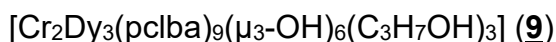
4.9 Summary of heteronuclear M₂Dy₃ systems

The introduction of metals above and below the {Dy₃} plane resulted in pentanuclear molecules with a general [M₂(μ₃-OH)₆Dy₃] core. The synthesized complexes were divided into two series: **Series-1** where M(III) = Cr ((7)-(12)) but different benzoate derivatives and **series-2**, where M = Fe (13), Al (14) and (15), and Co (16) but also (12), where the used benzoate derivative ligand is the same. The reaction schemes of **series-1** are given in Figure 4-30, the one of **series-2** is given in Figure 4-31. MAGELLAN calculations suggested vortex-like anisotropy axes of the Dy(III) ions for the complexes with nine benzoate derivative ligands which are [Cr₂Dy₃(pfba)₉(μ₃-OH)₆(C₃H₇OH)₃] (8), [Cr₂Dy₃(pclba)₉(μ₃-OH)₆(C₃H₇OH)₃] (9), [Cr₂Dy₃(dtbba)₉(μ₃-OH)₆(C₃H₇OH)₃] (12), [Fe₂Dy₃(dtbba)₉(μ₃-OH)₆(C₃H₇OH)₃] (13) and [Al₂Dy₃(dtbba)₉(μ₃-OH)₆(CH₃OH)_{0.75}(H₂O)_{1.5}(C₃H₇OH)_{0.75}] (14).

However, no evidence of a toroidal ground state could be found in the magnetization measurements. But it cannot be ruled out that toroidal states can be found at lower measurement temperatures.

In the complexes of **series-1**, ferromagnetic interactions were found, and it could be seen that the decrease of the Cr-Cr distances lead to a decrease of the χT product (Table 4-1). The Cr-Cr distances for (7) to (9), differ only slightly and have values of about 5.21 Å. In contrast to the complexes (10) to (12), where the Cr-Cr distances are significantly smaller at about 5.17 Å and 5.15 Å, respectively. This leads to squeezed bipyramids with larger Dy-Cr-Dy angles (> 70°) within the structures (10) to (12) compared to the Dy-Cr-Dy angles (≤ 70°) in (7) to (9). The Dy-Dy-Dy angles are approximately 60° for all complexes, resulting in an approximately equilateral triangle spanned by the Dy(III) ions. The Dy-OH-Cr angles with their maximum values of 105.85° are close to the H-O-H bond angle in water with 105°.^[91]

Two complexes in **series-1** exhibit slow relaxation of magnetization which could be identified from AC measurements:



The Dy(III) ions in both series always have an O₉ donor set whose coordination sphere can be described as muffin (MFF) and the Cr(III) ions have O₆ donor sets, best described as octahedron (OC). The exception is in complex (8), where the Dy(III)

ions have an O₈ donor set, and their coordination spheres are described as square antiprismatic (SAPR).

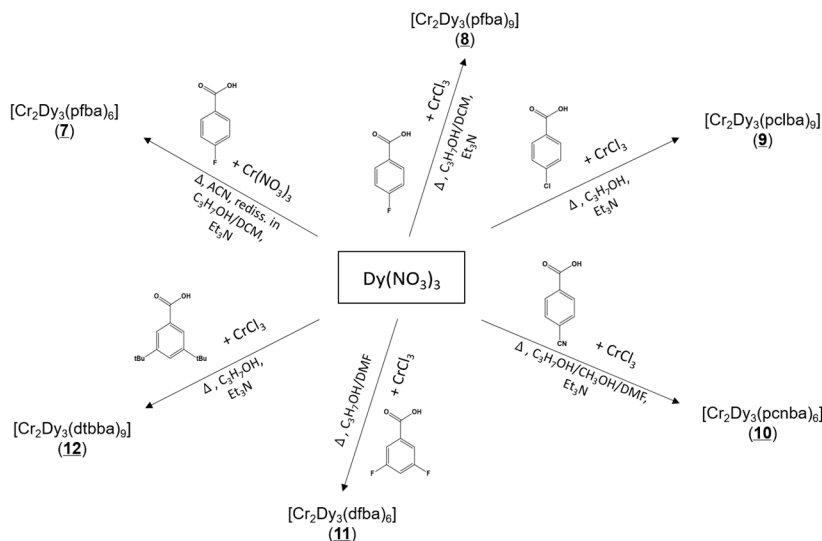


Figure 4-30 Reaction schemes of **series-1** with the complexes (**7**) to (**12**).

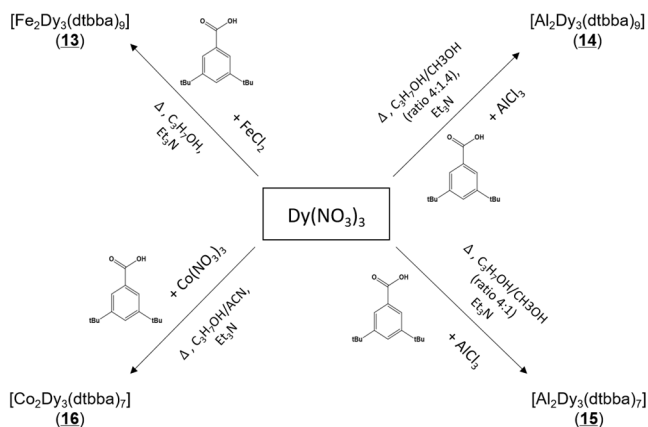


Figure 4-31 Reaction schemes **series-2** of (**13**) to (**16**) without (**12**).

In comparison to the Dy₃ triangles without capping metals, the coordination spheres of the Dy(III) ions are trigonal dodecahedral (TDD) with O₇Cl and O₇Cl/O₈ donor set (in (**1**) and (**2**), respectively). One might argue that the additional oxygen leads to the cancelling of the possible toroidicity in the systems, but it is more likely to be the influence of the additional metal ions. Only a few examples of {Cr₂Dy₃} with a similar bipyramidal shape have been reported in the literature, from Zhang et al. in 2013^[102] and from Li et al. in 2018^[90] where it was also possible to exchange the Cr(III) ion with the diamagnetic Al(III) ion. The dominant interactions in **series-2** shown in (Table 4-2)

(with exception of **(12)**) with M = Fe(III) for **(13)**, Al(III) for **(14)** and **(15)**, are antiferromagnetic interactions, which is expected for **(14)** and **(15)**, but not for **(13)**. Since Al(III) is diamagnetic, it can be assumed that the antiferromagnetic interactions exist between the Dy(III) ions, similar to the dysprosium pure complexes **(1)** and **(2)** in chapter 3. $[\text{Al}_2\text{Dy}_3(\text{dtbba})_7(\mu_3\text{-OH})_6(\text{NO}_3)_2(\text{C}_3\text{H}_7\text{OH})(\text{H}_2\text{O})_2]$ **(15)** showed slow relaxation which could be found by AC and confirmed with micro-SQUID measurements, resulting in a small hysteresis. The M-M distances within the molecules decrease in the following order Fe-Fe > Cr-Cr > Al-Al > Co-Co. The M-Dy-DyPlane angle in **(15)** and **(16)** in the complexes with seven dtbba⁻ ligands are with > 54° much bigger than those for the complexes with nine dtbba⁻ ligands in **(12)**, **(13)** and **(14)** with < 48°.

For a better overview in the tables, distances are given to three decimal places and angles to two decimal places. Figure 4-32 shows the scheme of the defined angles. Exact angles and distances are given in the appendix 12.3 together with the molecular structures, coordination spheres and packing of the molecules.

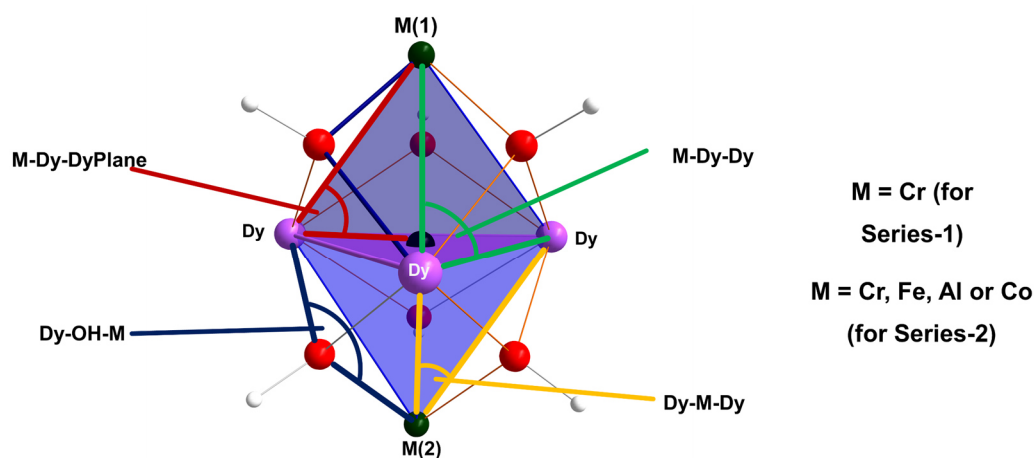


Figure 4-32 Scheme of the defined angles of the core structures from **series-1** and **series-2**. M stands either for Cr(III), Fe(III), Al(III) or Co(III). The black dummy atom in the middle of the Dy₃ triangle is for the determination of the M-Dy-DyPlane angle (red). The Dy-Dy-Dy angle is not shown here.

Table 4-1 Bond lengths, angles, space groups, coordination spheres and susceptibility measurements summarized of **series-1**, containing different organic ligands but the same metal(III) ions M = Cr.

	[Cr ₂ Dy ₃ (pfba) ₆] (7) – SMM	[Cr ₂ Dy ₃ (pfba) ₉] (8) – no SMM	[Cr ₂ Dy ₃ (pclba) ₉] (9) – SMM	[Cr ₂ Dy ₃ (pcnba) ₆] (10) – no SMM	[Cr ₂ Dy ₃ (dfba) ₆] (11) – no SMM	[Cr ₂ Dy ₃ (dtbba) ₉] (12) – no SMM
Space group	C2/m	P-1	R-3	P-3	R-3	P-1
Z	4	2	6	2	6	2
Cr··Cr [Å]	5.214	5.213	5.211	5.172	5.175	5.151
Cr(1)··DyPlane [Å]/ Cr(2)··DyPlane [Å]	2.607	2.600 2.613	2.600 2.615	2.590 2.582	2.618 2.557	2.562 2.589
Cr(1)-Dy-DyPlane [°]/ Cr(2)-Dy-DyPlane [°]	48.86 48.44 48.99	49.62 49.15 48.94/ 49.72 48.99 49.45	48.33/ 48.53	48.42/ 48.31	48.78/ 48.10	47.57 48.02 47.63/ 47.80 48.22 48.13
Cr-Dy-Dy [°]	54.89-55.65	55.13-55.99	54.85, 55.00	54.90, 54.85	55.52, 54.67	54.15-55.04
Dy-Cr-Dy [°]	69.24-70.10	68.45-69.07	70.00	70.20, 70.31	70.67	70.35-71.62
Dy··Dy [Å]	3.946 3.956 3.972	3.880 3.882 3.883	4.003	3.982	3.972	4.017 4.019 4.059
Cr··Dy [Å]	3.455- 3.484	3.413- 3.463	3.476- 3.490	3.458- 3.462	3.435- 3.480	3.446- 3.495
Dy-Dy-Dy [°]	59.70 59.94 60.35	59.95 60.01 60.04	60.00	60.00	60.00	59.63 59.68 60.69
Dy-OH-Cr [°]	103.20- 105.31	102.77- 104.67	103.77- 104.06	103.6- 104.7	104.18- 104.37	101.93- 105.85
Donor sets and geometry of the Dy ions	O ₉ (MFF) O ₉ (MFF) O ₉ (MFF)	O ₈ (SAPR) O ₈ (SAPR) O ₈ (SAPR)	O ₉ (MFF)	O ₉ (MFF)	O ₉ (MFF)	O ₉ (MFF) O ₉ (MFF) O ₉ (MFF)
Donor sets for the Cr ions	O ₆ (OC)	O ₆ (OC) O ₆ (OC)	O ₆ (OC) O ₆ (OC)	O ₆ (OC) O ₆ (OC)	O ₆ (OC) O ₆ (OC)	O ₆ (OC) O ₆ (OC)
χT (300 K) [cm ³ mol ⁻¹ K]	42.08	42.09	41.95	40.59	41.12	43.42
χT (2 K) [cm ³ mol ⁻¹ K]	92.76	90.41	91.12	79.70	77.70	74.50

Table 4-2 Bond lengths, angles, space groups, coordination spheres and susceptibility measurements summarized of **series-2**, containing the same organic ligand (dtbbaH). (**12**) is listed here again for the better comparison with different incorporated metal ions.

	[Cr ₂ Dy ₃ (dtbba) ₉] (12) – no SMM	[Fe ₂ Dy ₃ (dtbba) ₉] (13) – no SMM	[Al ₂ Dy ₃ (dtbba) ₉] (14) - no SMM	[Al ₂ Dy ₃ (dtbba) ₇] (15) - SMM	[Co ₂ Dy ₃ (dtbba) ₇] (16) - not meas.
Space group	P-1	P-1	P6 ₃ /m	P2 ₁ /n	P-1
Z	2	2	6	4	2
M··M [Å]	5.151	5.246	5.048	5.094	5.0179
M(1)··DyPlane [Å]/ M(2)··DyPlane [Å]	2.561/ 2.589	2.636/ 2.611	2.524	2.539 2.556	2.521 2.497
M(1)-Dy-DyPlane [°]/ M(2)-Dy-DyPlane [°]	47.57 48.02 47.63/ 47.80 48.22 48.13	48.24 48.86 48.59/ 48.29 48.13 48.44	47.75/ 47.75	54.63 54.58 54.69/ 54.63 55.09 54.30	54.27 53.64 54.80/ 54.88 53.50 53.58
M-Dy-Dy [°]	54.15-55.04	54.35-55.54	54.39	54.38-55.34	53.50-55.05
Dy-M-Dy [°]	70.35-71.62	69.71-70.28	71.23	70.00-70.93	70.73-72.43
Dy··Dy [Å]	4.017 4.019 4.059	4.015 4.020 4.057	3.971	3.936 3.947 3.963	3.950 3.967 4.019
M-Dy [Å]	3.446-3.495	3.489-3.534	3.410	3.406- 3.450	3.408- 3.430
Dy-Dy-Dy [°]	59.63 59.68 60.69	59.61 59.74 60.65	60.00	59.68 59.96 60.36	59.29 59.70 61.01
Dy-OH-M [°]	101.93 - 105.85	101.49- 106.50	103.40- 109.96	103.0- 105.0	102.60- 104.90
Donor sets of the Dy ions	O ₉ (MFF) O ₉ (MFF) O ₉ (MFF)	O ₉ (MFF) O ₉ (MFF) O ₉ (MFF)	O ₉ (MFF)	O ₉ (CSAPR) O ₉ (MFF) O ₉ (MFF)	O ₉ (MFF) O ₉ (MFF) O ₉ (MFF)
Donor sets of the Cr ions	O ₆ (OC) O ₆ (OC)	O ₆ (OC) O ₆ (OC)	O ₆ (OC)	O ₆ (OC) O ₆ (OC)	O ₆ (OC) O ₆ (OC)
χT (300 K) [cm ³ mol ⁻¹ K]	43.42	50.08	40.49	39.93	-
χT (2 K) [cm ³ mol ⁻¹ K]	74.50	28.15	18.25	17.77	-

5 Tetranuclear Ln₄ systems

The first lanthanide-containing SMM with a non-magnetic ground state was the tetranuclear Dy₄ cluster [Dy₄(μ₃-OH)₂(μ-OH)₂(2,2-bpt)₄(NO₃)₄(EtOH)₂], 2,2-bptH = 3,5-bis(pyridin-2-yl)-1,2,4-triazole, reported by Tong et al. in 2012 (Figure 5-1). Here the strong anisotropy of the dysprosium ions is responsible for the orientation of the spins and their toroidal arrangement results from the strong dipolar magnetic interactions between the dysprosium ions.^[12] In this molecule, the four anisotropy axes form an almost perfect parallelogram and lie practically in the Dy₄ plane with angles of 4.52° and 10.77°, respectively, for the two distinct Dy(III) ions and the angle between the main anisotropy axes is 82.48°, calculated by *ab initio*. The S-shaped magnetization curve often observed for a toroidal ground state is only just apparent here because the gap between the ground and first excited state is rather small (about 3 cm⁻¹). The drop of the χT curve to almost zero is an indication of a non-magnetic ground state. These conclusions were confirmed by *ab initio* calculations in the literature with a level-crossing from ground to first excited state at around $H = 0.25$ T. This compound will be named **Dy4-1** in the following section.

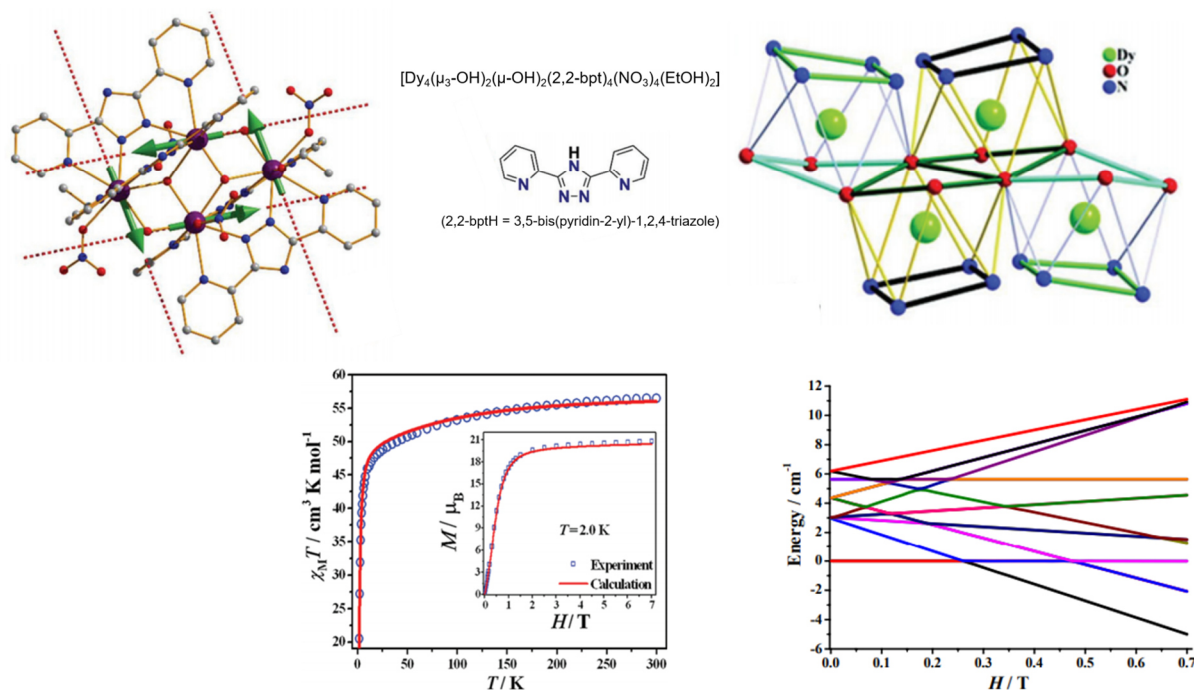


Figure 5-1 Molecular structure of the first reported {Dy₄} SMT with ligand and coordination spheres around the Dy(III) ions (top) and the χT vs T plot (bottom, left) and the M vs H plots (inlet). The level crossing at about 0.25 T is indicated by *ab initio* calculations (bottom right). The dashed lines in the molecular structure represent the anisotropy axes and the green arrows the direction of the magnetic moments. Reprinted with permission from reference^[12]. Copyright 2012 American Chemical Society.

Calculations of the single-ion anisotropy axes of **Dy4-1** using MAGELLAN, performed in this thesis, are in good agreement with the reported *ab initio* calculations in regards of the fact, that all anisotropy axes of the Dy(III) ions lie almost in one plane (15.4° and 6.8°) and forming a parallelogram with angles between the main axes of 111.7° and 68.3° respectively. The Dy(III) ions possess N₄O₄ donor sets, and their coordination spheres can best be described as square antiprismatic for Dy(1) and biaugmented trigonal prismatic for Dy(2) (Figure 5-2).

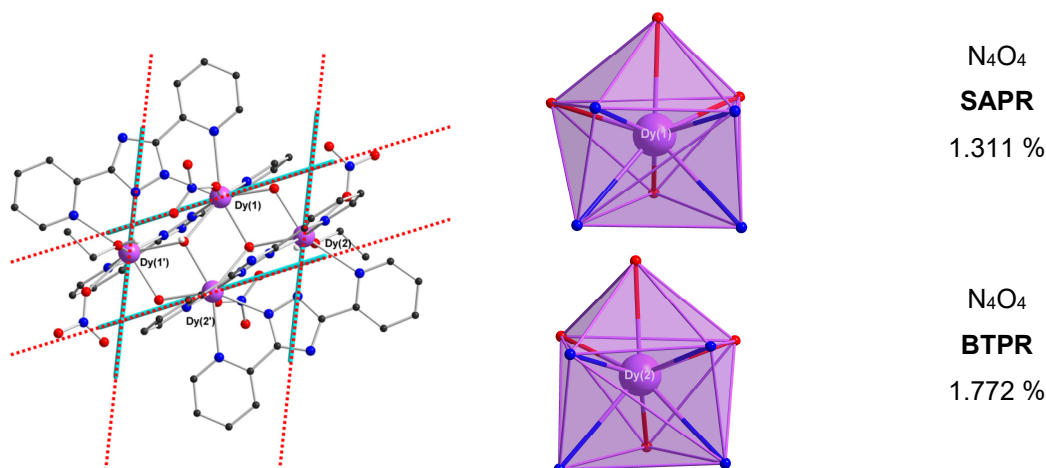


Figure 5-2 Single-ion anisotropy axes of the literature known **Dy4-1**, coordination spheres and deviations from the perfect geometry. Calculations of the anisotropy axes from MAGELLAN.

In this chapter, the new series of isostructural tetranuclear lanthanide coordination clusters with the general formula $\text{Ln}_4(\mu_3\text{-OH})_2(\text{NO}_3)_2(\text{DMF})_2(\text{ehimp})_4$ with Ln = Tb, Dy, Ho, Er, Yb, Y (**17**) to (**22**) and ehimpH₂ = 2-ethoxy-6-(((2-hydroxyphenyl)imino)methyl)phenol are first described and the magnetic properties of those analogues with oblate Dy(III) (**18**) and prolate Er(III) (**20**) are described. The anisotropy axes of the Dy-analogue were also determined out using MAGELLAN.

Following this, the magnetic properties of previously reported complexes with similar core structures to the complexes will be reviewed. For these clusters, the orientations of their Dy(III) anisotropy axes will be calculated using MAGELLAN, and their magnetization data will then be examined for an inflection point in the first derivative, in order to identify molecules with possible toroidal ground states.

5.1 Molecular structure of isostructural Ln₄ complexes (**17**)-(**22**)

The general synthetic procedure for the isostructural systems Ln₄(OH)₂(NO₃)₂(DMF)₂(ehimp)₄ with Ln = Tb, Dy, Ho, Er, Yb, Y (**17**) to (**22**) and ehimpH₂ = 2-ethoxy-6-(((2-hydroxyphenyl)imino)methyl)phenol, is an *in situ* solvothermal synthesis in which the starting materials (3-ethoxysalicylaldehyde, 2-aminophenol and the corresponding lanthanide nitrate) are dissolved in methanol and dimethylformamide. The solution is heated in a glass vial in the oven for five hours, and red crystals appeared after slow cooling. The ligand, which forms in-situ, is shown in Figure 5-3.

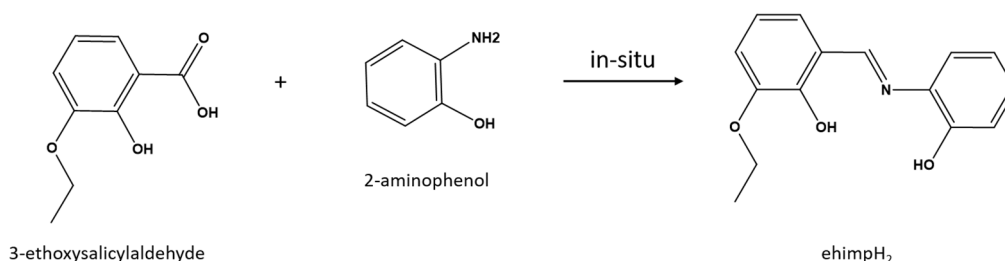


Figure 5-3 In situ reaction of 3-ethoxysalicy aldehyde and 2-aminophenol, leading to the Schiff base ehimpH₂.

The compounds (**17**) to (**22**) crystallize in the monoclinic space group P2₁/n with Z = 2. However, the Yb-analogue (**21**) crystallizes in P2₁/c. With the exception of (**21**), they thus all display a crystallographically centrosymmetric [Ln(III)₄(μ₃-OH)₂]¹²⁺ core. The core is held together by the two μ₃-OH⁻ bridges and also by four doubly deprotonated Schiff base ligands. The structures can be described as a butterfly, where Ln(2) and Ln(2') occupy the wing-tips and Ln(1) and Ln(1') the body sites. The core with four Ln centres are co-planar, with one μ₃-OH⁻ unit above and one below the plane and can also be defined as two edge-sharing [Ln₃(μ₃-OH)] triangle subunits. The structure is shown in Figure 5-4.

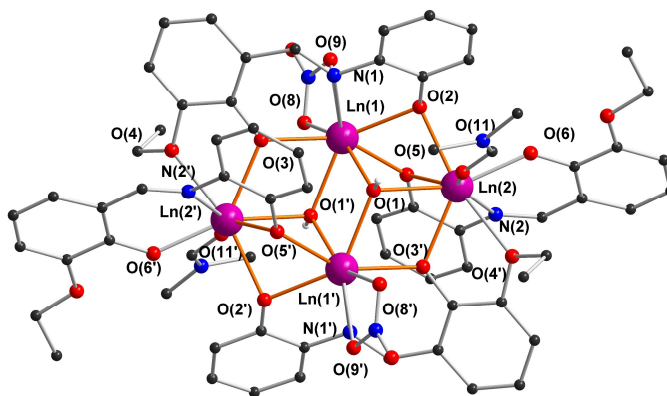


Figure 5-4 Molecular structure of (**17**) to (**22**) with Ln = Tb, Dy, Ho, Er, Yb, Y. Primed-atoms at 1-x, 1-y, 1-z.

Two of the organic ligands bridge three of the Ln(III) ions in a $\eta^1:\eta^2:\eta^1:\eta^2:\mu_3$ binding mode (Figure 5-5a). The other two organic ligands bridge two Ln(III) ions in a $\eta^0:\eta^1:\eta^1:\eta^2:\mu_2$ scheme (Figure 5-5b).

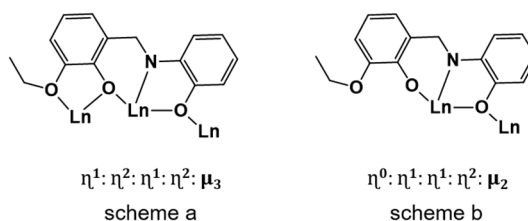


Figure 5-5 Binding mode of the organic ligands in (**17**) to (**22**).

Ln(1) is ligated by one bidentate nitrate through O(8) and O(9). Ln(2) is coordinated to one DMF *via* O(11). Each Ln(III) ion is eight-coordinate with an O₇N donor set. For the dysprosium-analogue (**18**) the coordination spheres and the deviations from the perfect geometry are shown in Figure 5-6. Dy(1) is closer to a triangular dodecahedral (TDD) with the deviation from the perfect geometry of 2.266 %, whereas the geometry of the coordination spheres around Dy(2) is closer to square antiprismatic (SAPR) with the deviation of 1.084 %. The next closest geometry is the biaugmented trigonal prismatic (BTPR). The powder patterns for the isostructural compounds are shown in Figure 5-7.

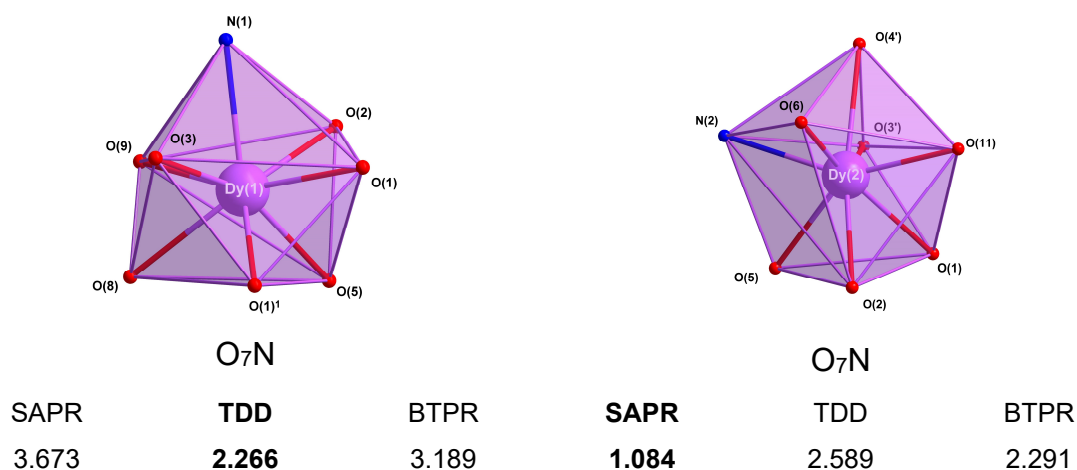


Figure 5-6 Coordination spheres around the Dy(III) ions of (**18**) and the deviations from the perfect geometries (in %).

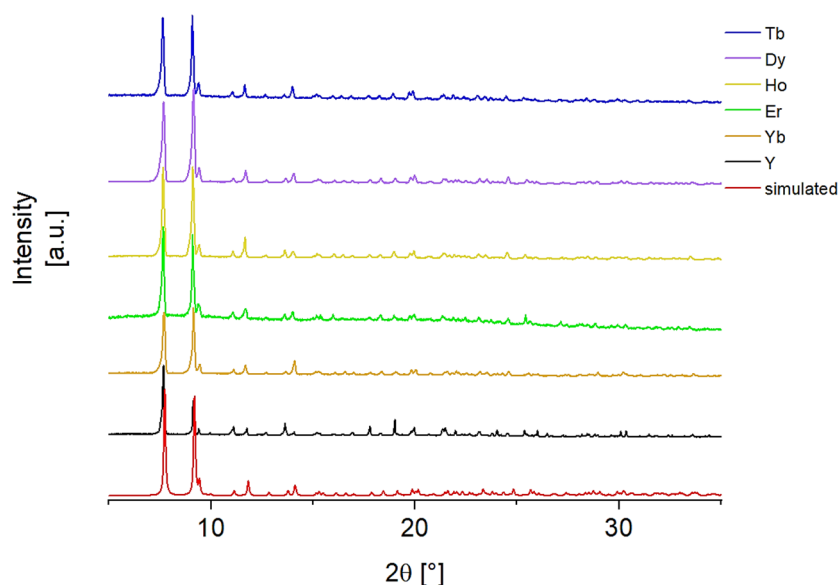


Figure 5-7 Powder patterns of (**17**) to (**22**) compared to the simulated one in red (out of the Dy-analogue).

The Ln··Ln distances and the Ln-O and Ln-N bond lengths decrease with increasing atomic number (from Tb to Yb) as expected due to the lanthanide contraction.^[88] Strictly speaking, yttrium is not a lanthanide, but a rare earth metal, but is often (as here) considered an “honorary” lanthanide. The Y-O and Y-N bond lengths usually fall between the values for the Dy and Ho-analogues. Y-Y distances and the Y-N bonds are somewhat larger than in the lanthanides. The Ln-OH-Ln angles and the Ln-O distances vary only slightly (Table 5-1). Selected distances and angles are shown in the appendix 12.4.

Table 5-1 Comparison of Ln-O and Ln-N bond lengths and Ln-O-Ln angles involving the bridging oxygens in (**17**) to (**22**).

	Tb (17)	Dy(18)	Ho(19)	Er (20)	Yb (21)	Y(22)
Ln···Ln [Å]	3.4945(5)	3.4716(1)	3.4468(5)	3.4313(5)	3.3850(2)	3.4473(5)
	3.8297(4)	3.8051(1)	3.7789(4)	3.7539(4)	3.6963(3)	3.7711(4)
	3.8941(5)	3.8754(1)	3.8583(5)	3.8412(5)	3.7861(5)	3.8508(5)
	6.3312(6)	6.2978(1)	6.2654(5)	6.2423(6)	6.15815(5)	6.2612(5)
Ln-OH-Ln [°]	93.66(10)-	93.89(7)-	93.57(8)-	93.29(11)-	93.64(10)-	93.90(4)-
	109.40(12)	109.61(8)	109.40(9)	109.17(12)	109.31(12)	109.29(5)
Ln-O	2.203(3)-	2.191(2)-	2.186(2) -	2.181(3)-	2.160(4)-	2.1861(13)-
	2.529(3)	2.521(2)	2.511(2)	2.509(4)	2.539(4)	2.5111(14)
Ln-N [Å]	2.451(4)	2.443(2)	2.432(3)	2.424(4)	2.375(5)	2.4363(15)
	2.506(3)	2.490(2)	2.479(3)	2.470(4)	2.446(5)	2.4870(15)

The anisotropy axes calculated by MAGELLAN for (**18**) are shown in Figure 5-8. The angles between the anisotropy axes and the Dy₄ plane are 16.9° for Dy(1) and 18.1° for Dy(2). From the top view, they form a parallelogram with angles between the anisotropy axes of 141.5° and 38.5°.

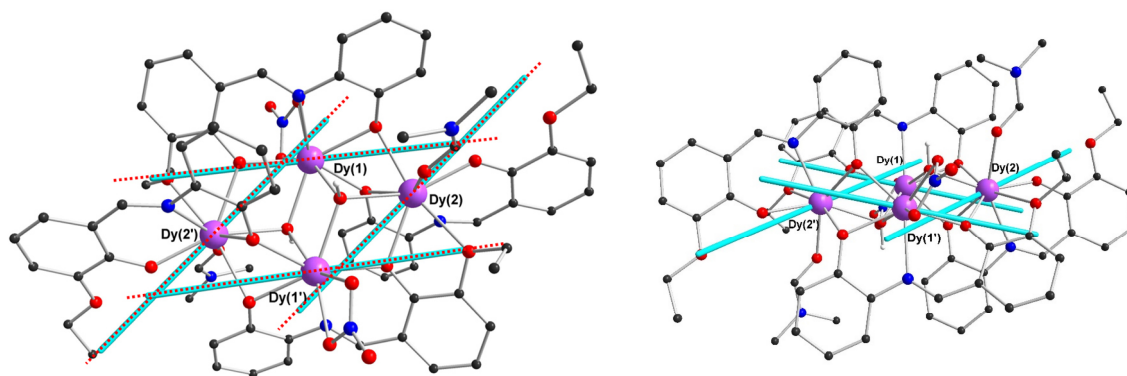


Figure 5-8 Anisotropy axes of (**18**) calculated using MAGELLAN.

5.2 Magnetic properties of (18) and (20)

The static magnetic susceptibilities of compounds $[\text{Dy}_4(\text{OH})_2(\text{NO}_3)_2(\text{DMF})_2(\text{ehimp})_4]$ (**18**) and $[\text{Er}_4(\text{OH})_2(\text{NO}_3)_2(\text{DMF})_2(\text{ehimp})_4]$ (**20**) were measured under a DC field of 0.1 T over the temperature range 2-300 K. The χT vs T plots are shown in Figure 5-9. The values of the χT products at 300 K are $54.44 \text{ cm}^3\text{mol}^{-1}\text{K}$ for the dysprosium compound (**18**) and $43.77 \text{ cm}^3 \text{mol}^{-1} \text{K}$ for the erbium compound (**20**).

These values are smaller than the calculated values of $56.68 \text{ cm}^3\text{mol}^{-1}\text{K}$ expected for four noninteracting Dy(III) ions ($S = \frac{5}{2}, g = \frac{4}{3}, C = 14.17 \text{ cm}^3\text{mol}^{-1}\text{K}$) and $45.92 \text{ cm}^3 \text{mol}^{-1} \text{K}$ for four noninteracting Er(III) ions ($S = \frac{3}{2}, g = \frac{6}{5}, C = 11.48 \text{ cm}^3\text{mol}^{-1}\text{K}$). In both systems the value of the χT product decreases slightly on cooling, to $47.09 \text{ cm}^3\text{mol}^{-1}\text{K}$ at 11 K for (**18**) and to $34.38 \text{ cm}^3\text{mol}^{-1}\text{K}$ at 30 K for (**20**). These slight decreases result from depopulation of excited m_j states. On cooling below these temperatures to 2 K, the curves both decrease more sharply, to $29.29 \text{ cm}^3\text{mol}^{-1}\text{K}$ for (**18**) and to $21.11 \text{ cm}^3\text{mol}^{-1}\text{K}$ for (**20**).

This is probably the result of further depopulation of excited m_j states (particularly for the Dy analogue) antiferromagnetic interactions between the metal centres. The magnetization (Figure 5-10) was measured for both systems under variable fields from 1-7 T at different temperatures. The magnetization for (**18**) at 2 K rises rapidly up to $18.39 \mu_B$ at 1.4 T, then increases more slowly and reach the maximum value at 7 T with $22.36 \mu_B$. There is no real saturation which indicates a high anisotropy in the system and/or low-lying excited states. The magnetization at 2 K for Er (**20**) rises rapidly up to a value of $13.16 \mu_B$ at 1.4 T, then slightly reach a maximum at 7 T with the value of $18.36 \mu_B$. The curve at 5 K increases more slowly than the one at 2 K but reaches the same value at 7 T. True saturation is not reached in any curves. This indicates a high anisotropy of the Er(III) ions and/or low-lying excited states. The insets in Figure 5-10 show enlargements of the magnetization curves at 2 K. In the Dy-system (**18**). A peak in the first derivate of the 2 K magnetization measurement is observed at $H = 0.2 \text{ T}$ and might give an indication of a toroidal state (Figure 5-11, left). For the Er-system (**20**) no peak was observed in the first derivative of the magnetization (Figure 5-11, right).

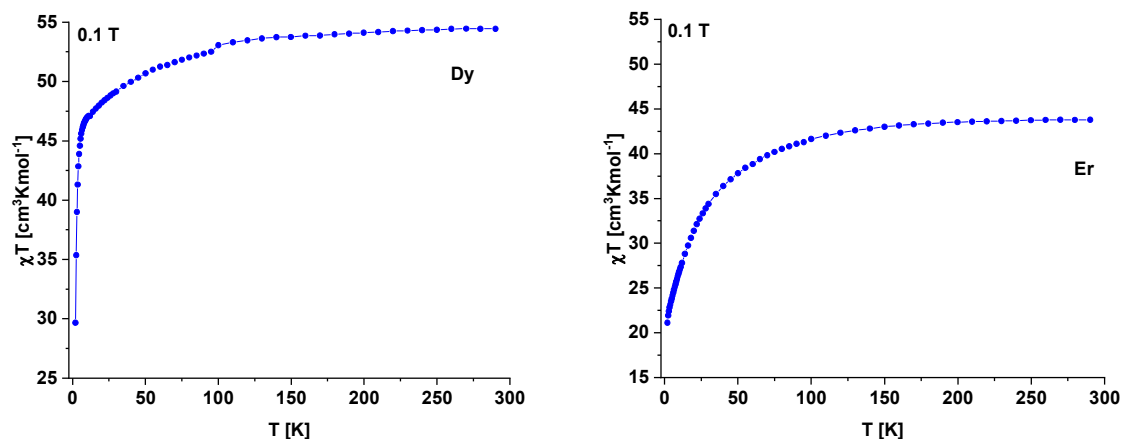


Figure 5-9 χT vs T plots for Dy (18) (left) and Er (20) (right) at 0.1 T.

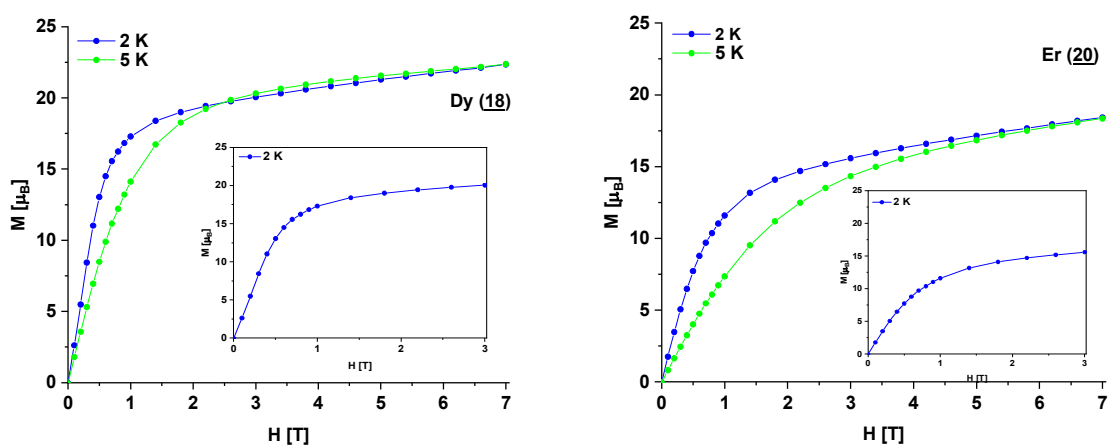


Figure 5-10 M vs H plot for Dy (18) (left) and Er (20) (right). The inset is the enlarged M vs H plot for 2 K.

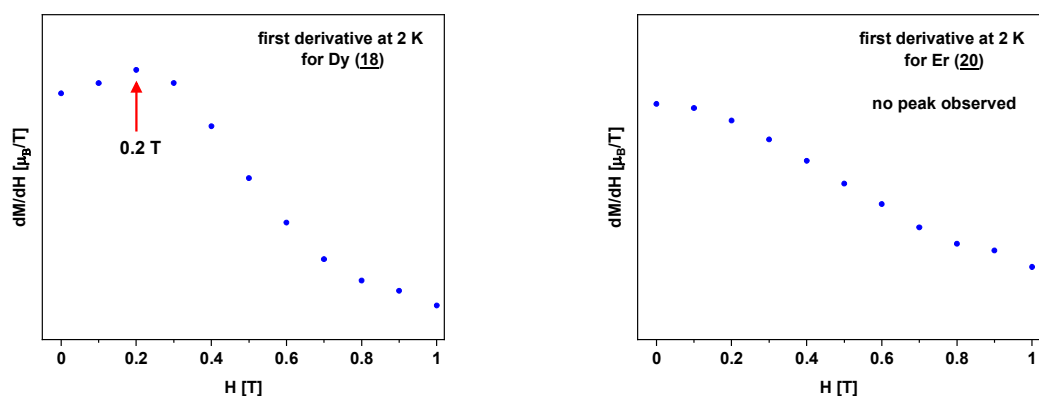


Figure 5-11 The first derivatives of the magnetizations at 2 K shows a peak at 0.2 T for Dy₄ (18) (left) but no peak is observed for the first derivative for Er₄ (20) (right).

Slow relaxation of magnetization was not observed for the Er-system (**20**) but for the Dy-system (**18**) signals were seen in the AC susceptibility at temperatures up to 13 K. The measurement results on (**18**) are shown in Figure 5-12. Energy barriers and preexponential factors could be estimated with the Arrhenius law in the high temperature area with values of $U_{eff} = 110.29 \text{ K}$ and $\tau_0 = 8.3 \cdot 10^{-9} \text{ s}$. The Cole-Cole plot gives α values between 0.24 and 0.03 indicating a small distribution between the relaxation processes.

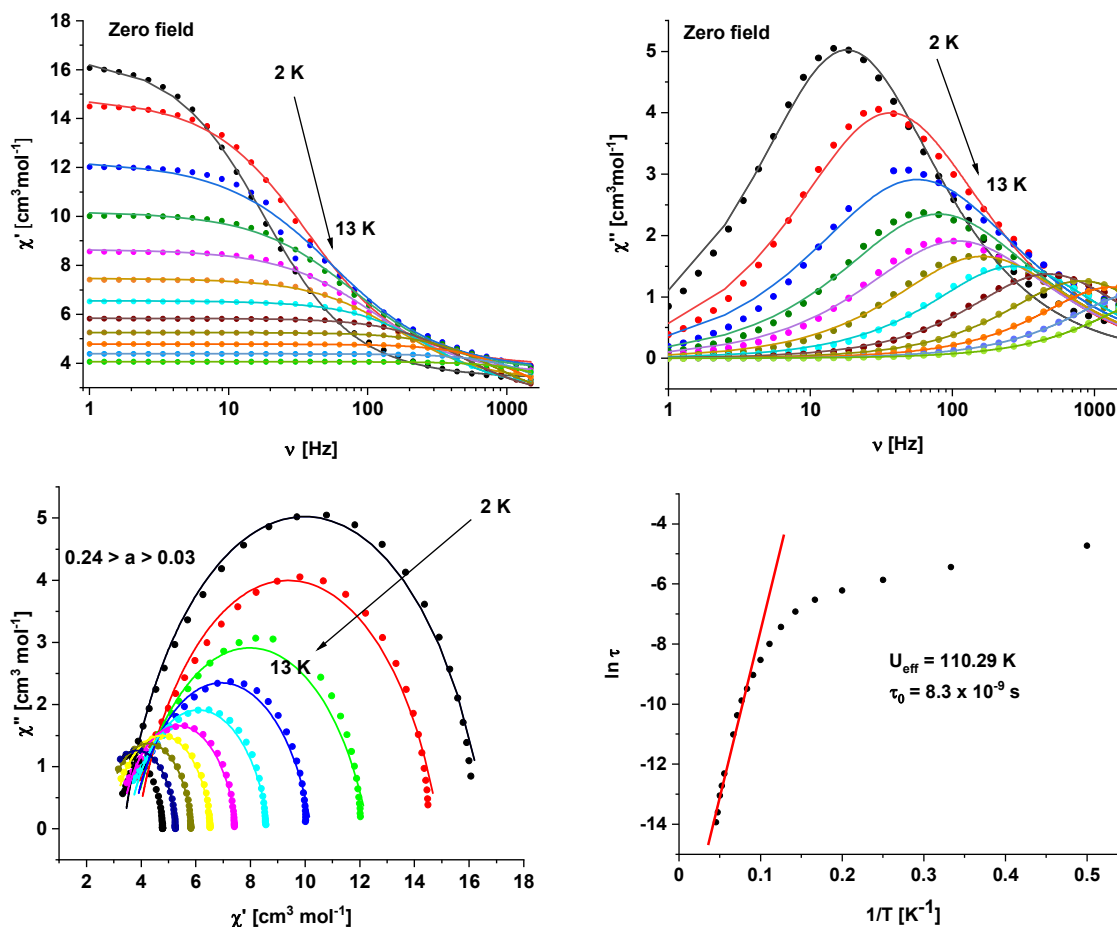


Figure 5-12 In-phase and out-of-phase susceptibility measurements on (**18**) at the top. Cole-Cole plot and Arrhenius plot at the bottom. The lines in the susceptibility measurements and in the Cole-Cole plot represent the best fit with the Debye model.

To further investigate the possible toroidal moment and SMM behaviour, single crystal measurements were performed on a micro-SQUID on the dysprosium system (**18**). Field-dependent magnetization measurements were taken at 30 mK for different sweep rates (Figure 5-13, left) and with a field-sweep rate of 8 mT/s in the temperature range from 33 mK to 4.5 K (Figure 5-13, right) and show only a very small open loop hysteresis in the range from -0.33 to 0.3 T for 30 mK, confirming the slow relaxation of magnetization at a molecular level. With higher temperatures the

hysteresis vanishes, indicating weak SMM behaviour only at very low temperatures. The first derivative dM/dH of the lowest temperature magnetization measurement at 33 mK under the sweep rate of 8 mT/s reveals several steps in the hysteresis in each direction of the field (Figure 5-13, bottom). The steps indicate a magnetization change in a small interval of applied magnetic field. The steps at zero field ($H = 0$) might indicate QTM and the step at ± 0.17 T and ± 0.03 T indicate the different spin flipping and the level-crossing of toroidal and paramagnetic states.^[85-86]

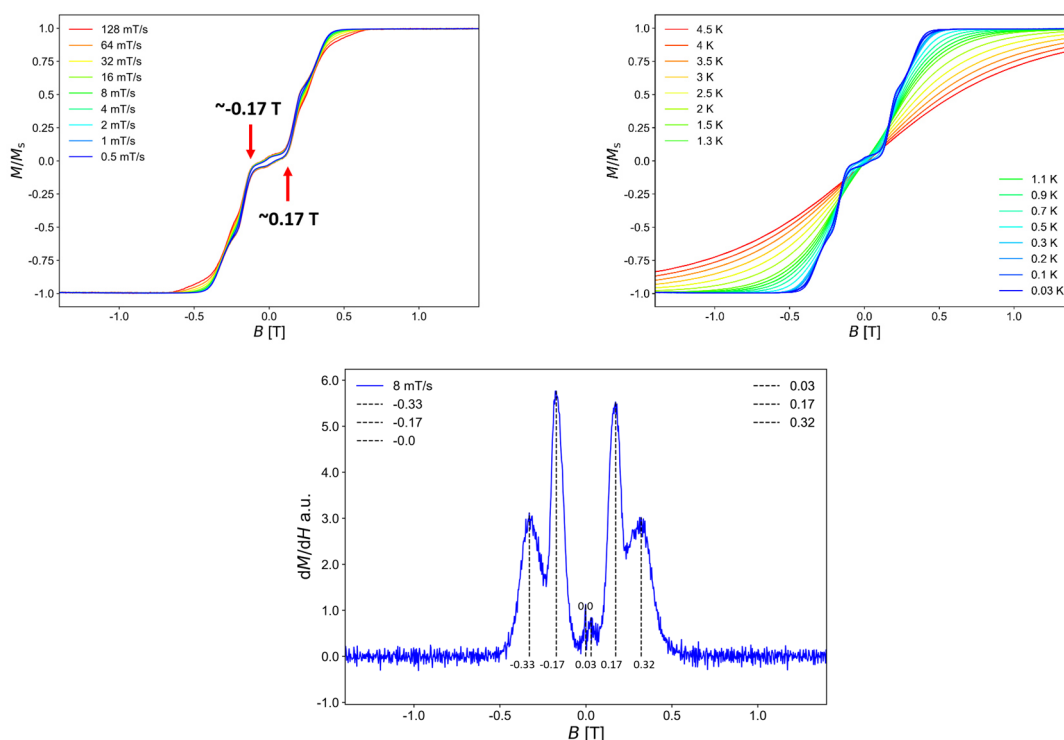


Figure 5-13 Single crystal micro-SQUID measurements of $\text{Dy}_4(\text{OH})_2(\text{NO}_3)_2(\text{DMF})_2(\text{ehimp})_4$ (**18**) (top) and the derivative of the magnetization (bottom). The red arrows indicate the possible level-crossing from the ground to first excited state.

In view of the fact that antiferromagnetic interactions prevail between the Dy centres and the anisotropy axes are almost in the Dy plane and nearly form a parallelogram (Figure 5-14), the following conclusions can be drawn with the help of the micro-SQUID measurements. At zero field, the spins have a toroidal arrangement (a), by increasing the field to 0.17 T, one spin flips according to the field directions (b). Further increase of the field flips the second spin at around 0.33 T (c).

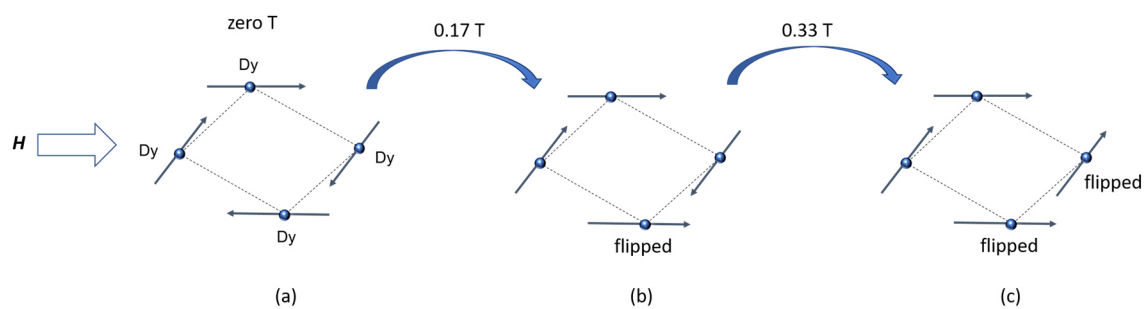


Figure 5-14 Scheme of the possible flipping of the spins if a field H is applied parallel to the Dy_4 plane. The toroidal arrangement of the spins at zero field ($H = 0$) (a), one flipped spin by increasing the field ($H = 0 - 0.17\text{ T}$) (b) and a second flipped spin at further increasing field ($H = 0.17 - 0.33\text{ T}$) (c).

5.3 Investigation of magnetization properties of planar Ln_4 systems in the literature

In the following section, the magnetic properties of previously-reported $\{\text{Dy}_4\}$ systems are investigated. If not already known, the orientations of their anisotropy axes will be calculated, and the existence of possible toroidal ground states will be checked by calculating the first derivative of the magnetizations at low temperatures. These complexes all have a common Dy_4 core, held together by two $\mu_3\text{-OH}^-$ bridges and at least four $\mu_2\text{-O-R}$ bridges. The four Dy(III) ions form a plane with one $\mu_3\text{-OH}^-$ unit above and one below the plane. Additional, bridging ligands are present and in some cases, peripheral ligands such as nitrates, chlorides, azides or pivalic acids are also present. These different ligands lead to various coordination spheres around the individual Dy(III) ions with different donor sets. The cluster cores are highlighted in the structures with bonds from Dy to bridging oxygens shown as orange bonds (Figure 5-15). They all have antiferromagnetic interactions between the Dy(III) ions.

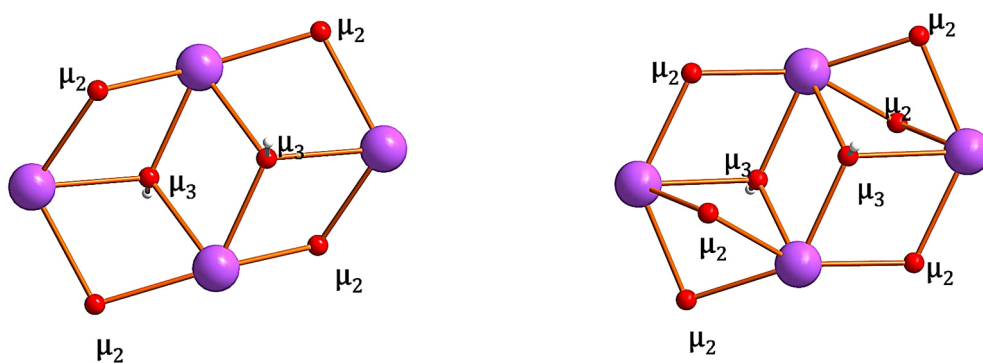
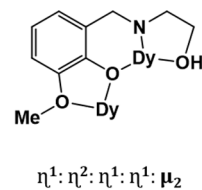
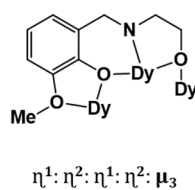
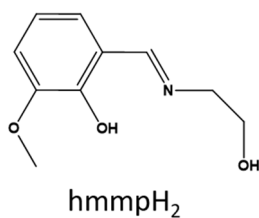
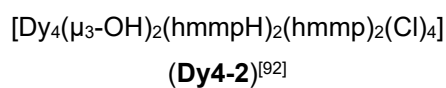
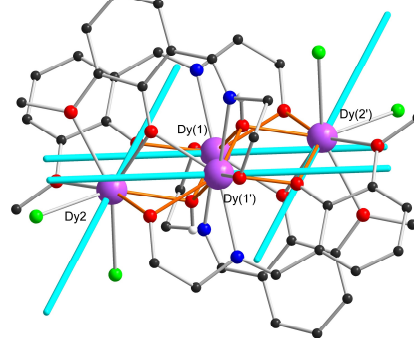
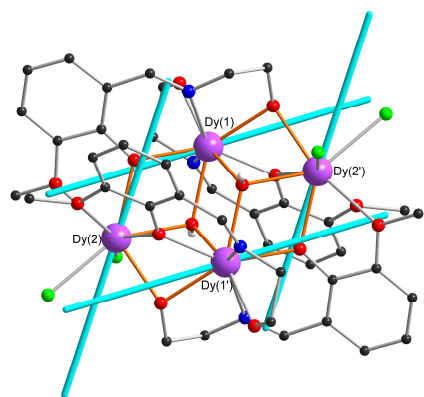


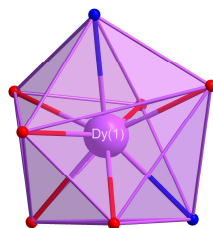
Figure 5-15 The core of the $\{\text{Dy}_4\}$ complexes with different number of $\mu_2\text{-O}^-$ bridging oxygens.

In 2008, four years before the discovery of the first $\{\text{Dy}_4\}$ toroidal system (**Dy4-1**), two isostructural $\{\text{Dy}_4\}$ complexes, were reported by Zheng et al, however no investigations of the single-ion anisotropy axes were made.^[92] The reaction of *ortho*-vanillin and 2-aminoethanol in methanol formed the in-situ Schiff base 2-[(2-hydroxyethylimino)methyl]-6-methoxyphenol} (hmmpH₂). The further reaction with $\text{DyCl}_3 \cdot 6\text{H}_2\text{O}$ and triethylamine led to crystals of $[\text{Dy}_4(\mu_3\text{-OH})_2(\text{hmmpH})_2(\text{hmmp})_2(\text{Cl})_4] \cdot 3\text{MeOH} \cdot \text{MeCN}$ (**Dy4-2**), showing no slow relaxation of magnetization in the measurement limit up to 1500 Hz. Carrying out the same reaction but with the addition of a saturated methanolic solution of NaN_3 led to

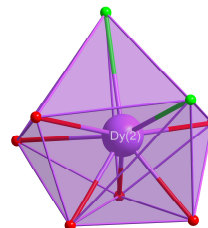
[Dy₄(μ₃-OH)₂(hmmpH)₂(hmmp)₂(N₃)₄]-4MeOH (**Dy4-3**), showing SMM behaviour. **Dy4-2** and **Dy4-3** crystallize isotopically in the triclinic space group P-1 and the centrosymmetric clusters differ only by the replacement of chloride ligands by azides. In both systems, two organic ligands can be found that link three dysprosium atoms *via* the ligand scheme η¹:η²:η¹:η²:μ₃ and two organic ligands that link two Dy(III) ions *via* the scheme η¹:η²:η¹:η¹:μ₂. In **Dy4-2** (Figure 5-16), the Dy(2) and Dy(2') ions are each coordinated by two chlorides, whereas in **Dy4-3** (Figure 5-17) these are exchanged with azides. This results in a coordination sphere with donor sets O₆Cl₂ for the Dy(2) in **Dy4-2** and O₆N₂ for Dy(2) in **Dy4-3**, with both coordination spheres best described as biaugmented trigonal prismatic (BTPR). The Dy(1) in both complexes has a coordination sphere with an O₆N₂ donor set which is best described as square antiprismatic (SAPR). The molecular structures with calculated anisotropy axes, the primary ligand, the binding mode of the ligand, the coordination spheres with donor sets around the Dy(III) ions and the magnetization at the lowest measured temperatures together with the first derivative are shown in Figure 5-16 for **Dy4-2** and in Figure 5-17 for **Dy4-3**. The dihedral angle between the two pairs of anisotropy axes is 38.91° in **Dy4-2** and 56.22° in **Dy4-3**. The angles of the anisotropy axes out of the Dy₄ plane are -12.75° and -38.68° for Dy(1) and Dy(2), respectively in **Dy4-2**. The corresponding out-of-plane angles for **Dy4-3** are 13.74° and 56.83°. These values are not ideal for a toroidal moment. However, the *M* vs *H* plots for both systems show characteristic S-shaped curves at 1.8 K and their first derivatives show peaks at 0.45 T for **Dy4-2** and 0.35 T for **Dy4-3**. This is a clear indication of the level crossing between ground states and first excited states in both systems. The significantly different orientations of the anisotropy axes calculated here for the two compounds allows a rationalization of their very different magnetic behaviours.



Cl⁻



O₆N₂
BTTPR
2.098 %



O₆Cl₂
SAPR
1.970 %

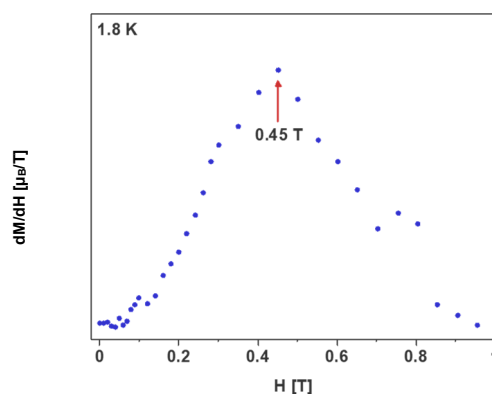
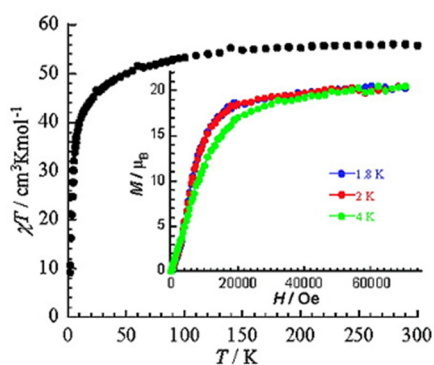
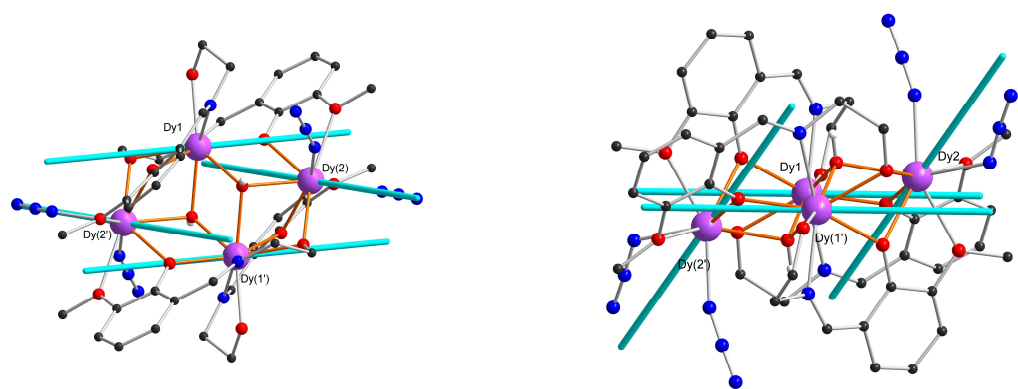
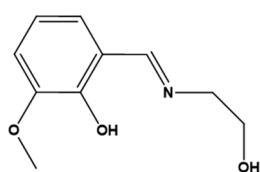


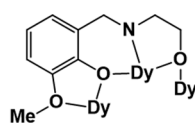
Figure 5-16 Molecular structure of **Dy4-2**^[92] with anisotropy axes calculated using MAGELLAN, corresponding ligand, binding mode and coordination spheres. The χT vs T and M vs H plots are taken from reference^[92]. The first derivative is for the magnetization at 1.8 K.



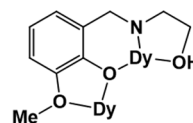
(**Dy4-3**)^[92]



hmmpH₂

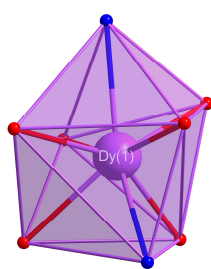


$\eta^1: \eta^2: \eta^1: \eta^2: \mu_3$



$\eta^1: \eta^2: \eta^1: \eta^1: \mu_2$

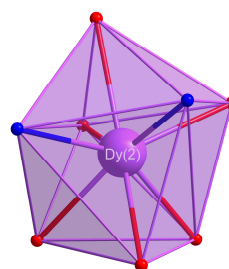
NO_3^-



O₆N₂

BTPR-8

2.026 %



O₆N₂

SAPR-8

1.379 %

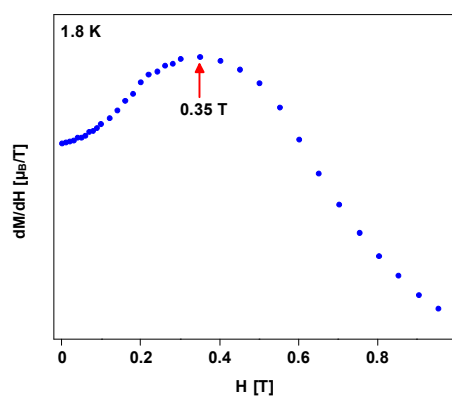
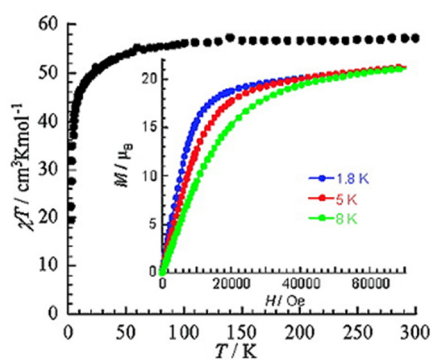


Figure 5-17 Molecular structure of **Dy4-3**^[92] with anisotropy axes calculated by MAGELLAN, corresponding ligand, binding mode and coordination spheres. The χT vs T and M vs H plots are taken from reference^[92]. The first derivative is for the magnetization at 1.8 K.

Two years later in 2010, the reaction of N-methyldiethanolamine (mdeaH₂), pivalic acid (pivH) and Dy(NO₃)₃·6H₂O in acetonitrile resulted in the cluster [Dy₄(μ₃-OH)₂(mdeaH)₂(piv)₈] (**Dy4-4**). Analogues with other lanthanides were also reported, but only the dysprosium analogue showed slow relaxation of magnetization.^[93] The cluster crystallized in the triclinic space group P-1 with the N-methyldiethanolamine (mdea)²⁻ ligand each bridging two Dy(III) ions in a η¹:η¹:η²:η²:μ₂ scheme. The pivalates either chelate η¹:η¹ one Dy(III), form bidentate η¹:η¹:μ₂ bridges, or monodentate η¹:η¹:μ₂ bridges. The coordination spheres can be described as triangular dodecahedral for both Dy(1) and Dy(2), with an O₈ donor set for Dy(1) and O₇N for Dy(2). The *M* vs *H* plot does not show a S-shaped curve and there is no peak observed in the first derivative of the magnetization at 1.8 K. This, together with the anisotropy axes with dihedral angles between the two pairs of anisotropy axes of 63.04°, leads to the conclusion that there is no toroidal moment in this system. The molecular structure together with their anisotropy axes in the Dy(III) ions, the corresponding ligands, the binding modes, the coordination spheres and the *M* vs *H* plots with the first derivative at 1.8 K are shown in Figure 5-18.

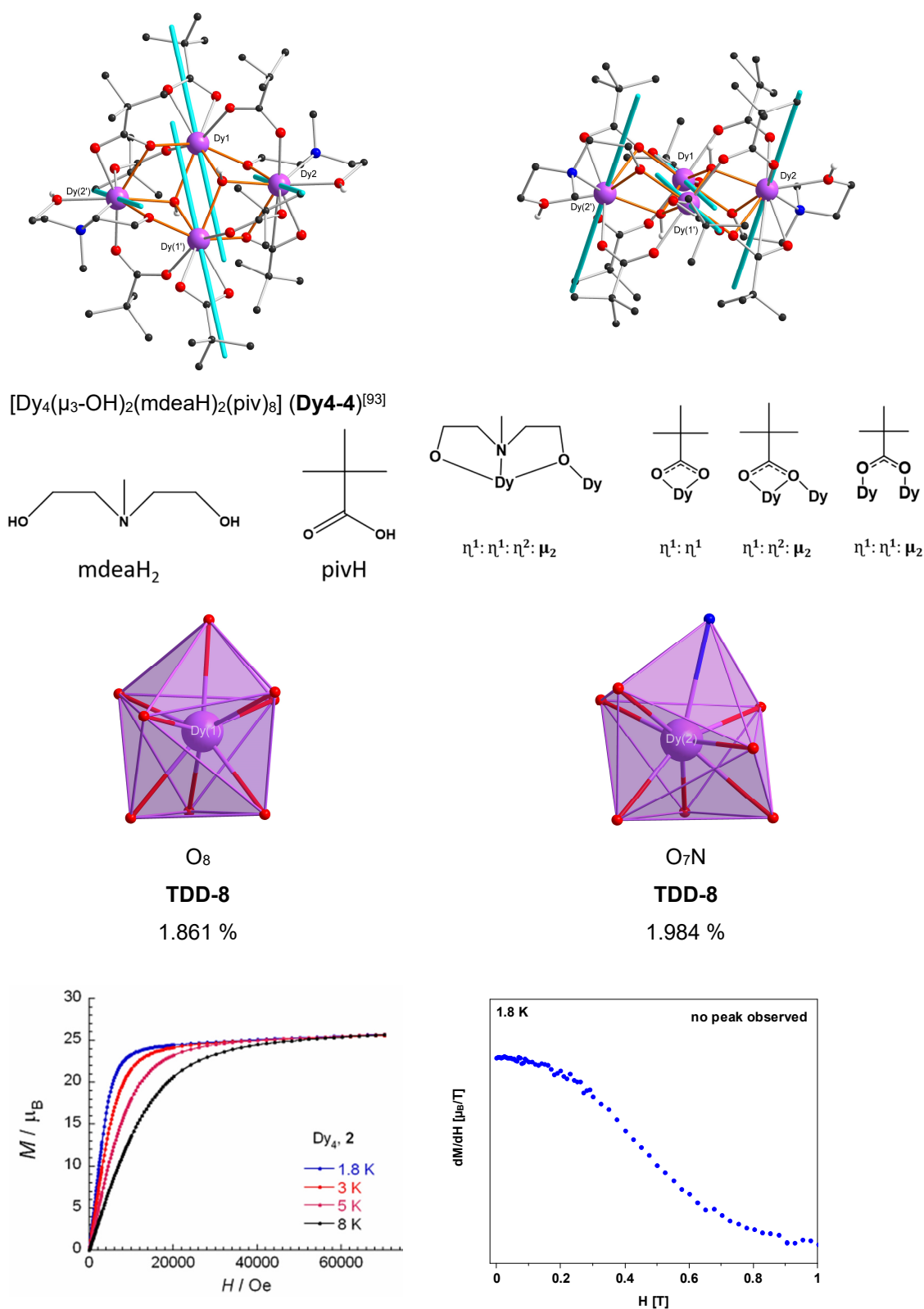


Figure 5-18 Molecular structure of **Dy4-4**^[93] with anisotropy axes calculated by MAGELLAN, corresponding ligand, binding mode and coordination spheres. The M vs H plot is taken from reference^[93]. The first derivative is for the magnetization at 1.8 K.

The crystal structure of $[\text{Dy}_4(\mu_3\text{-OH})_2(\text{o-van})_4(\text{piv})_4(\text{NO}_3)_2] \cdot \text{CH}_2\text{Cl}_2 \cdot 1.5\text{H}_2\text{O}$ (**Dy4-5**) was reported in 2011 by Murray et al.^[94], and this cluster showed slow relaxation of

magnetization. The same cluster molecule has since been obtained in this group as the acetonitrile solvate^[95] from the reaction *ortho*-vanillin, pivalic acid and Dy(NO₃)₃·6H₂O in acetonitrile. The cluster crystallized in the triclinic space group P-1. The deprotonated *ortho*-vanillin ligand is bridging two Dy(III) ions in a $\eta^1:\eta^2:\eta^1:\mu_2$ mode and the pivalate also bridges two Dy(III) ions in a $\eta^1:\eta^1:\mu_2$ scheme. One nitrate is chelating each Dy(2), resulting in an O₉ donor set for Dy(2), best described as capped square antiprismatic (CSAPR). The coordination sphere for Dy(1) with a O₈ donor set can be best described as triangular dodecahedron (TDD). The *M* vs *H* plots show an S-shaped curve at the lowest measured temperature (2 K), which can be confirmed by the first derivative with the highest point of 0.4 T. This indicates a non-magnetic ground state, although MAGELLAN calculations do not suggest a toroidal arrangement of the anisotropy axes. With the dihedral angle of 80.24°, the two pairs of anisotropy axes are almost perpendicular to each other, which is due to the negative charge of the nitrate and the pivalate ligands on Dy(2). The molecular structure together with their anisotropy axes in the Dy(III) ions, the corresponding ligands, the binding modes, the coordination spheres and the *M* vs *H* plot with the first derivative at 2 K shown in Figure 5-19.

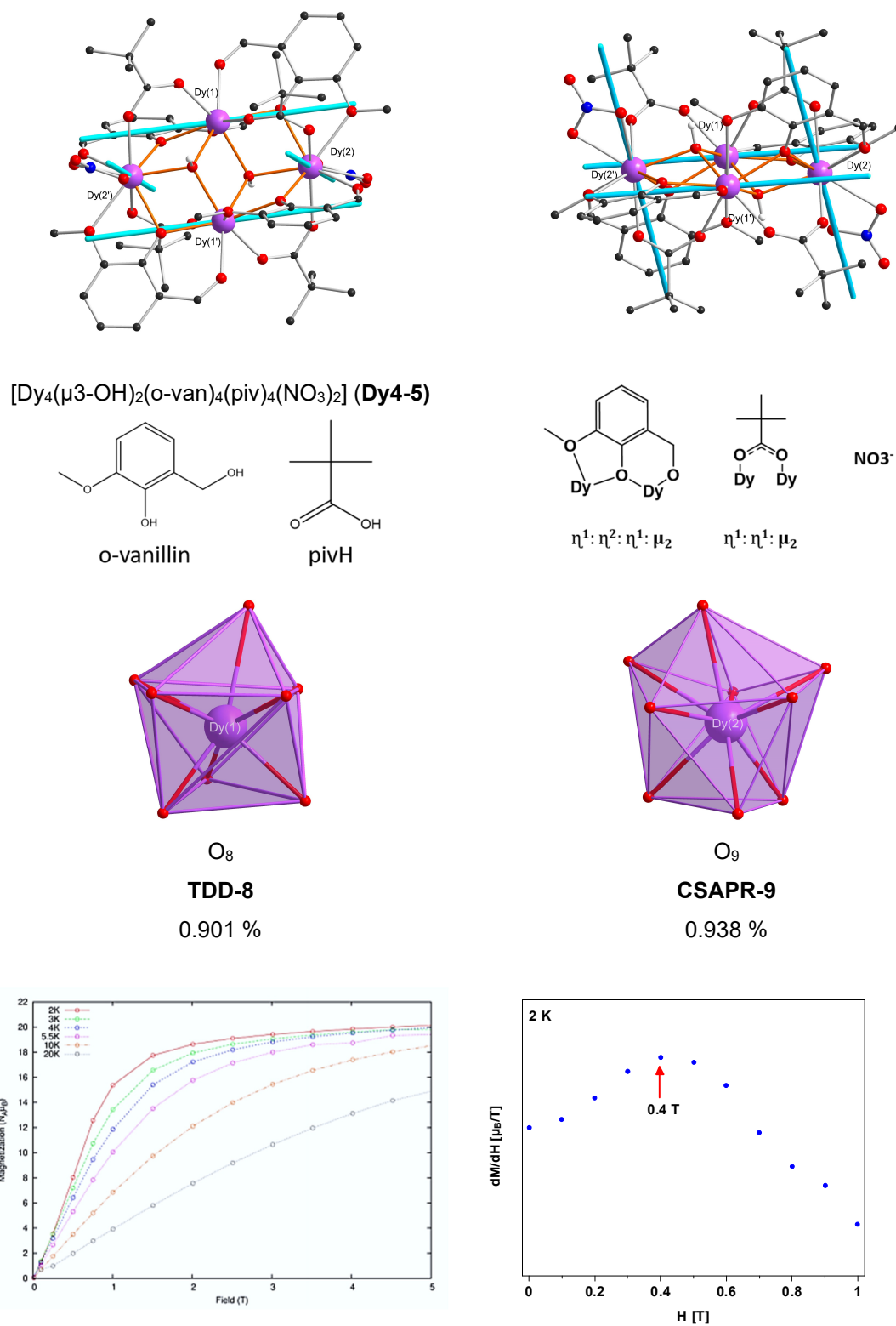
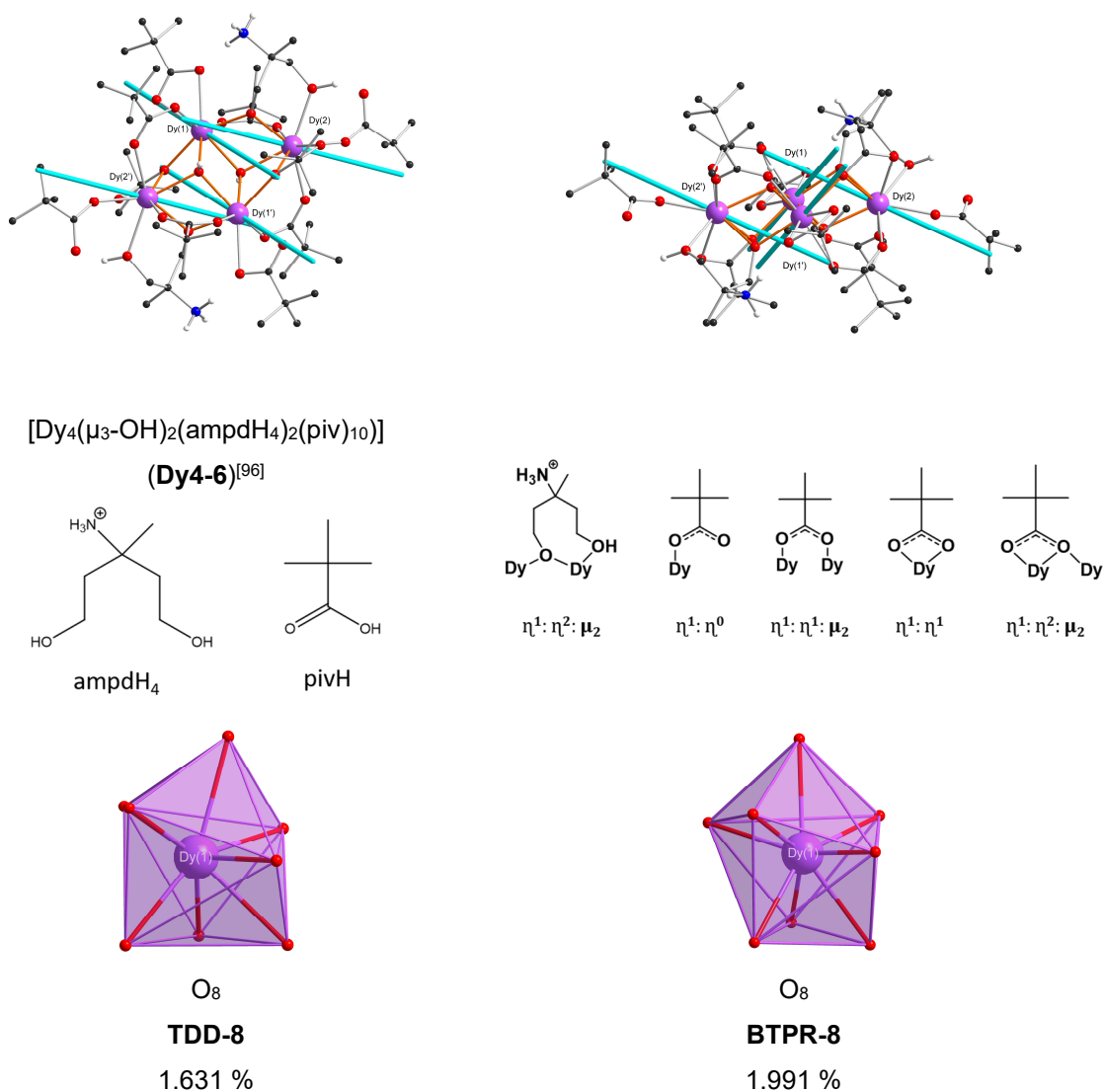


Figure 5-19 Molecular structure of **Dy4-5**^[93] with anisotropy axes calculated by MAGELLAN, corresponding ligand, binding mode and coordination spheres. The M vs H plots (bottom, left) are taken from reference^[94]. The first derivative is for the magnetization at 2 K (bottom, right).

In 2012, the $[\text{Dy}_4(\mu_3\text{-OH})_2(\text{ampdH}_4)_2(\text{piv})_{10}]\cdot 4\text{CH}_3\text{CN}$ (**Dy4-6**) was reported from the reaction of 3-amino-3-methylpentane-1,5-diol (ampdH₅), pivalic acid, triethylamine and $\text{Dy}(\text{NO}_3)_3\cdot 6\text{H}_2\text{O}$ in a mixture of methanol and acetonitrile.^[96] The cluster crystallized in the triclinic space group P-1. The ampdH₄ ligand is singly deprotonated and is bridging two Dy(III) ions in a $\eta^1:\eta^2:\mu_2$ mode. The pivalates are either monodentate ($\eta^1:\eta^0$), monodentate bridging ($\eta^1:\eta^1:\mu_2$), bidentate ($\eta^1:\eta^1$) or bidentate bridging ($\eta^1:\eta^2:\mu_2$). The O₈ coordination spheres around the Dy(III) ions are close to triangular dodecahedral (TDD) for Dy(1) and better describable as biaugmented trigonal prismatic for Dy(2). The pairs of anisotropy axes have a dihedral angle of 70.16° to each other and consequently no vortex-like arrangement of the spins. The *M* vs *H* plot also shows neither an S-shaped curve nor a maximum in the first derivative of the magnetization at 2 K (Figure 5-20).



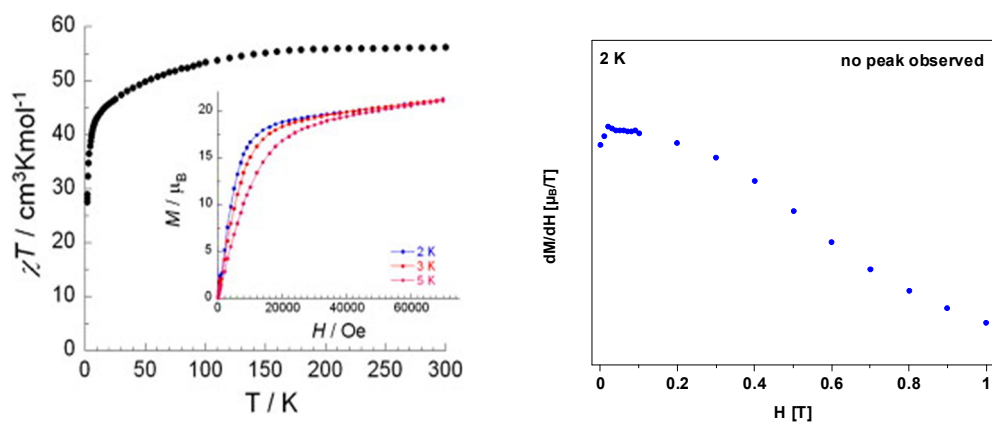


Figure 5-20 Molecular structure of **Dy4-6**^[93,96] with anisotropy axes calculated by MAGELLAN, corresponding ligand, binding mode and coordination spheres. The χT vs T and M vs H plots (bottom left) are taken from reference^[96]. The first derivative is for the magnetization at 2 K (bottom right).

5.4 Summary of tetranuclear Ln₄ systems

In this chapter, isostructural compounds of Ln₄(OH)₂(NO₃)₂(DMF)₂(ehimp)₄ with ehimpH₂ = 2-ethoxy-6-(((2-hydroxyphenyl)imino)methyl)phenol, were synthesized with Ln = Tb (**17**), Dy (**18**), Ho (**19**), Er (**20**), Yb (**21**) and Y (**22**). Magnetization and susceptibility measurements on (**18**) and (**20**) were carried out. (**18**) shows a peak at the first derivative of the magnetization ($H = 0.2$ T) and SMM behaviour with an energy barrier of $U_{eff} = 110.29$ K and preexponential factor $\tau_0 = 8.3 \cdot 10^{-9}$ s. The erbium system (**20**) does not show any peak at the first derivative of magnetization and no SMM behaviour in the measurement window.

For the {Dy₄} system reported here (**18**) and for six {Dy₄} systems taken from the literature (**Dy4-1**, [Dy₄(μ₃-OH)₂(hmmpH)₂(hmmp)₂(Cl)₄] **Dy4-2**, [Dy₄(μ₃-OH)₂(hmmpH)₂(hmmp)₂(N₃)₄] **Dy4-3**, [Dy₄(μ₃-OH)₂(mdeaH)₂(piv)₈] **Dy4-4**, [Dy₄(μ₃-OH)₂(o-van)₄(piv)₄(NO₃)₂] **Dy4-5** and [Dy₄(μ₃-OH)₂(ampdH₄)₂(piv)₁₀] **Dy4-6**), the positions of the anisotropy axes were calculated with MAGELLAN for this. MAGELLAN calculations on **Dy4-1**, in regard of the position of the anisotropy axes, show a good agreement with *ab initio* calculations from the literature.^[12] However, the anisotropy axes calculated using MAGELLAN do not give any information about a possible toroidicity, since in none of the cases mentioned can a vortex-like arrangement of the anisotropy axes or spins be recognised (with the exception of (**18**) and **Dy4-1**). The coordination spheres around the Dy(III) ions and their donor sets were also investigated. The first derivative of the magnetization was used for all complexes mentioned, with exception of **Dy4-1**, as an indicator of a possible toroidal ground state and level crossing from the ground to the first excited state, respectively. In Table 5-2, the comparison of the {Dy₄} systems are shown in regard of their Dy··Dy distances, Dy-OH-Dy angles, coordination spheres, ligands, magnetic results and toroidicity. For a better overview in this table, distances are given to three decimal places and angles to two decimal places. For the difference between the individual complexes, the number of bridging units (μ₃ and μ₂), bridging (bridg.) or terminal (term.) pivalates (R-CO₂⁻) and terminal ligands (Cl⁻, NO₃, N₃⁻, etc.) is considered and listed in Table 5-3.

The donor sets are different in all of the complexes and differ from mixed donor sets with O₆Cl₂, O₆N₂ and O₇N to a donor sets with only oxygens (O₈, O₉). **Dy4-2** with the highest value of the level crossing with $H = 0.45$ T is the only complex which does not

show SMM behaviour. The χT product of $9.12 \text{ cm}^3\text{mol}^{-1}\text{K}$ at 2 K indicate an almost non-magnetic ground state. Level crossing from the ground to the first excited state, examined by the first derivative of the magnetization, can also be observed for **Dy4-3** ($H = 0.35 \text{ T}$) and **Dy4-5** ($H = 0.4 \text{ T}$). The energy barriers of the complexes from the literature are quite low with 5.4 to 7 K. In contrast to this, the energy barrier of (**18**), is with a value over 100 K much higher. The minimum reversal energies (calculated by MAGELLAN) for the complexes with an observed level-crossing (**Dy4-2**, **Dy4-3**, **Dy4-5**) are close for the Dy(III) ions in the same molecule with exception of (**18**), where the energies differ from each other with more than 400 cm^{-1} .

The number of $\mu_2\text{-O}^-$ bridging atoms is in (**18**), **Dy4-2** and **Dy4-3** with six $\mu_2\text{-O}^-$ higher than the number in the other discussed complexes with only four $\mu_2\text{-O}^-$ bridging atoms and the bridging atoms lie practically in the Dy_4 plane with small distances from this plane ($\text{O} \cdots \text{DyPlane}$) as shown in Table 5-2. The distances of the $\mu_3\text{-OH}^-$ units from the Dy_4 plane are $< 1 \text{ \AA}$ ($\text{OH} \cdots \text{DyPlane}$) for all complexes. The range of Dy-OH-Dy angles is much larger in the three compounds (**18**), **Dy4-2** and **Dy4-3** than in the rest of the complexes considered. **Dy4-5** has a smaller number of $\mu_2\text{-O}^-$ bridging units, but also has a level-crossing at 0.4 T. Compared to **Dy4-4** and **Dy4-6**, which both show no toroidal moment, the **Dy4-5** system has fewer bridging and no terminal pivalate ligands but does have terminal nitrates. Comparing the χT products at 2 K, it is noteworthy, that they all drop significantly to values $< 30 \text{ cm}^3\text{mol}^{-1}\text{K}$ with exception of **Dy4-4** where the value is higher with $37.6 \text{ cm}^3\text{mol}^{-1}\text{K}$. Here, the drop could entirely occur through depopulation of the stark levels and not antiferromagnetic interactions between the Dy(III) ions.

Table 5-2 Comparison of the {Dy₄} systems in regard of distances, angles, donor sets and magnetic results.

	(18)	Dy4-2 ^[92]	Dy4-3 ^[92]	Dy4-4 ^[93]	Dy4-5 ^[94]	Dy4-6 ^[96]
Space group	P2 ₁ /n	P-1	P-1	P-1	P-1	P2 ₁ /n
Dy···Dy [Å]	3.471 3.805 3.875 6.297	3.487 3.865 3.889 6.296	3.464 3.867 3.869 6.244	3.650 3.831 4.040 6.300	3.753 3.787 3.846 6.588	3.713 3.812 3.954 6.403
Dy-O-Dy [°]	93.89- 112.03	95.16- 111.01	94.46- 112.76	101.72- 113.90	101.70- 109.83	103.93- 112.13
OH···DyPlane	0.961	0.916	0.919	0.871	0.819	0.868
O···DyPlane [Å]	0.734 0.824 1.550	0.676 0.826 1.549	0.664 0.811 1.545	1.244 1.456	0.199 1.200	1.207 1.441
Donor sets and geometry of the Dy(III) ions	O ₇ N O ₇ N	O ₆ N ₂ O ₆ Cl ₂	O ₆ N ₂ O ₆ N ₂	O ₈ O ₇ N	O ₈ O ₉	O ₈ O ₈
Toroidicity (dM/dH) Bulk	0.20 T	0.45 T	0.35 T	-	0.40 T	-
SMM (U _{eff} , τ ₀)	110.29 K, 8.3·10 ⁻⁹ s	none	7 K, 3.8·10 ⁻⁵	6.2 K, 2.4·10 ⁻⁵	6.25 K, 3.75·10 ⁻⁵ s	5.4 K, 1.1·10 ⁻⁵ s
χ _T (2 K) [cm ³ mol ⁻¹ K]	29.29	9.12	19.49	37.6	14.49	27.5
χ _T (300 K) [cm ³ mol ⁻¹ K]	54.44	55.91	57.32	57.7	54.7	56.16
Minimum Reversal Energy	401 cm ⁻¹ 848 cm ⁻¹	665.3 cm ⁻¹ 652.2 cm ⁻¹	738.6 cm ⁻¹ 829.5 cm ⁻¹	84.65 cm ⁻¹ 288.9 cm ⁻¹	409.2 cm ⁻¹ 488.3 cm ⁻¹	477.6 cm ⁻¹ 51.97 cm ⁻¹

Table 5-3 Comparison of the {Dy₄} systems in regard of their ligands and toroidicity.

compound & space group	μ ₃	μ ₂	NO ₃ ⁻	Cl ⁻	N ₃ ⁻	R-CO ₂ ⁻ (bridg.)	R-CO ₂ ⁻ (term.)	DMF	Toroidicity (dM/dH) Bulk
Dy ₄ (μ ₃ -OH) ₂ (NO ₃) ₂ (DMF) ₂ (ehimp) ₄ (18) P2 ₁ /n	2	6	2	-	-	-	-	2	0.2 T
Dy4-2 ^[92] [Dy ₄ (μ ₃ -OH) ₂ (hmpH) ₂ (hmp) ₂ (Cl) ₄] P-1	2	6	-	2	-	-	-	-	0.45 T
Dy4-3 ^[92] [Dy ₄ (μ ₃ -OH) ₂ (hmpH) ₂ (hmp) ₂ (N ₃) ₄] P-1	2	6	-	-	2	-	-	-	0.35 T
Dy4-4 ^[93] [Dy ₄ (μ ₃ -OH) ₂ (mdeaH) ₂ (piv) ₈] P-1	2	4	-	-	-	6	2	-	-
Dy4-5 ^[94] [Dy ₄ (μ ₃ -OH) ₂ (o-van) ₄ (piv) ₄ (NO ₃) ₂] P-1	2	4	2	-	-	4	-	-	0.4 T
Dy4-6 ^[96] [Dy ₄ (μ ₃ -OH) ₂ (ampdH) ₄ (piv) ₁₀] P2 ₁ /n	2	4	-	-	-	6	4	-	-

6 Hexanuclear Ln₆ systems

The very first hexanuclear homonuclear 4f-wheel compound [Dy₆(teaH)₆(NO₃)₆]·8MeOH (**Dy6-1**) with doubly-deprotonated triethanolamine (teaH₃) as ligand was reported in 2010 by Murray et al.^[82] Later on in 2015, two other Dy₆ wheel compounds were reported.^[83] One has the structure [Dy₆(Me-teaH)₆(NO₃)₆]·6MeCN (**Dy6-2**) synthesized from *rac*-1-[*N,N*-bis-(2-hydroxyethyl)amino]-2-propanol (Me-teaH₃), which has an additional methyl group on one of the ethanol arms compared to the ligand in **Dy6-1** and thus has a stereo-centre.

The other has the structure [Dy₆(apadH₂)₆(NO₃)₆]·2THF (**Dy6-3**) (apadH₄ = 2,2'-(3-aminopropylazanediyl)diethanol), where one of the ethanol arms of triethanolamine is exchanged by a propylamine. Another {Dy₆} wheel, synthesized in the Powell group, but not yet published, has the structure [Dy₆(NO₃)₃(pmide)₆] (**Dy6-4**) where H₂pmide = *N*-(2-pyridylmethyl)diethanolamine. The different ligands are shown in Figure 6-1. All the structures have an isostructural core and crystallize in the rhombohedral space group R-3, with exception of **Dy6-4** which crystallizes in the monoclinic space group P2₁/n.

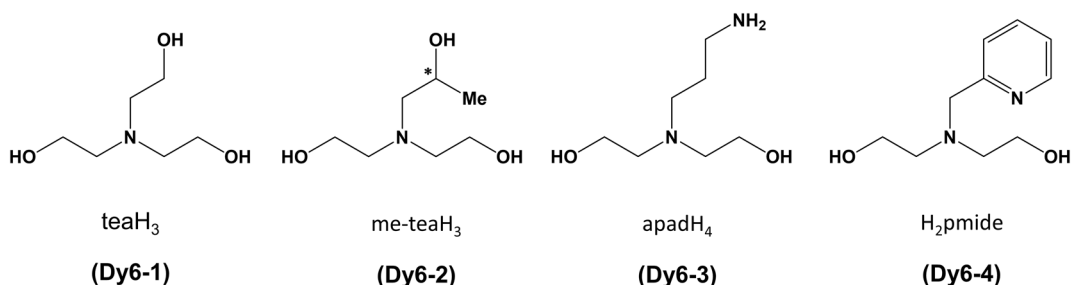


Figure 6-1 The used ligands for the {Dy₆} systems in the literature.

For **Dy6-2** and **Dy6-3** the first derivatives of the bulk magnetization at 2 K have peaks, corresponding to level-crossing from the ground to the respective first excited states at $H = 0.42\text{ T}$ for **Dy6-2** and at $H = 0.325\text{ T}$ for **Dy6-3** (Figure 6-2).^[83]

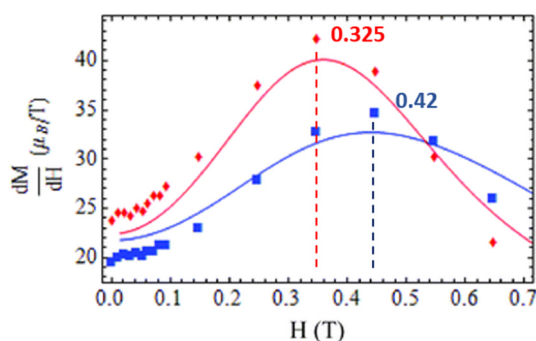


Figure 6-2 First derivatives of the magnetization at 2 K for $[\text{Dy}_6(\text{Me-teaH})_6(\text{NO}_3)_6] \cdot 6\text{MeCN}$ (**Dy6-2**) in blue and for $[\text{Dy}_6(\text{apadH}_2)_6(\text{NO}_3)_6] \cdot 2\text{THF}$ (**Dy6-3**) in red. The lines represent the fit. Adapted from reference [83].

For $[\text{Dy}_6(\text{teaH})_6(\text{NO}_3)_6] \cdot 8\text{MeOH}$ (**Dy6-1**) no first derivative of the magnetization was shown in the literature but *ab initio* calculations indicate the level-crossing from the ground state to the first excited state at around $H = 0.65 \text{ T}$ and gave the directions of the anisotropy axes (Figure 6-3 and Figure 6-4).^[16]

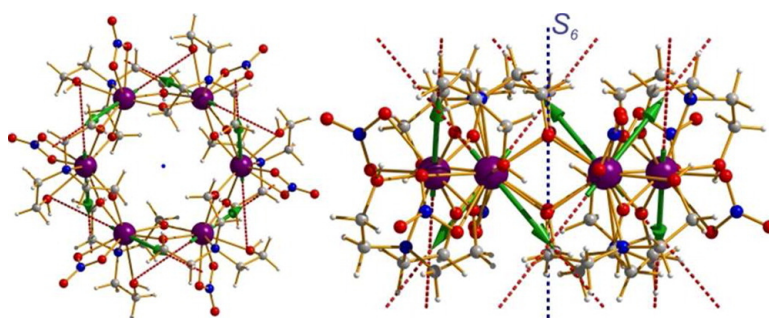


Figure 6-3 Structure of $[\text{Dy}_6(\text{teaH})_6(\text{NO}_3)_6] \cdot 8\text{MeOH}$ (**Dy6-1**) with the anisotropy axes (dotted lines) and the direction of the magnetic moments (green arrows). The dot and the dotted line in the middle of the molecule indicate the S_6 symmetry of the molecule.^[16]

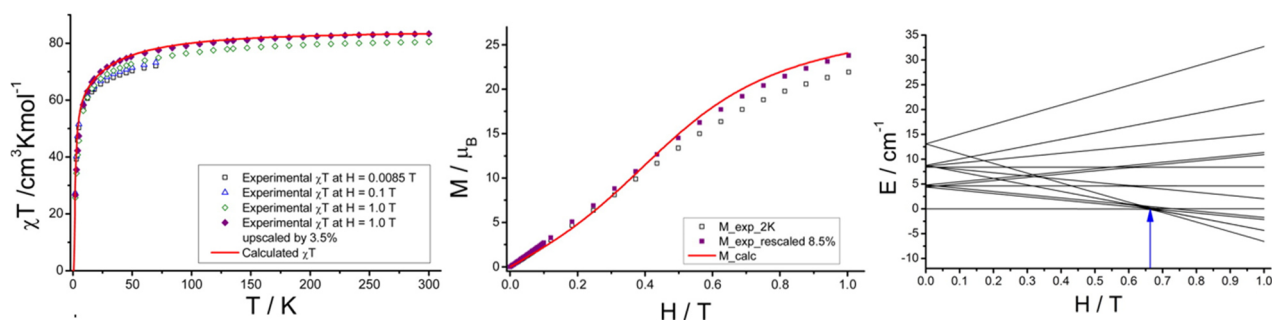


Figure 6-4 The χT vs T plot shows antiferromagnetic interactions (left), the M vs H plots out of bulk magnetization measurements show a S-Shaped curve (middle) and the level-crossing from the toroidal ground state to the first excited state gives a value of $H = 0.65 \text{ T}$ from *ab initio* calculations (right). Adapted with permission from reference^[16]. Copyright 2012 American Chemical Society.

The angle (θ) describes the angle between the anisotropy and the S_6 symmetry axis (Figure 6-5). MAGELLAN calculations on **Dy6-1** (Figure 6-6) with θ angles 35.2° show similar orientations of the anisotropy axes compared to those from the *ab initio* calculations with θ angles of 43° .^[16] These θ angles are similar in **Dy6-2** with 37.3° where an additional methyl group is attached on one ethanol arm (Figure 6-7). For **Dy6-3** where one ethanol arm is exchanged by an aminopropyl arm, the θ angles have increased to 47.6° (Figure 6-8).

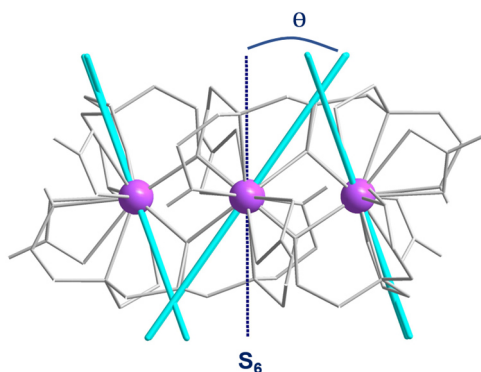


Figure 6-5 Angle θ between the S_6 symmetry axis (blue dotted line) and the anisotropy axes (turquoise lines).

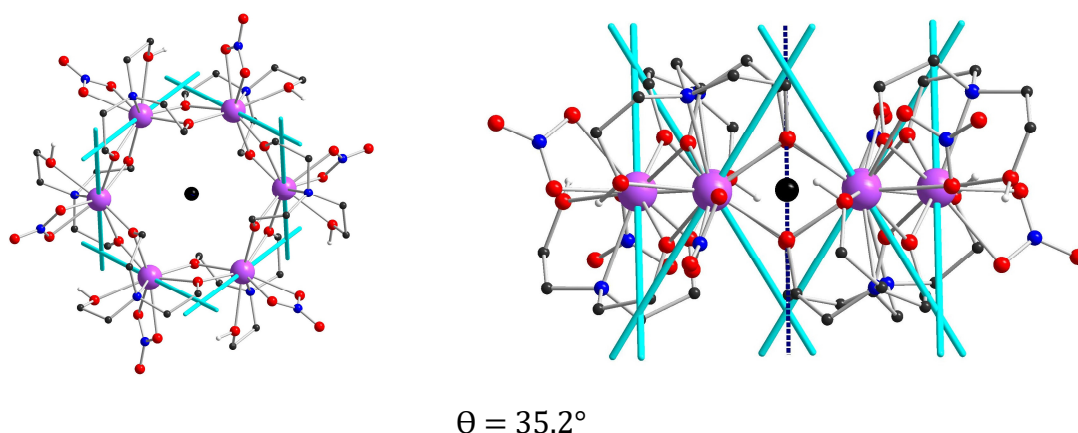
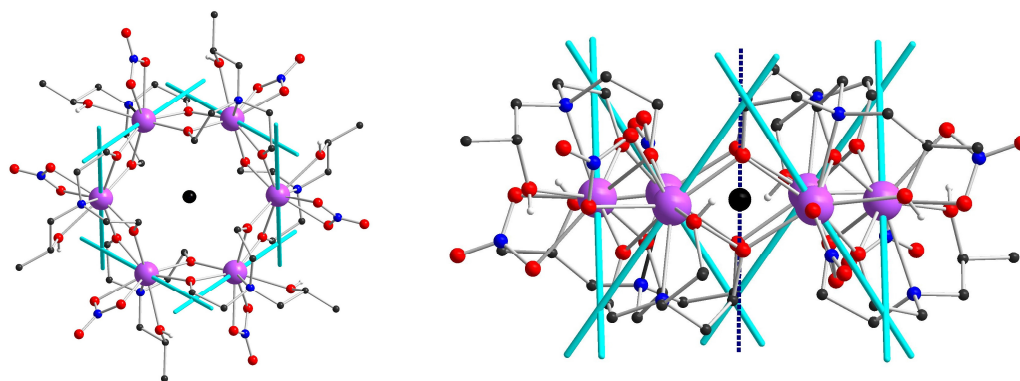
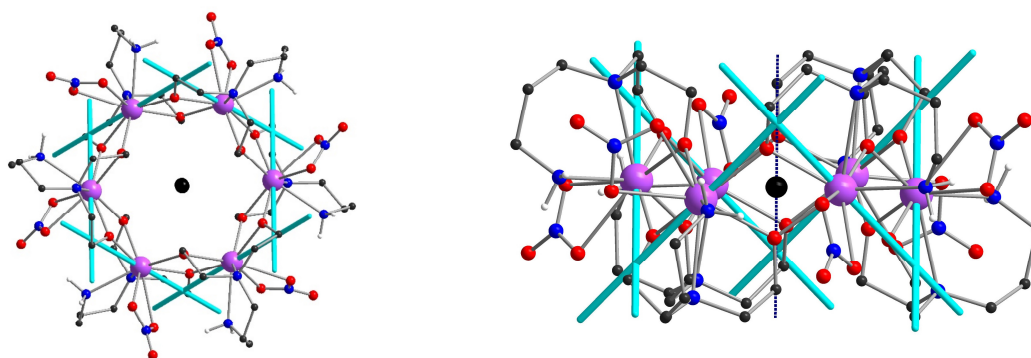


Figure 6-6 Anisotropy axes of $[\text{Dy}_6(\text{teaH})_6(\text{NO}_3)_6]$ (**Dy6-1**) calculated with MAGELLAN. The dot in the middle of the molecule and the dotted line both indicate the S_6 symmetry axis.



$$\theta = 37.3^\circ$$

Figure 6-7 Anisotropy axes of $[\text{Dy}_6(\text{Me-teaH})_6(\text{NO}_3)_6]$ (**Dy6-2**) calculated with MAGELLAN. The dot in the middle of the molecule and the dotted line both indicate the S_6 symmetry axis.



$$\theta = 47.6^\circ$$

Figure 6-8 Anisotropy axes of $[\text{Dy}_6(\text{apadH}_2)_6(\text{NO}_3)_6]$ (**Dy6-3**) calculated with MAGELLAN. The dot in the middle of the molecule and the dotted line both indicate the S_6 symmetry axis.

6.1 Properties of $[\text{Dy}_6(\text{NO}_3)_6(\text{teaH})_6] \cdot 2\text{C}_2\text{H}_5\text{OH}$ (**23**)

With the aim of carrying out micro-SQUID measurements, the synthesis of **Dy6-1** was reproduced in this thesis by carefully overlaying an ethanolic solution of Dy(III)-nitrate with triethanolamine and triethylamine in acetonitrile. Colourless crystals could be obtained after one day with the formula $[\text{Dy}_6(\text{NO}_3)_6(\text{teaH})_6] \cdot 2\text{C}_2\text{H}_5\text{OH}$ (**23**). The asymmetric unit contains one crystallographically independent Dy(III) ion, one nitrate and one doubly deprotonated triethanolamine ligand. Therefore, six Dy(III) ions, six doubly deprotonated teaH^{2-} ligands and six nitrates are present in the structure and together form a wheel. Two ethanol could be found in the lattice per molecule with one ethanol on the 6-fold axes. Each Dy(III) ion has one doubly protonated ligand and is capped by one bidentate nitrate. The wheel is formed through the doubly deprotonated teaH^{2-} ligands bridging between the dysprosium centres with the binding mode $\eta^2:\eta^1:\eta^1:\eta^2:\mu_3$ and six capping nitrates. The nitrogen of the ligand and the protonated oxygen of the third arm complete the coordination sphere of the Dy(III) ions.

The molecular structure of (**23**) with selected distances and angles are shown in Figure 6-9. The resulting structure of (**23**) differs from that of **Dy6-1**^[98] in the amount and type of solvent molecules in the lattice. Two lattice ethanol per ring are found in the structure of (**23**), whereas eight lattice methanols are in the crystal structure of **Dy6-1**. In the synthesis of (**23**) reported here, ether diffusion and methanol (as used in the synthesis of **Dy6-1**) were avoided. Slightly longer cell parameters (a, c) are found in (**23**) compared to **Dy6-1** (Table 6-1). The distances between the Dy(III) ions are essentially the same in both solvates. The average Dy-O bonds in (**23**) are also similar to **Dy6-1**.

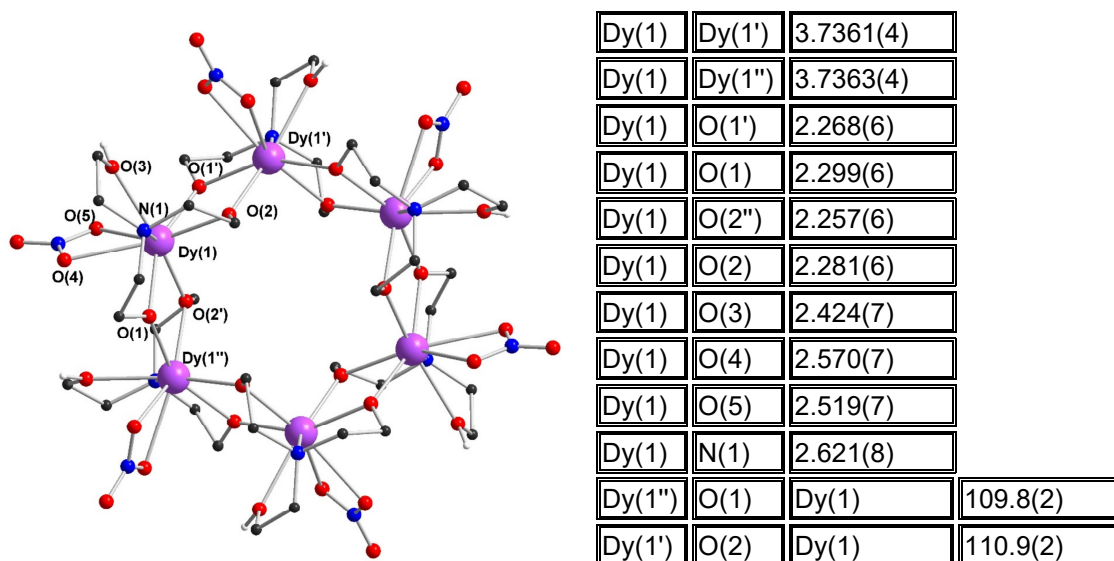


Figure 6-9 Molecular structure of (**23**) with selected distances [Å] and angles [°]. Primed atoms at $1/3+y$, $2/3-x+y$, $2/3-z$; double-primed atoms at $1/3+x-y$, $-1/3+x$, $2/3-z$.

Table 6-1 Comparison of the crystal structures of (**23**) and **Dy6-1**.

	$[\text{Dy}_6(\text{NO}_3)_6(\text{teaH})_6] \cdot 2\text{C}_2\text{H}_5\text{OH}$ (23) measured at 273 K	$[\text{Dy}_6(\text{teaH})_6(\text{NO}_3)_6] \cdot 8\text{MeOH}$ (Dy6-1) ^[82] measured at 123 K
Space group	R-3	R-3
Z	3	3
α [°]	90	90
β [°]	90	90
γ [°]	120	120
a [Å]	17.2007(3)	16.7756(3)
b [Å]	17.2007(3)	16.7756(3)
c [Å]	25.3280(5)	24.9858(9)
V [Å ³]	6489.7(2)	6089.5(3)
Dy··Dy [Å]	3.7361(4)	3.7297(17)
Dy–O [Å], average	2.37	2.36

The angles of the anisotropy axes, calculated by MAGELLAN, with the symmetry axes (Figure 6-10) in the middle of the molecule are with 46.9° a bit bigger than in

Dy6-1 (35.2°) and in **Dy6-2** (37.3°), respectively, but close to the one in **Dy6-3**. The Dy(III) ions in (**23**) and also in **Dy6-1**, are crystallographically identical and are eight-coordinate with a O_7N donor set, and are best described as biaugmented trigonal prismatic (BTPR) with a rather high deviation from this perfect geometry of 3.811 % (Figure 6-11, left), whereas the coordination sphere of the Dy(III) ions in **Dy6-1** can best be describes as triangular dodecahedron (TDD) with deviations from 2.094 % from this geometry (Figure 6-11, middle). The binding scheme of the ligand, which is identical in both complexes is shown in Figure 6-10, right.

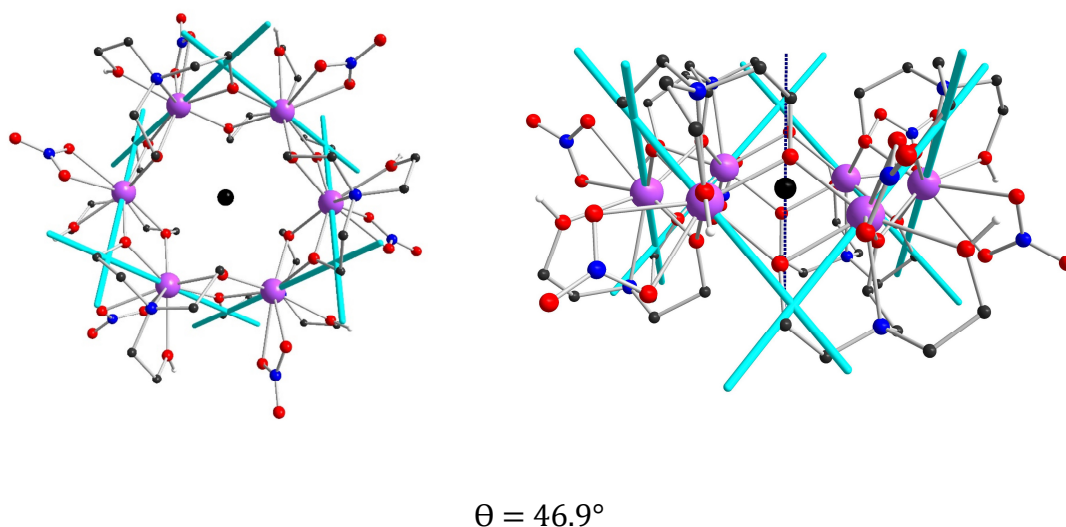


Figure 6-10 Anisotropy axes of $[Dy_6(NO_3)_6(teaH)_6] \cdot 2C_2H_5OH$ (**23**) calculated with MAGELLAN. The dot in the middle of the molecule and the dotted line both indicate the S_6 symmetry axis.

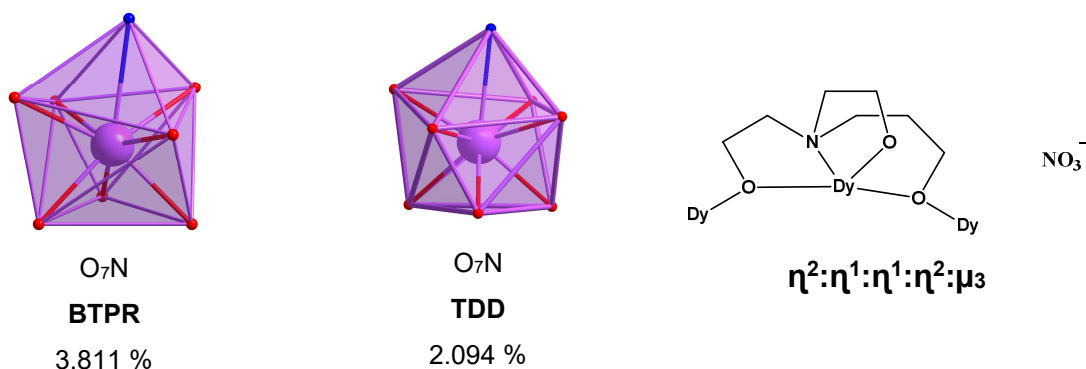


Figure 6-11 Coordination spheres around the Dy(III) ions in (**23**) (left) and in **Dy6-1** (middle) with the deviations from the perfect geometry. The ligand and the binding scheme (right) are the same in both structures.

Measurements on a single crystal on $[Dy_6(NO_3)_6(teaH)_6] \cdot 2EtOH$ (**23**) with the micro-SQUID technique were carried out. Magnetization curves at a range of temperatures from 30 mK to 3.5 K under a constant sweep rate of the magnetic field

of 16 mT/s over the range -1 to +1 T are shown in Figure 6-12 top left, while curves measured at 30 mK for a range of magnetic field sweep rates from 1 to 128 mT/s are shown in Figure 6-12, top right. They show stepped hysteresis loops between -0.7 to 0.7 T at 0.3 K, which is evidence both for magnetic level crossing and also for blocking of the magnetization at low temperatures on a molecular level. As expected, the coercivity increases with faster sweep rates and lower temperatures.^[9] The hysteresis loops almost close near to zero applied field with almost no magnetization ($M \sim 0$), indicating an essentially non-magnetic ground state with the level-crossing from ground state to first excited state at around $H = 0.5$ T, best seen in the derivative of the magnetization curve in Figure 6-12, bottom. The steps in the hysteresis probably result from the sequential flipping of Dy moments; three spins have to be reversed on going between the toroidal state and the final paramagnetic state. The steep rise of magnetization at around 0.5 T is a strong indication of a level-crossing of the toroidal ground state to the paramagnetic state.^[19] This is also seen in the derivatives of the curves (Figure 6-12, bottom). These measurements confirm the toroidal ground state in $[\text{Dy}_6(\text{NO}_3)_6(\text{teaH})_6] \cdot 2\text{C}_2\text{H}_5\text{OH}$ (**23**). However, the field required for the toroidal moment crossover at ~ 0.65 T^[16] from *ab initio* calculations in the literature for **Dy6-1**, is different to the experimental one of ~ 0.5 T.

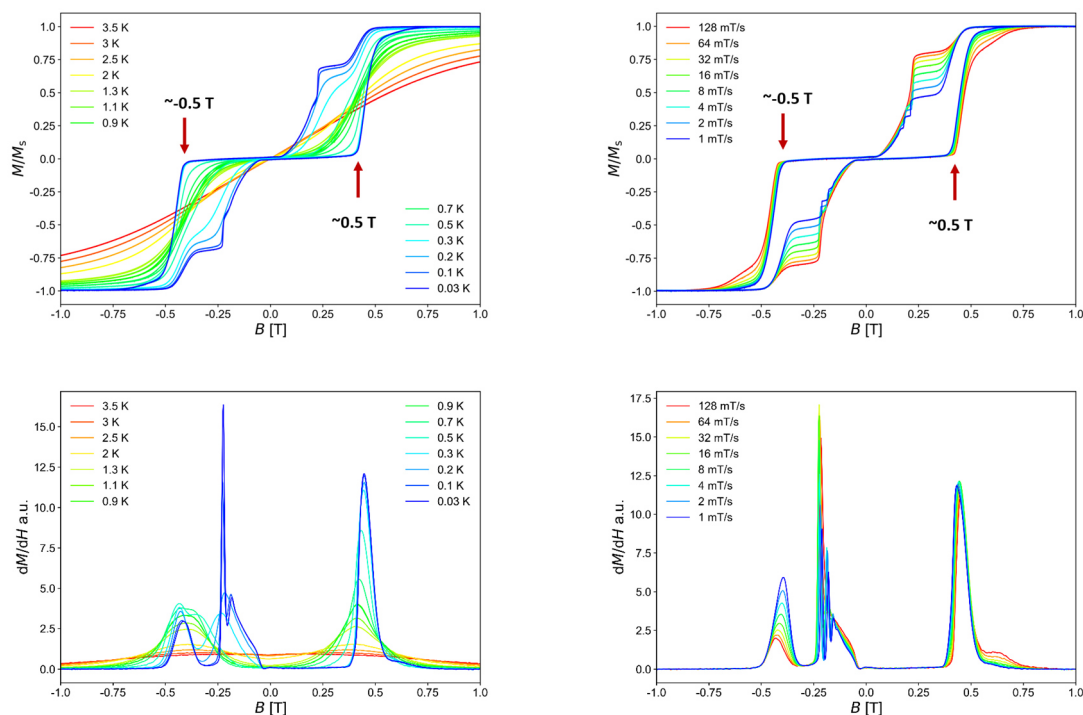


Figure 6-12 Single crystal micro-SQUID measurements of $[\text{Dy}_6(\text{NO}_3)_6(\text{teaH})_6] \cdot 2\text{C}_2\text{H}_5\text{OH}$ (**23**) (top) and the first derivatives of the magnetization (bottom).

6.2 Properties of [Dy₆(apadH₂)₆(NO₃)₆] (**24**)

The {Dy₆} system [Dy₆(apadH₂)₆(NO₃)₆].2THF (**Dy6-3**), was also reproduced in this thesis to perform micro-SQUID measurements. A solution of Dy(III)-nitrate in acetonitrile was overlaid with a methanolic solution of apadH₄ and trimethylamine. A MeOH:MeCN (1:1) layer was added between the different solutions to hinder fast diffusion. This led to the formation of colourless crystals with the formula [Dy₆(apadH₂)₆(NO₃)₆] (**24**) after one week. The only difference to the structure in (**23**) is the exchange of the protonated alcohol arm by a propylamine arm. The asymmetric unit contains one crystallographically independent Dy(III) ion, one nitrate and one doubly deprotonated apadH₂²⁻ ligand. Similarly to [Dy₆(NO₃)₆(teaH)₆] (**23**), the wheel is stabilised by six doubly deprotonated organic ligands with the binding mode $\eta^2:\eta^1:\eta^1:\eta^2:\mu_3$ and six bidentate nitrates. The organic ligands each bridge to the neighbouring Dy(III) ions via two μ_2 bridging oxygen arms. The aminopropyl arm coordinates to the Dy(III) ion.

The molecular structure of (**24**) with selected distances and angles are shown in Figure 6-13. The differences between (**24**) and the literature known **Dy6-3** regarding the cell parameters are negligible (Table 6-2). The Dy··Dy distances are slightly lower in (**24**) than in **Dy6-3** but the Dy-O distances are similar.

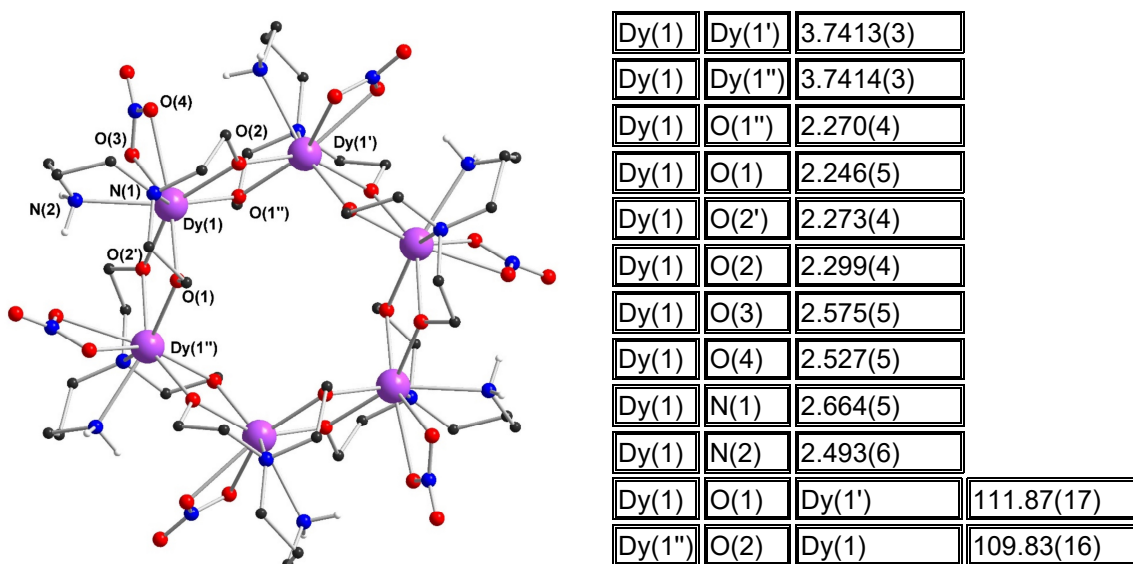
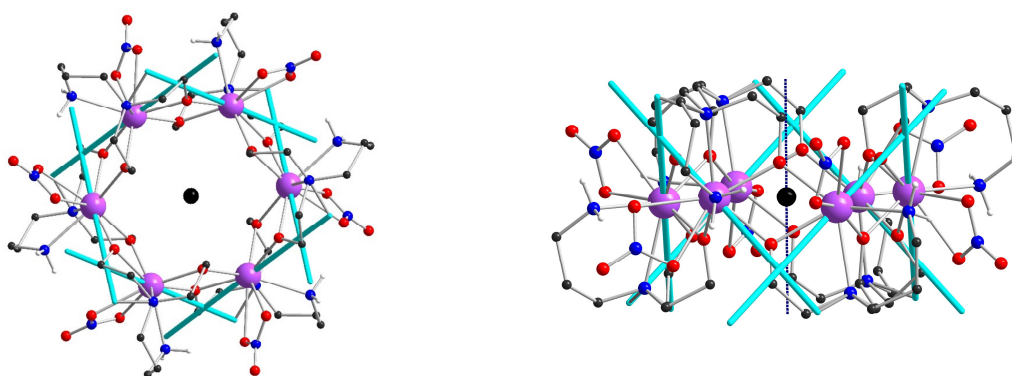


Figure 6-13 Molecular structure of (**23**) with selected distances [Å] and angles [°]. Primed atoms at $-1/3+y, 1/3-x+y, 4/3-z$; double-primed atoms at $2/3+x-y, 1/3+x, 4/3-z$.

Table 6-2 Comparison of (**24**) and **Dy6-3**.

	[Dy ₆ (apadH ₂) ₆ (NO ₃) ₆] (24) measured at 150 K	[Dy ₆ (apadH ₂) ₆ (NO ₃) ₆]·2THF (Dy6-3) ^[83] measured at 200 K
Space group	R-3	R-3
Z	3	3
α [°]	90	90
β [°]	90	90
γ [°]	120	120
a [Å]	15.7449(3)	15.7780(10)
b [Å]	15.7449(3)	15.7780(10)
c [Å]	26.0811(6)	26.4045(19)
V [Å ³]	5599.3(2)	5692.6(7)
Dy··Dy [Å]	3.7413(3)	3.7606(3)
Dy – O [Å], average	2.38	2.37

The angle θ , which defines the angle between the S_6 symmetry axis, and the anisotropy axes (calculated by MAGELLAN) are 47.3° in (**24**) (Figure 6-14) which is nearly the same value for the isostructural complex **Dy6-3** (47.6°). The Dy(III) ions are crystallographically identical and eight-coordinate with a O₆N₂ donor set and can be best described as triangular dodecahedron (TTD) with deviation from this perfect geometry of 2.795 % in (**24**) (Figure 6-15, left) and with a similar deviation of 2.862 % in **Dy6-3** (Figure 6-15, middle). The binding scheme of the ligand, which is identical in both complexes, is shown in Figure 6-15, right.



$$\theta = 47.3^\circ$$

Figure 6-14 Anisotropy axes of [Dy₆(NO₃)₆(teaH)₆]·2C₂H₅OH (**23**) calculated with MAGELLAN. The dot in the middle of the molecule and the dotted line both indicate the S_6 symmetry axis.

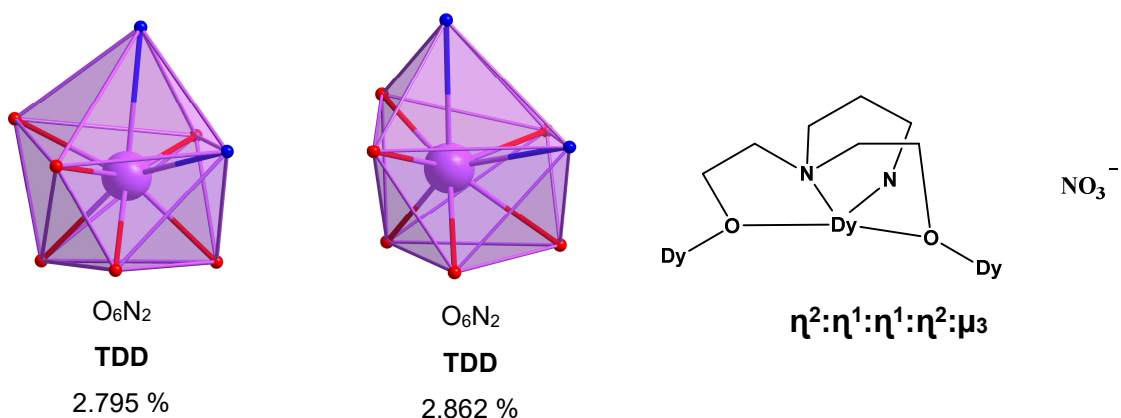


Figure 6-15 Coordination spheres around the Dy(III) ions in **(24)** (left) and in **Dy6-1** (middle) with the deviations from the perfect geometry. The ligand and the ligand scheme (right) are the same in both structures.

Single crystal micro-SQUID measurements on $[Dy_6(apadH_2)_6(NO_3)_6]$ (**24**) were carried out for temperatures from 30 mK to 3.5 K under a constant sweep rate of 64 mT/s (Figure 6-16, top left). The same crystal was measured at 30 mK in the field sweep range from 1 to 128 mT/s (Figure 6-16, top right). Hysteresis loops are observed for temperatures up to 0.9 K, indicating slow relaxation of magnetization on a molecular level. The coercivity increases with higher sweep rates and lower temperatures, as expected.^[97] Similarly to **(23)**, the hysteresis loops almost close at zero applied field. The level-crossing from the ground to the first excited state is at $H = 0.5 T$ as seen in the derivative of the magnetization at 30 mK (Figure 6-16, bottom). This value is higher than the level-crossing at $H = 0.325 T$, found from the derivative of the magnetization in the literature.^[83] This is due to the fact that in bulk magnetization measurements, the crystals are randomly distributed. Micro-SQUID measurements are performed using a single crystal orientated in the direction of the easy axis of the magnetization, which leads to different results compared to bulk magnetizations.

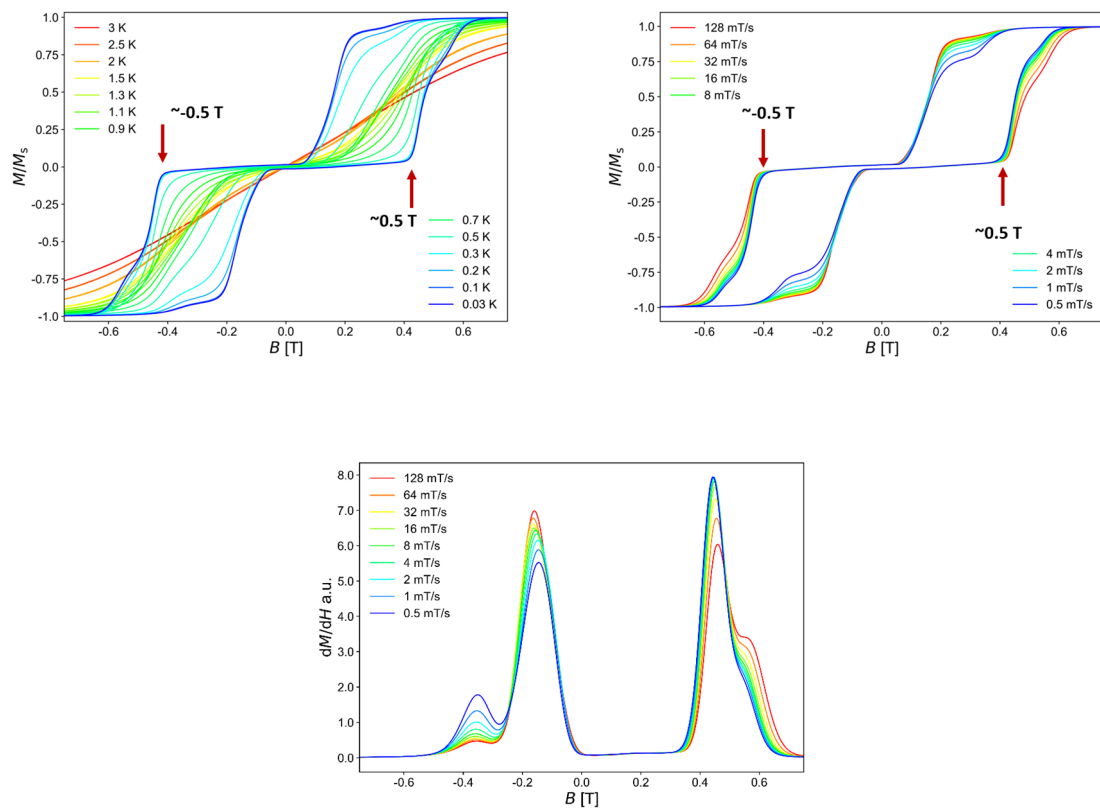


Figure 6-16 Single crystal micro-SQUID measurements of $[\text{Dy}_6(\text{apadH}_2)_6(\text{NO}_3)_6]$ (**24**) (top) and the derivative of the magnetization (bottom).

6.3 Properties of $[\text{Dy}_6(\text{NO}_3)_3(\text{pmide})_6]$ (**Dy6-4**)

Another $\{\text{Dy}_6\}$ ring synthesized in the Powell group, but not reported in the literature yet,^[98] has the formula $[\text{Dy}_6(\text{NO}_3)_3(\text{pmide})_6]$ (**Dy6-4**) with the ligand $\text{H}_2\text{pmide} = N$ -(2-pyridylmethyl)diethanolamine. The micro-SQUID data of this complex can be directly compared with the structurally very similar systems (**23**) and (**24**).

The system crystallizes in the monoclinic space group $P2_1/n$. The asymmetric unit contains half a cluster molecule, with three Dy(III) ions, three nitrates and three double deprotonated pmide²⁻ ligands. The only difference to the structure in (**23**) is the exchange of the protonated alcohol arm by a picolyl arm.

Each Dy(III) ion is coordinated by one doubly protonated ligand and one bidentate nitrate. Similarly to $[\text{Dy}_6(\text{NO}_3)_6(\text{teaH})_6]$ (**23**) and $[\text{Dy}_6(\text{apadH}_2)_6(\text{NO}_3)_6]$ (**24**), the wheel is stabilised by six doubly deprotonated organic ligands with the binding mode $\eta^2:\eta^1:\eta^1:\eta^2:\mu_3$ and six chelating nitrates. The organic ligands each bridge to the neighbouring Dy(III) ions via two μ_2 bridging oxygen arms. The pyridine is coordinated to the Dy(III) ions with its nitrogen. The molecular structure of **Dy6-4** is shown in Figure 6-17 and selected distances and angles are given in Table 6-3.

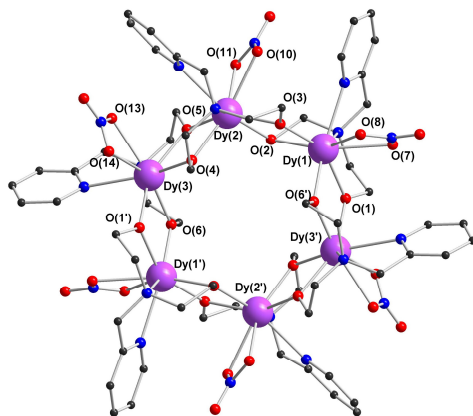


Figure 6-17 Molecular structure of **Dy6-4**. Primed atoms at 1-x, 1-y, 1-z.

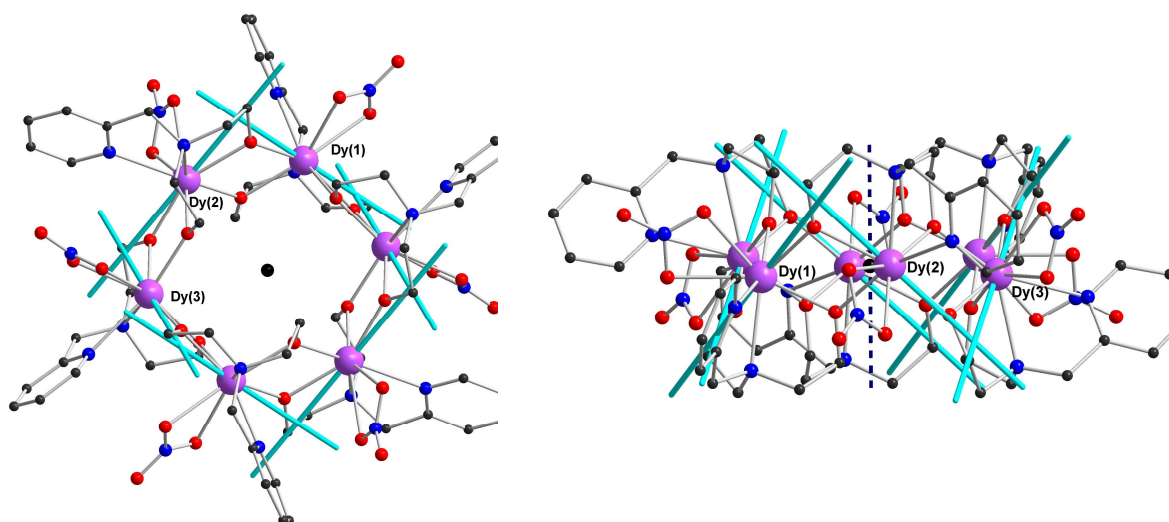
Table 6-3 Selected distances [Å] and angles [°] of **Dy6-4**.

Dy(1)	Dy(2)	3.7635(9)
Dy(1)	Dy(3')	3.7477(8)
Dy(2)	Dy(3)	3.7525(9)
Dy(1)	O(1)	2.279(6)
Dy(1)	O(2)	2.255(7)
Dy(1)	O(3)	2.275(7)
Dy(1)	O(6')	2.269(7)
Dy(1)	O(7)	2.557(9)
Dy(1)	O(8)	2.495(8)
Dy(2)	O(2)	2.271(7)
Dy(2)	O(3)	2.317(6)
Dy(2)	O(4)	2.265(6)
Dy(2)	O(5)	2.274(6)
Dy(2)	O(10)	2.557(8)
Dy(2)	O(11)	2.457(7)
Dy(3)	O(1')	2.286(6)
Dy(3)	O(4)	2.268(6)
Dy(3)	O(5)	2.307(6)
Dy(3)	O(6)	2.268(6)
Dy(3)	O(13)	2.502(7)
Dy(3)	O(14)	2.482(8)
Dy(1)	N(1)	2.595(8)
Dy(1)	N(2)	2.580(9)
Dy(2)	N(3)	2.605(8)
Dy(2)	N(4)	2.593(8)
Dy(3)	N(5)	2.598(8)
Dy(3)	N(6)	2.598(9)

Dy(1)	O(3)	Dy(2)	110.1(3)
Dy(2)	O(4)	Dy(3)	111.7(2)
Dy(2)	O(5)	Dy(3)	110.0(2)
Dy(3)	O(6)	Dy(1')	111.4(3)

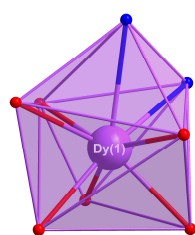
The anisotropy axes, calculated by MAGELLAN, are shown in Figure 6-18. The angles θ have values of 48.4° for Dy(1), 47.5° for Dy(2) and 49.3° for Dy(3).

The Dy(III) ions are all eight-coordinate with a O₆N₂ donor set best described as triangular dodecahedron (TTD) with deviations from this perfect geometry of 3.583, 3.901 and 3.750 % (Figure 6-19).

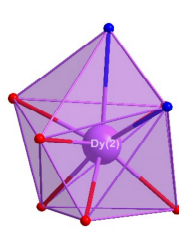


$$\theta = 48.4^\circ \text{ (for Dy(1))} \quad \theta = 47.5^\circ \text{ (for Dy(2))} \quad \theta = 49.3^\circ \text{ (for Dy(1))}$$

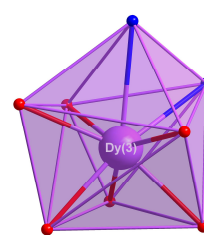
Figure 6-18 Anisotropy axes of $[\text{Dy}_6(\text{NO}_3)_6(\text{teaH})_6] \cdot 2\text{C}_2\text{H}_5\text{OH}$ (**23**) calculated with MAGELLAN. The dot in the middle of the molecule and the dotted line both indicate the pseudo S_6 symmetry axis.



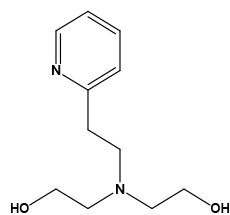
O₆N₂
TDD-8
3.583 %



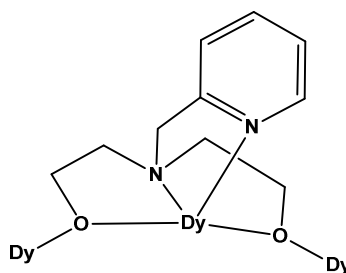
O₆N₂
TDD-8
3.901 %



O₆N₂
TDD-8
3.750 %



H₂pmide



$\eta^1:\eta^1:\eta^1:\eta^2:\mu_3$



Figure 6-19 Coordination spheres around the Dy(III) ions in **Dy6-4** (top) with the deviations from the perfect geometry. The ligand and the ligand scheme are illustrated at the bottom.

The micro-SQUID measurements on a single crystal were made at 30 mK under different sweep rates (Figure 6-20, top left) and at different temperatures under a constant sweep rate of 64 mT/s (Figure 6-20, top right). Stepped hysteresis loops are observed up to 0.5 K. The coercivity increases with higher sweep rates and lower temperatures as expected.^[97] The upper and lower curve of the hysteresis get closer

together to almost zero magnetization but the gap between them is clearly higher than the gap in (23) and (24). The level-crossing from the ground to the first excited state is at $H = 0.4$ T, best seen in the derivatives of the curves (Figure 6-20, bottom). The extra small steps in the hysteresis loops are a result of the three crystallographically-distinct Dy centres in the crystal structure.

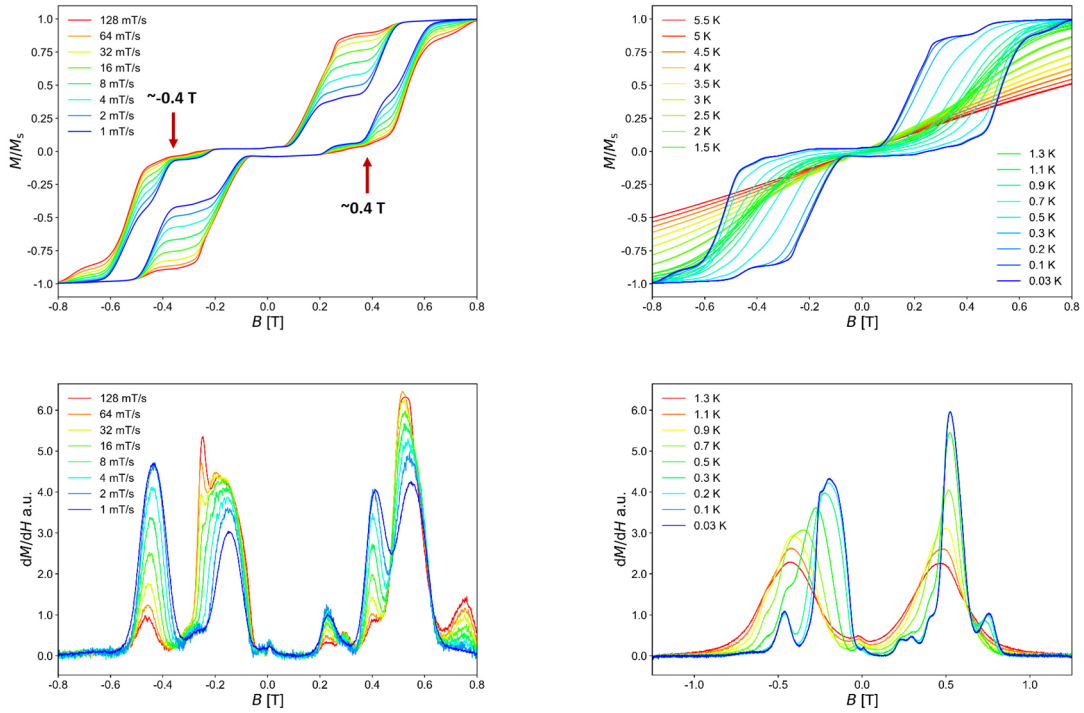


Figure 6-20 Single crystal micro-SQUID measurements of $[\text{Dy}_6(\text{NO}_3)_3(\text{pmide})_6]$ (**Dy6-4**) (top) and the derivatives of the magnetization (bottom).

6.4 Summary of hexanuclear Dy₆ systems

In this chapter, six {Dy₆} wheel complexes, which have an isostructural core, are described and investigated with regard to their toroidal moment. These are [Dy₆(teaH)₆(NO₃)₆]·8MeOH (**Dy6-1**), [Dy₆(Me-teaH)₆(NO₃)₆]·6MeCN (**Dy6-2**), [Dy₆(apadH₂)₆(NO₃)₆]·2THF (**Dy6-3**) known from the literature, [Dy₆(NO₃)₆(teaH)₆]·2C₂H₅OH (**23**) and [Dy₆(apadH₂)₆(NO₃)₆] (**24**) synthesized in this work and the complex [Dy₆(NO₃)₃(pmide)₆] (**Dy6-4**) synthesized earlier in this group but not reported yet. The complexes are compared with each other, whereas either *ab initio* calculations (**Dy6-1**) or magnetization data with the first derivative (**Dy6-2** and **Dy6-3**) are available from the literature. The complexes ((**23**) and (**24**)) synthesized in this work and in earlier work in the group (**Dy6-4**), were investigated with micro-SQUID measurements for level-crossing between them. The summary is given in Table 6-4.

In **Dy6-3**, the longest Dy··Dy distances of 3.7606(3) are observed and the system also shows the smallest value of *H* where the level-crossing from ground to the first excited state occurs (*H* = 0.33 T), as determined from the maximum of the first derivative of bulk magnetization measurements. It turns out, that the systems (**23**), (**24**) and **Dy6-4**, show hysteresis up to temperatures of 0.3, 0.5 and 0.9 K, respectively. In comparison to [Dy₆(apadH₂)₆(NO₃)₆] (**24**) the system [Dy₆(NO₃)₆(teaH)₆]·2C₂H₅OH (**23**) shows many small steps in the hysteresis curves. The steps in [Dy₆(NO₃)₃(pmide)₆] (**Dy6-4**) are spread out and this is typically the result of significant distribution of molecular environments due to disorder in the ligands and/or solvent molecules and/or the presence of a high number of low-lying excited states.^[101]

The anisotropy axes of **Dy6-1**, calculated using MAGELLAN, are in good agreement for those found from *ab initio* calculations. Furthermore, the results for MAGELLAN for the other {Dy₆} systems show similar orientations in line with their toroidal behaviour established from magnetization measurements. The minimum reversal energies do not lead to a correlation between SMT or SMM behaviour and ranges from 282.6 to 738 cm⁻¹ in the discussed complexes.

The Dy-N and Dy-O bond lengths, as well as the Dy-O-Dy angles of the compounds are similar and no correlation to the toroidicity can be developed from this. The

coordination spheres around the Dy(III) ions with O₇N compared to O₆N₂ donor sets, seem to have an influence on the SMM behaviour and increase with mixed species in the coordination spheres (observable hysteresis up to 0.5 K for **(24)** and up to 0.9 K for **Dy6-4** compared to 0.3 K for **(23)**).

Table 6-4 Comparison of the Dy₆ systems. The systems with the same colour are isostructural.

complex	Dy ₆ (teaH) ₆ (Dy6-1) ^[82]	Dy ₆ (teaH) ₆ (23)	Dy ₆ (Me- teaH) ₆ (Dy6-2) ^[83]	Dy ₆ (apadH ₂) ₆ (Dy6-3) ^[83]	Dy ₆ (apadH ₂) ₆ (24)	[Dy ₆ (NO ₃) ₃ (pmide) ₆] (Dy6-4) ^[98]
space group	R-3	R-3	R-3	R-3	R-3	P2 ₁ /n
Dy··Dy [Å]	3.7297(17)	3.7361(4)	3.7271(4)	3.7606(3)	3.7413(3) 3.7414(3)	3.7477(8) 3.7525(9) 3.7635(9)
Dy-N [Å]	2.582(4)	2.621(8)	2.586(2)	2.692(3), 2.507(4)	2.493(6), 2.664(5)	2.580(9)- 2.598(9)
Dy-O [Å]	2.242(4)- 2.534(3)	2.257(6)- 2.570(7)	2.2478(17)- 2.5313(18)	2.260(3)- 2.583(3)	2.270(4)- 2.575(5)	2.255(7)- 2.557(9)
Dy-O-Dy [°]	108.36(9)- 111.78(10)	109.8(2) 110.9(2)	107.96(7)- 111.50(7)	109.73(11), 111.91(11)	109.83(16)- 111.87(17)	110.0(2)- 111.7(2)
Toroidicity <i>H</i> =	0.65 (<i>ab initio</i>) ^[16]	0.50 (Micro-SQUID)	0.42 (peak in <i>dM vs dH</i>)	0.33 (peak in <i>dM vs dH</i>)	0.50 (Micro-SQUID)	0.40 (Micro-SQUID)
Donor sets	O ₇ N	O ₇ N	O ₇ N	O ₆ N ₂	O ₆ N ₂	O ₆ N ₂ O ₆ N ₂ O ₆ N ₂
SMM behaviour/ Hysteresis	SMM for T < 2 K ^[82]	Hysteresis up to 0.3 K (Micro-SQUID)	none ^[83]	SMM for T < 3 K ^[83]	Hysteresis up to 0.9 K (Micro-SQUID)	Hysteresis up to 0.5 K (Micro-SQUID)
Angle Θ (MAGELLAN)	35.2°	46.9°	37.3°	47.6°	47.3°	48.4° 47.5° 49.3°
Minimum Reversal Energy (MRE)	317.1 cm ³	400.6 cm ³	334.7 cm ³	289.5 cm ³	282.6 cm ³	738.3 cm ³ 543.0 cm ³ 330.0 cm ³

7 Overall summary and conclusion

In this thesis, a search for systems showing molecular-based slow relaxation of magnetization and magnetic toroidicity was conducted. Single Molecule Magnets (SMMs) are known for decades but the field of Single Molecule Toroids (SMTs) is relatively new, having been first described in 2006.^[6] Many new SMTs have since been added to the database, mostly dysprosium-based systems. These molecules have great potential to create ultra-dense energy storage devices, and because their ground state is well protected from small external magnetic fields, they are considered as the optimal building blocks for quantum computers.

The tools used in this thesis, to detect a vortex-like arrangement of the anisotropy axes and the spins, respectively, were MAGELLAN (an electrostatic model to determine the orientation of the anisotropy axes for the $m_j = \pm 15/2$ state of Dy(III) ions), and *ab initio* calculations (from co-workers). Experimentally, magnetic susceptibility measurements (direct current DC and alternating current AC), bulk magnetization measurements and single crystal measurements with the micro-SQUID technique were used for either detecting a non-magnetic ground state (DC measurements: $\chi T \rightarrow 0$) or possible SMM behaviour (AC measurements on bulk materials, hysteresis on single crystal measurements). Furthermore, through the first derivative of the magnetization (dM/dH for bulk magnetization and/or single crystal measurements) the level-crossing from the possible toroidal (non-magnetic) ground state to the first excited state can be identified. Several SMTs could be identified and using these theoretical and/or experimental methods.

In Chapter 3, it was shown that results calculated using MAGELLAN agree well with the results of the *ab initio* calculations on triangular $\{\text{Dy}_3\}$ molecules, giving the orientations of the anisotropy axes and allowing the identification of possible toroidal spin arrangements.

Two similar $\{\text{Dy}_3\}$ triangular systems were synthesized, $[\text{Dy}_3(\text{L})_3(\mu_3\text{-OH})_2(\text{H}_2\text{O})_4\text{Cl}_2]\text{Cl}_2$ (**1**) and $[\text{Dy}_3(\text{L})_3(\mu_3\text{-OH})_2(\text{H}_2\text{O})_2(\text{CH}_3\text{OH})\text{Cl}_3]\text{Cl}$ (**2**) with HL = 3-ethoxysalicylaldehyde. The DC measurements revealed antiferromagnetic interactions between the Dy(III) centres, such as other Dy_3 triangles in the literature^[6,8,99] and almost non-magnetic ground states in both systems with χT products of 6.61 and 1.58 cm³ mol⁻¹ K, respectively. Both systems show SMM behaviour under an applied DC field of 0.5 T

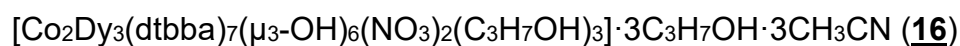
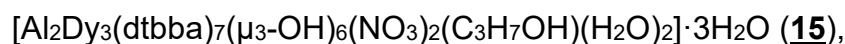
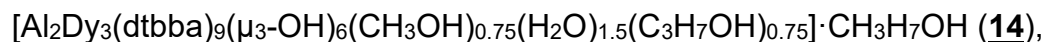
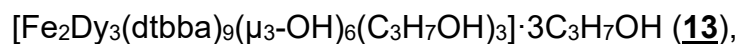
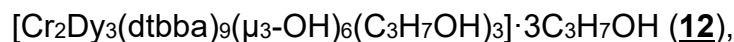
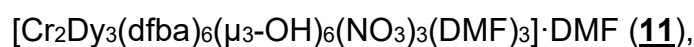
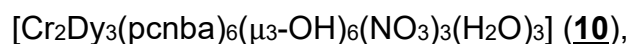
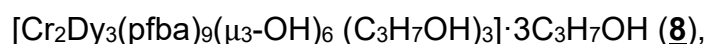
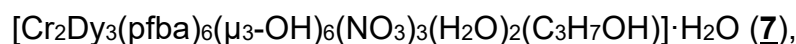
and the level-crossing from the ground toroidal state to the first excited state occurs at values of $H = 0.90$ T determined by bulk magnetization measurements for both systems. Furthermore, the values of 0.73 and 0.80 T were determined by micro-SQUID measurements on a single crystal of **(1)** and indicate individual spin flips. In comparison of two similar Dy₃ triangles from the literature, [Dy₃(μ₃-OH)₂L₃Cl₂(H₂O)₄][Dy₃(μ₃-OH)₂L₃Cl(H₂O)₅]Cl₅·19 H₂O (**Dy3-1**) and [Dy₃(μ₃-OH)₂L₃Cl(H₂O)₅]Cl₃·4 H₂O·2 MeOH·0.7 MeCN (**Dy3-2**), where the ligand only differs in one CH₂-group compared to the systems **(1)** and **(2)**, the level-crossing from the ground toroidal states to the first excited states occur at slightly higher values of $H = 0.95$ T and SMM behaviour can already be observed in zero applied DC field. In these systems the Dy··Dy distances are observed to be shorter than in **(1)** and **(2)**, which might lead to stronger dipolar-dipolar interactions (interactions through space between two dipoles) between the Dy(III) centres. For the isostructural compounds of **(2)** with the lanthanides europium **(3)**, terbium **(4)**, holmium **(5)** and erbium **(6)** instead of dysprosium, the *ab initio* calculations did not suggest a vortex-like toroidal arrangement of the anisotropy axes. Exchanging Dy(III) for other lanthanides within an isostructural system thus suppresses the toroidicity, as a result of the different single-ion electronic properties of the other lanthanides.

Even slight changes in the ligand environment can have a significant effect on the toroidicity and on the SMM behaviour in a system of {Dy₃} -triangles. It is however not possible to say with certainty whether the different environment of the Dy(III) ions (mainly mixed donor sets of O₇Cl and O₈) or the additional CH₂ group at the ligand leads to the different magnetic properties.

In conclusion, these systems remain highly interesting in terms of their sensitivity to synthesis, toroidicity and SMM behaviour. In Single-Ion dysprosium systems, strong axuality can be enforced by designing very specific idealized coordination geometries using ligands with specific soft and hard donor atoms.^[36,100] This seems to apply also in the discussed {Dy₃} systems. The rather hard donor oxygens from the phenoxides in the plane, compared to the fairly soft axial ligands, water and chloride, play a leading role in the orientation of the anisotropy axes. This allows for example a triangular system to arrange the easy axes such that they attend to lie in the plane in a toroidal arrangement. This finding is consistent with the recently published triangular [Dy₃(μ₃-CO₃)(Clbbpen)₃](CF₃SO₃)·6MeCN with a O₄N₄ donor set complex,

where hard donor atoms such as oxygens in the axial positions compared to soft donor atoms such as nitrogens in the equatorial positions are the dominant factors for the position of the anisotropy axes and leading to a spin-frustrated triangle rather than to a toroidal arrangement of the spins.^[99]

In Chapter 4, additional two ions from the same heterometal – either diamagnetic (Al(III)) or paramagnetic (Cr(III), Fe(III), Co(III)) – were introduced into the system of isostructural cores, forming a trigonal bipyramid with a dysprosium triangle defining the trigonal plane and apical metal ions providing the caps. This resulted in two series: **series-1** and **series-2**. The used ligands are benzoic acid derivatives such as 4-fluorobenzoic acid (pfbaH), 4-chlorobenzoic acid (pclbaH), 4-cyanobenzoic acid (pcnbaH), 3,5-difluorobenzoic acid (dfbaH) and 3,5-ditertbutylbenzoic acid (dtbbaH). The resulting {M₂Dy₃} complexes with M = Cr, Fe, Al or Co, are listed below:



with (7), (9) and (15), showing SMM behaviour in the measurement window of 1-1500 Hz. **Series-1** contains the same {Cr₂Dy₃} core, but different benzoic acid derivatives ((7) to (12)). **Series-2** contains the same ligand (dtbbaH) but different heterometal(III) ions ((12) to (16)).

The slightly changes of electronegativity in the ligand sphere, may sufficiently control the asphericity of the 4f shell of lanthanide ions and their shape anisotropy and thus the interaction between lanthanides and other magnetic centres and result in different magnetic properties, as shown, for example, in Fe₂Dy₂ complexes with differently substituted benzoate ligands.^[101]

The chromium-containing complexes (7), (8), (9), (10), (11) and (12) (**series-1**) show dominant ferromagnetic interactions, which increase with the increase of the Cr···Cr

distances. In similar $\{\text{Cr}_2\text{Dy}_3\}$ complexes compounds in the literature, where diamagnetic substitution giving the isostructural $\{\text{Al}_2\text{Dy}_3\}$ and $\{\text{Cr}_2\text{Y}_3\}$ compounds proved experimentally the ferromagnetic interactions between the Dy(III) and Cr(III) ions, and the weaker antiferromagnetic interactions between the Cr(III) ions.^[90] This might be also the case in the synthesized $\{\text{Cr}_2\text{Dy}_3\}$ complexes. Only a few examples of $\{\text{Cr}_2\text{Dy}_3\}$ complexes with a similar bipyramidal shape exist in the literature.^[90,102]

In the complexes (**13**), (**14**) and (**15**), where the Cr(III) is exchanged by either Fe(III) in (**13**) or by Al(III) in (**14**) and (**15**), antiferromagnetic interactions were observed within the molecules. This is expected for the Al-containing samples (**14**) and (**15**), because of the diamagnetic nature of the Al(III) ion, and was also observed for the $\{\text{Al}_2\text{Dy}_3\}$ compound in the literature.^[90] The dominant antiferromagnetic interactions in (**13**) are highly interesting and only one similar $\{\text{Fe}_2\text{Dy}_3\}$ complex is known to date in the literature from 2015, performing also antiferromagnetic interactions between the spin carriers.^[103]

The amount of the sample for the $\{\text{Co}_2\text{Dy}_3\}$ complex (**16**) was too small to allow any investigation of its magnetic properties. Also here, there is to date only one example of a $\{\text{Co}_2\text{Dy}_3\}$ complex, reported recently in 2020.^[104] The M-M distances in **series-2** decrease in the following order Fe-Fe > Cr-Cr > Al-Al > Co-Co.

In conclusion, the incorporation of heterometal(III) ions above and below the Dy_3 plane seems to suppress the toroidal moment. The ferromagnetic interactions in the $\{\text{Cr}_2\text{Dy}_3\}$ compounds increase with increasing Cr-Cr distances. The exchange of the heterometal(III) ions led to different M-M distances and angles within the molecule and the systems can be switched from ferromagnetic interactions in $\{\text{Cr}_2\text{Dy}_3\}$ complexes to antiferromagnetic interactions in $\{\text{Fe}_2\text{Dy}_3\}$ and $\{\text{Al}_2\text{Dy}_3\}$ complexes. MAGELLAN calculations suggested vortex-like arrangements of the anisotropy axes in $[\text{Cr}_2\text{Dy}_3(\text{pfba})_9]$ (**8**), $[\text{Cr}_2\text{Dy}_3(\text{pclba})_9]$ (**9**), $[\text{Cr}_2\text{Dy}_3(\text{dtbba})_9]$ (**12**), $[\text{Fe}_2\text{Dy}_3(\text{dtbba})_9]$ (**13**) and $[\text{Al}_2\text{Dy}_3(\text{dtbba})_9]$ (**14**), but no evidence for a toroidal ground state was found experimentally *via* bulk magnetization measurements. The ferromagnetic interactions for **series-1**, together with the non-existent or not experimentally determined toroidal ground states, also for (**13**) and (**14**) with antiferromagnetic interactions, leads to the conclusion that the results for the anisotropy axes with MAGELLAN calculations, at least with an additional paramagnetic metal besides dysprosium, should be treated

with caution. Also, the individual Dy(III) ions often do not possess a pure $m_J = 15/2$ ground state, which is a requirement for MAGELLAN.^[77]

However, the absence of an S-shaped curve in the M vs H plot is not an indication that no toroidal ground state exists. The formation of an S-shaped curve depends on the width of the gap that exists between the ground state and the first excited state. If the gap is too small, no S-shaped curve can be observed.^[12] In order to gain more insight into the $\{M_2Dy_3\}$ systems discussed, *ab initio* calculations will be indispensable. It may be that the energy difference between the two possible orientations of the Dy spins (either in the Dy_3 plane and tangential to the triangle, or perpendicular to the Dy_3 plane) is rather small for the $\{M_2Dy_3\}$ systems in Chapter 4, and that any errors resulting from the simplified electrostatic model used by MAGELLAN are then sufficient for this program to make the wrong choice in this case.

The original goal, to synthesize two $\{Dy_3\}$ triangles sandwiching one heterometal ion, forming a heptanuclear core, e.g. $\{CrDy_6\}$, was not achieved.^[20,68] However, several new complexes with the pentanuclear cores $\{M_2Dy_3\}$, in which a Dy_3 triangle is sandwiched by two heterometal ions, could be obtained, and such complexes are rare in the literature. Also, it was possible to switch from an antiferromagnetic to a ferromagnetic system on changing $M = Fe$ to $M = Cr$. Furthermore, the $M = Al$ systems made it possible to look at the bulk magnetic behaviour for the central $\{Dy_3\}$ triangle only.

In Chapter 5, a total of six isostructural $\{Ln_4\}$ complexes ($Ln = Tb, Dy, Ho, Er, Yb, Y$) were synthesized. The dysprosium compound and its magnetization properties, including the first derivative of the M vs H plot, was compared with five other $\{Dy_4\}$ complexes from the literature. Of these six $\{Dy_4\}$ complexes, four showed an S-shaped curve in the M vs H plot, which is indicative of a level-crossing between the ground state and the first excited state. The first derivative of the magnetization was used to establish the turning point of the S-shaped curve, giving an indication of the applied field necessary for the level-crossing from a non-magnetic, possible toroidal, ground state to the first excited state.

From the observations it can be concluded that the number of μ_2-O^- bridging atoms has a direct effect on the distances between the Dy(III) ions. If the number of μ_2-O^- bridging atoms increases, the distance between the Dy(III) ions decreases. The hard

negatively charged bridges are generally close to the Dy₄ plane, which favours a toroidal moment/non-magnetic ground state. This might lead to stronger interactions between the Dy(III) ions and seems to favour the formation of a toroidal moment/non-magnetic ground state. This is best seen in the first derivative of the magnetization for Dy₄(μ₃-OH)₂(NO₃)₂(DMF)₂(ehimp)₄ (**18**), [Dy₄(μ₃-OH)₂(hmmpH)₂(hmmp)₂(Cl)₄] (**Dy4-2**)^[92] and [Dy₄(μ₃-OH)₂(hmmpH)₂(hmmp)₂(N₃)₄] (**Dy4-3**)^[92] with values for level-crossing of 0.2, 0.45 and 0.35 T, respectively. Here, the replacement of the terminal chlorides (**Dy4-2**) by azides (**Dy4-3**) seems to reduce the toroidicity. However, this improves the slow relaxation of magnetization.^[92] A system with a strong toroidal ground state needs a strong applied field to overcome the vortex-like arrangement of the magnetic moments, otherwise it would stay in its non-magnetic ground state and show no SMM behaviour. The terminal ligands in (**18**) are negatively charged nitrates and neutral DMF molecules. In addition to the toroidal moment, slow relaxation of magnetization can be observed for temperatures up to 13 K. Micro-SQUID measurements indicate level crossings and spin flipping, respectively, at 0.17 T and 0.33 T, where the value 0.17 T is close to the value 0.2 T for toroidicity determined from the derivative of the magnetization at 2 K. [Dy₄(μ₃-OH)₂(o-van)₄(piv)₄(NO₃)₂] (**Dy4-5**)^[94] has a smaller number of μ₂-O⁻ bridging units, but also has a level crossing at 0.4 T and show SMM behaviour. Compared to [Dy₄(μ₃-OH)₂(mdeaH)₂(piv)₈] (**Dy4-4**)^[93] and [Dy₄(μ₃-OH)₂(ampdH₄)₂(piv)₁₀] (**Dy4-6**)^[96], which both show no toroidal moment but SMM behaviour, the **Dy4-5** system has fewer bridging and no terminal pivalates, but does have terminal nitrates. It can be assumed, that negatively charged ligands, such as Cl⁻, N₃⁻ and NO₃⁻ are preferable to neutral ligands, such as DMF, when it comes to stabilizing a toroidal moment/non-magnetic ground state. Also, the use of Schiff base ligands (in (**18**), (**Dy4-2**), (**Dy4-3**) and (**18**)) and/or the use of *ortho*-vanillin (in (**Dy4-5**)) seems to be advantageous for synthesising a system with a toroidal moment/non-magnetic ground state.

The anisotropy axes in the {Dy₄} complexes in this chapter were examined by MAGELLAN calculations and, except for (**18**), did not suggested any vortex-like arrangements of the spins that might favour a toroidal arrangement. Nevertheless, in some of these complexes (**Dy4-2**, **Dy4-3**, **Dy4-5** and (**18**)), level crossing from the ground states to excited states could be observed experimentally by examination of

the magnetization measurements. In this case, the axes calculated by MAGELLAN should not be an exclusion criterion for finding a toroidal or non-magnetic ground state. Especially in the discussed $\{\text{Dy}_4\}$ complexes, the two body Dy(III) ions might have strong antiferromagnetic dipolar coupling across the middle “ring”, unlike the $\{\text{Dy}_3\}$ and $\{\text{Dy}_6\}$ systems and have the possibility of non-magnetic ground states, but not necessarily to a toroidal arrangement of the spins. In view of these results, it would be interesting to consider further systems already known in the literature and examine them for their possible toroidicity/non-magnetic ground state. There are many other $\{\text{Dy}_4\}$ compounds in the literature, similar to those already discussed.^[105-108]

The discussed $\{\text{Dy}_6\}$ wheel-like complexes in chapter 6 are listed below:

$[\text{Dy}_6(\text{teaH})_6(\text{NO}_3)_6] \cdot 8\text{MeOH}$ (**Dy6-1**),

$[\text{Dy}_6(\text{NO}_3)_6(\text{teaH})_6]$ (**23**),

$[\text{Dy}_6(\text{Me-teaH})_6(\text{NO}_3)_6] \cdot 6\text{MeCN}$ (**Dy6-2**),

$[\text{Dy}_6(\text{apadH}_2)_6(\text{NO}_3)_6] \cdot 2\text{THF}$ (**Dy6-3**),

$[\text{Dy}_6(\text{apadH}_2)_6(\text{NO}_3)_6]$ (**24**) and

$[\text{Dy}_6(\text{NO}_3)_3(\text{pmide})_6]$ (**Dy6-4**).

The compounds were investigated and compared for their toroidicity and the strength of the toroidal moment, which is defined as the value of the magnetic field H , where the level-crossing from the ground state to the first excited state occur. MAGELLAN calculations on these systems show similar anisotropy axes in all $\{\text{Dy}_6\}$ wheels but no vortex-like arrangement of the spins is observed. But due to their high symmetry, where the dipolar components cancel each other out exactly, in all complexes toroidal states with clear level-crossings to first excited states can be either seen by single crystal micro-SQUID measurements ($H = 0.5 \text{ T}$ for (**23**) and (**24**), $H = 0.4 \text{ T}$ for **Dy6-4**) or by bulk magnetization measurements and the first derivatives ($H = 0.42 \text{ T}$ for **Dy6-2** and $H = 0.33 \text{ T}$ for **Dy6-3**). There was no evidence of any influence from the different ligand environment for **Dy6-1** and **Dy6-2** on the hyperfine interactions (interactions between nuclei and electrons), experimentally explored using the ^{161}Dy nuclear forward scattering (NFS), time-domain synchrotron Mössbauer spectroscopy (SMS).^[108] Nevertheless, the toroidicity of the two isostructural systems were found to be different (0.65 T for **Dy6-1**, 0.42 for **Dy6-2**). The results have to be treated with caution because the value of 0.65 T for **Dy6-1** was estimated using *ab initio*

calculations and the value of 0.42 for **Dy6-2** from the first derivative of the bulk magnetization.

Because the toroidicity of the complexes (**Dy6-2**) and (**Dy6-3**) were investigated in the literature with bulk materials, using these bulk magnetization studies to quantify the field at which the ground state crosses to the first excited state should be compared with the results with the micro-SQUID measurements with some caution since the latter are performed on orientated crystals in a given direction. Also, mostly *ab initio* calculations are performed by assuming zero kelvin, which is for obvious reason not consistent to experimental situations – but close to that – can lead to different results in the value of H for the level-crossing from ground to first excited state using micro-SQUID techniques and *ab initio* calculations. The coordination spheres around the Dy(III) ions with O₇N (compared to O₆N₂ donor sets) seem to have an influence on the SMM behaviour and increase with mixed species in the coordination spheres (observable hysteresis up to 0.5 K for (**24**) and up to 0.9 K for **Dy6-4** compared to 0.3 K for (**23**)).

The number of systems under consideration is rather small. Although numerous homonuclear Dy₆ systems can be found in the literature^[109-111] and even bigger wheel systems, only containing Dy(III) as metal ions, reaching from eight^[112] over ten^[113] to even twelve^[114] metal ions, these examples here are the only hexanuclear {Dy₆} structures with a wheel-shaped form.

In conclusion, MAGELLAN is well suited for an initial prediction of the single-ion anisotropy axes for homonuclear dysprosium complexes within {Dy₃} -triangles (chapter 3), {Dy₆} -wheel complexes (chapter 6) and may also give a decent prediction for the positions of the anisotropy axes in {Dy₄} complexes (chapter 5). MAGELLAN is a good starting point to evaluate the positions of the anisotropy axes but has its limitations, especially for heteronuclear complexes (chapter 4), and the results should always be treated with caution. Also, it is required for MAGELLAN, that the Dy(III) ions possess a pure $m_J = 15/2$ state,^[77] which is often not given in the complexes considered.

It still remains a challenge to find SMTs and, more importantly, to characterize them, even with so many tools in hand such as MAGELLAN and *ab initio* calculations to determine the anisotropy axes, magnetic susceptibility measurements (DC) to detect

a possible non-magnetic ground state, bulk magnetization measurements and single crystal measurements (micro-SQUID) to examine the level-crossing from the ground to the first excited state experimentally. The comparison of several molecular systems, especially with regard to their toroidicity, should always be investigated with the same experimental measurement techniques with same parameter such as temperature and sweep rate and with the same theoretical approach in order to obtain comparable data.

In order to gain more insight into the discussed systems in regard of dipolar (through space interactions) and exchange interactions (through bond interactions) between the spin carriers and the energy gaps between the states, high-level *ab initio* calculations are indispensable where the fitting of experimental data is required.

8 Experimental section

8.1 General procedures

The coordination spheres and their deviations from the perfect geometries were calculated by the software SHAPE 2.1. Images of molecular structures were generated by the software Diamond 4.6.4.

FT-IR-spectroscopy. The infrared spectra were collected by a “Platinum Alpha ATR” from Bruker in a range from 400 cm^{-1} to 4000 cm^{-1} with a resolution of 1 cm^{-1} .

Elemental analysis. For the determination of the carbon-, hydrogen- and nitrogen proportion the CHNS-analysis device “Vario Micro Cube” from Perkin Elmer was used.

Powder diffraction measurements. Powder diffraction patterns were collected by a “Stoe STADI-P diffractometer” with a $\text{Cu-K}\alpha$ source with $\lambda = 1.5405 \text{ \AA}$ at room temperature. The files were processed using the software “WinXPOW” and the simulated Powder patterns were generated using Mercury 2020.1.

Single crystal x-ray diffraction measurements. The crystal structures were measured with different types of diffractometers: Agilent “SuperNova” (dual source: $\text{MoK}\alpha$, $\lambda = 0.71073$; $\text{CuK}\alpha$, $\lambda = 1.54184$; detector: EosS2 (detector type: CCD)). Stoe “StadiVari” (single source: $\text{MoK}\alpha$, $\lambda = 0.71073$; detector: Dectris Pilatus (300K) (detector type: CMOS). Stoe “StadiVari” (single source: $\text{GaK}\alpha$, $\lambda = 1.34143$; detector: Dectris Eiger2 R 4M (detector type: HPC).

The crystals were attached to the goniometer head with perfluoro ether oil. In order to determine the unit cell, first some frames were recorded at different angles of rotation.

Then a complete measurement based on the orientation matrix and the lattice constant was performed, the data integrated and corrected for Lorentz-polarisation and crystal absorption effects. The structure determination and refinement were performed using SHELXT and SHELXL, using the program OLEX2.^[115]

The data reduction was performed by the software supplied by the diffractometer manufacturers with R_{int} values defined as:

$$R_{int} = \frac{\sum |F_0^2 - F_0^2(mean)|}{\sum F_0^2}$$

where the summation involves all input reflections for which more than one symmetry equivalent is averaged. After the data reduction, the crystal structure is solved and refined using successive cycles of full-matrix least-squares Fourier refinement of the atomic parameters (coordinates and temperature factors) against F^2 using all data, minimising wR_2 with F_0 and F_c (observed and calculated structure factors for each reflection, and w as a weighting factor):

$$wR_2 = \sqrt{\frac{\sum [\omega(F_0^2 - F_c^2)^2]}{\sum [\omega(F_0^2)]}}$$

In general, ordered non-hydrogen atoms were refined with anisotropic temperature factors, and organic hydrogen atoms were placed in calculated positions. After the refinement, the GooF (goodness-of-fit) is calculated using all data, and R_1 is calculated using the data with $F_0 > 4\sigma(F_0)$:

$$GooF = \sqrt{\frac{\sum [\omega(F_0^2 - F_c^2)^2]}{(n - p)}}$$

SQUID measurements. The investigation of magnetic properties of a polycrystalline sample was carried out with either a MPMS SQUID VSM (Magnetization measurements) and a MPMS-XL5 (χT and AC measurements) or with a MPMS-XL7 (Magnetization, χT and AC measurements) from Quantum Design. The range from the temperature is 1.8 to 400 K (MPMS SQUID VSM) and 1.9 to 400 K (MPMS-XL5 and 7). The DC field has a range from -5 to 5 Tesla (MPMS-XL5) and -7 to 7 Tesla (VSM, MPMS-XL7). AC-susceptibility measurements were carried out under a frequency between 1-1500 Hz with an oscillating magnetic field of $3 \cdot 10^{-4}$ T for the MPMS-XL7 and $3.5 \cdot 10^{-4}$ T for the MPMS-XL5.

Micro-SQUID measurements. Single crystal measurements were carried out on a micro-SQUID from AK Wernsdorfer (KIT) for different temperatures and different sweep rates.

8.2 Synthesis

The following reactions were carried out under aerobic condition. Organic chemicals and solvents were obtained from commercial sources and used without further purification. Lanthanide salts were synthesized out of the oxides and the appropriate acid. Obtained crystals were measured via single crystal diffraction measurements.

(1) $[\text{Dy}_3(3\text{-ethoxysalicyl})_3(\mu_3\text{-OH})_2(\text{H}_2\text{O})_4\text{Cl}_2]\text{Cl}_2 \cdot 5\text{H}_2\text{O} \cdot 3\text{MeOH}$

453 mg (1.2 mmol, 1.0 eq.) $\text{DyCl}_3 \cdot 6\text{H}_2\text{O}$ and 166 mg, (1.0 mmol, 0.83 eq.) 3-ethoxysalicyl aldehyde were dissolved in a mixture of dichloromethane (10 mL) and methanol (10 mL). 139 μL (1.9 mmol, 0.83 eq.) triethylamine and 60 μL (1.0 mmol, 0.83 eq.) ethanolamine were added to the yellow solution. The solution was stirred at 70°C for 10 minutes, then filtered. Yellow crystals were obtained after two months of slow solvent evaporation. Yield: 330 mg (19 %, based on Dy). Elemental analysis for $\text{Dy}_3\text{C}_{30}\text{H}_{59}\text{O}_{23}\text{Cl}_4$: Calc%(found%) C/H/N: 25.43 (25.97), 4.20 (3.91), 0.00 (0.14). Selected IR peaks (cm^{-1}): $\tilde{\nu}$ = 453(m), 552(s), 640(s), 724(s), 781(w), 841(w), 886(m), 1028(m), 1093(m), 1173(m), 1215(s), 1299(s), 1453(s), 1555(m), 1627(s), 2686(w), 2971(m).

(2) $[\text{Dy}_3(3\text{-ethoxysalicyl})_3(\mu_3\text{-OH})_2(\text{H}_2\text{O})_2(\text{CH}_3\text{OH})\text{Cl}_3]\text{Cl} \cdot 2\text{H}_2\text{O} \cdot 2\text{CH}_3\text{OH}$

453 mg (1.2 mmol, 1.2 eq.) $\text{DyCl}_3 \cdot 6\text{H}_2\text{O}$ and 166 mg (1.0 mmol, 1.0 eq.) 3-ethoxysalicylaldehyde were dissolved in 7 mL methanol. 139 μL (1.0 mmol, 1.0 eq.) triethylamine and 60.0 μL (1.0 mmol, 1.0 eq.) ethanolamine were added to the yellow solution, stirred at 70°C for 30 minutes, then filtered. The clear solution was transferred into one side of a H-Tube. The other side was filled with diethyl ether (~10 mL). Yellow crystals were obtained after two weeks in the methanol region of the H-Tube. Yield: 308 mg (24 %, based on Dy). Elemental analysis for $\text{Dy}_3\text{C}_{30}\text{H}_{49}\text{O}_{18}\text{Cl}_4$: Calc%(found%) C/H/N: 27.15 (26.37), 3.72 (3.58), 0.00 (0.60). Selected IR peaks (cm^{-1}): $\tilde{\nu}$ = 463(m), 545(s), 636(s), 722(s), 786(m), 837(w), 880(s), 1454(s), 1095(m), 1176(s), 1212(s), 1414(s), 1440(s), 1555(m), 1625(s), 3628(w).

(3) $[\text{Eu}_3(3\text{-ethoxysalicyl})_3(\mu_3\text{-OH})_2(\text{H}_2\text{O})_2(\text{CH}_3\text{OH})\text{Cl}_3]\text{Cl} \cdot 2\text{CH}_3\text{OH} \cdot 2\text{H}_2\text{O}$

366 mg (1.0 mmol, 1.0 eq.) $\text{EuCl}_3 \cdot 6\text{H}_2\text{O}$ and (166 mg (1.0 mmol, 1.0 eq.) 3-ethoxysalicylaldehyde were dissolved in 10 mL methanol. 139 μL (1.0 mmol,

1.0 eq.) triethylamine and 60.0 μL (1.0 mmol, 1.0 eq.) ethanolamine were added to the yellow solution, stirred at 70°C for 30 minutes, then filtered. The clear solution was transferred into one side of a H-Tube. The other side was filled with diethyl ether (~10 mL). Yellow crystals were obtained after three weeks in the methanol region of the H-Tube. Yield: 314 mg (24 % based on Eu). Elemental analysis for $\text{Eu}_3\text{C}_{30}\text{H}_{48}\text{O}_{17}\text{Cl}_4$: Calc%(found%) C/H/N: 28.19 (27.53); 3.78 (3.37); 0.00 (0.12).

(4) $[\text{Tb}_3(3\text{-ethoxysalicyl})_3(\mu_3\text{-OH})_2(\text{H}_2\text{O})_2(\text{CH}_3\text{OH})\text{Cl}_3]\text{Cl}\cdot 3\text{CH}_3\text{OH}$

374 mg (1.0 mmol, 1.0 eq.) $\text{TbCl}_3\cdot 6\text{H}_2\text{O}$ and 166 mg (1.0 mmol, 1.0 eq.) 3-ethoxysalicyl aldehyde were dissolved in 15 mL methanol. 139 μL (1.0 mmol, 1.0 eq.) triethylamine and 60.0 μL (1.0 mmol, 1.0 eq.) ethanolamine were added to the yellow solution, stirred at 70°C for 30 minutes, then filtered. The clear solution was transferred into one side of a H-Tube. The other side was filled with diethyl ether (~10 mL). Yellow crystals were obtained after two weeks in the methanol region of the H-Tube. Yield: 147 mg (11 %, based on Tb). Elemental analysis for $\text{Tb}_3\text{C}_{31}\text{H}_{49}\text{O}_{17}\text{Cl}_4$: Calc%(found%) C/H/N: 28.37 (27.53), 2.76(2.69), 0.00 (0.20). Selected IR peaks (cm^{-1}): 459(s), 543(s), 642(s), 722(s), 779(w), 886(m), 985(m), 1056(m), 1093(m), 1198(s), 1212(s), 1235(w), 1292(s), 1412(s), 1547(m), 1623(s), 3177(w).

(5) $[\text{Ho}_3(3\text{-ethoxysalicyl})_3(\mu_3\text{-OH})_2(\text{H}_2\text{O})_2(\text{CH}_3\text{OH})\text{Cl}_3]\text{Cl}\cdot 3\text{CH}_3\text{OH}$

379 mg (1.0 mmol, 1.0 eq.) $\text{HoCl}_3\cdot 6\text{H}_2\text{O}$ and 166 mg (1.0 mmol, 1.0 eq.) 3-ethoxysalicyl aldehyde were dissolved in 10 mL methanol. 139 μL (1.0 mmol, 1.0 eq.) triethylamine and 60.0 μL (1.0 mmol, 1.0 eq.) ethanolamine were added to the yellow solution, stirred at 70°C for 30 minutes, then filtered. The clear solution was transferred into one side of a H-Tube. The other side was filled with diethyl ether (~10 mL). Yellow crystals were obtained after one week in the methanol region of the H-Tube. Yield: 350 mg (26 % based on Ho). Elemental analysis for $\text{Ho}_3\text{C}_{31}\text{H}_{49}\text{O}_{17}\text{Cl}_4$: Calc%(found%) C/H/N: 27.99 (27.00), 3.71(3.04), 0.00 (0.11). Selected IR peaks (cm^{-1}): $\tilde{\nu}$ = 459(m), 541(s), 648(s), 718(s), 784(w), 880(m), 989(m), 1056(m), 1102(m), 1217(s), 1292(m), 1405(m), 1442(s), 1547(m), 1635(s), 3480(w).

(6) $[\text{Er}_3(3\text{-ethoxysalicyl})_3(\mu_3\text{-OH})_2(\text{H}_2\text{O})_2(\text{CH}_3\text{OH})\text{Cl}_3]\text{Cl}\cdot\text{H}_2\text{O}\cdot 2\text{CH}_3\text{OH}$

463 mg (1.2 mmol, 1.2 eq.) $\text{ErCl}_3\cdot 6\text{H}_2\text{O}$ and 166 mg (1.0 mmol, 1.0 eq.) 3-ethoxysalicyl aldehyde were dissolved in 5 mL methanol. 139 μL (1.0 mmol, 1.0 eq.) triethylamine and 60.0 μL (1.0 mmol, 1.0 eq.) ethanolamine were added to the yellow solution, stirred at 70°C for 30 minutes, then filtered. The clear solution was transferred into one side of a H-Tube. The other side was filled with diethyl ether (~10 mL). Yellow crystals were obtained after three week in the methanol region of the H-Tube. Yield: 180 mg (11% based on Er). Selected IR data (cm^{-1}): $\tilde{\nu}$ = 465(s), 508(s), 550(s), 646(m), 720(s), 743(s), 781(s), 816(s), 841(s), 882(s), 991(m), 1017(s), 1056(s), 1089(s), 1173(s), 1210(s), 1233(s), 1301(m), 1370(s), 1414(s), 1444(s), 1465(s), 1555(s), 1609(s), 1633(m), 2785(w), 3154(w), 3388(w), 3519(w), 3630(m).

(7) $[\text{Cr}_2\text{Dy}_3(\text{pfba})_6(\mu_3\text{-OH})_6(\text{NO}_3)_3(\text{H}_2\text{O})_2(\text{C}_3\text{H}_7\text{OH})]\cdot\text{H}_2\text{O}$

225 mg (0.49 mmol, 1.0 eq.) $\text{Dy}(\text{NO}_3)_3\cdot 6\text{H}_2\text{O}$, 400 mg (1.0 mmol, 2.0 eq.) $\text{Cr}(\text{NO}_3)_3\cdot 9\text{H}_2\text{O}$ and 141 mg (1.0 mmol, 2.0 eq.) 4-fluoro benzoic acid were dissolved in 20 mL acetonitrile. 550 μL (4.0 mmol, 8.1 eq.) triethylamine was added to the suspension. The mixture was heated at 80°C and stirred for 1.5 hours, then filtered and redissolved in a mixture of isopropanol and dichloromethane (ratio 1:1). Purple crystals were obtained after six weeks of slow solvent evaporation. Selected IR data (cm^{-1}): $\tilde{\nu}$ = 515(s), 584(m), 625(s), 678(m), 775(m), 864(m), 944(w), 1040(m), 1149(s), 1215(m), 1297(s), 1397(s), 1568(m), 1615(m), 1664(w), 3601(w).

(8) $[\text{Cr}_2\text{Dy}_3(\text{pfba})_9(\mu_3\text{-OH})_6(\text{C}_3\text{H}_7\text{OH})_3]\cdot 3\text{C}_3\text{H}_7\text{OH}$

113 mg (0.25 mmol, 1.5 eq.) $\text{Dy}(\text{NO}_3)_3\cdot 6\text{H}_2\text{O}$, 113 mg (0.16 mmol, 1.0 eq.) $\text{CrCl}_3\cdot 6\text{H}_2\text{O}$ and 103 mg (0.74 mmol, 4.6 eq.) 4-fluoro-benzoic acid were dissolved in 40 mL isopropanol. 262 μL (1.9 mmol, 11.9 eq.) triethylamine was added to the green solution. The mixture was refluxed for 35 hours, 10 mL dichloromethane was added to the purple solution, then filtered. Purple crystals were obtained after four weeks of slow solvent evaporation. Yield: 88 mg (24 % based on Cr). Elemental analysis for $\text{Cr}_2\text{Dy}_3\text{C}_{81}\text{H}_{90}\text{F}_9\text{O}_{30}$ Calc%(found%) C/H/N: 42.19 (41.17), 3.93 (3.58), 0.00 (0.25). Selected IR data (cm^{-1}): $\tilde{\nu}$ = 414(s), 537(s), 619(s), 693(m), 775(s),

822(w), 861(m), 939(w), 1011(w), 1093(m), 1149(s), 1217(s), 1377(s), 1467(w), 1557(s), 1609(m), 2963(w).

(9) $[\text{Cr}_2\text{Dy}_3(\text{pclba})_9(\mu_3\text{-OH})_6(\text{C}_3\text{H}_7\text{OH})_3]\cdot\text{H}_2\text{O}\cdot\text{C}_3\text{H}_7\text{OH}$

133 mg (0.29 mmol, 1.8 eq.) $\text{Dy}(\text{NO}_3)_3\cdot 6\text{H}_2\text{O}$, 43 mg (0.16 mmol, 1.0 eq.) $\text{CrCl}_3\cdot 6\text{H}_2\text{O}$ and 114 mg (0.73 mmol, 4.5 eq.) 4-chloro-benzoic acid were dissolved in 40 mL isopropanol. 200 μL (1.4 mmol, 9.0 eq.) triethylamine was added to the green solution. The mixture was refluxed for 16 hours, then filtered. Purple crystals were obtained after 16 days of slow solvent evaporation. Yield: 105 mg (28 % based on Cr). Elemental analysis for $\text{Cr}_2\text{Dy}_3\text{C}_{75}\text{H}_{76}\text{O}_{29}\text{Cl}_9$ Calc%(found%) C/H/N: 38.30 (38.28), 3.26 (3.50), 0.00 (0.16). Selected IR peaks: $\tilde{\nu}$ = 474(m), 537(w), 609(w), 683(m), 773(s), 855(m), 1013(s), 1090(m), 1171(m), 1280(m), 1403(w), 1465(w), 1547(m), 1596(s), 3310(w).

(10) $[\text{Cr}_2\text{Dy}_3(\text{pcnba})_6(\mu_3\text{-OH})_6(\text{NO}_3)_3(\text{H}_2\text{O})_3]$

134 mg (0.29 mmol, 1.9 eq.) $\text{Dy}(\text{NO}_3)_3\cdot 6\text{H}_2\text{O}$, 41 mg (0.15 mmol, 1.0 eq.) $\text{CrCl}_3\cdot 6\text{H}_2\text{O}$ and 107 mg (0.73 mmol, 4.7 eq.) 4-cyano-benzoic acid were dissolved in a mixture of isopropanol (40 mL), methanol (10 mL) and dimethylformamide (2 mL). 200 μL (1.6 mmol, 9.6 eq.) triethylamine was added to the green solution. The mixture was refluxed for 15 hours, then filtered. A mixture of dichloromethane and isopropanol (ratio 1:1) was added. Purple crystals were obtained after several weeks of slow solvent evaporation. Yield 24 mg (8.8 %, based on Cr). Elemental analysis for $\text{Cr}_2\text{Dy}_3\text{C}_{48}\text{H}_{36}\text{O}_{30}\text{N}_9$ Calc%(found%) C/H/N: 39.45 (40.45), 2.89 (3.12); 7.96 (8.18). Selected IR peaks (cm^{-1}): $\tilde{\nu}$ = 541(s), 601(m), 687(m), 698(m), 775(s), 876(w), 1020(w), 1091(w), 1362(s), 1551(m), 1607(s), 1650(m), 2224(w), 2922(w).

(11) $[\text{Cr}_2\text{Dy}_3(\text{dfba})_6(\mu_3\text{-OH})_6(\text{NO}_3)_3(\text{DMF})_3]\cdot\text{DMF}$

133 mg (0.29 mmol, 1.9 eq.) $\text{Dy}(\text{NO}_3)_3\cdot 6\text{H}_2\text{O}$, 41.0 mg (0.15 mmol, 1.0 eq.) $\text{CrCl}_3\cdot 6\text{H}_2\text{O}$ and 111 mg (0.70 mmol, 4.6 eq.) 3,5-difluoro-benzoic acid were dissolved in a mixture of isopropanol (20 mL) and dimethylformamide (2 mL). 200 μL (1.4 mmol, 9.4 eq.) triethylamine was added to the green solution. The purple solution was refluxed for 21 hours, 10 mL dichloromethane were added, then filtered. Purple crystals were obtained after around three weeks of slow solvent evaporation.

Yield: 41 mg (13 %, based on Cr). Elemental analysis for $\text{Cr}_2\text{Dy}_3\text{C}_{54}\text{H}_{52}\text{N}_7\text{F}_{12}\text{O}_{31}$ Calc%(found%) C/H/N: 30.67 (31.89); 2.48 (2.95); 4.64 (5.52). Selected IR data (cm^{-1}): $\tilde{\nu}$ = 439(m), 539(s), 654(s), 753(s), 786(s), 878(w), 972(w), 985(s), 1065(w), 1108(s), 1305(s), 1383(s), 1451(m), 1582(s), 1619(w), 1660(s), 3608(w).

(12) $[\text{Cr}_2\text{Dy}_3(\text{dtbba})_9(\mu_3\text{-OH})_6(\text{C}_3\text{H}_7\text{OH})_3] \cdot 3\text{C}_3\text{H}_7\text{OH}$

134 mg (0.29 mmol, 1.9 eq.) $\text{Dy}(\text{NO}_3)_3 \cdot 6\text{H}_2\text{O}$, 41 mg (0.15 mmol, 1.0 eq.) $\text{CrCl}_3 \cdot 6\text{H}_2\text{O}$ and 164 mg (0.70 mmol, 4.6 mmol) 3,5-ditertbutyl benzoic acid were dissolved in 20 mL isopropanol. 200 μL (1.4 mmol, 9.4 eq.) triethylamine was added to the green solution and refluxed for 3 hours, then filtered. 10 mL dichloromethane was added to the purple solution. Purple crystals were obtained after three weeks of slow solvent evaporation. Yield: 142 mg (29 %, based on Cr). Elemental analysis for $\text{Cr}_2\text{Dy}_3\text{C}_{153}\text{H}_{243}\text{O}_{30}$: Calc%(found%) C/H/N: 58.26 (57.21); 7.77 (7.18); 0.00 (0.17). Selected IR peaks (cm^{-1}): $\tilde{\nu}$ = 482(m), 543(m), 634(s), 706(s), 734(s), 747(s), 790(s), 818(s), 892(s), 950(w), 1026(w), 1102(w), 1128(m), 1161(m), 1200(s), 1245(s), 1262(s), 1290(s), 1362(s), 1389(m), 1438(m), 1574(m), 1613(s), 2867(m), 2906(m), 2961(m), 3341(w).

(13) $[\text{Fe}_2\text{Dy}_3(\text{dtbba})_9(\mu_3\text{-OH})_6(\text{C}_3\text{H}_7\text{OH})_3] \cdot 3\text{C}_3\text{H}_7\text{OH}$

134 mg (0.29 mmol, 1.8 eq.) $\text{Dy}(\text{NO}_3)_3 \cdot 6\text{H}_2\text{O}$, 32 mg (0.16 mmol, 1.0 eq.) $\text{FeCl}_2 \cdot 4\text{H}_2\text{O}$ and 167 mg (0.71 mmol, 4.4 eq.) 3,5-difluoro-benzoic acid were dissolved in 20 mL isopropanol. 200 μL (1.4 mmol, 8.8 eq.) triethylamine was added to the colourless solution. The slight brown solution was heated for 3 hours at 80°C. Pale yellow crystals were obtained after three weeks of slow solvent evaporation. Yield: 105 mg (21 %, based on Fe). Elemental analysis for $\text{Fe}_2\text{Dy}_3\text{C}_{153}\text{H}_{243}\text{O}_{30}$: Calc%(found%) C/H/N: 58.12(57.07); 7.75 (7.02); 0.00 (0.07). Selected IR peaks (cm^{-1}): $\tilde{\nu}$ = 408 (w), 516 (w), 707 (w), 790 (w), 1286 (m), 1383 (s), 1575 (s), 2866 (w), 2909 (w), 2960 (s), 3630 (w).

(14) $[\text{Al}_2\text{Dy}_3(\text{dtbba})_9(\mu_3\text{-OH})_6(\text{CH}_3\text{OH})_{0.75}(\text{H}_2\text{O})_{1.5}(\text{C}_3\text{H}_7\text{OH})_{0.75}] \cdot \text{CH}_3\text{H}_7\text{OH}$

134 mg (0.29 mmol, 1.7 eq.) $\text{Dy}(\text{NO}_3)_3 \cdot 6\text{H}_2\text{O}$, 41 mg (0.17 mmol, 1.0 eq.) $\text{AlCl}_3 \cdot 6\text{H}_2\text{O}$ and 134 mg (0.29 mmol, 1.7 eq.) 3,5-ditertbutyl-benzoic were dissolved in a mixture of methanol (7 mL) and isopropanol (20 mL). 200 μL (1.4 mmol, 8.2 eq.)

triethylamine was added. The solution was heated for three hours at 80°C, then filtered. White crystals were obtained after three weeks of slow solvent evaporation. Yield: 105 mg (21 %, based on Al). Elemental analysis for $\text{Al}_2\text{Dy}_3\text{C}_{139}\text{H}_{218.75}\text{O}_{28}$: Calc%(found%) C/H/N: 58.00 (56.98); 7.63 (7.25); 0.00 (0.19). Selected IR peaks (cm^{-1}): $\tilde{\nu}$ = 420(s), 484(m), 543(s), 634(m), 708(m), 736(m), 892(w), 956(w), 1122(w), 1245(w),

(15) $[\text{Al}_2\text{Dy}_3(\text{dtbba})_7(\mu_3\text{-OH})_6(\text{NO}_3)_2(\text{C}_3\text{H}_7\text{OH})(\text{H}_2\text{O})_2]\cdot 3\text{H}_2\text{O}$

115 mg (0.25 mmol, 1.5 eq.) $\text{Dy}(\text{NO}_3)_3\cdot 6\text{H}_2\text{O}$, 42 mg (0.17 mmol, 1.0 eq.) $\text{AlCl}_3\cdot 6\text{H}_2\text{O}$ and 116 mg (0.50 mmol, 2.9 eq.) 3,5-ditertbutyl-benzoic acid were dissolved in a mixture of methanol (5 mL) and isopropanol (20 mL). 200 μL (1.4 mmol, 8.3 eq.) triethylamine was added. The solution was refluxed for 23 hours, 15 mL dichloromethane was added, then filtered. White crystals were obtained after ten weeks of slow solvent evaporation. Yield: 34 mg (8 %, based on Al). Elemental analysis for $\text{Al}_2\text{Dy}_3\text{C}_{108}\text{H}_{171}\text{O}_{32}$: Calc%(found%) C/H/N: 50.85 (50.67); H, 6.76 (6.32); 1.10 (1.14). Selected IR peaks (cm^{-1}): $\tilde{\nu}$ = 424(s), 441(s), 476(m), 547(s), 644(m), 706(m), 734(m), 792(m), 898(w), 946(w), 1024(w), 1124(w), 1200(w), 1247(m), 1290(m), 1399(s), 1438(m), 1508(w), 1582(m), 1623(w), 2871(w), 2906(w), 2961(w), 3640(w).

(16) $[\text{Co}_2\text{Dy}_3(\text{dtbba})_7(\mu_3\text{-OH})_6(\text{NO}_3)_2(\text{C}_3\text{H}_7\text{OH})_3]\cdot 3\text{C}_3\text{H}_7\text{OH}\cdot 3\text{CH}_3\text{CN}$

110 mg (0.24 mmol, 1.4 eq.) $\text{Dy}(\text{NO}_3)_3\cdot 6\text{H}_2\text{O}$, 50.0 mg (0.17 mmol, 1.0 eq.) $\text{Co}(\text{NO}_3)_2\cdot 6\text{H}_2\text{O}$ and 50.0 mg (0.21 mmol, 1.2 eq.) 3,5-ditertbutyl-benzoic acid were dissolved in a mixture of acetonitrile (30 mL) and isopropanol (10 mL). 50.0 μL (0.36 mmol, 2.1 eq.) triethylamine was added. The solution was heated at 70°C and stirred for 1.5 hours, then filtered. Green crystals were obtained after several weeks of slow solvent evaporation. Yield < 1%.

(17) $\text{Tb}_4(\text{OH})_2(\text{NO}_3)_2(\text{DMF})_2(\text{ehimp})_4$

45 mg (0.1mmol, 1.0 eq.) $\text{Tb}(\text{NO}_3)_3\cdot 6\text{H}_2\text{O}$, 19 mg(0.1mmol, 1.0 eq.) 3-ethoxysalicylaldehyde and 11mg (0.1mmol, 1.0 eq.) 2-aminophenol were dissolved in MeOH (10ml) and dimethylformamide (1ml) in a glass vial. 20 μL (0.15mmol, 1.5 eq.) triethylamine were added to the red solution. The mixture was

heated by 80°C in the oven. After five hours red crystals suitable for X-Ray diffraction appeared. Yield: 29 mg (15 %, based on Tb). Elemental analysis for $\text{Tb}_4\text{C}_{66}\text{H}_{68}\text{N}_8\text{O}_{22}$: Calc%(found%) C/H/N: 40.42 (40.50), 3.50 (3.44), 5.71 (5.62). Selected IR peaks (cm^{-1}): $\tilde{\nu}$ = 455(m), 504(s), 566(s), 613(m), 636(m), 724(s), 730(s), 814(m), 864(m), 931(w), 997(m), 1017(w), 1065(m), 1176(s), 1254(s), 1381(s), 1442(s), 1498(m), 1545(w), 1604(s), 1650(s), 2922(w), 2988(w), 2060(w), 3614(w).

(18) $\text{Dy}_4(\text{OH})_2(\text{NO}_3)_2(\text{DMF})_2(\text{ehimp})_4$

47mg (0.1mmol, 1.0 eq.) $\text{Dy}(\text{NO}_3)_3 \cdot 6\text{H}_2\text{O}$, 19mg (0.1 mmol, 1.0 eq.) 3-ethoxysalicylaldehyde and 11mg (0.1 mmol, 1.0 eq.) 2-aminophenol were dissolved in MeOH (10ml) and dimethylformamide (1ml) in a glass vial. 20 μ l (0.15 mmol, 1.5 eq.) triethylamine were added to the red solution. The mixture was heated by 80°C in the oven. After five hours red crystals suitable for X-Ray diffraction appeared. Yield: 30 mg (15%, based on Dy). Elemental analysis for $\text{Dy}_4\text{N}_8\text{O}_{22}\text{C}_{66}\text{H}_{68}$: Calc%(found%) C/H/N: 40.13 (39.26), 3.47 (3.51), 5.67 (5.69). Selected IR peaks (cm^{-1}): $\tilde{\nu}$ = 467(m), 500(s), 564(s), 677(s), 736(s), 814(m), 869(w), 1024(m), 1089(m), 1176(s), 1254(s), 1317(w), 1375(s), 1448(s), 1545(w), 1582(s), 1650(s), 2926(w), 2982(w), 3049(w), 3608(w).

(19) $\text{Ho}_4(\text{OH})_2(\text{NO}_3)_2(\text{DMF})_2(\text{ehimp})_4$

44 mg (0.1mmol, 1.0 eq.) $\text{Ho}(\text{NO}_3)_3 \cdot 6\text{H}_2\text{O}$, 19mg (0.1mmol, 1.0 eq.) , 3-ethoxysalicylaldehyde and 11mg (0.1 mmol, 1.0 eq.) 2-aminophenol were dissolved in MeOH (10ml) and dimethylformamide (1ml) in a glass vial. 20 μ l (0.15 mmol, 1.5 eq.) triethylamine were added to the red solution. The mixture was heated by 80°C in the oven. After five hours red crystals suitable for X-Ray diffraction appeared. Yield: 20 mg (10 %, based on Ho). Elemental analysis for $\text{Ho}_4\text{C}_{66}\text{H}_{68}\text{N}_8\text{O}_{22}$ Calc%(found%) C/H/N: C, 39.93 (39.51); H, 3.45 (3.49); N 5.64 (5.64). Selected IR peaks (cm^{-1}): $\tilde{\nu}$ = 453(m), 515(s), 568(s), 613(m), 636(m), 725(s), 732(s), 814(m), 864(m), 933(w), 997(m), 1015(w), 1065(m), 1179(s), 1243(s), 1381(s), 1442(s), 1494(m), 1545(w), 1602(s), 1654(s), 2925(w), 2983(w), 2062(w), 3615(w).

(20) $\text{Er}_4(\text{OH})_2(\text{NO}_3)_2(\text{DMF})_2(\text{ehimp})_4$

44 mg (0.1 mmol, 1.0 eq.) $\text{Er}(\text{NO}_3)_3 \cdot 6\text{H}_2\text{O}$, 19mg (0.1 mmol, 1.0 eq.) 3-ethoxysalicylaldehyde and 11mg (0.1 mmol, 1.0 eq.) 2-aminophenol were dissolved in MeOH (10ml) and dimethylformamide (1ml) in a glass vial. 20 μl (0.15 mmol, 1.5 eq.) triethylamine were added to the red solution. The mixture was heated by 80°C in the oven. After five hours red crystals suitable for X-Ray diffraction appeared. Yield: 29 mg (14 %, based on Er). Elemental analysis for $\text{Er}_4\text{C}_{66}\text{H}_{68}\text{N}_8\text{O}_{22}$ Calc%(found%) C/H/N: 39.75 (38.42), 3.44 (4.11), 5.62 (5.66). Selected IR peaks (cm^{-1}): $\tilde{\nu}$ = 457(m), 523(s), 568(s), 615(m), 636(m), 724(s), 732(s), 814(m), 864(m), 933(w), 997(m), 1019(w), 1065(m), 1179(s), 1248(s), 1381(s), 1442(s), 1493(m), 1545(w), 1602(s), 1654(s), 2925(w), 2983(w), 2064(w), 3623(w).

(21) $\text{Yb}_4(\text{OH})_2(\text{NO}_3)_2(\text{DMF})_2(\text{ehimp})_4$

45 mg (0.1mmol, 1.0 eq.) $\text{Yb}(\text{NO}_3)_3 \cdot 6\text{H}_2\text{O}$, 19mg (0.1 mmol, 1.0 eq.) 3-ethoxysalicylaldehyde and 11mg (0.1 mmol, 1.0 eq.) 2-aminophenol were dissolved in MeOH (10ml) and dimethylformamide (1ml) in a glass vial. 20 μl (0.15mmol, 1.5 eq.) triethylamine were added to the red solution. The mixture was heated by 80°C in the oven. After five hours red crystals suitable for X-Ray diffraction appeared. Yield: 20 mg (10 %, based on Yb). Elemental analysis for $\text{Yb}_4\text{C}_{66}\text{H}_{68}\text{N}_8\text{O}_{22}$ Calc%(found%) C/H/N: 39.29 (38.56), 3.40 (3.42), 5.55 (5.53). Selected IR peaks (cm^{-1}): $\tilde{\nu}$ = 453(m), 515(s), 568(s), 613(m), 636(m), 725(s), 732(s), 814(m), 864(m), 933(w), 997(m), 1015(w), 1065(m), 1179(s), 1243(s), 1381(s), 1442(s), 1494(m), 1545(w), 1602(s), 1654(s), 2925(w), 2983(w), 2062(w), 3623(w).

(22) $\text{Y}_4(\text{OH})_2(\text{NO}_3)_2(\text{DMF})_2(\text{ehimp})_4$

38 mg (0.1mmol, 1.0 eq.) $\text{Y}(\text{NO}_3)_3 \cdot 6\text{H}_2\text{O}$, 19mg (0.1 mmol, 1.0 eq.) 3-ethoxysalicylaldehyde and 11mg (0.1 mmol, 1.0 eq.) 2-aminophenol were dissolved in MeOH (10ml) and dimethylformamide (1ml) in a glass vial. 20 μl (0.15 mmol, 1.5 eq.) triethylamine were added to the red solution. The mixture was heated by 80°C in the oven. After five hours red crystals suitable for X-Ray diffraction appeared. Yield: 20 mg (7 %, based on Y). Elemental analysis for $\text{Y}_4\text{C}_{66}\text{H}_{68}\text{N}_8\text{O}_{22}$ Calc%(found%) C/H/N: 47.16 (46.95), 4.08 (4.06), 6.67 (6.76). Selected IR peaks

(cm⁻¹): $\tilde{\nu}$ = 457(m), 502(s), 576(s), 617(m), 697(s), 736(s), 814(m), 870(m), 905(w), 993(m), 1020(m), 1087(m), 1173(s), 1219(s), 1251(s), 1375(s), 1446(s), 1574(w), 1580(m), 1607(s), 1646(s), 2916(w), 2984(w), 3060(w), 3614(w).

(23) [Dy₆(NO₃)₆(teaH)₆]·2C₂H₅OH

228 mg (0.50 mmol, 1.0 eq.) Dy(NO₃)₃·6H₂O was dissolved in 14 ml ethanol. 297 mg (2.0 mmol, 4.0 eq.) Triethanolamine was dissolved in 18 mL acetonitrile and 300 μ L (2.16 mmol, 4.32 eq.) triethylamine was added. The ethanol solution was carefully overlayed with the acetonitrile solution. Colourless crystals appeared at the border of the solutions overnight. Yield: 220 mg (22 % based on Dy). Elemental analysis for Dy₆C₄₀H₉₀O₂₀N₁₂ Calc%(found%) C/H/N: 23.62 (24.05), 4.46 (4.40), 8.26 (8.15). Selected IR peaks (cm⁻¹): $\tilde{\nu}$ = 454(m), 554(m), 575(m), 738(w), 816(w), 899(m), 1037(s), 1075(s), 1303(s), 1428(s), 2851(s), 2869(m), 2974(m), 3329(w).

(24) [Dy₆(NO₃)₆(apadH₂)₆]

226 mg (0.50 mmol, 1.0 eq.) Dy(NO₃)₃·6H₂O was dissolved in 14 ml methanol. 333 mg (2.05 mmol, 4.32 eq.) 2,2'-(3-aminopyrrolylazanediyl)diethanol was dissolved in 18 mL acetonitrile and 300 μ L (2.16 mmol, 4.32 eq.) triethylamine was added. The methanol solution was carefully overlayed with the acetonitrile solution by a 10 mL separation layer of methanol:acetonitrile (1:1). Colourless crystals appeared at the border of the solutions in one week. Yield: 170 mg (15 % based on Dy). Elemental analysis for Dy₆C₄₂H₉₆O₃₀N₁₈ Calc%(found%) C/H/N: 21.85 (21.60), 4.19 (4.16), 10.92 (10.73). Selected IR peaks (cm⁻¹): $\tilde{\nu}$ = 438 (w), 486 (w), 563 (w), 730 (w), 1088 (s), 1444 (s), 1281 (s), 1460 (s), 1600 (w), 2842 (m), 3344 (w).

9 Crystallographic data

Table 9-1 Crystallographic data and structure refinement for (1) and (2).

Compound	(1)	(2)
Empirical formula	Dy ₃ C ₃₀ H ₅₉ O ₂₃ Cl ₄	Dy ₃ C ₃₀ H ₄₉ O ₁₈ Cl ₄
Formula weight/ gmol ⁻¹	1417.09	1327.01
Temperature/K	293(2)	150.0
Crystal system	monoclinic	monoclinic
Space group	I2/a	P2 ₁ /c
a/Å	17.6864(4)	18.5193(6)
b/Å	18.0888(4)	17.0719(4)
c/Å	32.6179(6)	13.9357(4)
α/°	90	90
β/°	99.482(2)	99.005(3)
γ/°	90	90
Volume/Å ³	10292.7(4)	4351.6(2)
Z	8	4
ρ _{calc} /cm ³	1.627	2.032
μ/mm ⁻¹	4.568	28.631
F(000)	4780.0	2572.0
Diffractometer type	Agilent SuperNova	Stoe StadiVari
Radiation	MoKα (λ = 0.71073)	GaKα (λ = 1.34143)
2θ range for data collection/°	4.346 to 58.17	6.162 to 118.608
Index ranges	-23 ≤ h ≤ 21, -24 ≤ k ≤ 23, -27 ≤ l ≤ 44	-23 ≤ h ≤ 23, -21 ≤ k ≤ 11, -17 ≤ l ≤ 15
Reflections collected	34218	24833
Independent reflections	11826 [R _{int} = 0.0409, R _{sigma} = 0.0426]	9403 [R _{int} = 0.0409, R _{sigma} = 0.0398]
Data/restraints/parameters	11826/21/486	9403/8/520
Goodness-of-fit on F ²	1.076	1.030
Final R indexes [I ≥ 2σ (I)]	R ₁ = 0.0459, wR ₂ = 0.1528	R ₁ = 0.0587, wR ₂ = 0.1616
Final R indexes [all data]	R ₁ = 0.0632, wR ₂ = 0.1710	R ₁ = 0.0687, wR ₂ = 0.1698
Largest diff. peak/hole / e Å ⁻³	2.35/-0.97	3.88/-2.98

Table 9-2 Crystallographic data and structure refinement for (3) and (4).

Compound	(3)	(4)
Empirical formula	Eu ₃ C ₃₀ H ₄₈ O ₁₇ Cl ₄	Tb ₃ C ₃₁ H ₄₉ O ₁₇ Cl ₄
Formula weight/ gmol ⁻¹	1278.39	1312.30
Temperature/K	170.0	150.0
Crystal system	monoclinic	monoclinic
Space group	P2 ₁ /c	P2 ₁ /c
a/Å	18.5606(10)	18.4767(3)
b/Å	17.1901(6)	17.1995(3)
c/Å	14.0183(6)	13.9410(4)
α/°	90	90
β/°	98.276(4)	98.526(2)
γ/°	90	90
Volume/Å ³	4426.1(3)	4381.35(16)
Z	4	4
ρ _{calc} /g/cm ³	1.944	1.979
μ/mm ⁻¹	24.381	27.212
F(000)	2520.0	2520.0
Diffractometer type	Stoe StadiVari	Stoe StadiVari
Radiation	GaKα (λ = 1.34143)	GaKα (λ = 1.34143)
2θ range for data collection/°	6.126 to 124.96	7.15 to 118.608
Index ranges	-22 ≤ h ≤ 24, -9 ≤ k ≤ 22, -18 ≤ l ≤ 16	-21 ≤ h ≤ 23, -22 ≤ k ≤ 19, -17 ≤ l ≤ 8
Reflections collected	22980	26240
Independent reflections	10293 [R _{int} = 0.0732, R _{sigma} = 0.0620]	9416 [R _{int} = 0.0286, R _{sigma} = 0.0381]
Data/restraints/parameters	10293/9/519	9416/7/523
Goodness-of-fit on F ²	1.068	1.013
Final R indexes [I ≥ 2σ (I)]	R1 = 0.0936, wR2 = 0.2597	R1 = 0.0338, wR2 = 0.0802
Final R indexes [all data]	R1 = 0.1200, wR2 = 0.2850	R1 = 0.0502, wR2 = 0.0850
Largest diff. peak/hole / e Å ⁻³	3.19/-2.68	1.13/-0.95

Table 9-3 Crystallographic data and structure refinement for **(5)** and **(6)**

Compound	(5)	(6)
Empirical formula	Ho ₃ C ₃₁ H ₄₉ O ₁₇ Cl ₄	Er ₃ C ₃₀ H ₄₇ O ₁₇ Cl ₄
Formula weight/ gmol ⁻¹	1330.31	1323.27
Temperature/K	170.0	273.15
Crystal system	monoclinic	monoclinic
Space group	P2 ₁ /c	P2 ₁ /c
a/Å	18.2524(4)	18.3818(9)
b/Å	17.1098(3)	17.0830(5)
c/Å	13.8954(3)	13.8926(5)
α /°	90	90
β /°	98.475(2)	98.761(3)
γ /°	90	90
Volume/Å ³	4292.08(15)	4311.6(3)
Z	4	4
ρ_{calc} /cm ³	2.059	2.054
μ /mm ⁻¹	26.580	6.100
F(000)	2560.0	2556.0
Diffraction type	Stoe StadiVari	Stoe StadiVari
Radiation	GaK α (λ = 1.34143)	MoK α (λ = 0.71073)
2 θ range for data collection/°	7.178 to 118.602	4.182 to 54.206
Index ranges	-22 \leq h \leq 23, -21 \leq k \leq 8, -16 \leq l \leq 17	-23 \leq h \leq 22, -21 \leq k \leq 18, -17 \leq l \leq 17
Reflections collected	20798	23443
Independent reflections	9183 [R _{int} = 0.0266, R _{sigma} = 0.0266]	9370 [R _{int} = 0.0654, R _{sigma} = 0.0757]
Data/restraints/parameters	9183/6/521	9370/194/511
Goodness-of-fit on F ²	1.041	1.065
Final R indexes [$I \geq 2\sigma(I)$]	R ₁ = 0.0426, wR ₂ = 0.1142	R ₁ = 0.0764, wR ₂ = 0.2054
Final R indexes [all data]	R ₁ = 0.0477, wR ₂ = 0.1178	R ₁ = 0.1031, wR ₂ = 0.2205
Largest diff. peak/hole / e Å ⁻³	3.16/-2.72	1.67/-1.43

Table 9-4 Crystallographic data and structure refinement for **(7)** and **(8)**.

Compound	(7)	(8)
Empirical formula	Cr ₂ Dy ₃ C ₄₅ H ₄₄ F ₆ O ₃₁ N ₃	Cr ₂ Dy ₃ C ₈₁ H ₉₀ F ₉ O ₃₀
Formula weight/ gmol ⁻¹	1828.31	2306.04
Temperature/K	293	150.0
Crystal system	monoclinic	triclinic
Space group	C2/m	P-1
a/Å	26.5672(3)	15.4386(4)
b/Å	20.2352(3)	16.1887(4)
c/Å	15.5829(2)	19.1561(5)
α/°	90	73.883(2)
β/°	95.7780(10)	82.562(2)
γ/°	90	73.514(2)
Volume/Å ³	8334.69(19)	4403.8(2)
Z	8	2
ρ _{calc} /cm ³	1.423	1.716
μ/mm ⁻¹	15.831	15.106
F(000)	3414.0	2252.0
Diffractometer type	Stoe StadiVari	Stoe StadiVari
Radiation	GaKα (λ = 1.34143)	GaKα (λ = 1.34143)
2θ range for data collection/°	4.784 to 119.998	5.12 to 124
Index ranges	-34 ≤ h ≤ 33, -26 ≤ k ≤ 26, -20 ≤ l ≤ 11	-18 ≤ h ≤ 20, -21 ≤ k ≤ 20, -18 ≤ l ≤ 25
Reflections collected	42075	47099
Independent reflections	9591 [R _{int} = 0.0217, R _{sigma} = 0.0136]	20175 [R _{int} = 0.0249, R _{sigma} = 0.0214]
Data/restraints/parameters	9591/0/443	20175/13/1133
Goodness-of-fit on F ²	1.059	1.048
Final R indexes [I ≥ 2σ (I)]	R ₁ = 0.0342, wR ₂ = 0.0962	R ₁ = 0.0399, wR ₂ = 0.1068
Final R indexes [all data]	R ₁ = 0.0372, wR ₂ = 0.0985	R ₁ = 0.0435, wR ₂ = 0.1091
Largest diff. peak/hole / e Å ⁻³	1.47/-0.60	1.05/-1.74

Table 9-5

Crystallographic data and structure refinement for **(9)** and **(10)**.

Compound	(9)	(10)
Empirical formula	Cr ₂ Dy ₃ C ₇₅ H ₇₆ O ₂₉ Cl ₉	Cr ₂ Dy ₃ C ₄₈ H ₃₆ O ₃₀ N ₉
Formula weight/ gmol ⁻¹	2351.95	1810.33
Temperature/K	150.0	180.0
Crystal system	trigonal	trigonal
Space group	R-3	P-3
a/Å	23.9220(3)	16.1593(6)
b/Å	23.9220(3)	16.1593(6)
c/Å	29.8462(4)	22.3698(8)
$\alpha/^\circ$	90	90
$\beta/^\circ$	90	90
$\gamma/^\circ$	120	120
Volume/Å ³	14791.6(4)	5058.7(4)
Z	5.99994	2
$\rho_{\text{calc}}/\text{g}/\text{cm}^3$	1.665	1.189
μ/mm^{-1}	14.883	13.007
F(000)	7350.0	1746.0
Diffractometer type	Stoe StadiVari	0.25 × 0.07 × 0.06
Radiation	GaK α (λ = 1.34143)	GaK α (λ = 1.34143)
2 θ range for data collection/ $^\circ$	4.518 to 128.414	6.482 to 124.97
Index ranges	-31 ≤ h ≤ 32, -31 ≤ k ≤ 23, -38 ≤ l ≤ 29	-18 ≤ h ≤ 21, -19 ≤ k ≤ 20, -29 ≤ l ≤ 18
Reflections collected	33465	20086
Independent reflections	8088 [R_{int} = 0.0708, R_{sigma} = 0.0414]	7970 [R_{int} = 0.0914, R_{sigma} = 0.0802]
Data/restraints/parameters	8088/5/389	7970/0/279
Goodness-of-fit on F^2	1.081	1.184
Final R indexes [$ I \geq 2\sigma(I)$]	R_1 = 0.0431, wR_2 = 0.1175	R_1 = 0.1439, wR_2 = 0.3558
Final R indexes [all data]	R_1 = 0.0493, wR_2 = 0.1211	R_1 = 0.1884, wR_2 = 0.3853
Largest diff. peak/hole / e Å ⁻³	1.23/-1.23	6.22/-1.49

Table 9-6 Crystallographic data and structure refinement for **(11)** and **(12)**.

Compound	(11)	(12)
Empirical formula	Cr ₂ Dy ₃ C ₅₄ H ₅₂ N ₇ F ₁₂ O ₃₁	Cr ₂ Dy ₃ C ₁₅₃ H ₂₄₃ O ₃₀
Formula weight/ g mol ⁻¹	2114.49	3154.03
Temperature/K	180.0	150.0
Crystal system	trigonal	triclinic
Space group	R-3	P-1
a/Å	22.6886(14)	21.1233(3)
b/Å	22.6886(14)	21.8680(3)
c/Å	28.3090(16)	21.9520(3)
α/°	90	71.4140(10)
β/°	90	73.6210(10)
γ/°	120	74.8110(10)
Volume/Å ³	12620.3(17)	9054.6(2)
Z	6	2
ρ _{calc} /g cm ⁻³	1.785	1.179
μ/mm ⁻¹	2.993	7.390
F(000)	6642.0	3362.0
Diffractometer type	Stoe StadiVari	Stoe StadiVari
Radiation	MoKα (λ = 0.71073)	GaKα (λ = 1.34143)
2θ range for data collection/°	4.316 to 57.996	3.864 to 124.998
Index ranges	-29 ≤ h ≤ 30, -29 ≤ k ≤ 30, -37 ≤ l ≤ 24	-19 ≤ h ≤ 27, -28 ≤ k ≤ 27, -29 ≤ l ≤ 28
Reflections collected	14080	105668
Independent reflections	6975 [R _{int} = 0.0179, R _{sigma} = 0.0276]	41842 [R _{int} = 0.0267, R _{sigma} = 0.0331]
Data/restraints/parameters	6975/0/362	41842/52/1766
Goodness-of-fit on F ²	1.003	1.038
Final R indexes [I ≥ 2σ (I)]	R ₁ = 0.0231, wR ₂ = 0.0546	R ₁ = 0.0495, wR ₂ = 0.1304
Final R indexes [all data]	R ₁ = 0.0334, wR ₂ = 0.0562	R ₁ = 0.0662, wR ₂ = 0.1393
Largest diff. peak/hole / e Å ⁻³	0.53/-0.48	1.81/-2.26

Table 9-7 Crystallographic data and structure refinement for **(13)** and **(14)**.

Compound	(13)	(14)
Empirical formula	Fe ₂ Dy ₃ C ₁₅₃ H ₂₄₃ O ₃₀	Al ₂ Dy ₃ C ₁₃₉ H _{218.75} O ₂₈
Formula weight/ gmol ⁻¹	3161.73	2879.41
Temperature/K	180.15	293(2)
Crystal system	triclinic	trigonal
Space group	P-1	P-3
a/Å	20.978(2)	23.0491(4)
b/Å	22.104(2)	23.0491(4)
c/Å	22.286(4)	26.6664(5)
α/°	70.728(11)	90
β/°	73.800(12)	90
γ/°	75.453(8)	120
Volume/Å ³	9222(2)	12268.8(5)
Z	2	6
ρ _{calc} /cm ³	1.202	1.378
μ/mm ⁻¹	1.416	14.715
F(000)	3500.0	4956.0
Diffractometer type	Stoe StadiVari	Stoe StadiVari
Radiation	MoKα (λ = 0.71073)	GaKα (λ = 1.34143)
2θ range for data collection/°	3.906 to 52.044	3.852 to 105.03
Index ranges	-23 ≤ h ≤ 25, -27 ≤ k ≤ 27, -27 ≤ l ≤ 27	-21 ≤ h ≤ 27, -27 ≤ k ≤ 24, -29 ≤ l ≤ 31
Reflections collected	99370	127369
Independent reflections	36096 [R _{int} = 0.0523, R _{sigma} = 0.0716]	14181 [R _{int} = 0.0670, R _{sigma} = 0.0384]
Data/restraints/parameters	36096/169/1611	14181/3/552
Goodness-of-fit on F ²	0.971	1.082
Final R indexes [I ≥ 2σ (I)]	R ₁ = 0.0516, wR ₂ = 0.1311	R ₁ = 0.0793, wR ₂ = 0.2426
Final R indexes [all data]	R ₁ = 0.0772, wR ₂ = 0.1404	R ₁ = 0.1034, wR ₂ = 0.2596
Largest diff. peak/hole / e Å ⁻³	2.25/-1.65	2.32/-0.91

Table 9-8 Crystallographic data and structure refinement for **(15)** and **(16)**.

Compound	(15)	(16)
Empirical formula	Al ₂ Dy ₃ C ₁₀₈ H ₁₇₁ O ₃₂	Co ₂ Dy ₃ C ₁₂₉ H ₂₁₀ O ₃₂ N ₅
Formula weight/ gmol ⁻¹	2522.95	2948.42
Temperature/K	150.0	180.0
Crystal system	monoclinic	triclinic
Space group	P2 ₁ /n	P-1
a/Å	21.5802(5)	17.6505(4)
b/Å	25.9004(7)	21.6864(6)
c/Å	27.6352(7)	21.7028(5)
α/°	90	92.125(2)
β/°	102.391(2)	103.963(2)
γ/°	90	108.712(2)
Volume/Å ³	15086.5(7)	7576.2(3)
Z	4	2
ρ _{calc} /cm ³	1.255	1.292
μ/mm ⁻¹	8.040	9.179
F(000)	5932.0	3054.0
Diffractometer type	Stoe StadiVari	Stoe StadiVari
Radiation	GaKα (λ = 1.34143)	GaKα (λ = 1.34143)
2θ range for data collection/°	6.426 to 113.94	5.588 to 118.608
Index ranges	-26 ≤ h ≤ 24, -25 ≤ k ≤ 32, -34 ≤ l ≤ 26	-22 ≤ h ≤ 22, -27 ≤ k ≤ 27, -27 ≤ l ≤ 19
Reflections collected	87234	84403
Independent reflections	29919 [R _{int} = 0.0621, R _{sigma} = 0.0829]	32799 [R _{int} = 0.0496, R _{sigma} = 0.0487]
Data/restraints/parameters	29919/452/1263	32799/154/1823
Goodness-of-fit on F ²	0.994	1.002
Final R indexes [I ≥ 2σ (I)]	R ₁ = 0.0670, wR ₂ = 0.1730	R ₁ = 0.0702, wR ₂ = 0.1787
Final R indexes [all data]	R ₁ = 0.1354, wR ₂ = 0.2029	R ₁ = 0.0982, wR ₂ = 0.2022
Largest diff. peak/hole / e Å ⁻³	0.90/-0.85	2.47/-1.78

Table 9-9 Crystallographic data and structure refinement for **(17)** and **(18)**.

Compound	(17)	(18)
Empirical formula	Tb ₄ C ₆₆ H ₆₈ N ₈ O ₂₂	Dy ₄ N ₈ O ₂₂ C ₆₆ H ₆₈
Formula weight/ gmol ⁻¹	1960.99	1975.28
Temperature/K	180.0	180.0
Crystal system	monoclinic	monoclinic
Space group	P2 ₁ /n	P2 ₁ /n
a/Å	12.8556(4)	12.8286(3)
b/Å	14.9414(4)	14.9545(5)
c/Å	18.1435(7)	18.1076(4)
α/°	90	90
β/°	102.062(3)	101.928(2)
γ/°	90	90
Volume/Å ³	3408.1(2)	3398.85(16)
Z	2	2
ρ _{calc} /cm ³	1.911	1.930
μ/mm ⁻¹	4.183	4.429
F(000)	1912.0	1920.0
Diffractometer type	Stoe StadiVari	Stoe StadiVari
Radiation	MoKα (λ = 0.71073)	MoKα (λ = 0.71073)
2θ range for data collection/°	4.482 to 57.998	4.598 to 63.012
Index ranges	-13 ≤ h ≤ 17, -19 ≤ k ≤ 20, -22 ≤ l ≤ 24	-18 ≤ h ≤ 14, -21 ≤ k ≤ 21, -25 ≤ l ≤ 26
Reflections collected	15512	26498
Independent reflections	8607 [R _{int} = 0.0348, R _{sigma} = 0.0305]	10947 [R _{int} = 0.0218, R _{sigma} = 0.0277]
Data/restraints/parameters	8607/0/455	10947/13/467
Goodness-of-fit on F ²	1.027	1.023
Final R indexes [I ≥ 2σ (I)]	R ₁ = 0.0527, wR ₂ = 0.1428	R ₁ = 0.0280, wR ₂ = 0.0649
Final R indexes [all data]	R ₁ = 0.0585, wR ₂ = 0.1473	R ₁ = 0.0389, wR ₂ = 0.0698
Largest diff. peak/hole / e Å ⁻³	8.92/-2.61	1.44/-1.08

Table 9-10 Crystallographic data and structure refinement for **(19)** and **(20)**.

Compound	(19)	(20)
Empirical formula	Ho ₄ C ₆₆ H ₆₈ N ₈ O ₂₂	Er ₄ C ₆₆ H ₆₈ N ₈ O ₂₂
Formula weight/ gmol ⁻¹	1985.01	1994.32
Temperature/K	180.0	180
Crystal system	monoclinic	monoclinic
Space group	P2 ₁ /n	P2 ₁ /n
a/Å	12.8221(4)	12.7840(4)
b/Å	14.9469(4)	14.9111(5)
c/Å	18.0621(6)	18.0383(6)
α/°	90	90
β/°	101.857(3)	101.917(2)
γ/°	90	90
Volume/Å ³	3387.75(18)	3364.42(19)
Z	2	2
ρ _{calc} /cm ³	1.946	1.969
μ/mm ⁻¹	4.704	5.022
F(000)	1928.0	1936.0
Diffractometer type	Stoe StadiVari	Stoe StadiVari
Radiation	MoKα (λ = 0.71073)	MoKα (λ = 0.71073)
2θ range for data collection/°	4.608 to 62.478	4.362 to 57.998
Index ranges	-17 ≤ h ≤ 15, -21 ≤ k ≤ 21, -18 ≤ l ≤ 26	-17 ≤ h ≤ 16, -20 ≤ k ≤ 20, -24 ≤ l ≤ 24
Reflections collected	18521	22551
Independent reflections	9357 [R _{int} = 0.0255, R _{sigma} = 0.0313]	8878 [R _{int} = 0.0412, R _{sigma} = 0.0492]
Data/restraints/parameters	9357/12/467	8878/0/455
Goodness-of-fit on F ²	1.013	1.084
Final R indexes [I ≥ 2σ (I)]	R ₁ = 0.0259, wR ₂ = 0.0573	R ₁ = 0.0481, wR ₂ = 0.1326
Final R indexes [all data]	R ₁ = 0.0394, wR ₂ = 0.0622	R ₁ = 0.0665, wR ₂ = 0.1411
Largest diff. peak/hole / e Å ⁻³	0.75/-0.62	7.96/-1.90

Table 9-11 Crystallographic data and structure refinement for **(21)** and **(22)**.

Compound	(21)	(22)
Empirical formula	Yb ₄ C ₆₆ H ₆₈ N ₈ O ₂₂	Y ₄ C ₆₆ H ₆₈ N ₈ O ₂₂
Formula weight/ g mol ⁻¹	2017.44	1680.91
Temperature/K	180.0	180.0
Crystal system	monoclinic	monoclinic
Space group	P2 ₁ /c	P2 ₁ /n
a/Å	24.1254(3)	12.8128(4)
b/Å	17.0053(3)	14.9170(5)
c/Å	18.3696(2)	18.0624(5)
α/°	90	90
β/°	110.6240(10)	101.970(2)
γ/°	90	90
Volume/Å ³	7053.32(18)	3377.18(18)
Z	4	2
ρ _{calc} /g cm ⁻³	1.900	1.653
μ/mm ⁻¹	5.335	3.455
F(000)	3904.0	1704.0
Diffractometer type	Stoe StadiVari	Stoe StadiVari
Radiation	MoKα (λ = 0.71073)	GaKα (λ = 1.34143)
2θ range for data collection/°	2.998 to 66.596	6.746 to 125.094
Index ranges	-25 ≤ h ≤ 36, -24 ≤ k ≤ 26, -28 ≤ l ≤ 23	-16 ≤ h ≤ 7, -19 ≤ k ≤ 18, -20 ≤ l ≤ 23
Reflections collected	99587	21568
Independent reflections	25364 [R _{int} = 0.0291, R _{sigma} = 0.0309]	7942 [R _{int} = 0.0177, R _{sigma} = 0.0192]
Data/restraints/parameters	25364/0/909	7942/12/467
Goodness-of-fit on F ²	1.127	1.079
Final R indexes [I ≥ 2σ (I)]	R ₁ = 0.0334, wR ₂ = 0.0676	R ₁ = 0.0267, wR ₂ = 0.0733
Final R indexes [all data]	R ₁ = 0.0624, wR ₂ = 0.0834	R ₁ = 0.0303, wR ₂ = 0.0745
Largest diff. peak/hole / e Å ⁻³	1.83/-1.41	0.47/-0.65

Table 9-12 Crystallographic data and structure refinement for **(23)** and **(24)**

Compound	(23)	(24)
Empirical formula	Dy ₆ C ₄₀ H ₉₀ O ₂₀ N ₁₂	Dy ₆ C ₄₂ H ₉₆ O ₃₀ N ₁₈
Formula weight/ gmol ⁻¹	2034.21	2308.31
Temperature/K	273.15	150.15
Crystal system	trigonal	trigonal
Space group	R-3	R-3
a/Å	17.2007(3)	15.7449(3)
b/Å	17.2007(3)	15.7449(3)
c/Å	25.3280(5)	26.0811(6)
α/°	90	90
β/°	90	90
γ/°	120	120
Volume/Å ³	6489.7(3)	5599.3(2)
Z	3	3
ρ _{calc} /g/cm ³	1.990	2.054
μ/mm ⁻¹	27.399	31.614
F(000)	3792.0	3330.0
Diffractionmeter type	Stoe StadiVari	Stoe StadiVari
Radiation	GaKα (λ = 1.34143)	GaKα (λ = 1.34143)
2θ range for data collection/°	7.972 to 113.852	6.364 to 125.038
Index ranges	-14 ≤ h ≤ 21, -21 ≤ k ≤ 20, -27 ≤ l ≤ 31	-20 ≤ h ≤ 13, -18 ≤ k ≤ 20, -30 ≤ l ≤ 34
Reflections collected	17337	24108
Independent reflections	2956 [R _{int} = 0.0843, R _{sigma} = 0.0411]	3014 [R _{int} = 0.0898, R _{sigma} = 0.0338]
Data/restraints/parameters	2956/10/193	3014/0/147
Goodness-of-fit on F ²	1.139	1.061
Final R indexes [I ≥ 2σ (I)]	R ₁ = 0.0773, wR ₂ = 0.2207	R ₁ = 0.0598, wR ₂ = 0.1570
Final R indexes [all data]	R ₁ = 0.0807, wR ₂ = 0.2250	R ₁ = 0.0651, wR ₂ = 0.1620
Largest diff. peak/hole / e Å ⁻³	2.59/-5.63	2.98/-1.08

10 Literature

- [1] G. F. Garcia, D. Guettas, V. Montigaud, P. Larini, R. Sessoli, F. Totti, O. Cador, G. Pilet, B. Le Guennic, *A Dy-4 Cubane: A New Member in the Single-Molecule Toroids Family*, *Angew. Chem. Int. Edit.* **2018**, 57, 17089-17093.
- [2] J. F. Wu, X. L. Li, M. Guo, L. Zhao, Y. Q. Zhang, J. K. Tang, *Realization of toroidal magnetic moments in heterometallic 3d-4f metallocycles*, *Chem. Commun.* **2018**, 54, 1065-1068.
- [3] X. Li, J. Tang, *Recent developments in single-molecule toroids*, *Dalton Trans.* **2019**, 48, 15358-15370.
- [4] H. L. Zhang, Y. Q. Zhai, L. Qin, L. Ungur, H. Nojiri, Y. Z. Zheng, *Single - Molecule Toric Design through Magnetic Exchange Coupling*, *Matter* **2020**, 2, 1481-1493.
- [5] M. Gysler, F. El Hallak, L. Ungur, R. Marx, M. Hakl, P. Neugebauer, Y. Rechkemmer, Y. H. Lan, I. Sheikin, M. Orlita, C. E. Anson, A. K. Powell, R. Sessoli, L. F. Chibotaru, J. van Slageren, *Multitechnique investigation of Dy₃-implications for coupled lanthanide clusters*, *Chem. Sci.* **2016**, 7, 4347-4354.
- [6] J. K. Tang, I. Hewitt, N. T. Madhu, G. Chastanet, W. Wernsdorfer, C. E. Anson, C. Benelli, R. Sessoli, A. K. Powell, *Dysprosium triangles showing single-molecule magnet behavior of thermally excited spin states*, *Angew. Chem. Int. Edit.* **2006**, 45, 1729-1733.
- [7] I. J. Hewitt, J. Tang, N. T. Madhu, C. E. Anson, Y. Lan, J. Luzon, M. Etienne, R. Sessoli, A. K. Powell, *Coupling Dy-3 Triangles Enhances Their Slow Magnetic Relaxation*, *Angew. Chem. Int. Edit.* **2010**, 49, 6352-6356.
- [8] S. F. Xue, X. H. Chen, L. Zhao, Y. N. Guo, J. K. Tang, *Two Bulky-Decorated Triangular Dysprosium Aggregates Conserving Vortex-Spin Structure*, *Inorg. Chem.* **2012**, 51, 13264-13270.
- [9] Y. X. Wang, W. Shi, H. Li, Y. Song, L. Fang, Y. H. Lan, A. K. Powell, W. Wernsdorfer, L. Ungur, L. F. Chibotaru, M. R. Shen, P. Cheng, *A single-molecule magnet assembly exhibiting a dielectric transition at 470 K*, *Chem. Sci.* **2012**, 3, 3366-3370.
- [10] X. L. Li, J. F. Wu, J. K. Tang, B. Le Guennic, W. Shi, P. Cheng, *A planar triangular Dy-3 + Dy-3 single-molecule magnet with a toroidal magnetic moment*, *Chem. Commun.* **2016**, 52, 9570-9573.
- [11] S. K. Langley, K. R. Vignesh, T. Gupta, C. J. Gartshore, G. Rajaraman, C. M. Forsyth, K. S. Murray, *New examples of triangular terbium(iii) and holmium(iii) and hexagonal dysprosium(iii) single molecule toroids*, *Dalton Trans.* **2019**, 48, 15657-15667.
- [12] P. H. Guo, J. L. Liu, Z. M. Zhang, L. Ungur, L. F. Chibotaru, J. D. Leng, F. S. Guo, M. L. Tong, *The First {Dy-4} Single-Molecule Magnet with a Toroidal Magnetic Moment in the Ground State*, *Inorg. Chem.* **2012**, 51, 1233-1235.
- [13] A. Gusev, R. Herchel, I. Nemec, V. Shul'gin, I. L. Eremenko, K. Lyssenko, W. Linert, Z. Travnicka, *Tetranuclear Lanthanide Complexes Containing a Hydrazone-type Ligand. Dysprosium [2 x 2] Gridlike Single-Molecule Magnet and Toric*, *Inorg. Chem.* **2016**, 55, 12470-12476.
- [14] J. F. Wu, S. Y. Lin, S. Shen, X. L. Li, L. Zhao, L. Zhang, J. K. Tang, *Probing the magnetic relaxation and magnetic moment arrangement in a series of Dy-4 squares*, *Dalton Trans.* **2017**, 46, 1577-1584.

- [15] S. Biswas, S. Das, T. Gupta, S. K. Singh, M. Pissas, G. Rajaraman, V. Chandrasekhar, *Observation of Slow Relaxation and Single-Molecule Toroidal Behavior in a Family of Butterfly-Shaped Ln(4) Complexes*, *Chem. Eur. J.* **2016**, 22, 18532-18550.
- [16] L. Ungur, S. K. Langley, T. N. Hooper, B. Moubaraki, E. K. Brechin, K. S. Murray, L. F. Chibotaru, *Net Toroidal Magnetic Moment in the Ground State of a {Dy-6}-Triethanolamine Ring*, *J. Am. Chem. Soc.* **2012**, 134, 18554-18557.
- [17] J. Lu, V. Montigaud, O. Cador, J. Wu, L. Zhao, X. Li, M. Guo, B. Le Guennic, J. Tang, *Lanthanide(III) Hexanuclear Circular Helicates: Slow Magnetic Relaxation, Toroidal Arrangement of Magnetic Moments, and Magnetocaloric Effects*, *Inorg. Chem.* **2019**, 58, 11903-11911.
- [18] Q. Zhang, M. L. Baker, S. Q. Li, M. P. Sarachik, J. J. Baldovi, A. Gaita-Arino, E. Coronado, D. I. Alexandropoulos, T. C. Stamatatos, *Experimental determination of single molecule toroic behaviour in a Dy-8 single molecule magnet*, *Nanoscale* **2019**, 11, 15131-15138.
- [19] S. Y. Lin, W. Wernsdorfer, L. Ungur, A. K. Powell, Y. N. Guo, J. K. Tang, L. Zhao, L. F. Chibotaru, H. J. Zhang, *Coupling Dy-3 Triangles to Maximize the Toroidal Moment*, *Angew. Chem. Int. Edit.* **2012**, 51, 12767-12771.
- [20] K. R. Vignesh, A. Soncini, S. K. Langley, W. Wernsdorfer, K. S. Murray, G. Rajaraman, *Ferrotoroidic ground state in a heterometallic {(CrDy6III)-Dy-III} complex displaying slow magnetic relaxation*, *Nat. Commun.* **2017**, 8.
- [21] K. R. Vignesh, S. K. Langley, A. Swain, B. Moubaraki, M. Damjanovic, W. Wernsdorfer, G. Rajaraman, K. S. Murray, *Slow Magnetic Relaxation and Single-Molecule Toroidal Behaviour in a Family of Heptanuclear {Cr(III)Ln(6)(III)} (Ln=Tb, Ho, Er) Complexes*, *Angew. Chem. Int. Edit.* **2018**, 57, 779-784.
- [22] G. Novitchi, G. Pilet, L. Ungur, V. V. Moshchalkov, W. Wernsdorfer, L. F. Chibotaru, D. Luneau, A. K. Powell, *Heterometallic Cu-II/Dy-III 1D chiral polymers: chirogenesis and exchange coupling of toroidal moments in trinuclear Dy-3 single molecule magnets*, *Chem. Sci.* **2012**, 3, 1169-1176.
- [23] H. Kaemmerer, A. Baniodeh, Y. Peng, E. Moreno-Pineda, M. Schulze, C. E. Anson, W. Wernsdorfer, J. Schnack, A. K. Powell, *Inorganic Approach to Stabilizing Nanoscale Toroidicity in a Tetraicosanuclear Fe₁₈Dy₆ Single Molecule Magnet*, *J. Am. Chem. Soc.* **2020**, 142, 14838-14842.
- [24] S. Langley, K. Vignesh, T. Gupta, C. Gartshore, G. Rajaraman, C. Forsyth, K. Murray, *New examples of triangular terbium(iii) and holmium(iii) and hexagonal dysprosium(iii) single molecule toroics*, *Dalton Trans.* **2019**, 48, 15657-15667.
- [25] B. Weber, *Koordinationschemie : Grundlagen und aktuelle Trends*, **2014**.
- [26] C. Janiak, H.-J. r. Meyer, D. Gudat, R. Alsfasser, E. Riedel, *Riedel Moderne Anorganische Chemie*, De Gruyter, Berlin/Boston, **2012**.
- [27] O. Kahn, *Molecular magnetism*, Wiley-VCH, New York (N.Y.), **1993**.
- [28] H. Lueken, *Magnetochemie : Eine Einführung in Theorie und Anwendung*, Vieweg+Teubner, Wiesbaden, **1999**.
- [29] G. A. Bain, J. F. Berry, *Diamagnetic corrections and Pascal's constants*, *J. Chem. Educ.* **2008**, 85, 532-536.
- [30] J.-P. Launay, M. Verdaguer, *Electrons in molecules from basic principles to molecular electronics*, Oxford Univ. Press, Oxford, **2014**.
- [31] C. P. Landee, M. M. Turnbull, *Review: A gentle introduction to magnetism: units, fields, theory, and experiment*, *J. Coord. Chem.* **2014**, 67, 375-439.

- [32] J. Tang, *Lanthanide Single Molecule Magnets*, Springer, Berlin **2016**.
- [33] D. Gatteschi, R. Sessoli, J. Villain, *Molecular nanomagnets*, Oxford University Press, Oxford; New York, **2007**.
- [34] R. Marin, G. Brunet, M. Murugesu, *Shining New Light on Multifunctional Lanthanide Single-Molecule Magnets*, *Angew. Chem. Int. Edit.* **2020**.
- [35] J. M. Frost, K. L. M. Harriman, M. Murugesu, *The rise of 3-d single-ion magnets in molecular magnetism: towards materials from molecules?*, *Chem. Sci.* **2016**, 7, 2470-2491.
- [36] D. Shao, X. Y. Wang, *Development of Single-Molecule Magnets*, *Chinese J. Chem.* **2020**, 38, 1005-1018.
- [37] D. Aravena, E. Ruiz, *Spin dynamics in single-molecule magnets and molecular qubits*, *Dalton Trans.* **2020**, 49, 9916-9928.
- [38] L. Ungur, L. F. Chibotaru, *Strategies toward High-Temperature Lanthanide-Based Single-Molecule Magnets*, *Inorg. Chem.* **2016**, 55, 10043-10056.
- [39] S. T. Liddle, J. van Slageren, *Improving f-element single molecule magnets*, *Chem. Soc. Rev.* **2015**, 44, 6655-6669.
- [40] Y. F. Deng, T. Han, B. Yin, Y. Z. Zheng, *On balancing the QTM and the direct relaxation processes in single-ion magnets - the importance of symmetry control*, *Inorg. Chem. Front.* **2017**, 4, 1141-1148.
- [41] X. M. Zhang, Y. Y. Duan, H. L. Gao, J. Z. Cui, *Solvent-induced single-molecule magnet behavior and near-infrared luminescence properties of rare earth complexes*, *New J. Chem.* **2020**, 44, 19135-19143.
- [42] N. E. Chakov, W. Wernsdorfer, K. A. Abboud, G. Christou, *Mixed-valence (MnMnIV)-Mn-III clusters [Mn₇O₈(O₂SePh)(8)(O₂CMe)(H₂O)] and [Mn₇O₈(O₂SePh)(9)(H₂O)]: Single-chain magnets exhibiting quantum tunneling of magnetization*, *Inorg. Chem.* **2004**, 43, 5919-5930.
- [43] C. Thirion, W. Wernsdorfer, M. Jamet, V. Dupuis, P. Melinon, A. Perez, D. Mailly, *Micro-SQUID technique for studying the temperature dependence of switching fields of single nanoparticles*, *J. Magn. Magn. Mater.* **2002**, 242, 993-995.
- [44] M. Murugesu, R. Clerac, W. Wernsdorfer, C. E. Anson, A. K. Powell, *Hierarchical assembly of {Fe-13} oxygen-bridged clusters into a close-packed superstructure*, *Angew. Chem. Int. Edit.* **2005**, 44, 6678-6682.
- [45] N. E. Chakov, M. Soler, W. Wernsdorfer, K. A. Abboud, G. Christou, *Single-molecule magnets: Structural characterization, magnetic properties, and F-19 NMR spectroscopy of a Mn-12 family spanning three oxidation levels*, *Inorg. Chem.* **2005**, 44, 5304-5321.
- [46] R. Layfield, M. Murugesu, *Lanthanides and Actinides in Molecular Magnetism*, Wiley, Hoboken **2015**.
- [47] J. D. Rinehart, J. R. Long, *Exploiting single-ion anisotropy in the design of f-element single-molecule magnets*, *Chem. Sci.* **2011**, 2, 2078-2085.
- [48] J. Sievers, *Asphericity of 4f-Shells in Their Hund Rule Ground-States*, *Z. Phys. B Con. Mat.* **1982**, 45, 289-296.
- [49] F. S. Guo, B. M. Day, Y. C. Chen, M. L. Tong, A. Mansikkamaki, R. A. Layfield, *Magnetic hysteresis up to 80 kelvin in a dysprosium metallocene single-molecule magnet*, *Science* **2018**, 362, 1400-+.
- [50] J. L. Liu, Y. C. Chen, M. L. Tong, *Symmetry strategies for high performance lanthanide-based single-molecule magnets*, *Chem. Soc. Rev.* **2018**, 47, 2431-2453.

- [51] A. Dey, P. Kalita, V. Chandrasekhar, *Lanthanide(III)-Based Single-Ion Magnets*, *Acs Omega* **2018**, 3, 9462-9475.
- [52] J. E. Greedan, *Geometrically frustrated magnetic materials*, *J. Mater. Chem.* **2001**, 11, 37-53.
- [53] R. Moessner, A. P. Ramirez, *Geometrical frustration*, *Phys. Today* **2006**, 59, 24-29.
- [54] L. Balents, *Spin liquids in frustrated magnets*, *Nature* **2010**, 464, 199-208.
- [55] I. B. Zeldovich, *Electromagnetic Interaction with Parity Violation*, *Sov. Phys. JETP-Ussr* **1958**, 6, 1184-1186.
- [56] V. M. Dubovik, A. A. Cheshkov, *Form factors and multipoles in electromagnetic interactions*, *Sov. Phys. JETP* **1967**, 24, 924-926.
- [57] T. Raybould, N. Zheludev, University of Southampton, Southampton **2017**.
- [58] A. S. Zimmermann, D. Meier, M. Fiebig, *Ferroic nature of magnetic toroidal order*, *Nat. Commun.* **2014**, 5.
- [59] Y. Gao, C. M. Ho, R. J. Scherrer, *Anapole dark matter at the LHC*, *Phys. Rev. D* **2014**, 89.
- [60] C. S. Wood, S. C. Bennett, D. Cho, B. P. Masterson, J. L. Roberts, C. E. Tanner, C. E. Wieman, *Measurement of parity nonconservation and an anapole moment in cesium*, *Science* **1997**, 275, 1759-1763.
- [61] V. Savinov, N. Papasimakis, D. P. Tsai, N. I. Zheludev, *Optical anapoles*, *Commun. Phys.-Uk* **2019**, 2.
- [62] S. Nanz, *Toroidal multipole moments in classical electrodynamics : an analysis of their emergence and physical significance*, Springer Spektrum, Wiesbaden **2016**.
- [63] K. M. Rabe, *Solid-state physics - Response with a twist*, *Nature* **2007**, 449, 674-675.
- [64] W. C. Jin, E. Drueke, S. W. Li, A. Admasu, R. Owen, M. Day, K. Sun, S. W. Cheong, L. Y. Zhao, *Observation of a ferro-rotational order coupled with second-order nonlinear optical fields*, *Nat. Phys.* **2020**, 16, 42-46.
- [65] B. B. Van Aken, J. P. Rivera, H. Schmid, M. Fiebig, *Observation of ferrotoroidic domains*, *Nature* **2007**, 449, 702-705.
- [66] M. Fiebig, *Revival of the magnetoelectric effect*, *J. Phys. D Appl. Phys.* **2005**, 38, R123-R152.
- [67] N. A. Spaldin, M. Fiebig, M. Mostovoy, *The toroidal moment in condensed-matter physics and its relation to the magnetoelectric effect*, *J. Phys.: Condens. Matter* **2008**, 20.
- [68] J. M. Ashtree, I. Borilović, K. R. Vignesh, A. Swain, S. H. Hamilton, Y. L. Whyatt, S. L. Benjamin, W. Phonsri, C. M. Forsyth, W. Wernsdorfer, A. Soncini, G. Rajaraman, S. K. Langley, K. S. Murray, *Tuning the Ferrotoroidic Coupling and Magnetic Hysteresis in Double-Triangle Complexes {Dy₃MIIIDy₃} via the MIII-linker*, *Eur. J. Inorg. Chem.* **2021**, 2021, 435-444.
- [69] L. Ungur, W. Van den Heuvel, L. F. Chibotaru, *Ab initio investigation of the non-collinear magnetic structure and the lowest magnetic excitations in dysprosium triangles*, *New J. Chem.* **2009**, 33, 1224-1230.
- [70] L. Thomas, F. Lioni, R. Ballou, D. Gatteschi, R. Sessoli, B. Barbara, *Macroscopic quantum tunnelling of magnetization in a single crystal of nanomagnets*, *Nature* **1996**, 383, 145-147.
- [71] V. Chandrasekhar, F. Pointillart, *Organometallic magnets*, Springer, Cham **2020**.

- [72] M. Perfetti, *Cantilever torque magnetometry on coordination compounds: from theory to experiments*, *Coordin. Chem. Rev.* **2017**, 348, 171-186.
- [73] R. Ahlrichs, M. Bar, M. Haser, H. Horn, C. Kolmel, *Electronic-Structure Calculations on Workstation Computers - the Program System Turbomole*, *Chem. Phys. Lett.* **1989**, 162, 165-169.
- [74] F. Furche, R. Ahlrichs, C. Hattig, W. Klopper, M. Sierka, F. Weigend, *Turbomole*, *Wires. Comput. Mol. Sci.* **2014**, 4, 91-100.
- [75] L. F. Chibotaru, L. Ungur, *Ab initio calculation of anisotropic magnetic properties of complexes. I. Unique definition of pseudospin Hamiltonians and their derivation*, *J. Chem. Phys.* **2012**, 137.
- [76] T. Bodenstein, Dissertation, Karlsruhe Institute of Technology, Karlsruhe **2015**.
- [77] N. F. Chilton, D. Collison, E. J. L. McInnes, R. E. P. Winpenny, A. Soncini, *An electrostatic model for the determination of magnetic anisotropy in dysprosium complexes*, *Nat. Commun.* **2013**, 4.
- [78] T. Takui, G. Hanson, L. Berliner, L. L. C. Springer Science + Business Media, *Electron Spin Resonance (ESR) Based Quantum Computing*, **2016**.
- [79] T. Xin, B. X. Wang, K. R. Li, X. Y. Kong, S. J. Wei, T. Wang, D. Ruan, G. L. Long, *Nuclear magnetic resonance for quantum computing: Techniques and recent achievements*, *Chinese Phys. B.* **2018**, 27.
- [80] H. L. Wang, J. M. Peng, Z. H. Zhu, K. Q. Mo, X. F. Ma, B. Li, H. H. Zou, F. P. Liang, *Step-by-Step and Competitive Assembly of Two Dy(III) Single-Molecule Magnets with Their Performance Tuned by Schiff Base Ligands*, *Cryst. Growth Des.* **2019**, 19, 5369-5375.
- [81] K. Zhang, V. Montigaud, O. Cador, G. P. Li, B. Le Guennic, J. K. Tang, Y. Y. Wang, *Tuning the Magnetic Interactions in Dy(III)(4) Single-Molecule Magnets*, *Inorg. Chem.* **2018**, 57, 8550-8557.
- [82] S. K. Langley, B. Moubaraki, C. M. Forsyth, I. A. Gass, K. S. Murray, *Structure and magnetism of new lanthanide 6-wheel compounds utilizing triethanolamine as a stabilizing ligand*, *Dalton Trans.* **2010**, 39, 1705-1708.
- [83] A. Baniodeh, N. Magnani, S. Brase, C. E. Anson, A. K. Powell, *Ligand field variations: tuning the toroidal moment of Dy-6 rings*, *Dalton Trans.* **2015**, 44, 6343-6347.
- [84] L. F. Chibotaru, L. Ungur, A. Soncini, *The origin of nonmagnetic Kramers doublets in the ground state of dysprosium triangles: Evidence for a toroidal magnetic moment*, *Angew. Chem. Int. Edit.* **2008**, 47, 4126-4129.
- [85] A. D. Mighell, *Conventional cells: monoclinic I- and C-centered cells*, *Acta Crystallographica Section B-Structural Science* **2003**, 59, 300-302.
- [86] M. Schulze, Master thesis, Karlsruhe Institut of Technology, Karlsruhe **2019**.
- [87] Q. Zhang, M. Baker, S. Li, M. Sarachik, J. Baldovi, A. Gaita-Arino, E. Coronado, D. Alexandropoulos, T. Stamatatos, *Experimental determination of single molecule toroic behaviour in a Dy-8 single molecule magnet*, *Nanoscale* **2019**, 11, 15131-15138.
- [88] D. A. Johnson, *Principles of Lanthanide Chemistry*, *J. Chem. Educ.* **1980**, 57, 475-477.
- [89] K. A. Mueller, *Effective-Spin Hamiltonian for Non-Kramers Doublets*, *Phys. Rev.* **1968**, 171, 350-&.
- [90] X. Q. Zhao, S. Xiang, J. Wang, D. X. Bao, Y. C. Li, *Magnetic Nature of the Cr-III-Ln(III) Interactions in [Cr(2)(III)Ln(3)(III)] Clusters with Slow Magnetic Relaxation*, *Chemistryopen* **2018**, 7, 192-200.

- [91] E. Riedel, C. Janiak, *Anorganische Chemie*, **2015**.
- [92] Y. Z. Zheng, Y. Lan, C. E. Anson, A. K. Powell, *Anion-Perturbed Magnetic Slow Relaxation in Planar {Dy-4} Clusters*, *Inorg. Chem.* **2008**, 47, 10813-10815.
- [93] G. Abbas, Y. H. Lan, G. E. Kostakis, W. Wernsdorfer, C. E. Anson, A. K. Powell, *Series of Isostructural Planar Lanthanide Complexes [Ln(4)(III)(μ₃-OH)(2)(mdeaH)(2)(piv)(8)] with Single Molecule Magnet Behavior for the Dy-4 Analogue*, *Inorg. Chem.* **2010**, 49, 8067-8072.
- [94] S. K. Langley, N. F. Chilton, I. A. Gass, B. Moubaraki, K. S. Murray, *Planar tetranuclear lanthanide clusters with the Dy-4 analogue displaying slow magnetic relaxation*, *Dalton Trans.* **2011**, 40, 12656-12659.
- [95] F. K. A. Al-Zeidaneen, Dissertation, Karlsruhe Institute of Technology, Karlsruhe, **2021**.
- [96] G. Abbas, G. E. Kostakis, Y. Lan, A. K. Powell, *Synthesis and characterization of isostructural tetranuclear lanthanide complexes [Ln₄(μ₃-OH)₂(ampdH₄)₂(piv)₁₀]·4CH₃CN (Ln=Sm, Eu, Gd, Tb, Dy, Ho, Er)*, *Polyhedron* **2012**, 41, 1-6.
- [97] R. Bagai, G. Christou, *The Drosophila of single-molecule magnetism: [Mn₁₂O₁₂(O₂CR)(16)(H₂O)(4)]*, *Chem. Soc. Rev.* **2009**, 38, 1011-1026.
- [98] Y. Peng, M. K. Singh, C. E. Anson, G. Rajaraman, A. K. Powell, *manuscript in preparation*.
- [99] G. Lu, Y. Liu, W. Deng, G. Z. Huang, Y. C. Chen, J. L. Liu, Z. P. Ni, M. Giansiracusa, N. F. Chilton, M. L. Tong, *A perfect triangular dysprosium single-molecule magnet with virtually antiparallel Ising-like anisotropy*, *Inorg. Chem. Front.* **2020**, 7, 2941-2948.
- [100] Y. S. Meng, S. D. Jiang, B. W. Wang, S. Gao, *Understanding the Magnetic Anisotropy toward Single-Ion Magnets*, *Acc. Chem. Res.* **2016**, 49, 2381-2389.
- [101] V. Mereacre, A. Baniodeh, C. Anson, A. Powell, *Effect of Ligand Substitution on the Interaction Between Anisotropic Dy(III) Ions and Fe-57 Nuclei in Fe₂Dy₂ Coordination Clusters*, *J. Am. Chem. Soc.* **2011**, 133, 15335-15337.
- [102] X. Q. Wang, Z. Y. Li, Z. X. Zhu, J. Zhu, S. Q. Liu, J. Ni, J. J. Zhang, *Pentanuclear {Cr(2)Ln(3)} (Ln = Dy, Tb) Heterometallic Clusters Based on an Amino Acid Ligand: Slow Relaxation of Magnetization and Substitution Reactions*, *Eur. J. Inorg. Chem.* **2013**, 2013, 5153-5160.
- [103] H. Li, W. Shi, Z. Niu, J. M. Zhou, G. Xiong, L. L. Li, P. Cheng, *Remarkable Ln(3)(III)Fe(2)(III) clusters with magnetocaloric effect and slow magnetic relaxation*, *Dalton Trans.* **2015**, 44, 468-471.
- [104] H. J. Lun, X. J. Kong, L. S. Long, L. S. Zheng, *Trigonal bipyramidal CoII₂Dy(3) cluster exhibiting single-molecule magnet behavior*, *Dalton Trans.* **2020**, 49, 2421-2425.
- [105] P. H. Lin, T. J. Burchell, L. Ungur, L. F. Chibotaru, W. Wernsdorfer, M. Murugesu, *A Polynuclear Lanthanide Single-Molecule Magnet with a Record Anisotropic Barrier*, *Angew. Chem. Int. Edit.* **2009**, 48, 9489-9492.
- [106] S. F. Xue, L. Zhao, Y. N. Guo, R. P. Deng, Y. Guo, J. K. Tang, *A series of tetranuclear lanthanide complexes comprising two edge-sharing triangular units with field-induced slow magnetic relaxation for Dy-4 species*, *Dalton Trans.* **2011**, 40, 8347-8352.
- [107] P. F. Yan, P. H. Lin, F. Habib, T. Aharen, M. Murugesu, Z. P. Deng, G. M. Li, W. B. Sun, *Planar Tetranuclear Dy(III) Single-Molecule Magnet and Its Sm(III)*,

- Gd(III), and Tb(III) Analogues Encapsulated by Salen-Type and beta-Diketonate Ligands, Inorg. Chem.* **2011**, 50, 7059-7065.
- [108] J. Ji, K. J. Jiang, H. Y. Shen, Y. Tian, Y. L. Hou, H. L. Gao, W. M. Wang, J. Z. Cui, *Structures and magnetic properties of rhombus-shaped tetranuclear [Ln(4)] clusters: Dy-4 cluster displaying single molecule magnet behavior, J. Mol. Struct.* **2021**, 1228.
- [109] H. Yao, G. Calvez, C. Daiguebonne, K. Bernot, Y. Suffren, O. Guillou, *Hetero-hexalanthanide Complexes: A New Synthetic Strategy for Molecular Thermometric Probes, Inorg. Chem.* **2019**, 58, 16180-16193.
- [110] S. Yu, Z. B. Hu, Z. L. Chen, B. Li, Y. Q. Zhang, Y. N. Liang, D. C. Liu, D. Yao, F. P. Liang, *Two Dy(III) Single-Molecule Magnets with Their Performance Tuned by Schiff Base Ligands, Inorg. Chem.* **2019**, 58, 1191-1200.
- [111] L. Zhong, W.-B. Chen, Z.-J. OuYang, M. Yang, Y.-Q. Zhang, S. Gao, M. Schulze, W. Wernsdorfer, W. Dong, *Unprecedented one-dimensional chain and two-dimensional network dysprosium, Chem. Commun.* **2020**, 56, 2590-2593.
- [112] T. Kajiwara, H. S. Wu, T. Ito, N. Iki, S. Miyano, *Octalanthanide wheels supported by p-tert-butylsulfonycalix[4]arene, Angew. Chem. Int. Edit.* **2004**, 43, 1832-1835.
- [113] L. G. Westin, M. Kritikos, A. Caneschi, *Self assembly, structure and properties of the decanuclear lanthanide ring complex, Dy-10(OC₂H₄OCH₃)(30), Chem. Commun.* **2003**, 1012-1013.
- [114] T. Kajiwara, K. Katagiri, S. Takaishi, M. Yamashita, N. Iki, *A dodecalanthanide wheel supported by p-tert-butylsulfonycalix[4]arene, Chem. Asian J.* **2006**, 1, 349-351.
- [115] O. V. Dolomanov, L. J. Bourhis, R. J. Gildea, J. A. K. Howard, H. Puschmann, *OLEX2: a complete structure solution, refinement and analysis program, J. Appl. Crystallogr.* **2009**, 42, 339-341.

11 Acknowledgements

As part of this work, I would like to thank many people who have accompanied me along the way.

First and foremost, I would like to thank my doctoral mother, Prof. **Annie** K. Powell, who has always shown me support and trust.

Likewise, special thanks go to Christopher (**Chris**) E. Anson, who was able to provide me with valuable feedback through proofreading with the English language and his expertise.

For the measurements and refinements of my crystals, I also thank Chris, Dr. **Olaf** Fuhr, and Prof. Dr. **Dieter** Fenske very much.

For valuable tips and instruction on the PXRD I would like to thank Dr. **Andreas** Eichhöfer.

I thank Dr. **Eufemio** Moreno Pineda, Dr. **Nithin** Suryadevara, Dr. **Björn** Schwarz and of course **Soeren** Schlittenhardt for numerous magnetic measurements at the SQUID and the VSM.

I would like to thank **Michael** Schulze for the micro-SQUID measurements.

Yadav Twinkle and Dr. **Marko** Damjanovic I thank for the ab initio calculations of the $\{Ln_3\}$ complexes in this work.

I **thank** the whole AK Powell for the pleasant working atmosphere especially: Dr. **Massoma** Ibrahim, **Hagen** Kämmerer, **Jonas** Braun, Dr. **Rouven** Pfleger, Dr. **Marcel** Merkel, Dr. Krisana Peewasan (**Jacky**), Dr. Anthony **Blue** Carter, Dr. **Yan** Peng, **Umaira** Shuaib (Udo Shubi) and **Luis** Basche. Special **thanks** also go to **Gertraud** Amschlenger, who always has an open ear for problems of any kind and always helps us with documents and paperwork of any kind. Also thank you to all other current and former group members I forgot to mention here ...

Last but not least, I would like to thank my parents **Jürgen** and **Andrea** Ruppert and my sister **Monika**, my whole family (here a special thank to my aunt **Anke** und my uncle **Reinhard** Bott) and my friends but especially **Rami** and **Dani** and my girlfriend **Martina** who gave me encouragement and motivation during this time.

For the financial support I thank the **SFB/TRR 88 3MET**.

12 Appendix

12.1 Molecular structures, bond lengths, angles and distances of (1) and (2)

Molecular structure of

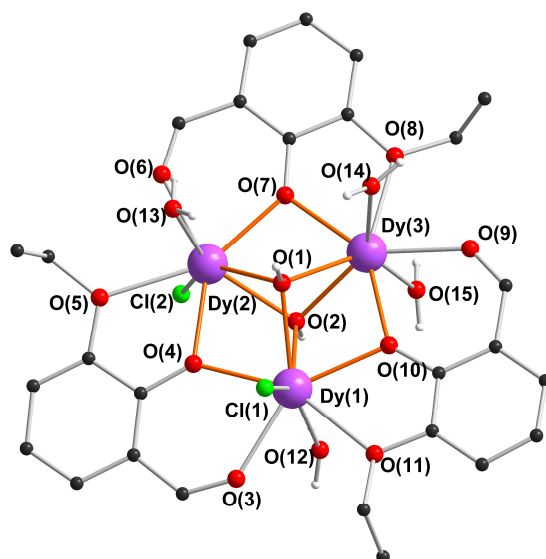
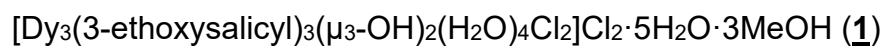


Figure 12-1 Molecular structure of $[\text{Dy}_3(3\text{-ethoxysalicyl})_3(\mu_3\text{-OH})_2(\text{H}_2\text{O})_4\text{Cl}_2]\text{Cl}_2 \cdot 5\text{H}_2\text{O} \cdot 3\text{MeOH}$ (1)

Table 12-1 Distances [Å] and angles [°] of (1).

Dy(3)	Dy(2)	3.5495(5)
Dy(3)	Dy(1)	3.5497(5)
Dy(2)	Dy(1)	3.5683(5)
Dy(3)	O(2)	2.358(5)
Dy(3)	O(1)	2.380(5)
Dy(3)	O(15)	2.340(6)
Dy(3)	O(14)	2.365(7)
Dy(3)	O(9)	2.350(7)
Dy(3)	O(10)	2.330(6)
Dy(3)	O(8)	2.501(6)
Dy(3)	O(7)	2.337(6)
Dy(2)	Cl(2)	2.684(2)
Dy(2)	O(2)	2.385(5)
Dy(2)	O(1)	2.377(5)
Dy(2)	O(13)	2.349(7)
Dy(2)	O(7)	2.329(5)

Dy(2)	O(6)	2.371(6)
Dy(2)	O(4)	2.345(5)
Dy(2)	O(5)	2.505(6)
Dy(1)	Cl(1)	2.687(3)
Dy(1)	O(2)	2.396(5)
Dy(1)	O(1)	2.366(5)
Dy(1)	O(12)	2.358(8)
Dy(1)	O(10)	2.343(6)
Dy(1)	O(11)	2.512(7)
Dy(1)	O(3)	2.349(7)
Dy(1)	O(4)	2.320(5)

Dy(2)	Dy(3)	Dy(1)	60.349(10)
Dy(1)	Dy(2)	Dy(3)	59.83(1)
Dy(3)	Dy(1)	Dy(2)	59.82(1)
Dy(3)	O(2)	Dy(2)	96.89(18)
Dy(3)	O(2)	Dy(1)	96.61(18)
Dy(2)	O(2)	Dy(1)	96.55(18)
Dy(2)	O(1)	Dy(3)	96.51(18)
Dy(1)	O(1)	Dy(3)	96.82(18)
Dy(1)	O(1)	Dy(2)	97.58(18)

Molecular structure of
 $[\text{Dy}_3(3\text{-ethoxysalicyl})_3(\mu_3\text{-OH})_2(\text{H}_2\text{O})_2(\text{CH}_3\text{OH})\text{Cl}_3]\text{Cl}\cdot 2\text{H}_2\text{O}\cdot 2\text{CH}_3\text{OH}$ (**2**)

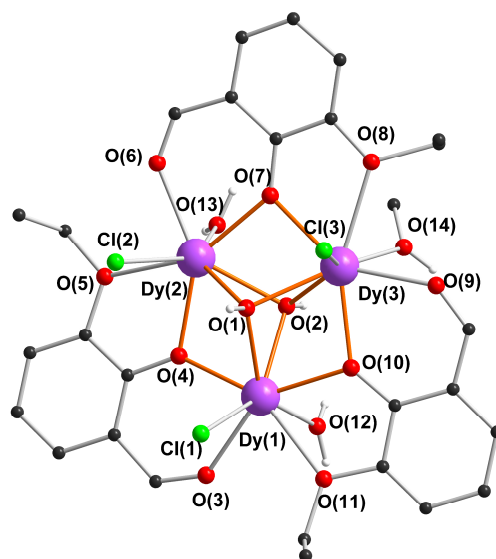


Figure 12-2 Molecular structure of $[\text{Dy}_3(3\text{-ethoxysalicyl})_3(\mu_3\text{-OH})_2(\text{H}_2\text{O})_2(\text{CH}_3\text{OH})\text{Cl}_3]\text{Cl}\cdot 2\text{H}_2\text{O}\cdot 2\text{CH}_3\text{OH}$ (**2**).

Table 12-2 Distances [Å] and angles [°] of (**2**).

Dy(1)	Dy2	3.5129(5)
Dy(1)	Dy3	3.5463(5)
Dy(2)	Dy(3)	3.5370(6)
Dy(1)	Cl(1)	2.6957(19)
Dy(1)	O(1)	2.352(5)
Dy(1)	O(2)	2.372(5)
Dy(1)	O(12)	2.349(6)
Dy(1)	O(11)	2.487(5)
Dy(1)	O(10)	2.346(5)
Dy(1)	O(3)	2.355(5)
Dy(1)	O(4)	2.310(5)
Dy(2)	Cl(2)	2.710(2)
Dy(2)	O(1)	2.346(5)
Dy(2)	O(2)	2.384(6)
Dy(2)	O(13)	2.389(6)
Dy(2)	O(4)	2.313(5)
Dy(2)	O(5)	2.484(6)
Dy(2)	O(6)	2.338(6)
Dy(2)	O(7)	2.320(6)
Dy(3)	Cl(3)	2.676(2)

Dy(3)	O(1)	2.353(5)
Dy(3)	O(2)	2.350(5)
Dy(3)	O(14)	2.329(6)
Dy(3)	O(10)	2.324(5)
Dy(3)	O(9)	2.362(7)
Dy(3)	O(7)	2.346(6)
Dy(3)	O(8)	2.507(7)

Dy(2)	Dy(1)	Dy(3)	60.138(11)
Dy(1)	Dy(2)	Dy(3)	60.40(1)
Dy(2)	Dy(3)	Dy(1)	59.46(1)
Dy(1)	O(1)	Dy(3)	97.8(2)
Dy(2)	O(1)	Dy(1)	96.80(18)
Dy(2)	O(1)	Dy(3)	97.65(19)
Dy(1)	O(2)	Dy(2)	95.2(2)
Dy(3)	O(2)	Dy(1)	97.37(18)
Dy(3)	O(2)	Dy(2)	96.70(19)

12.2 Molecular structure, bond lengths, angles and distances of (3) to (6)

Molecular structure of isostructural
 $[\text{Ln}_3(3\text{-ethoxysalicyl})_3(\mu_3\text{-OH})_2(\text{H}_2\text{O})_2(\text{CH}_3\text{OH})\text{Cl}_3]\text{Cl}$

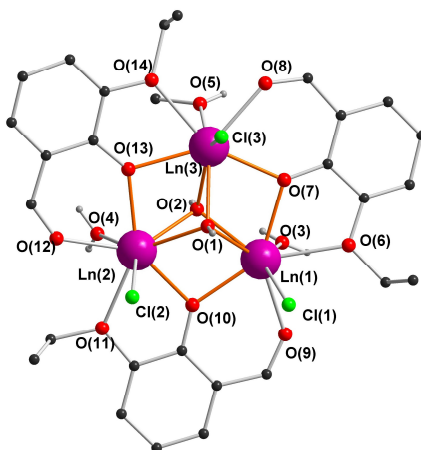


Figure 12-3 Molecular structure of (3) to (6) with Ln = Eu in (3), Tb in (4), Ho in (5) and Er in (6).

Table 12-3 Distances [Å] and angles [°] of (3).

Eu(1)	Eu(2)	3.5782(9)
Eu(1)	Eu(3)	3.6167(9)
Eu(2)	Eu(3)	3.6061(11)
Eu(1)	Cl(1)	2.723(3)
Eu(1)	O(1)	2.404(8)
Eu(1)	O(2)	2.416(8)
Eu(1)	O(3)	2.408(10)
Eu(1)	O(6)	2.525(9)
Eu(1)	O(7)	2.393(9)
Eu(1)	O(9)	2.367(10)
Eu(1)	O(10)	2.387(9)
Eu(2)	Cl(2)	2.743(3)
Eu(2)	O(1)	2.394(8)
Eu(2)	O(2)	2.409(9)
Eu(2)	O(4)	2.431(8)
Eu(2)	O(10)	2.362(8)
Eu(2)	O(11)	2.514(10)
Eu(2)	O(12)	2.361(10)
Eu(2)	O(13)	2.359(9)
Eu(2)	C(12)	3.258(13)
Eu(3)	Cl(3)	2.715(3)
Eu(3)	O(1)	2.391(10)

Eu(3)	O(2)	2.381(8)
Eu(3)	O(5)	2.356(9)
Eu(3)	O(7)	2.370(9)
Eu(3)	O(8)	2.409(12)
Eu(3)	O(13)	2.384(10)
Eu(3)	O(14)	2.539(10)

Eu(1)	Eu(2)	Eu(3)	60.45(2)
Eu(2)	Eu(3)	Eu(1)	59.39(2)
Eu(3)	Eu(1)	Eu(2)	60.16(2)
Eu(2)	O(1)	Eu(1)	96.4(3)
Eu(3)	O(1)	Eu(1)	97.9(3)
Eu(3)	O(1)	Eu(2)	97.8(3)
Eu(2)	O(2)	Eu(1)	95.7(3)
Eu(3)	O(2)	Eu(1)	97.9(3)
Eu(3)	O(2)	Eu(2)	97.7(3)

Table 12-4 Distances [Å] and angles [°] of **(4)**.

Tb(1)	Tb(2)	3.5388(5)
Tb(1)	Tb(3)	3.5772(5)
Tb(2)	Tb(3)	3.5555(6)
Tb(1)	Cl(1)	2.7032(19)
Tb(1)	O(1)	2.355(5)
Tb(1)	O(2)	2.401(5)
Tb(1)	O(3)	2.364(6)
Tb(1)	O(6)	2.497(5)
Tb(1)	O(7)	2.366(5)
Tb(1)	O(9)	2.368(5)
Tb(1)	O(10)	2.339(5)
Tb(2)	Cl(2)	2.7141(19)
Tb(2)	O(1)	2.349(5)
Tb(2)	O(2)	2.383(5)
Tb(2)	O(4)	2.398(5)
Tb(2)	O(10)	2.329(5)
Tb(2)	O(11)	2.504(6)
Tb(2)	O(12)	2.359(5)
Tb(2)	O(13)	2.336(5)
Tb(3)	Cl(3)	2.685(2)
Tb(3)	O(1)	2.367(5)
Tb(3)	O(2)	2.361(5)
Tb(3)	O(5)	2.347(6)

Tb(3)	O(7)	2.354(5)
Tb(3)	O(8)	2.388(6)
Tb(3)	O(13)	2.366(5)
Tb(3)	O(14)	2.512(6)

Tb(1)	Tb(2)	Tb(3)	60.56(1)
Tb(2)	Tb(3)	Tb(1)	59.49(1)
Tb(3)	Tb(1)	Tb(2)	59.95(1)
Tb(1)	O(1)	Tb(3)	98.52(19)
Tb(2)	O(1)	Tb(1)	97.59(18)
Tb(2)	O(1)	Tb(3)	97.86(18)
Tb(2)	O(2)	Tb(1)	95.43(18)
Tb(3)	O(2)	Tb(1)	97.39(18)
Tb(3)	O(2)	Tb(2)	97.10(17)

Table 12-5 Distances [Å] and angles [°] of **(5)**.

Ho(1)	Ho(2)	3.4969(4)
Ho(1)	Ho(3)	3.5321(4)
Ho(2)	Ho(3)	3.5234(4)
Ho(1)	Cl(1)	2.6852(13)
Ho(1)	O(1)	2.334(4)
Ho(1)	O(2)	2.368(4)
Ho(1)	O(3)	2.338(4)
Ho(1)	O(6)	2.477(4)
Ho(1)	O(7)	2.337(4)
Ho(1)	O(9)	2.335(4)
Ho(1)	O(10)	2.305(4)
Ho(2)	Cl(2)	2.6891(14)
Ho(2)	O(1)	2.334(4)
Ho(2)	O(2)	2.369(4)
Ho(2)	O(4)	2.357(4)
Ho(2)	O(10)	2.303(4)
Ho(2)	O(11)	2.482(4)
Ho(2)	O(12)	2.332(4)
Ho(2)	O(13)	2.314(4)
Ho(3)	Cl(3)	2.6669(14)
Ho(3)	O(1)	2.332(4)
Ho(3)	O(2)	2.343(4)
Ho(3)	O(5)	2.322(4)
Ho(3)	O(7)	2.314(4)

Ho(3)	O(8)	2.376(4)
Ho(3)	O(13)	2.327(4)
Ho(3)	O(14)	2.506(4)

Ho(1)	Ho(2)	Ho(3)	60.41(1)
Ho(2)	Ho(3)	Ho(1)	59.42(1)
Ho(3)	Ho(1)	Ho(2)	60.17(1)
Ho(2)	O(1)	Ho(1)	97.05(13)
Ho(3)	O(1)	Ho(1)	98.41(13)
Ho(3)	O(1)	Ho(2)	98.09(13)
Ho(1)	O(2)	Ho(2)	95.15(13)
Ho(3)	O(2)	Ho(1)	97.13(13)
Ho(3)	O(2)	Ho(2)	96.79(13)

Table 12-6 Distances [Å] and angles [°] of **(6)**.

Er(1)	Er(2)	3.4824(9)
Er(1)	Er(3)	3.5182(8)
Er(2)	Er(3)	3.5074(9)
Er(1)	Cl(1)	2.675(3)
Er(1)	O(1)	2.335(9)
Er(1)	O(2)	2.356(9)
Er(1)	O(3)	2.316(10)
Er(1)	O(6)	2.466(10)
Er(1)	O(7)	2.316(10)
Er(1)	O(9)	2.330(10)
Er(1)	O(10)	2.314(10)
Er(2)	Cl(2)	2.682(3)
Er(2)	O(1)	2.320(9)
Er(2)	O(2)	2.373(10)
Er(2)	O(4)	2.363(9)
Er(2)	O(10)	2.283(9)
Er(2)	O(11)	2.477(10)
Er(2)	O(12)	2.310(10)
Er(2)	O(13)	2.292(10)
Er(3)	Cl(3)	2.655(3)
Er(3)	O(1)	2.335(9)
Er(3)	O(2)	2.327(9)
Er(3)	O(5)	2.308(9)
Er(3)	O(7)	2.312(9)
Er(3)	O(8)	2.337(11)
Er(3)	O(13)	2.312(10)

Er(3) | O(14) | 2.498(10)

Er(1)	Er(2)	Er(3)	60.44(2)
Er(2)	Er(3)	Er(1)	59.43(2)
Er(3)	Er(1)	Er(2)	60.13(2)
Er(2)	O(1)	Er(1)	96.8(3)
Er(2)	O(1)	Er(3)	97.8(3)
Er(3)	O(1)	Er(1)	97.8(3)
Er(1)	O(2)	Er(2)	94.9(3)
Er(3)	O(2)	Er(1)	97.4(3)
Er(3)	O(2)	Er(2)	96.5(3)

12.3 Molecular structure, coordination spheres, bond lengths, angles, distances and packing of (7) to (16)

Molecular structure of $[\text{Cr}_2\text{Dy}_3(\text{pfba})_6(\mu_3\text{-OH})_6(\text{NO}_3)_3(\text{H}_2\text{O})_2(\text{C}_3\text{H}_7\text{OH})]\cdot\text{H}_2\text{O}$ (**7**)

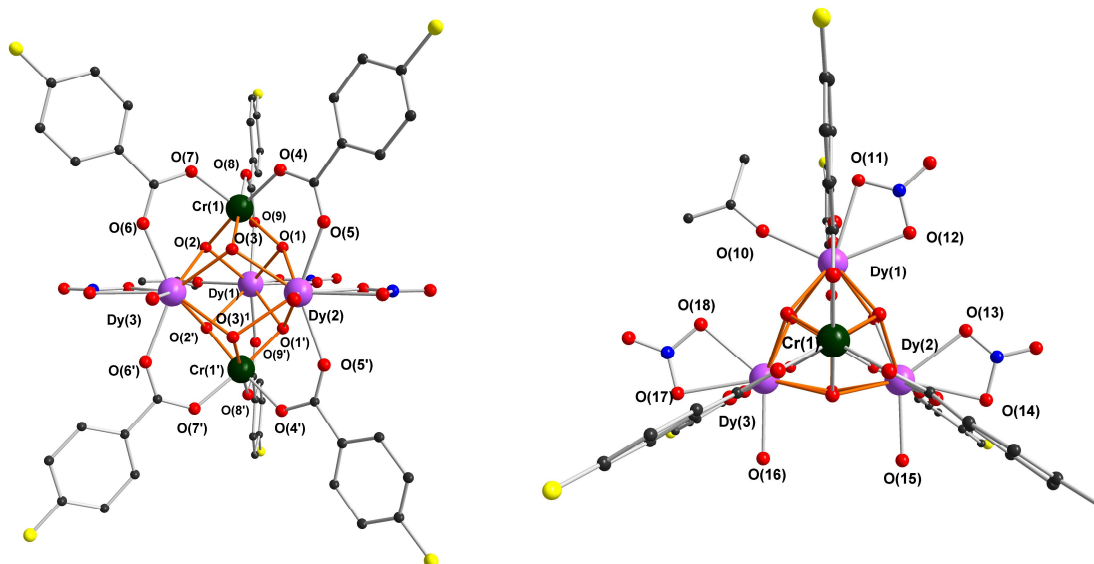


Figure 12-4 Molecular structure of $[\text{Cr}_2\text{Dy}_3(\text{pfba})_6(\mu_3\text{-OH})_6(\text{NO}_3)_3(\text{H}_2\text{O})_2(\text{C}_3\text{H}_7\text{OH})]\cdot\text{H}_2\text{O}$ (**7**) from the side view (left) and down the pseudo 3-fold axis (right). Primed atoms at $x, 1-y, z$.

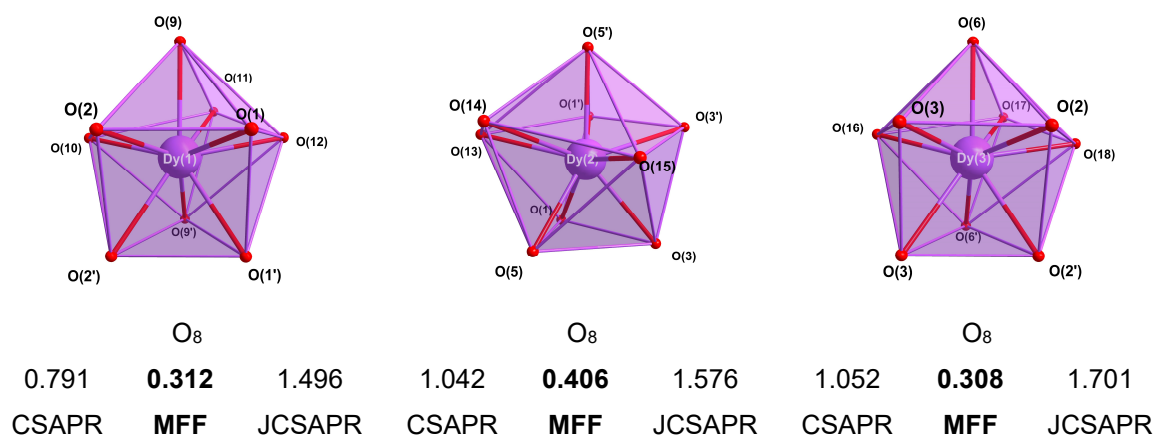


Figure 12-5 Coordination spheres around the Dy(III) ions with deviations from the perfect geometries in %.

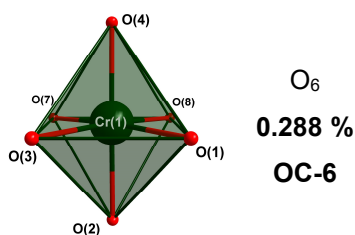


Figure 12-6 Coordination spheres around the Cr(III) ions with deviations from the perfect geometry.

The packing of the molecules is stabilized by hydrogen bonding between coordinated isopropanol and the fluorides of the organic ligands. The smallest inter-triangle {Dy₃} distance is 12.405 Å. The smallest intermolecular distance between the Cr(III) ions is 10.405 Å. The packing with the coordination spheres around the ions is shown in Figure 12-7.

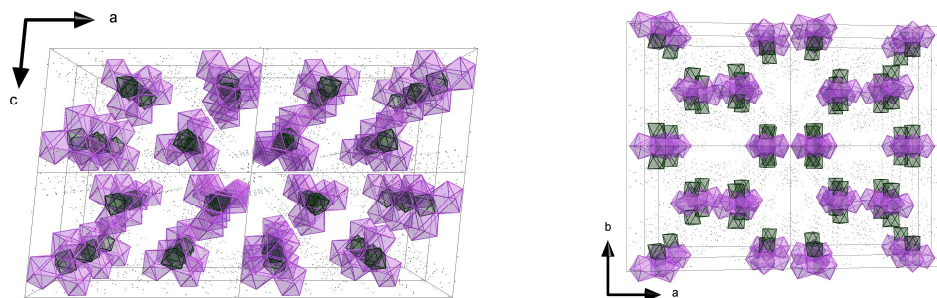


Figure 12-7 Packing of (**7**) from different viewing directions. Coordination spheres of the Dy(III) ions in lavender and of the Cr(III) ions in dark green.

Table 12-7 Distances [Å] of (**7**).

Cr(1)	Cr(1')	5.2136(1)
Dy(1)	Dy(2)	3.9558(4)
Dy(1)	Dy(3)	3.9462(3)
Dy(2)	Dy(3)	3.9719(4)
Dy(1)	Cr(1)	3.4841(6)
Dy(2)	Cr(1)	3.4546(6)
Dy(3)	Cr(1)	3.4616(5)
Dy(1)	O(1)	2.425(3)
Dy(1)	O(1')	2.425(3)
Dy(1)	O(3)	2.419(2)
Dy(1)	O(3')	2.419(2)
Dy(1)	O(9)	2.335(2)
Dy(1)	O(9')	2.335(2)
Dy(1)	O(11)	2.567(5)
Dy(1)	O(12)	2.433(4)
Dy(1)	O(10)	2.278(4)
Dy(2)	O(1)	2.390(3)
Dy(2)	O(1')	2.390(3)
Dy(2)	O(2)	2.425(3)
Dy(2)	O(2')	2.425(3)
Dy(2)	O(5)	2.343(3)

Dy(2)	O(5')	2.343(3)
Dy(2)	O(13)	2.432(5)
Dy(2)	O(14)	2.602(10)
Dy(2)	O(15)	2.364(5)
Dy(3)	O(2)	2.435(3)
Dy(3)	O(2')	2.435(3)
Dy(3)	O(3')	2.390(3)
Dy(3)	O(3)	2.390(3)
Dy(3)	O(6')	2.340(3)
Dy(3)	O(6)	2.340(3)
Dy(3)	O(16)	2.347(5)
Dy(3)	O(17)	2.584(5)
Dy(3)	O(18)	2.459(5)
Cr(1)	O(1)	1.964(3)
Cr(1)	O(2)	1.967(3)
Cr(1)	O(3)	1.952(3)
Cr(1)	O(4)	1.984(3)
Cr(1)	O(7)	1.977(2)
Cr(1)	O(8)	1.982(3)

Table 12-8 Angles [°] of (**7**).

Dy(1)	Dy(2)	Dy(3)	59.70(1)
Dy(1)	Dy(3)	Dy(2)	59.94(1)
Dy(2)	Dy(1)	Dy(3)	60.35(1)
Cr(1)	Dy(1)	Cr(1')	96.869
Cr(1)	Dy(2)	Cr(1')	97.974
Cr(1)	Dy(3)	Cr(1')	97.715
Cr(1)	O(1)	Dy(1)	104.59(12)
Cr(1)	O(1)	Dy(2)	104.60(14)
Cr(1)	O(2)	Dy(2)	103.26(12)
Cr(1)	O(2)	Dy(3)	103.20(12)
Cr(1)	O(3)	Dy(1)	105.23(11)
Cr(1)	O(3)	Dy(3)	105.31(13)
Dy(2)	O(1)	Dy(1)	110.49(12)
Dy(2)	O(2)	Dy(3)	109.65(10)
Dy(3)	O(3)	Dy(1)	110.31(10)
Cr(1)	Dy(1)	Dy(2)	54.89(1)
Cr(1)	Dy(2)	Dy(1)	55.59(1)
Cr(1)	Dy(2)	Dy(3)	55.03(1)
Cr(1)	Dy(3)	Dy(2)	54.87(1)
Cr(1)	Dy(1)	Dy(3)	55.11(1)
Cr(1)	Dy(3)	Dy(1)	55.65(1)

The packing is stabilized by hydrogen bonding between isopropanol and $\mu_3\text{-OH}^-$ units. The shortest inter-triangle $\{\text{Dy}_3\}$ distance is with 11.500 Å smaller than in (**7**) and also the shortest intermolecular Cr-Cr distance is with 6.307 Å a lot smaller than in (**7**). The packing is shown with the coordination spheres around the ions in Figure 12-11.

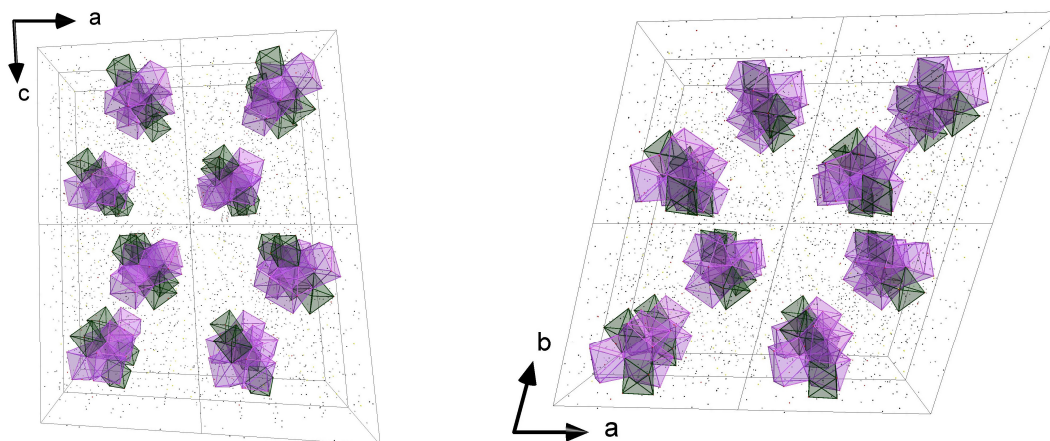


Figure 12-11 Packing of (**8**) from different viewing directions. Coordination spheres of the Dy(III) ions in lavender and of the Cr(III) ions in dark green.

Table 12-9 Distances [Å] of (**8**).

Cr(1)	Cr(2)	5.2129(8)
Dy(1)	Dy(2)	3.8798(3)
Dy(1)	Dy(3)	3.8823(3)
Dy(2)	Dy(3)	3.8833(3)
Dy(1)	Cr(1)	3.4476(6)
Dy(1)	Cr(2)	3.4394(6)
Dy(2)	Cr(1)	3.4126(6)
Dy(2)	Cr(2)	3.4256(6)
Dy(3)	Cr(1)	3.4372(6)
Dy(3)	Cr(2)	3.4632(6)
Dy(1)	O(1)	2.391(3)
Dy(1)	O(2)	2.371(3)
Dy(1)	O(4)	2.384(3)
Dy(1)	O(5)	2.391(3)
Dy(1)	O(16)	2.360(3)
Dy(1)	O(17)	2.352(3)
Dy(1)	O(19)	2.276(3)
Dy(1)	O(27)	2.392(3)
Dy(2)	O(2)	2.388(3)
Dy(2)	O(3)	2.374(3)
Dy(2)	O(5)	2.402(3)
Dy(2)	O(6)	2.389(3)

Dy(2)	O(8)	2.317(3)
Dy(2)	O(11)	2.313(3)
Dy(2)	O(23)	2.317(3)
Dy(2)	O(26)	2.376(3)
Dy(3)	O(1)	2.384(3)
Dy(3)	O(3)	2.384(3)
Dy(3)	O(4)	2.412(3)
Dy(3)	O(6)	2.405(3)
Dy(3)	O(10)	2.355(3)
Dy(3)	O(14)	2.335(3)
Dy(3)	O(20)	2.281(3)
Dy(3)	O(25)	2.385(3)
Cr(1)	O(1)	1.969(3)
Cr(1)	O(2)	1.967(3)
Cr(1)	O(3)	1.962(3)
Cr(1)	O(7)	1.986(3)
Cr(1)	O(9)	1.973(3)
Cr(1)	O(15)	1.979(3)
Cr(2)	O(4)	1.964(3)
Cr(2)	O(5)	1.960(3)
Cr(2)	O(6)	1.956(3)
Cr(2)	O(12)	1.995(3)
Cr(2)	O(13)	2.004(3)
Cr(2)	O(18)	1.987(3)

Table 12-10 Angles [°] of (**8**).

Dy(1)	Dy(2)	Dy(3)	60.01(1)
Dy(1)	Dy(3)	Dy(2)	59.95(1)
Dy(2)	Dy(1)	Dy(3)	60.04(1)
Cr(1)	Dy(1)	Cr(2)	98.39(1)
Cr(1)	Dy(2)	Cr(2)	99.34(1)
Cr(1)	Dy(3)	Cr(2)	98.13(1)
Cr(1)	O(1)	Dy(1)	104.09(11)
Cr(1)	O(1)	Dy(3)	103.90(11)
Cr(1)	O(2)	Dy(1)	104.89(11)
Cr(1)	O(2)	Dy(2)	102.77(11)
Cr(1)	O(3)	Dy(2)	103.43(11)
Cr(1)	O(3)	Dy(3)	104.10(11)
Cr(2)	O(4)	Dy(1)	104.12(11)
Cr(2)	O(4)	Dy(3)	104.15(12)
Cr(2)	O(5)	Dy(1)	104.02(11)
Cr(2)	O(5)	Dy(2)	103.03(11)
Cr(2)	O(6)	Dy(2)	103.62(11)

Cr(2)	O(6)	Dy(3)	104.67(12)
Dy(1)	O(2)	Dy(2)	109.23(10)
Dy(1)	O(4)	Dy(3)	108.08(10)
Dy(1)	O(5)	Dy(2)	108.07(10)
Dy(2)	O(6)	Dy(3)	108.19(10)
Dy(2)	O(3)	Dy(3)	109.41(10)
Dy(3)	O(1)	Dy(1)	108.81(10)
Cr(1)	Dy(1)	Dy(2)	55.13(1)
Cr(1)	Dy(2)	Dy(1)	55.99(1)
Cr(1)	Dy(2)	Dy(3)	55.76(1)
Cr(1)	Dy(3)	Dy(2)	55.17(1)
Cr(1)	Dy(1)	Dy(3)	55.55(1)
Cr(1)	Dy(3)	Dy(1)	55.80(1)
Cr(2)	Dy(1)	Dy(2)	55.42(1)
Cr(2)	Dy(2)	Dy(1)	55.75(1)
Cr(2)	Dy(2)	Dy(3)	56.15(1)
Cr(2)	Dy(3)	Dy(2)	55.23(1)
Cr(2)	Dy(1)	Dy(3)	56.07(1)
Cr(2)	Dy(3)	Dy(2)	55.23(1)
Cr(2)	Dy(1)	Dy(3)	56.07(1)
Cr(2)	Dy(3)	Dy(1)	55.48(1)
Dy(1)	Cr(1)	Dy(2)	68.88(1)
Dy(2)	Cr(1)	Dy(3)	69.07(1)
Dy(3)	Cr(2)	Dy(1)	68.45(1)
Dy(3)	Cr(1)	Dy(1)	58.65(1)
Dy(1)	Cr(2)	Dy(2)	68.83(1)
Dy(2)	Cr(2)	Dy(3)	68.62(1)

Molecular structure of $[\text{Cr}_2\text{Dy}_3(\text{pclba})_9(\mu_3\text{-OH})_6(\text{C}_3\text{H}_7\text{OH})_3]\cdot\text{H}_2\text{O}\cdot\text{C}_3\text{H}_7\text{OH}$ (**9**)

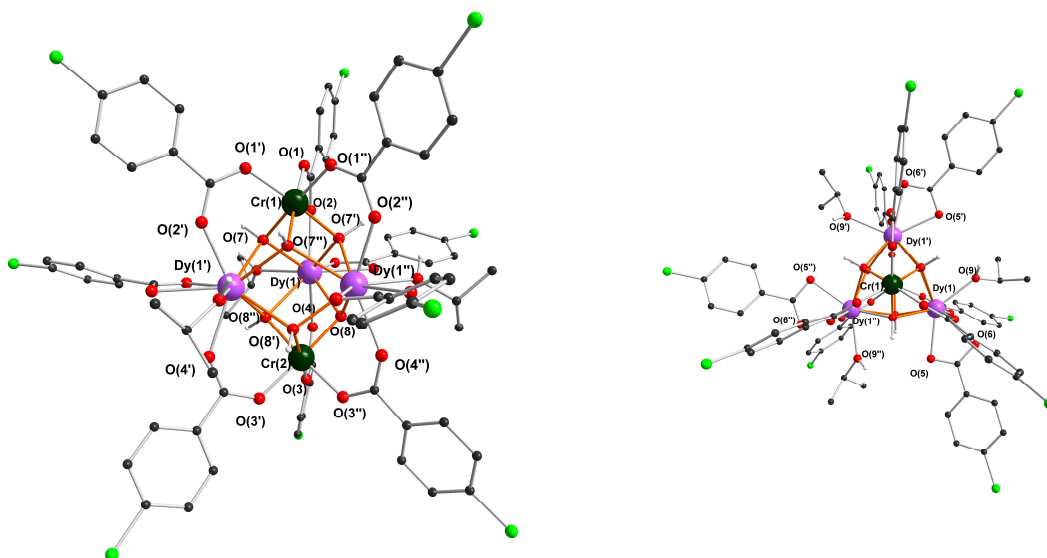


Figure 12-12 Molecular structure of $[\text{Cr}_2\text{Dy}_3(\text{pclba})_9(\mu_3\text{-OH})_6(\text{C}_3\text{H}_7\text{OH})_3]\cdot\text{H}_2\text{O}\cdot\text{C}_3\text{H}_7\text{OH}$ (**9**) from the side view (left) and down the pseudo 3-fold axis (right). Primed atoms at 1-x, x-y, z; double-primed atoms at 1-x+y, 1-x.

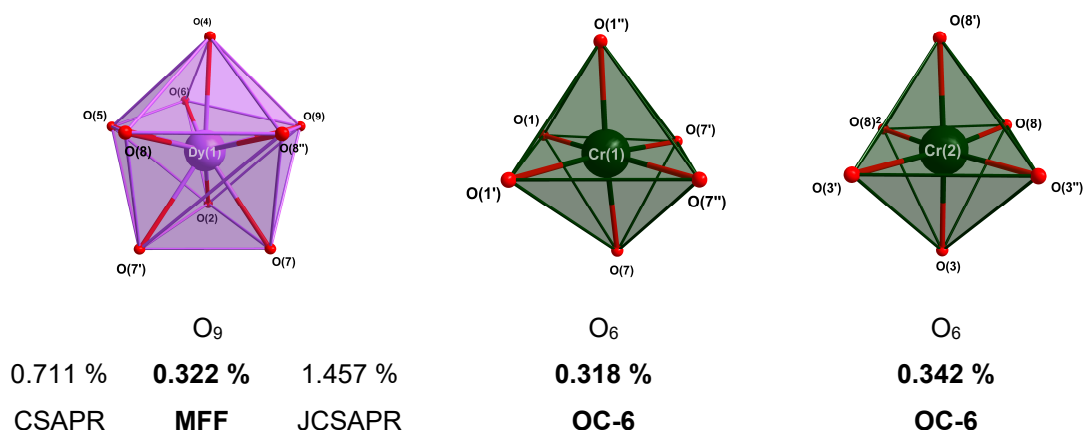


Figure 12-13 Coordination spheres around the Dy(III) and Cr(III) ions with deviations from the perfect geometries.

The packing is stabilized via hydrogen bonding between coordinated and uncoordinated isopropanol molecules and $\mu_3\text{-OH}^-$ units. The shortest inter-triangle distance is with 11.230 Å a bit shorter than in (**8**) and the shortest intermolecular Cr-Cr distance is with 6.001 Å also shorter than in (**8**). The packing is shown with the coordination spheres around the ions in Figure 12-14.

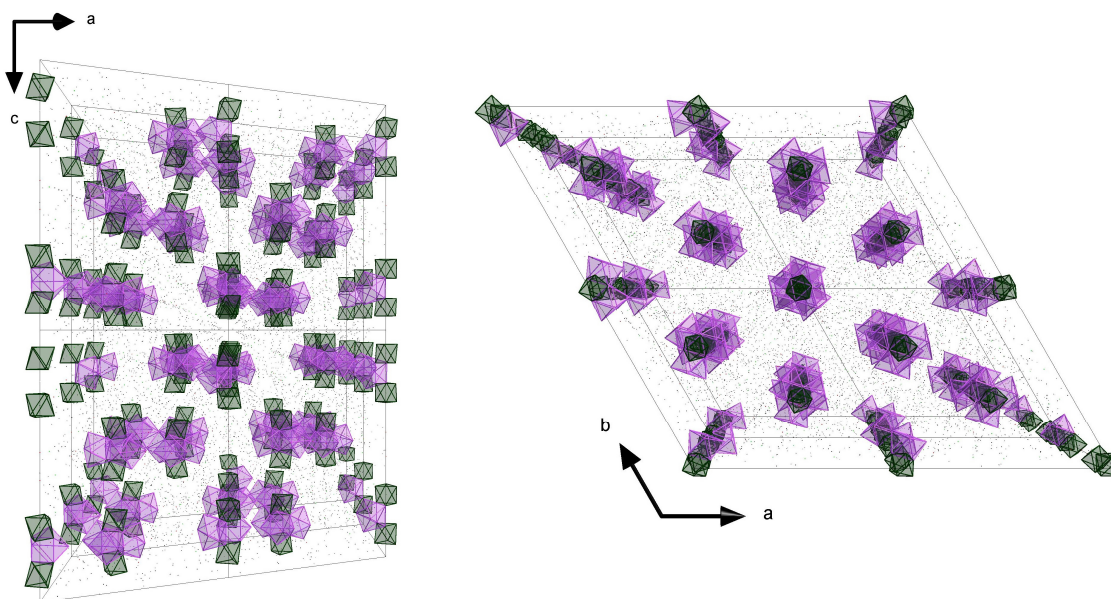


Figure 12-14 Packing of **(9)** from different viewing directions. Coordination spheres of the Dy(III) ions in lavender and of the Cr(III) ions in dark green.

Table 12-11 Distances [Å] of **(9)**.

Cr(1)	Cr(2)	5.2111(14)
Dy(1)	Dy(1')	4.0027(7)
Dy(1)	Cr(1)	3.4761(8)
Dy(1)	Cr(2)	3.4895(7)
Dy(1)	O(2)	2.326(3)
Dy(1)	O(4)	2.373(3)
Dy(1)	O(5)	2.411(3)
Dy(1)	O(6)	2.539(3)
Dy(1)	O(7)	2.429(3)
Dy(1)	O(7')	2.437(3)
Dy(1)	O(8)	2.395(3)
Dy(1)	O(8'')	2.479(3)
Dy(1)	O(9)	2.376(3)
Cr(1)	O(1'')	1.994(3)
Cr(1)	O(1')	1.994(3)
Cr(1)	O(1)	1.994(3)
Cr(1)	O(7'')	1.966(3)
Cr(1)	O(7')	1.966(3)
Cr(1)	O(7)	1.966(3)
Cr(2)	O(3'')	1.968(3)
Cr(2)	O(3)	1.968(3)
Cr(2)	O(3')	1.968(3)
Cr(2)	O(8)	1.971(3)

Cr(2)	O(8'')	1.971(3)
Cr(2)	O(8')	1.971(3)

Table 12-12 Angles [°] of **(9)**.

Dy(1)	Dy(1')	Dy(1'')	60.00(0)
Cr(1)	Dy(1)	Cr(2)	96.857(16)
Dy(1)	O(7)	Dy(1'')	110.69(10)
Dy(1)	O(8)	Dy(1')	110.40(10)
Cr(1)	O(7)	Dy(1'')	103.77(12)
Cr(1)	O(7)	Dy(1)	104.06(12)
Cr(2)	O(8)	Dy(1')	102.69(11)
Cr(2)	O(8)	Dy(1)	105.68(11)
Dy(1')	Cr(2)	Dy(1'')	69.996(17)

Molecular structure, coordination spheres, bond lengths, distances, angles and packing of $[\text{Cr}_2\text{Dy}_3(\text{pcnba})_6(\mu_3\text{-OH})_6(\text{NO}_3)_3(\text{H}_2\text{O})_3]$ (**10**)

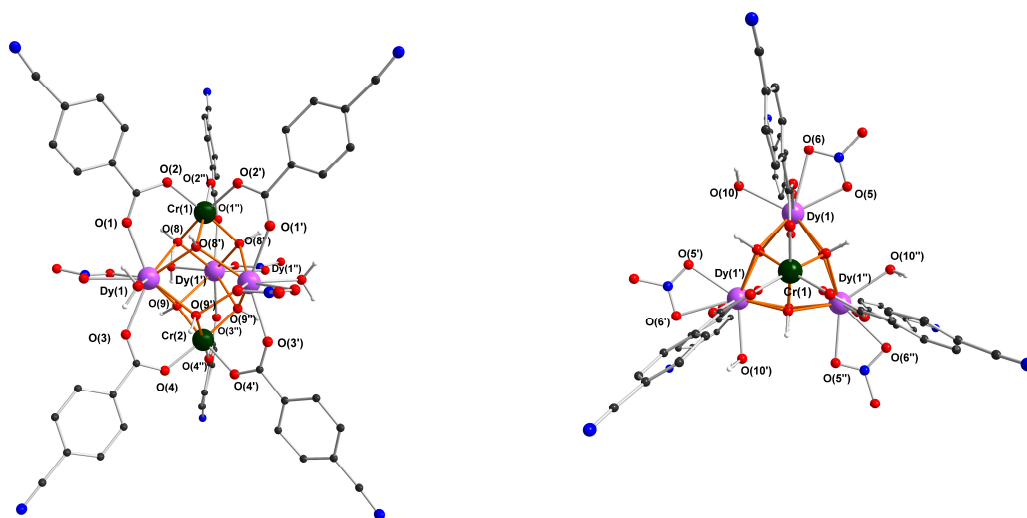


Figure 12-15 Molecular structure of $[\text{Cr}_2\text{Dy}_3(\text{pcnba})_6(\mu_3\text{-OH})_6(\text{NO}_3)_3(\text{H}_2\text{O})_3]$ (**10**) from the side view (left) and down the pseudo 3-fold axis (right). Primed atoms at 1-y, x-y, z; double-primed atoms at 1-x+y, 1-x.

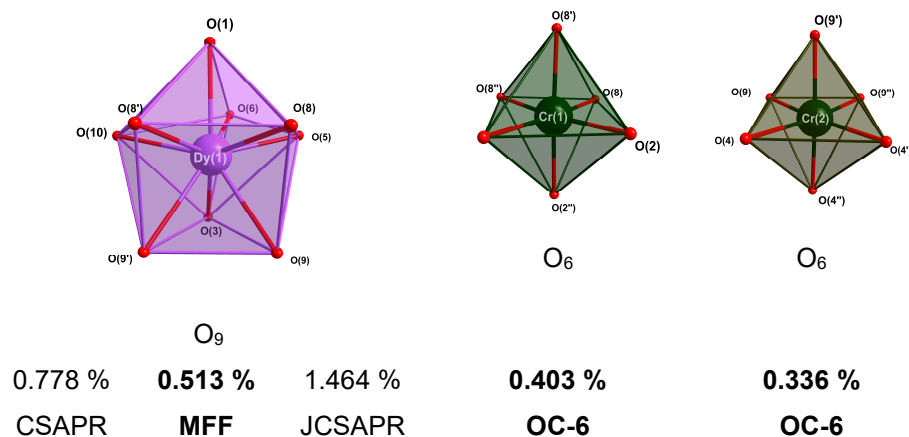


Figure 12-16 Coordination spheres around the Dy(III) and Cr(III) ions with deviations from the perfect geometries.

The packing with the coordination spheres around the ions is shown in Figure 12-17. The shortest inter-triangle $\{\text{Dy}_3\}$ distance is 14.565 Å and the shortest intermolecular Cr-Cr distance is 11.1040 Å.

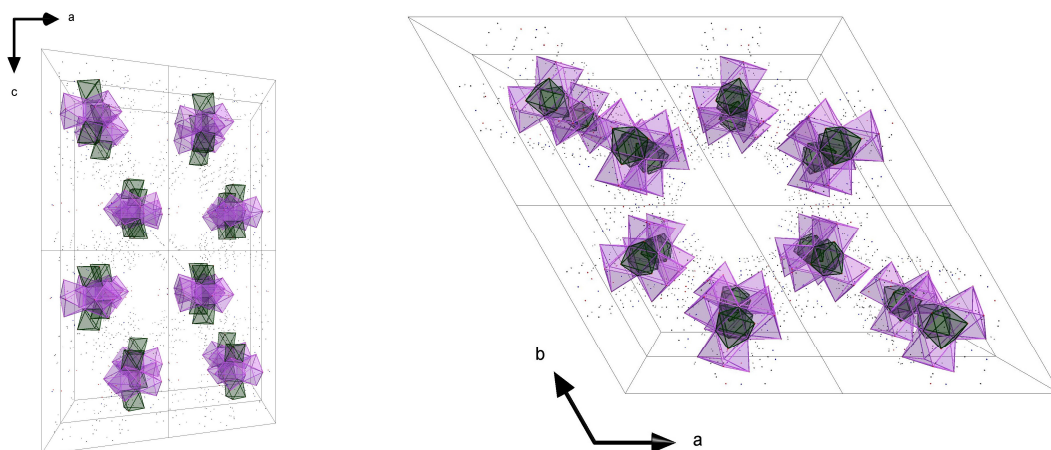


Figure 12-17 Packing of **(10)** from different viewing directions. Coordination spheres of the Dy(III) ions in lavender and of the Cr(III) ions in dark green.

Table 12-13 Distances [Å] of **(10)**.

Cr(1)	Cr(2)	5.1718(5)
Dy(1)	Dy(1')	3.9816(10)
Dy(1)	Cr(1)	3.462(3)
Dy(1)	Cr(2)	3.458(3)
Dy(1)	O(1)	2.368(9)
Dy(1)	O(3)	2.380(10)
Dy(1)	O(5)	2.352(16)
Dy(1)	O(6)	2.519(13)
Dy(1)	O(8')	2.397(10)
Dy(1)	O(8)	2.429(9)
Dy(1)	O(9)	2.419(9)
Dy(1)	O(9')	2.416(10)
Dy(1)	O(10)	2.361(12)
Cr(1)	O(2'')	1.969(12)
Cr(1)	O(2')	1.969(11)
Cr(1)	O(2)	1.969(11)
Cr(1)	O(8')	1.961(10)
Cr(1)	O(8'')	1.961(10)
Cr(1)	O(8)	1.961(10)
Cr(2)	O(4'')	1.988(11)
Cr(2)	O(4)	1.988(11)

Cr(2)	O(4')	1.988(11)
Cr(2)	O(9'')	1.940(9)
Cr(2)	O(9')	1.940(10)
Cr(2)	O(9)	1.940(9)

Table 12-14 Angles [°] of (**10**).

Dy(1)	Dy(1')	Dy(1'')	60.00(0)
Cr(1)	Dy(1)	Cr(2)	96.73(6)
Dy(1'')	O(8)	Dy(1)	111.2(4)
Dy(1'')	O(9)	Dy(1)	110.8(3)
Cr(1)	O(8)	Dy(1)	103.6(4)
Cr(1)	O(8)	Dy(1'')	104.7(5)
Cr(2)	O(9)	Dy(1'')	104.5(4)
Cr(2)	O(9)	Dy(1)	104.4(4)

Molecular structure, coordination spheres, bond lengths, distances, angles and packing of $[\text{Cr}_2\text{Dy}_3(\text{dfba})_6(\mu_3\text{-OH})_6(\text{NO}_3)_3(\text{DMF})_3]\cdot\text{DMF}$ (**11**)

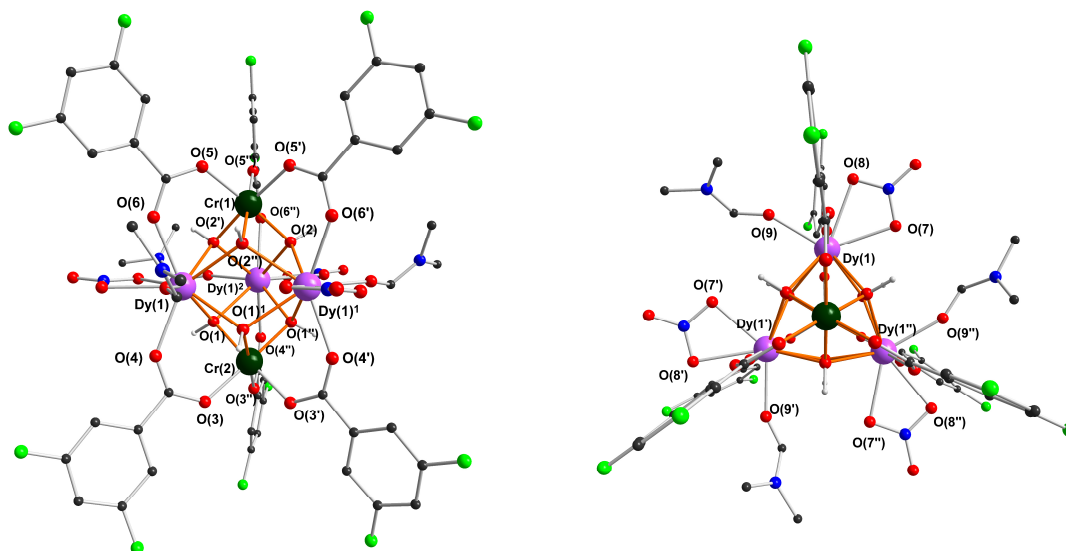


Figure 12-18 Molecular structure of $[\text{Cr}_2\text{Dy}_3(\text{dfba})_6(\mu_3\text{-OH})_6(\text{NO}_3)_3(\text{DMF})_3]\cdot\text{DMF}$ (**11**) from the side view (left) and down the pseudo 3-fold axis (right). Primed atoms at $-x+y, 1-x, z$; double-primed atoms at $1-y, 1+x-y, z$.

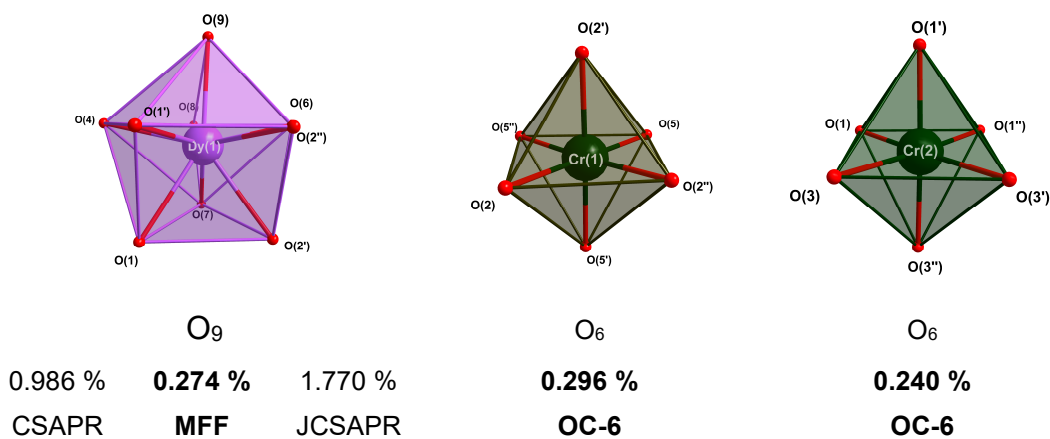


Figure 12-19 Coordination spheres around the Dy(III) and Cr(III) ions with deviations from the perfect geometries.

The packing of the molecules (Figure 12-20) is stabilized by hydrogen bonding between the DMF solvent molecules and $\mu_3\text{-OH}^-$ units. The shortest inter-triangle $\{\text{Dy}_3\}$ distance is 11.170 Å and the shortest intermolecular Cr-Cr distance is 5.933 Å.

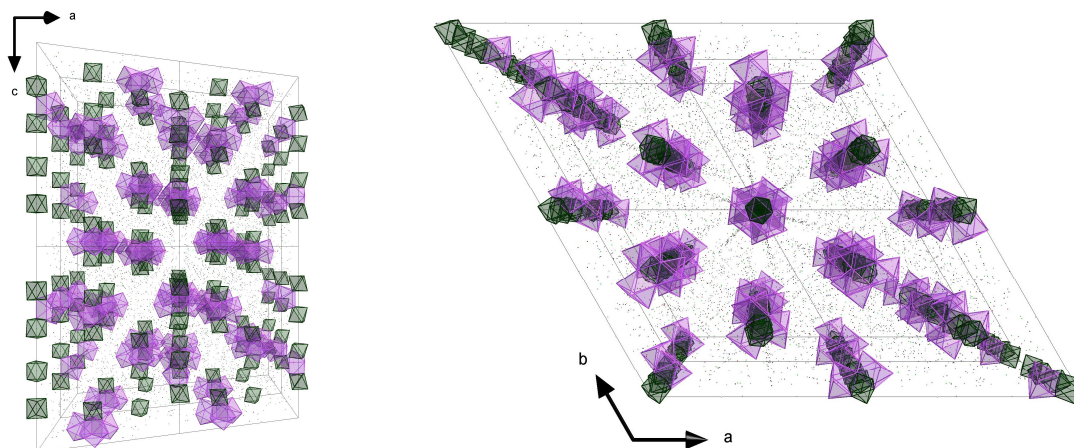


Figure 12-20 Packing of **(11)** from different viewing directions. Coordination spheres of the Dy(III) ions in lavender and of the Cr(III) ions in dark green.

Table 12-15 Distances [Å] of **(11)**.

Cr(1)	Cr(2)	5.1749(9)
Dy(1)	Dy(1')	3.9728(7)
Dy(1)	Cr(1)	3.4808(4)
Dy(1)	Cr(2)	3.4349(5)
Dy(1)	O(6)	2.3799(16)
Dy(1)	O(4)	2.3596(17)
Dy(1)	O(7)	2.4405(19)
Dy(1)	O(8)	2.530(2)
Dy(1)	O(2')	2.4307(15)
Dy(1)	O(2'')	2.4361(15)
Dy(1)	O(1)	2.4094(16)
Dy(1)	O(1')	2.4309(15)
Dy(1)	O(9)	2.2941(19)
Cr(1)	O(5)	1.9775(16)
Cr(1)	O(5'')	1.9776(16)
Cr(1)	O(5')	1.9776(16)
Cr(1)	O(2)	1.9602(15)
Cr(1)	O(2')	1.9601(15)
Cr(1)	O(2'')	1.9602(15)
Cr(2)	O(3)	1.9828(18)
Cr(2)	O(3'')	1.9828(18)
Cr(2)	O(3')	1.9828(18)
Cr(2)	O(1)	1.9538(16)
Cr(2)	O(1')	1.9538(16)
Cr(2)	O(1'')	1.9538(16)

Table 12-16 Angles [°] of (**11**).

Dy(1)	Dy(1')	Dy(1'')	60.00(0)
Cr(1)	Dy(1)	Cr(2)	96.88(1)
Dy(1) ¹	O(2)	Dy(1'')	109.44(5)
Cr(1)	O(2)	Dy(1')	104.37(6)
Cr(1)	O(2)	Dy(1'')	104.18(6)
Dy(1)	O(1)	Dy(1')	110.33(6)
Cr(2)	O(1)	Dy(1')	102.60(7)
Cr(2)	O(1)	Dy(1)	103.36(7)

Molecular structure, coordination spheres, bond lengths, distances, angles and packing of $[\text{Cr}_2\text{Dy}_3(\text{dtbba})_9(\mu_3\text{-OH})_6(\text{C}_3\text{H}_7\text{OH})_3]\cdot 3\text{C}_3\text{H}_7\text{OH}$ (**12**)

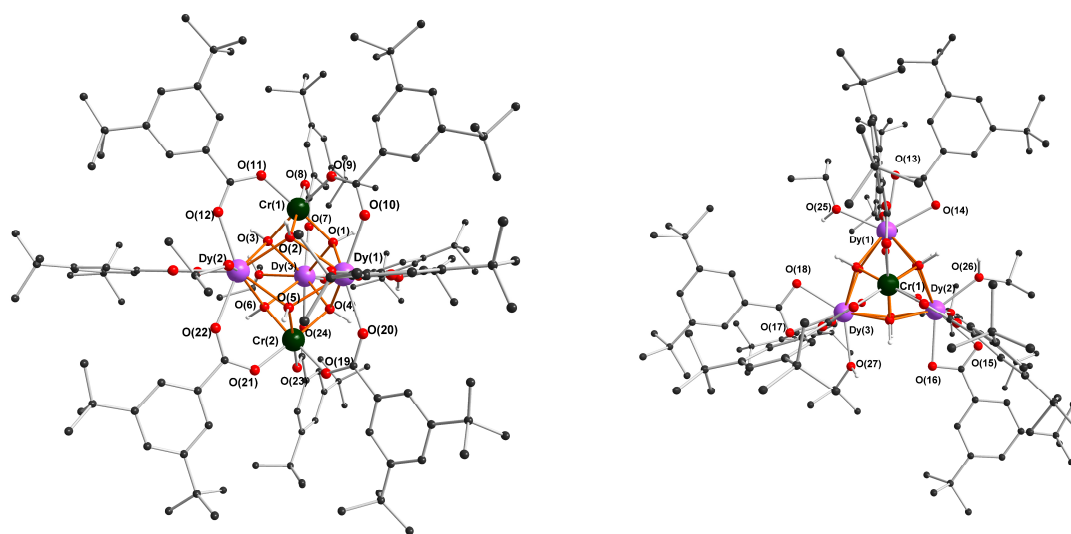


Figure 12-21 Molecular structure of $[\text{Cr}_2\text{Dy}_3(\text{dtbba})_9(\mu_3\text{-OH})_6(\text{C}_3\text{H}_7\text{OH})_3]\cdot 3\text{C}_3\text{H}_7\text{OH}$ (**12**) from the side view (left) and down the pseudo 3-fold axis (right).

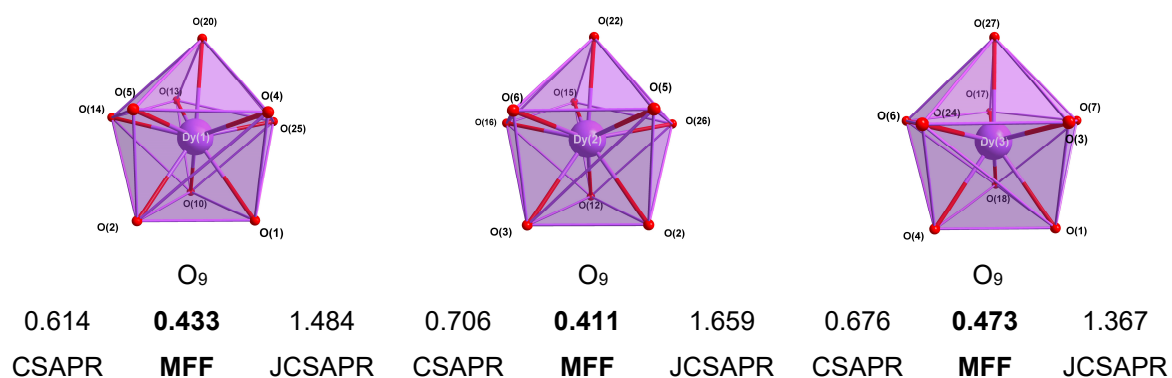


Figure 12-22 Coordination spheres around the Dy(III) ions with deviations from the perfect geometries in %.

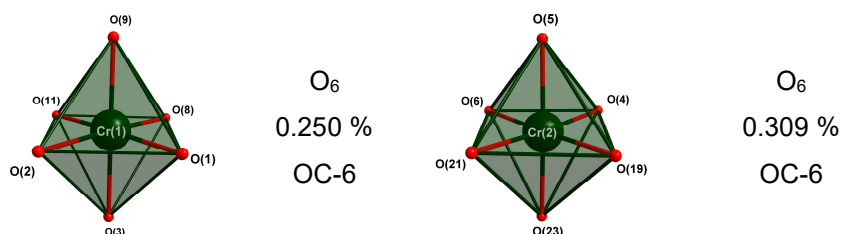


Figure 12-23 Coordination spheres around the Cr(III) ions with deviations from the perfect geometry.

The packing of the molecules is stabilized by hydrogen bonding between solvent molecules (isopropanol), coordinated isopropanol and $\mu_3\text{-OH}^-$ units. The shortest

inter-triangle $\{\text{Dy}_3\}$ distance is 14.713 Å and the shortest intermolecular Cr-Cr distance is 15.427 Å. The packing together with the coordination spheres around the Dy(III) and Cr(III) ions is shown in Figure 12-24.

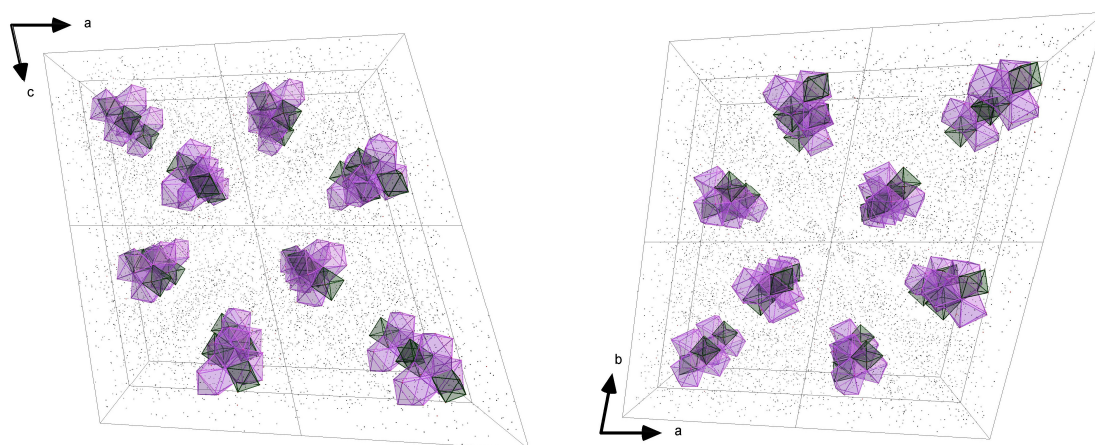


Figure 12-24 Packing of (**12**) from different viewing directions. Coordination spheres of the Dy(III) ions in lavender and of the Cr(III) ions in dark green.

Table 12-17 Distances [Å] of (**12**).

Cr(1)	Cr(2)	5.1510(8)
Dy(1)	Dy(2)	4.0592(3)
Dy(1)	Dy(3)	4.0186(2)
Dy(2)	Dy(3)	4.0167(3)
Dy(1)	Cr(1)	3.4673(6)
Dy(1)	Cr(2)	3.4726(6)
Dy(2)	Cr(1)	3.4704(6)
Dy(2)	Cr(2)	3.4953(6)
Dy(3)	Cr(1)	3.4461(6)
Dy(3)	Cr(2)	3.4771(6)
Dy(1)	O(10)	2.371(3)
Dy(1)	O(20)	2.369(3)
Dy(1)	O(13)	2.467(3)
Dy(1)	O(14)	2.435(3)
Dy(1)	O(2)	2.445(3)
Dy(1)	O(1)	2.434(3)
Dy(1)	O(5)	2.407(3)
Dy(1)	O(4)	2.454(3)
Dy(1)	O(25)	2.396(3)
Dy(2)	O(12)	2.385(3)
Dy(2)	O(22)	2.388(3)
Dy(2)	O(15)	2.459(3)
Dy(2)	O(16)	2.454(3)
Dy(2)	O(2)	2.448(3)

Dy(2)	O(3)	2.426(3)
Dy(2)	O(5)	2.494(3)
Dy(2)	O(6)	2.394(3)
Dy(2)	O(26)	2.376(3)
Dy(3)	O(7)	2.358(3)
Dy(3)	O(24)	2.349(3)
Dy(3)	O(17)	2.531(3)
Dy(3)	O(18)	2.405(3)
Dy(3)	O(3)	2.420(3)
Dy(3)	O(1)	2.430(3)
Dy(3)	O(6)	2.482(2)
Dy(3)	O(4)	2.410(3)
Dy(3)	O(27)	2.374(3)
Cr(1)	O(9)	1.969(3)
Cr(1)	O(11)	1.963(3)
Cr(1)	O(8)	1.978(3)
Cr(1)	O(2)	1.959(3)
Cr(1)	O(3)	1.964(3)
Cr(1)	O(1)	1.971(3)
Cr(2)	O(19)	1.973(3)
Cr(2)	O(21)	1.959(3)
Cr(2)	O(23)	1.983(3)
Cr(2)	O(5)	1.971(3)
Cr(2)	O(6)	1.975(3)
Cr(2)	O(4)	1.962(3)

Table 12-18 Angles [°] of **(12)**.

Dy(1)	Dy(2)	Dy(3)	59.68(0)
Dy(1)	Dy(3)	Dy(2)	60.69(0)
Dy(2)	Dy(1)	Dy(3)	59.63(0)
Cr(1)	Dy(3)	Cr(2)	96.15(1)
Cr(1)	Dy(2)	Cr(2)	95.37(1)
Cr(1)	Dy(1)	Cr(2)	95.844(14)
Dy(1)	O(2)	Dy(2)	112.14(10)
Cr(1)	O(2)	Dy(1)	103.34(11)
Cr(1)	O(2)	Dy(2)	103.37(10)
Cr(1)	O(3)	Dy(2)	103.96(10)
Cr(1)	O(3)	Dy(3)	103.13(11)
Cr(1)	O(1)	Dy(1)	103.33(11)
Cr(1)	O(1)	Dy(3)	102.57(11)
Cr(2)	O(5)	Dy(1)	104.53(11)

Cr(2)	O(5)	Dy(2)	102.43(10)
Cr(2)	O(6)	Dy(2)	105.85(10)
Cr(2)	O(6)	Dy(3)	101.93(10)
Cr(2)	O(4)	Dy(1)	103.10(11)
Cr(2)	O(4)	Dy(3)	104.91(11)
Dy(3)	O(3)	Dy(2)	111.96(10)
Dy(3)	O(1)	Dy(1)	111.42(10)
Dy(1)	O(5)	Dy(2)	111.82(10)
Dy(1)	O(4)	Dy(3)	111.41(11)
Dy(2)	O(6)	Dy(3)	110.90(10)
Cr(1)	Dy(1)	Dy(2)	54.23(1)
Cr(1)	Dy(2)	Dy(1)	54.15(1)
Cr(1)	Dy(2)	Dy(3)	54.22(1)
Cr(1)	Dy(3)	Dy(1)	54.71(1)
Cr(2)	Dy(1)	Dy(2)	54.63(1)
Cr(2)	Dy(2)	Dy(1)	54.11(1)
Cr(2)	Dy(2)	Dy(3)	54.61(1)
Cr(2)	Dy(3)	Dy(2)	55.04(1)
Cr(2)	Dy(1)	Dy(3)	54.72(1)
Cr(2)	Dy(3)	Dy(1)	54.62(1)
Dy(1)	Cr(1)	Dy(2)	71.62(1)
Dy(2)	Cr(1)	Dy(3)	71.00(1)
Dy(3)	Cr(2)	Dy(1)	70.65(1)
Dy(3)	Cr(1)	Dy(1)	71.08(1)
Dy(1)	Cr(2)	Dy(2)	71.26(1)
Dy(2)	Cr(2)	Dy(3)	70.35(1)

Molecular structure, coordination spheres, bond lengths, distances, angles and packing of $[\text{Fe}_2\text{Dy}_3(\text{dtbba})_9(\mu_3\text{-OH})_6(\text{C}_3\text{H}_7\text{OH})_3]\cdot 3\text{C}_3\text{H}_7\text{OH}$ (**13**)

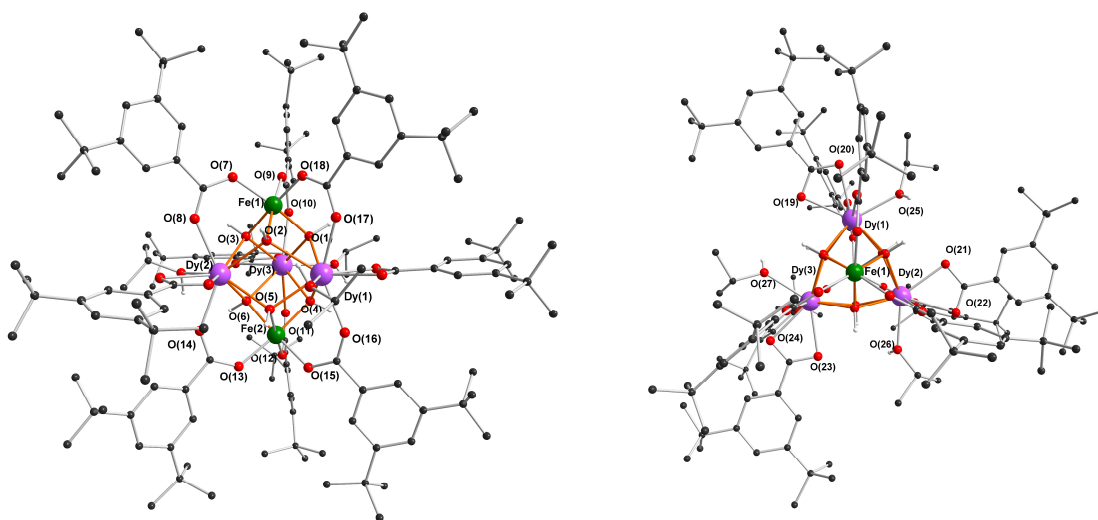


Figure 12-25 Molecular structure of $[\text{Fe}_2\text{Dy}_3(\text{dtbba})_9(\mu_3\text{-OH})_6(\text{C}_3\text{H}_7\text{OH})_3]\cdot 3\text{C}_3\text{H}_7\text{OH}$ (**13**) from the side view (left) and down the pseudo 3-fold axis (right).

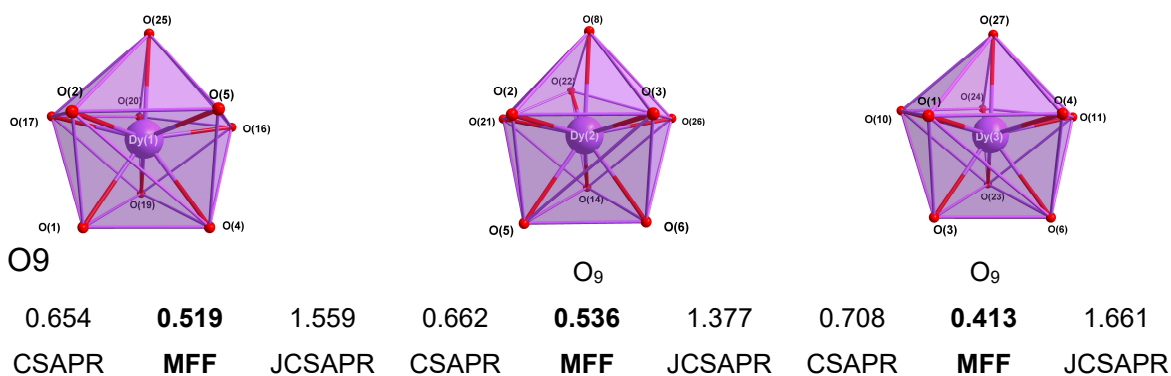


Figure 12-26 Coordination spheres around the Dy(III) ions with deviations from the perfect geometries in %.

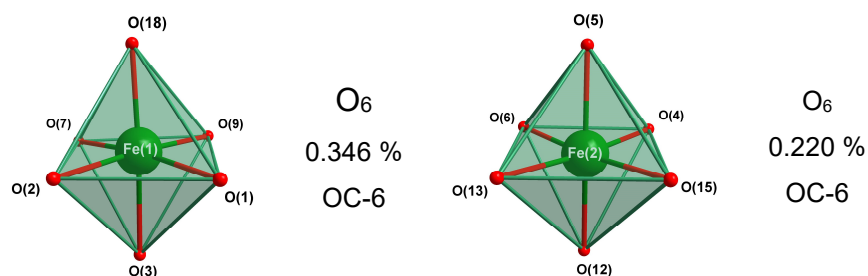


Figure 12-27 Coordination spheres around the Cr(III) ions with deviations from the perfect geometry.

The packing is stabilized by hydrogen bonding between solvent molecules (isopropanol), coordinated isopropanol and $\mu_3\text{-OH}^-$ units, such as in (**12**) but the shortest inter-triangle $\{\text{Dy}_3\}$ distance is with 15.382 Å significant longer than in (**12**). The shortest intermolecular Fe-Fe distance is with 14.749 Å shorter than the shortest intermolecular Cr-Cr distance in (**12**). The packing with the coordination spheres of the Dy(III) and Fe(III) ions is

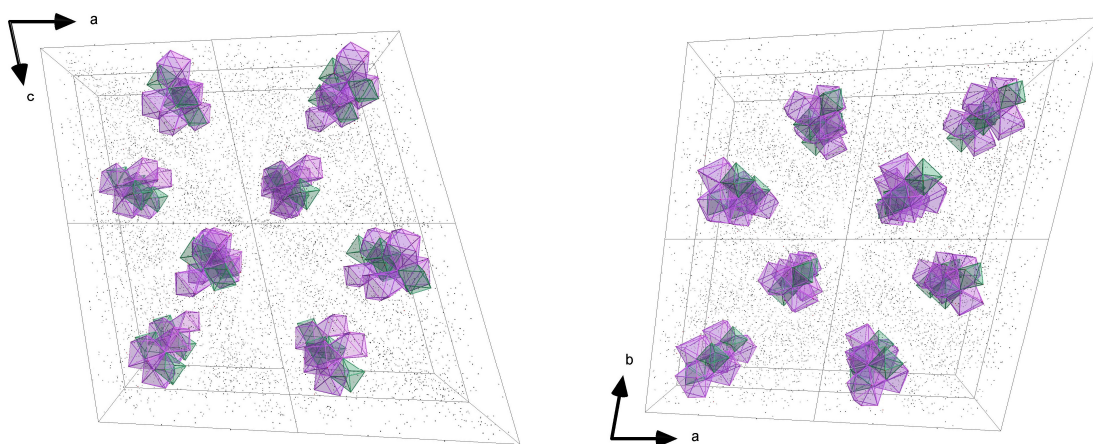


Figure 12-28 Packing of (**13**) from different viewing directions. Coordination spheres of the Dy(III) ions in lavender and of the Fe(III) ions in green.

Table 12-19 Distances [Å] of (**13**).

Fe(1)	Fe(2)	5.2463(11)
Dy(1)	Dy(2)	4.0145(7)
Dy(1)	Dy(3)	4.0565(8)
Dy(2)	Dy(3)	4.0197(6)
Dy(1)	Fe(2)	3.4885(10)
Dy(1)	Fe(1)	3.5146(8)
Dy(2)	Fe(1)	3.5000(8)
Dy(2)	Fe(2)	3.4968(8)
Dy(3)	Fe(1)	3.5336(9)
Dy(3)	Fe(2)	3.5056(8)
Dy(1)	O(1)	2.396(3)
Dy(1)	O(2)	2.481(3)
Dy(1)	O(4)	2.438(3)
Dy(1)	O(5)	2.419(3)
Dy(1)	O(16)	2.414(3)
Dy(1)	O(17)	2.393(3)
Dy(1)	O(19)	2.449(3)

Dy(1)	O(20)	2.466(3)
Dy(1)	O(25)	2.399(4)
Dy(2)	O(2)	2.381(3)
Dy(2)	O(3)	2.487(3)
Dy(2)	O(5)	2.441(3)
Dy(2)	O(6)	2.435(3)
Dy(2)	O(8)	2.387(3)
Dy(2)	O(14)	2.355(3)
Dy(2)	O(21)	2.427(3)
Dy(2)	O(22)	2.537(3)
Dy(2)	O(26)	2.387(4)
Dy(3)	O(1)	2.505(3)
Dy(3)	O(3)	2.384(3)
Dy(3)	O(4)	2.454(3)
Dy(3)	O(6)	2.423(3)
Dy(3)	O(10)	2.401(3)
Dy(3)	O(11)	2.390(4)
Dy(3)	O(23)	2.461(3)
Dy(3)	O(24)	2.470(3)
Dy(3)	O(27)	2.397(3)
Fe(1)	O(1)	2.013(3)
Fe(1)	O(2)	1.999(3)
Fe(1)	O(3)	2.017(3)
Fe(1)	O(7)	1.992(3)
Fe(1)	O(9)	1.969(3)
Fe(1)	O(18)	1.976(3)
Fe(2)	O(4)	2.009(3)
Fe(2)	O(5)	2.000(3)
Fe(2)	O(6)	2.010(3)
Fe(2)	O(12)	1.981(4)
Fe(2)	O(13)	1.986(3)
Fe(2)	O(15)	1.984(4)

Table 12-20 Angles [°] of (13).

Dy(1)	Dy(2)	Dy(3)	60.65(1)
Dy(1)	Dy(3)	Dy(2)	59.61(1)
Dy(2)	Dy(1)	Dy(3)	59.74(1)
Fe(1)	Dy(1)	Fe(2)	97.03(2)
Fe(1)	Dy(2)	Fe(2)	97.15(2)
Fe(1)	Dy(3)	Fe(2)	96.37(2)
Dy(1)	O(4)	Dy(3)	112.02(12)

Dy(1)	O(5)	Dy(2)	111.40(12)
Dy(1)	O(1)	Dy(3)	111.73(12)
Dy(2)	O(2)	Dy(1)	111.32(11)
Dy(3)	O(3)	Dy(2)	111.22(12)
Dy(3)	O(6)	Dy(2)	111.70(12)
Fe(1)	O(3)	Dy(2)	101.49(13)
Fe(1)	O(3)	Dy(3)	106.50(13)
Fe(1)	O(1)	Dy(1)	105.38(13)
Fe(1)	O(1)	Dy(3)	102.36(13)
Fe(1)	O(2)	Dy(1)	102.84(12)
Fe(1)	O(2)	Dy(2)	105.77(13)
Fe(2)	O(6)	Dy(2)	103.36(13)
Fe(2)	O(6)	Dy(3)	104.15(13)
Fe(2)	O(4)	Dy(1)	102.89(12)
Fe(2)	O(4)	Dy(3)	103.06(13)
Fe(2)	O(5)	Dy(1)	103.86(12)
Fe(2)	O(5)	Dy(2)	103.44(14)
Fe(1)	Dy(1)	Dy(2)	54.92(1)
Fe(1)	Dy(2)	Dy(1)	55.26(2)
Fe(1)	Dy(2)	Dy(3)	55.54(2)
Fe(1)	Dy(3)	Dy(2)	54.75(2)
Fe(1)	Dy(1)	Dy(3)	55.08(2)
Fe(1)	Dy(3)	Dy(1)	54.64(2)
Fe(2)	Dy(1)	Dy(2)	55.02(2)
Fe(2)	Dy(2)	Dy(1)	54.82(2)
Fe(2)	Dy(2)	Dy(3)	55.07(1)
Fe(2)	Dy(3)	Dy(2)	54.86(1)
Fe(2)	Dy(1)	Dy(3)	54.75(2)
Fe(2)	Dy(3)	Dy(1)	54.35(2)
Dy(1)	Fe(1)	Dy(2)	69.82(2)
Dy(2)	Fe(1)	Dy(3)	69.71(2)
Dy(3)	Fe(2)	Dy(1)	70.90(2)
Dy(3)	Fe(1)	Dy(1)	70.28(2)
Dy(2)	Fe(2)	Dy(3)	70.07(2)

Molecular structure, coordination spheres, bond lengths, distances, angles and packing of $[\text{Al}_2\text{Dy}_3(\text{dtbba})_9(\mu_3\text{-OH})_6(\text{CH}_3\text{OH})_{0.75}(\text{H}_2\text{O})_{1.5}(\text{C}_3\text{H}_7\text{OH})_{0.75}]\cdot\text{CH}_3\text{H}_7\text{OH}$ (**14**)

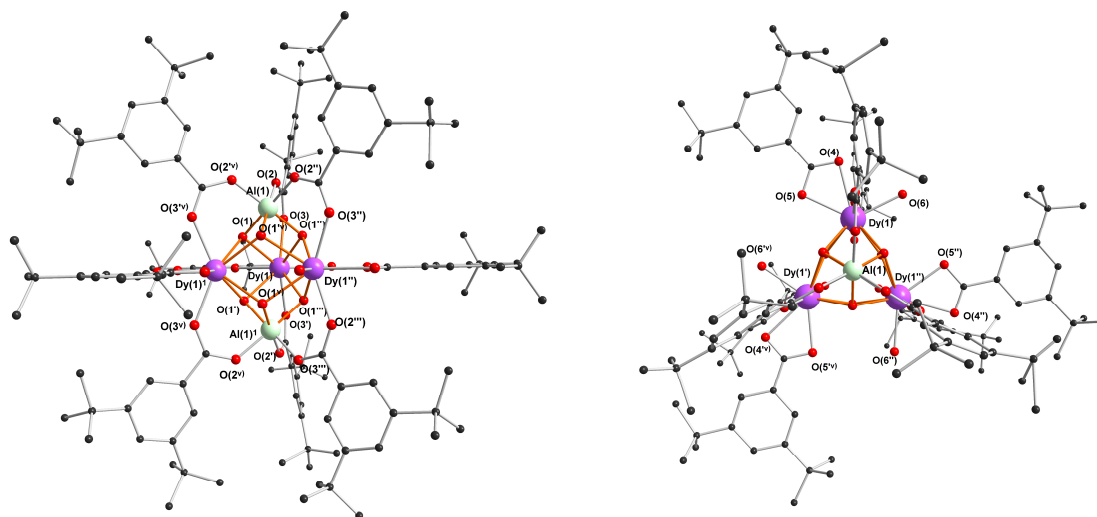


Figure 12-29 Molecular structure of $[\text{Al}_2\text{Dy}_3(\text{dtbbba})_9(\mu_3\text{-OH})_6(\text{CH}_3\text{OH})_{0.75}(\text{H}_2\text{O})_{1.5}(\text{C}_3\text{H}_7\text{OH})_{0.75}]\cdot\text{CH}_3\text{H}_7\text{OH}$ (**14**) from the side view (left) and down the pseudo 3-fold axis (right). Hydrogens are omitted for clarity. For the disorder at the Dy(III) ions, water is chosen to be displayed. Primed atoms at $x, y, 3/2-z$; double-primed atoms at $1-y, 1+x-y, z$; triple-primed atoms at $1-y, 1+x-y, 3/2-z$; $^{\text{v}}$ -primed atoms at $-x+y, 1-x, z$; $^{\text{v}}$ -primed atoms at $-x+y, 1-x, 3/2-z$.

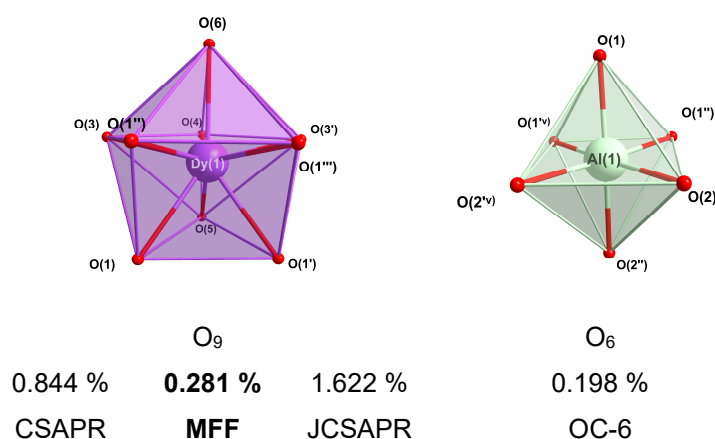


Figure 12-30 Coordination spheres around the Dy(III) and Al(III) ions with deviations from the perfect geometries.

The packing of (**14**) with the coordination spheres of the Al(III) and Dy(III) ions is shown in Figure 12-31. The shortest inter-triangle $\{\text{Dy}_3\}$ distance is with 14.884 Å shorter than in $[\text{Fe}_2\text{Dy}_3(\text{dtbbba})_9(\mu_3\text{-OH})_6(\text{C}_3\text{H}_7\text{OH})_3]$ (**13**) and a bit longer than in $[\text{Cr}_2\text{Dy}_3(\text{dtbbba})_9(\mu_3\text{-OH})_6(\text{C}_3\text{H}_7\text{OH})_3]$ (**12**). The shortest intermolecular Al-Al distance

is 15.676 Å. This is longer than the intermolecular Fe-Fe in (**13**) or the intermolecular Cr-Cr distance in (**12**).

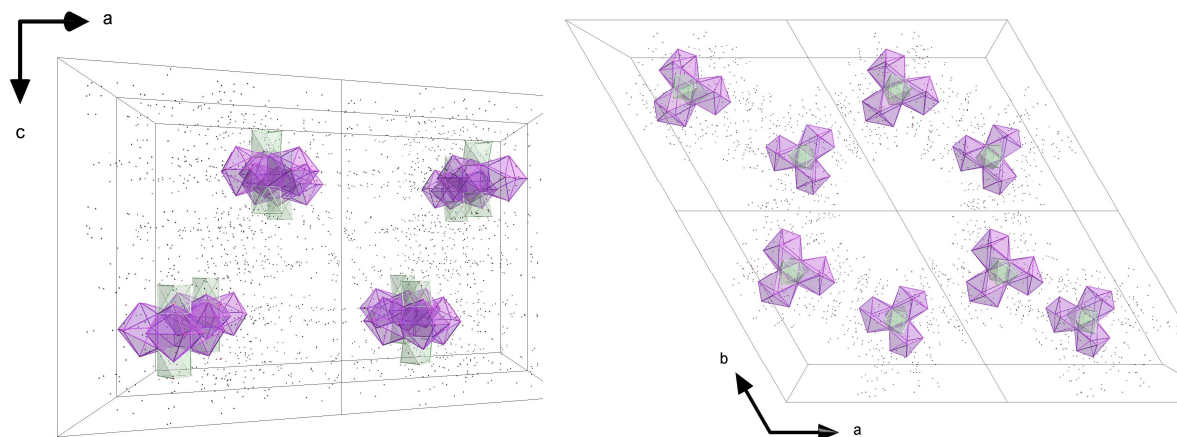


Figure 12-31 Packing of (**14**) from different viewing directions. Coordination spheres of the Dy(III) ions in lavender and of the Al(III) ions in light green.

Table 12-21 Distances [Å] of (**14**).

Al(1)	Al(1')	5.0479(34)
Dy(1)	Dy(1')	3.9712(5)
Dy(1)	Al(1')	3.4099(19)
Dy(1)	O(1)	2.411(4)
Dy(1)	O(1'')	2.438(4)
Dy(1)	O(3')	2.368(4)
Dy(1)	O(3)	2.367(4)
Dy(1)	O(6)	2.407(7)
Dy(1)	O(5)	2.469(7)
Dy(1)	O(4)	2.559(7)
Al(1)	O(2'')	1.881(4)
Al(1)	O(1)	1.885(4)

Table 12-22 Angles [°] of (**14**).

Dy(1)	Dy(1')	Dy(1'')	60.00(0)
Al(1')	Dy(1)	Al(1)	95.49(6)
Dy(1)	O(1)	Dy(1''')	109.96(13)
Al(1)	O(1)	Dy(1''')	103.40(15)
Al(1)	O(1)	Dy(1)	104.39(16)

Molecular structure, coordination spheres, bond lengths, distances, angles and packing of $[\text{Al}_2\text{Dy}_3(\text{dtbba})_7(\mu_3\text{-OH})_6(\text{NO}_3)_2(\text{C}_3\text{H}_7\text{OH})(\text{H}_2\text{O})_2]\cdot 3\text{H}_2\text{O}$ (**15**)

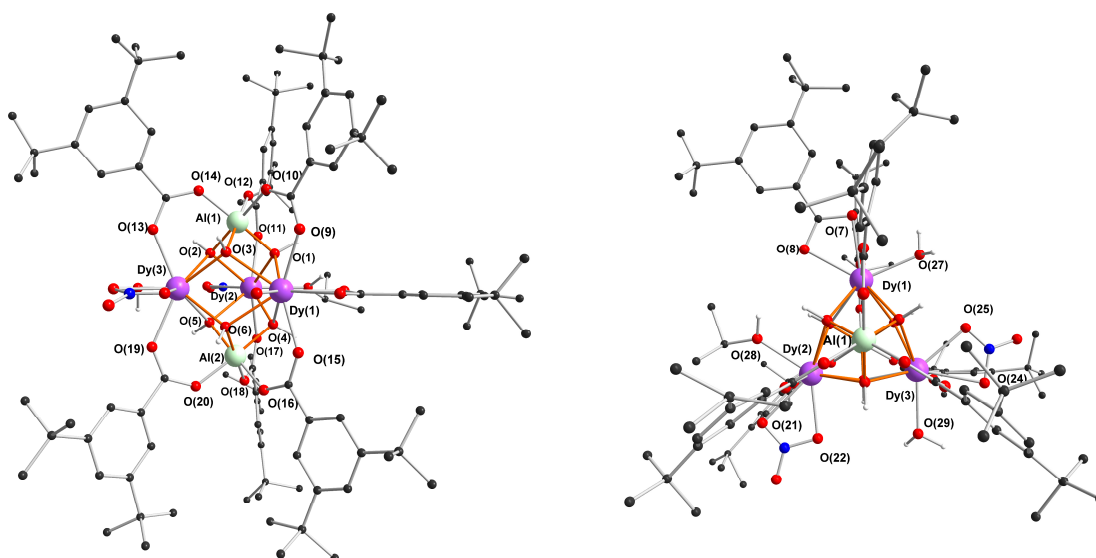


Figure 12-32 Molecular structure of $[\text{Al}_2\text{Dy}_3(\text{dtbba})_7(\mu_3\text{-OH})_6(\text{NO}_3)_2(\text{C}_3\text{H}_7\text{OH})(\text{H}_2\text{O})_2]\cdot 3\text{H}_2\text{O}$ (**15**) from the side view (left) and down the pseudo 3-fold axis (right).

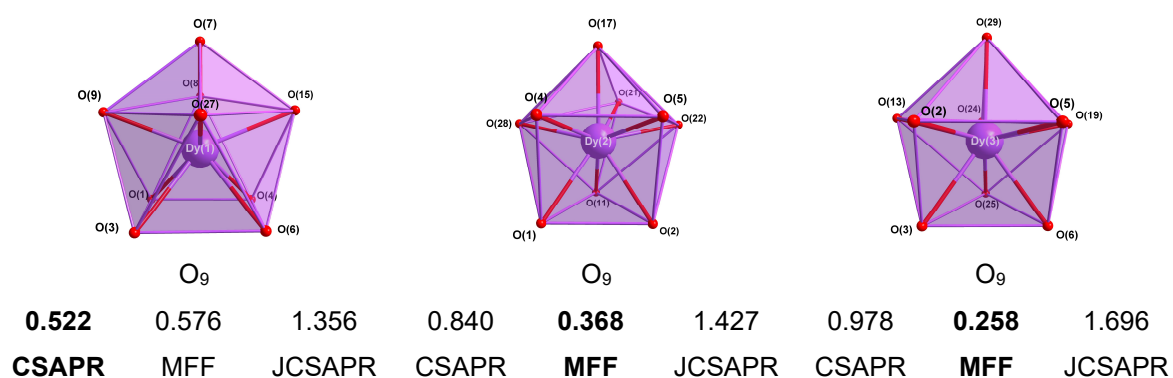


Figure 12-33 Coordination spheres around the Dy(III) ions with deviations from the perfect geometries in %.

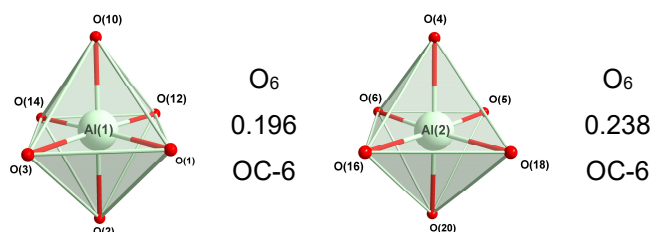


Figure 12-34 Coordination spheres around the Al(III) ions with deviations from the perfect geometry.

The packing is stabilized via hydrogen bonding between solvent molecules (water, isopropanol) and $\mu_3\text{-OH}^-$ units. The shortest inter-triangle $\{\text{Dy}_3\}$ distance is with 15.119 Å longer than the ones in (**14**) but the shortest intermolecular Al-Al distance is with 14.400 Å shorter than the ones in (**14**). The packing with the coordination spheres around the Dy(III) and Al(III) ions is shown Figure 12-35.

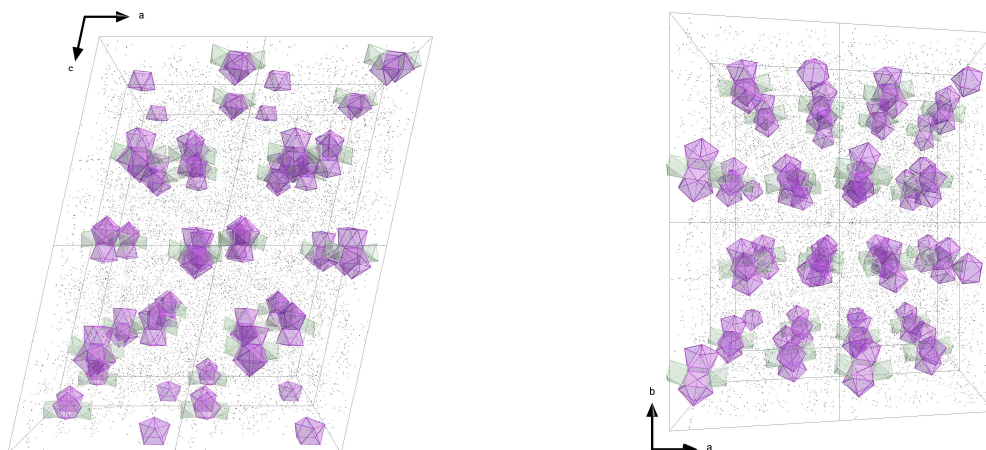


Figure 12-35 Packing of (**15**) from different viewing directions. Coordination spheres of the Dy(III) ions in lavender and of the Al(III) ions in light green.

Table 12-23 Distances [Å] of (**15**).

Al(1)	Al(2)	5.0941(28)
Dy(1)	Dy(2)	3.9628(6)
Dy(1)	Dy(3)	3.9359(6)
Dy(2)	Dy(3)	3.9469(5)
Dy(1)	Al(1)	3.421(2)
Dy(1)	Al(2)	3.445(2)
Dy(2)	Al(1)	3.408(2)
Dy(2)	Al(2)	3.4120(18)
Dy(3)	Al(1)	3.406(2)
Dy(3)	Al(2)	3.417(2)
Dy(1)	O(1)	2.418(4)
Dy(1)	O(3)	2.440(5)
Dy(1)	O(4)	2.432(5)
Dy(1)	O(6)	2.420(5)
Dy(1)	O(7)	2.475(6)
Dy(1)	O(8)	2.432(7)
Dy(1)	O(9)	2.378(6)
Dy(1)	O(15)	2.349(5)
Dy(1)	O(27)	2.394(6)
Dy(2)	O(1)	2.442(5)

Dy(2)	O(2)	2.417(5)
Dy(2)	O(4)	2.409(4)
Dy(2)	O(5)	2.406(4)
Dy(2)	O(11)	2.314(5)
Dy(2)	O(17)	2.329(5)
Dy(2)	O(21)	2.577(7)
Dy(2)	O(22)	2.417(6)
Dy(2)	O(28)	2.382(6)
Dy(3)	O(2)	2.420(4)
Dy(3)	O(3)	2.392(5)
Dy(3)	O(5)	2.430(5)
Dy(3)	O(6)	2.393(4)
Dy(3)	O(13)	2.367(5)
Dy(3)	O(19)	2.371(5)
Dy(3)	O(24)	2.572(7)
Dy(3)	O(25)	2.425(7)
Dy(3)	O(29)	2.378(6)
Al(1)	O(1)	1.892(5)
Al(1)	O(2)	1.886(5)
Al(1)	O(3)	1.885(5)
Al(1)	O(10)	1.860(6)
Al(1)	O(12)	1.902(5)
Al(1)	O(14)	1.868(6)
Al(2)	O(4)	1.903(5)
Al(2)	O(5)	1.890(5)
Al(2)	O(6)	1.896(5)
Al(2)	O(16)	1.863(6)
Al(2)	O(18)	1.878(6)
Al(2)	O(20)	1.882(5)

Table 12-24 Angles [°] of **(15)**.

Dy(1)	Dy(2)	Dy(3)	59.68(1)
Dy(1)	Dy(3)	Dy(2)	60.36(1)
Dy(2)	Dy(1)	Dy(3)	59.96(1)
Al(1)	Dy(1)	Al(2)	95.78(5)
Al(1)	Dy(2)	Al(2)	96.65(5)
Al(1)	Dy(3)	Al(2)	96.60(5)
Dy(1)	O(1)	Dy(2)	109.26(18)
Dy(1)	O(6)	Dy(3)	109.72(16)
Dy(2)	O(4)	Dy(1)	109.88(18)
Dy(2)	O(2)	Dy(3)	109.36(16)

Dy(3)	O(3)	Dy(1)	109.09(18)
Dy(3)	O(5)	Dy(2)	109.39(17)
Al(1)	O(1)	Dy(1)	104.4(2)
Al(1)	O(1)	Dy(2)	103.0(2)
Al(1)	O(3)	Dy(1)	103.8(2)
Al(1)	O(3)	Dy(3)	105.0(2)
Al(1)	O(2)	Dy(2)	104.1(2)
Al(1)	O(2)	Dy(3)	103.9(2)
Al(2)	O(4)	Dy(1)	104.6(2)
Al(2)	O(4)	Dy(2)	104.0(2)
Al(2)	O(5)	Dy(2)	104.5(2)
Al(2)	O(5)	Dy(3)	103.8(2)
Al(2)	O(6)	Dy(1)	105.3(2)
Al(2)	O(6)	Dy(3)	105.0(2)
Al(1)	Dy(1)	Dy(2)	54.38(4)
Al(1)	Dy(2)	Dy(1)	54.69(4)
Al(1)	Dy(2)	Dy(3)	54.58(4)
Al(1)	Dy(3)	Dy(2)	54.63(4)
Al(1)	Dy(1)	Dy(3)	54.62(4)
Al(1)	Dy(3)	Dy(1)	54.98(4)
Al(2)	Dy(1)	Dy(2)	54.31(3)
Al(2)	Dy(2)	Dy(1)	55.09(4)
Al(2)	Dy(2)	Dy(3)	54.75(4)
Al(2)	Dy(3)	Dy(2)	54.64(3)
Al(2)	Dy(1)	Dy(3)	54.66(4)
Al(2)	Dy(3)	Dy(1)	55.34(4)
Dy(1)	Al(1)	Dy(2)	70.93(4)
Dy(2)	Al(1)	Dy(3)	70.79(4)
Dy(3)	Al(2)	Dy(1)	70.00(4)
Dy(1)	Al(2)	Dy(2)	70.60(4)
Dy(2)	Al(2)	Dy(3)	70.62(4)

Molecular structure, coordination spheres, bond lengths, distances, angles and packing of $[\text{Co}_2\text{Dy}_3(\text{dtbba})_7(\mu_3\text{-OH})_6(\text{NO}_3)_2(\text{C}_3\text{H}_7\text{OH})_3]\cdot 3\text{C}_3\text{H}_7\text{OH}\cdot 3\text{CH}_3\text{CN}$ (**16**)

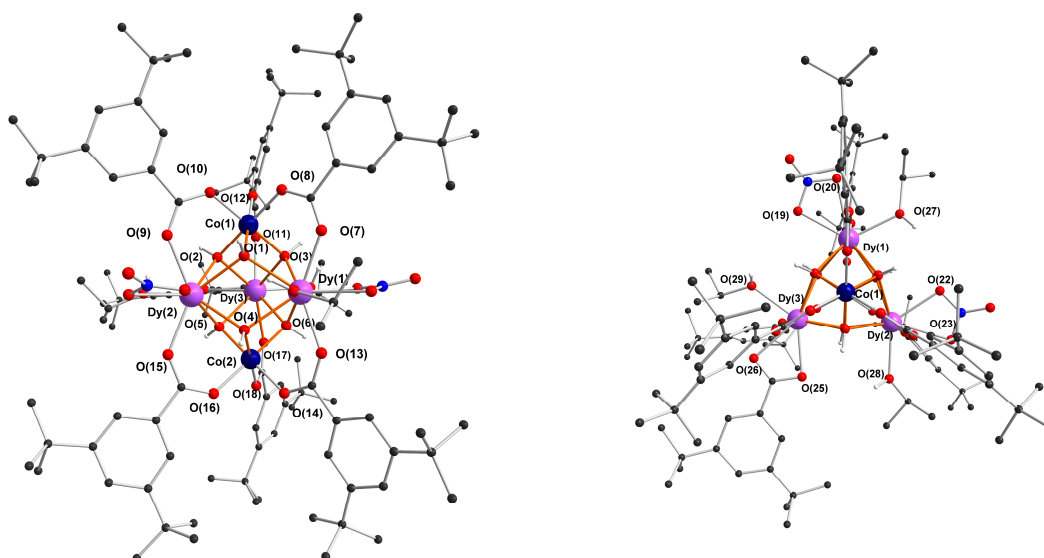


Figure 12-36 Molecular structure of $[\text{Co}_2\text{Dy}_3(\text{dtbbba})_7(\mu_3\text{-OH})_6(\text{NO}_3)_2(\text{C}_3\text{H}_7\text{OH})_3]\cdot 3\text{C}_3\text{H}_7\text{OH}\cdot 3\text{CH}_3\text{CN}$ (**16**) from the side view (left) and down the pseudo 3-fold axis (right).

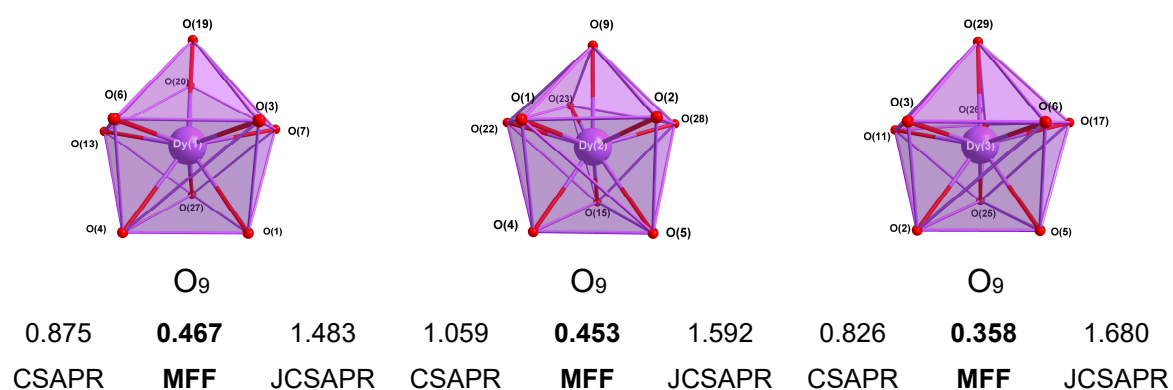


Figure 12-37 Coordination spheres around the Dy(III) with deviations from the perfect geometries in %.

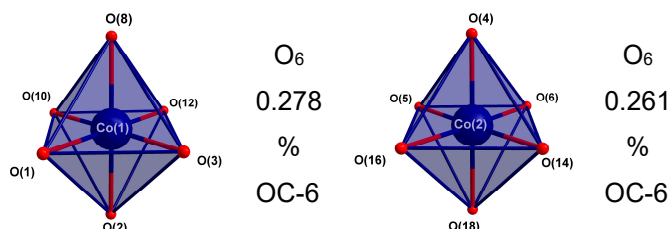


Figure 12-38 Coordination spheres around the Co(III) with deviations from the perfect geometry.

The packing is stabilized via hydrogen bonding between solvent molecules (acetonitrile, isopropanol), coordinated isopropanol and $\mu_3\text{-OH}^-$ units. The shortest

inter-triangle {Dy₃} distance is with 16.791 Å longer than in (**15**). The shortest intermolecular Co-Co distance is with 16.720 Å significantly longer than the shortest intermolecular Al-Al distance in (**15**). The packing with the coordination spheres of the Dy(III) and the Co(III) ions is shown in Figure 12-39.

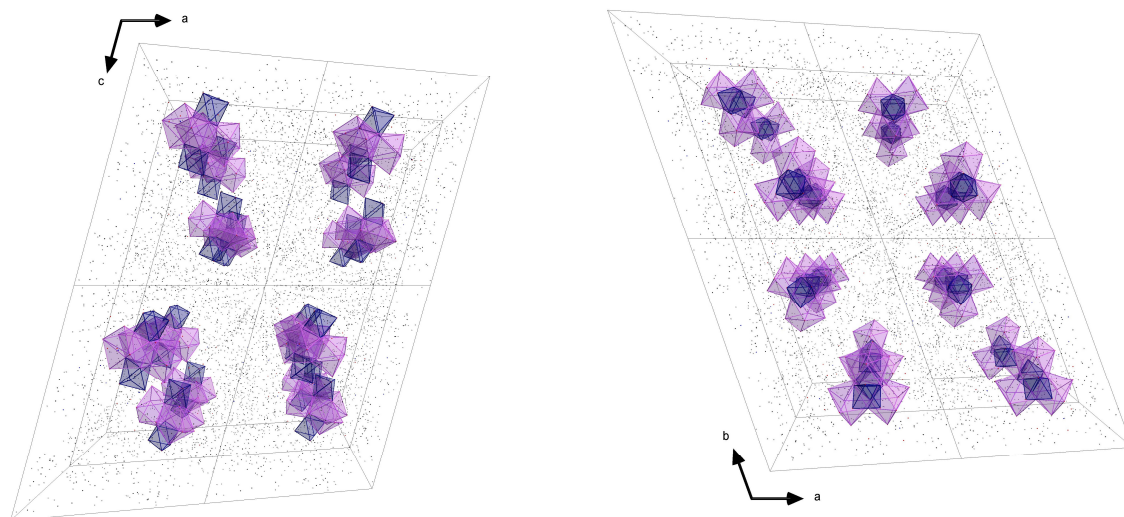


Figure 12-39 Packing of (**16**) from different viewing directions. Coordination spheres of the Dy(III) ions in lavender and of the Co(III) ions in dark blue.

Table 12-25 Distances [Å] of (**16**).

Co(1)	Co(2)	5.0179(11)
Dy(1)	Dy(2)	3.9503(5)
Dy(1)	Dy(3)	4.0192(5)
Dy(2)	Dy(3)	3.9670(5)
Dy(1)	Co(1)	3.3952(9)
Dy(1)	Co(2)	3.3914(9)
Dy(2)	Co(1)	3.4300(9)
Dy(2)	Co(2)	3.3656(8)
Dy(3)	Co(1)	3.4077(9)
Dy(3)	Co(2)	3.4211(9)
Dy(1)	O(1)	2.384(4)
Dy(1)	O(3)	2.438(4)
Dy(1)	O(4)	2.417(4)
Dy(1)	O(6)	2.392(4)
Dy(1)	O(7)	2.344(5)
Dy(1)	O(13)	2.321(4)
Dy(1)	O(19)	2.434(5)
Dy(1)	O(20)	2.578(6)
Dy(1)	O(27)	2.384(6)

Dy(2)	O(1)	2.436(4)
Dy(2)	O(2)	2.409(4)
Dy(2)	O(4)	2.365(4)
Dy(2)	O(5)	2.405(4)
Dy(2)	O(9)	2.337(4)
Dy(2)	O(15)	2.326(4)
Dy(2)	O(22)	2.414(5)
Dy(2)	O(23)	2.614(6)
Dy(2)	O(28)	2.382(5)
Dy(3)	O(2)	2.420(4)
Dy(3)	O(3)	2.426(4)
Dy(3)	O(5)	2.401(4)
Dy(3)	O(6)	2.460(4)
Dy(3)	O(11)	2.342(4)
Dy(3)	O(17)	2.323(4)
Dy(3)	O(25)	2.423(4)
Dy(3)	O(26)	2.488(5)
Dy(3)	O(29)	2.397(5)
Co(1)	O(1)	1.902(4)
Co(1)	O(2)	1.899(4)
Co(1)	O(3)	1.891(4)
Co(1)	O(8)	1.917(4)
Co(1)	O(10)	1.900(4)
Co(1)	O(12)	1.912(5)
Co(2)	O(4)	1.908(4)
Co(2)	O(5)	1.895(4)
Co(2)	O(6)	1.907(4)
Co(2)	O(14)	1.890(4)
Co(2)	O(16)	1.899(5)
Co(2)	O(18)	1.912(4)

Table 12-26 Angles [°] of **(16)**.

Dy(1)	Dy(2)	Dy(3)	61.01(1)
Dy(1)	Dy(3)	Dy(2)	59.29(1)
Dy(2)	Dy(1)	Dy(3)	59.70(1)
Co(1)	Dy(1)	Co(2)	95.36(2)
Co(1)	Dy(2)	Co(2)	95.19(2)
Co(1)	Dy(3)	Co(2)	94.58(2)
Dy(1)	O(1)	Dy(2)	110.10(16)
Dy(1)	O(6)	Dy(3)	111.85(15)
Dy(2)	O(4)	Dy(1)	111.39(16)

Dy(2)	O(2)	Dy(3)	110.45(15)
Dy(3)	O(3)	Dy(1)	111.44(15)
Dy(3)	O(5)	Dy(2)	111.26(15)
Co(1)	O(1)	Dy(1)	104.21(19)
Co(1)	O(1)	Dy(2)	103.83(18)
Co(1)	O(2)	Dy(2)	104.90(19)
Co(1)	O(2)	Dy(3)	103.51(18)
Co(1)	O(3)	Dy(1)	102.60(18)
Co(1)	O(3)	Dy(3)	103.56(17)
Co(2)	O(4)	Dy(1)	102.62(19)
Co(2)	O(4)	Dy(2)	103.42(18)
Co(2)	O(5)	Dy(2)	102.36(19)
Co(2)	O(5)	Dy(3)	104.96(18)
Co(2)	O(6)	Dy(1)	103.58(19)
Co(2)	O(6)	Dy(3)	102.39(17)
Co(1)	Dy(1)	Dy(2)	55.05(2)
Co(1)	Dy(2)	Dy(1)	54.22(2)
Co(1)	Dy(2)	Dy(3)	54.28(2)
Co(1)	Dy(3)	Dy(2)	54.80(2)
Co(1)	Dy(1)	Dy(3)	53.93(2)
Co(1)	Dy(3)	Dy(1)	53.64(2)
Co(2)	Dy(1)	Dy(2)	53.92(2)
Co(2)	Dy(2)	Dy(3)	54.88(2)
Co(2)	Dy(3)	Dy(2)	53.58(2)
Co(2)	Dy(1)	Dy(3)	54.19(2)
Co(2)	Dy(3)	Dy(1)	53.50(2)
Dy(1)	Co(1)	Dy(2)	70.73(2)
Dy(2)	Co(1)	Dy(3)	70.92(2)
Dy(3)	Co(2)	Dy(1)	72.31(2)
Dy(3)	Co(1)	Dy(1)	72.43(2)
Dy(1)	Co(2)	Dy(2)	71.55(2)
Dy(2)	Co(2)	Dy(3)	71.53(2)

12.4 Molecular structure, bond lengths, angles and distances of (17) to (22)

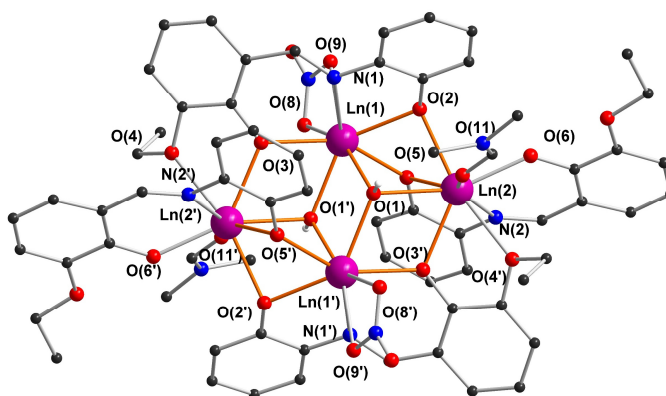


Figure 12-40 Molecular structure of (17) to (22) with Ln = Tb, Dy, Ho, Er, Yb, Y. Primed-atoms at 1-x, 1-y, 1-z.

Table 12-27 Distances [Å] and angles [°] of Tb (17).

Tb(1)	Tb(2)	3.4945(5)
Tb(1')	Tb(2')	3.4945(5)
Tb(1)	Tb(2')	3.8941(5)
Tb(2)	Tb(1')	3.8941(5)
Tb(1)	Tb(1')	3.8297(4)
Tb(2)	Tb(2')	6.3312(6)
Tb(1)	O(1')	2.337(3)
Tb(1)	O(1)	2.357(3)
Tb(1)	O(2)	2.369(3)
Tb(1)	O(3)	2.309(3)
Tb(1)	O(5)	2.321(3)
Tb(1)	O(8)	2.471(4)
Tb(1)	O(9)	2.441(4)
Tb(2)	O(1)	2.434(3)
Tb(2)	O(2)	2.397(3)
Tb(2)	O(3')	2.382(3)
Tb(2)	O(4')	2.529(3)
Tb(2)	O(5)	2.371(3)
Tb(2)	O(6)	2.203(3)
Tb(2)	O(11)	2.368(3)
Tb(1)	N(1)	2.506(3)
Tb(2)	N(2)	2.451(4)

Tb(1)	O(3)	Tb(2')	111.84(17)
-------	------	--------	------------

Tb(1')	O(1)	Tb(1)	109.33(12)
Tb(1')	O(1)	Tb(2)	109.40(12)
Tb(1)	O(5)	Tb(2)	96.25(15)
Tb(1)	O(1)	Tb(2)	93.66(10)
Tb(1)	O(2)	Tb(2)	94.32(10)

Table 12-28 Distances [Å] and angles [°] of Dy (**18**).

Dy(1)	Dy(2)	3.4716(1)
Dy(2')	Dy(1')	3.4716(1)
Dy(1)	Dy(2')	3.8754(1)
Dy(1) ¹	Dy(2)	3.8754(1)
Dy(1)	Dy(1')	3.8051(1)
Dy(2)	Dy(2')	6.2978(1)
Dy(1)	O(1)	2.336(2)
Dy(1)	O(1')	2.328(2)
Dy(1)	O(2)	2.359(2)
Dy(1)	O(3)	2.300(2)
Dy(1)	O(5)	2.308(2)
Dy(1)	O(8)	2.461(3)
Dy(1)	O(9)	2.432(3)
Dy(2)	O(1)	2.414(2)
Dy(2)	O(2)	2.386(2)
Dy(2)	O(3')	2.373(2)
Dy(2)	O(4')	2.521(2)
Dy(2)	O(5)	2.365(2)
Dy(2)	O(6)	2.191(2)
Dy(2)	O(11)	2.361(2)
Dy(1)	N(1)	2.490(2)
Dy(2)	N(2)	2.443(2)

Dy(1)	O(3)	Dy(2')	112.03(8)
Dy(1')	O(1)	Dy(1)	109.36(8)
Dy(1')	O(1)	Dy(2)	109.61(8)
Dy(1)	O(5)	Dy(2)	95.95(7)
Dy(1)	O(1)	Dy(2)	93.89(7)
Dy(1)	O(2)	Dy(2)	94.07(7)

Table 12-29 Distances [Å] and angles [°] of Ho (**19**).

Ho(1)	Ho(2)	3.4468(5)
Ho(1')	Ho(2')	3.4468(5)
Ho(1)	Ho(2')	3.8583(5)
Ho(2)	Ho(1')	3.8583(5)
Ho(1)	Ho(1')	3.7789(4)
Ho(2)	Ho(2')	6.2654(5)
Ho(1)	O(1')	2.318(2)
Ho(1)	O(1)	2.319(2)
Ho(1)	O(2)	2.352(2)
Ho(1)	O(3)	2.287(2)
Ho(1)	O(5)	2.296(2)
Ho(1)	O(8)	2.447(3)
Ho(1)	O(9)	2.418(3)
Ho(2)	O(1)	2.410(2)
Ho(2)	O(2)	2.364(2)
Ho(2)	O(3')	2.364(2)
Ho(2)	O(4')	2.511(2)
Ho(2)	O(5)	2.353(2)
Ho(2)	O(6)	2.186(2)
Ho(2)	O(11)	2.348(2)
Ho(1)	N(1)	2.479(3)
Ho(2)	N(2)	2.432(3)

Ho(1)	Ho(3)	Ho(2')	112.11(9)
Ho(1')	O(1)	Ho(1)	109.17(9)
Ho(1')	O(1)	Ho(2)	109.40(9)
Ho(1)	O(5)	Ho(2)	95.71(8)
Ho(1)	O(1)	Ho(2)	93.57(8)
Ho(1)	O(2)	Ho(2)	93.92(8)

Table 12-30 Distances [Å] and angles [°] of Er (**20**).

Er(1)	Er(2)	3.4313(5)
Er(1')	Er(2')	3.4313(5)
Er(1)	Er(2')	3.8412(5)
Er(2)	Er(1')	3.8412(5)
Er(1)	Er(1')	3.7539(4)
Er(2)	Er(2')	6.2423(6)
Er(1)	O(1')	2.301(3)
Er(1)	O(1)	2.307(3)
Er(1)	O(2)	2.341(3)
Er(1)	O(3)	2.284(3)
Er(1)	O(5)	2.283(3)
Er(1)	O(8)	2.435(4)
Er(1)	O(9)	2.397(4)
Er(2)	O(1)	2.411(3)
Er(2)	O(2)	2.349(3)
Er(2)	O(3')	2.345(3)
Er(2)	O(4')	2.509(4)
Er(2)	O(5)	2.340(3)
Er(2)	O(6)	2.181(3)
Er(2)	O(11)	2.335(3)
Er(1)	N(1)	2.470(4)
Er(2)	N(2)	2.424(4)

Er(1)	O(2)	Er(2')	111.85(18)
Er(1')	O(1)	Er(1)	109.11(13)
Er(1')	O(1)	Er(2)	109.17(12)
Er(1)	O(5)	Er(2)	95.88(15)
Er(1)	O(1)	Er(2)	93.29(11)
Er(1)	O(2)	Er(2)	94.06(12)

Table 12-31 Distances [Å] and angles [°] of Yb (**21**)

Yb(1)	Yb(2)	3.3850(2)
Yb(1')	Yb(2')	3.3850(2)
Yb(1)	Yb(2')	3.7861(5)
Yb(2)	Yb(1')	3.7861(5)
Yb(1)	Yb(1')	3.6963(3)
Yb(2)	Yb(2')	6.15815(5)
Yb(1)	O(2)	2.310(3)
Yb(1)	O(1')	2.286(3)
Yb(1)	O(1)	2.273(3)
Yb(1)	O(3)	2.235(3)
Yb(1)	O(5)	2.262(3)
Yb(1)	O(8)	2.427(4)
Yb(1)	O(9)	2.365(4)
Yb(2)	O(6)	2.160(4)
Yb(2)	O(2)	2.332(3)
Yb(2)	O(1)	2.355(3)
Yb(2)	O(3')	2.328(4)
Yb(2)	O(5)	2.320(3)
Yb(2)	O(11)	2.290(4)
Yb(2)	O(4')	2.539(4)
Yb(1)	N(1)	2.446(5)
Yb(2)	N(2)	2.375(5)

Yb(1)	O(1)	Yb(1')	108.33(12)
Yb(1')	O(1)	Yb(2)	109.31(12)
Yb(1)	O(1)	Yb(2)	93.98(10)
Yb(1)	O(2)	Yb(2)	93.64(10)

Table 12-32 Distances [Å] and angles [°] of Y (**22**).

Y(1)	Y(2)	3.4473(5)
Y(1')	Y(2')	3.4473(5)
Y(1)	Y(2')	3.8508(5)
Y(2)	Y(1')	3.8508(5)
Y(1)	Y(1')	3.7711(4)
Y(2)	Y(2')	6.2612(5)
Y(1)	O(1')	2.3154(12)
Y(1)	O(1)	2.3082(13)
Y(1)	O(2)	2.3497(13)
Y(1)	O(3)	2.2877(13)
Y(1)	O(5)	2.2972(12)
Y(1)	O(8)	2.4378(15)
Y(1)	O(9)	2.4105(15)
Y(2)	O(1)	2.4085(13)
Y(2)	O(2)	2.3665(13)
Y(2)	O(3')	2.3589(13)
Y(2)	O(4')	2.5111(14)
Y(2)	O(5)	2.3480(13)
Y(2)	O(6)	2.1861(13)
Y(2)	O(11)	2.3373(13)
Y(1)	N(1)	2.4870(15)
Y(2)	N(2)	2.4363(15)

Y(1)	O(1)	Y(1')	109.29(5)
Y(1')	O(1)	Y(2)	109.19(5)
Y(1)	O(2)	Y(2)	93.93(4)
Y(1)	O(1)	Y(2)	93.90(4)

12.5 List of abbreviations

SMT	Single Molecule Toric
SMM	Single Molecule Magnet
Å	Angstrom
VSM	Vibrating Sample Magnetometer
SQUID	Superconducting Quantum Interference Device
H	Magnetic field
M	Magnetization
χ	Susceptibility
C	Curie-constant
U_{eff}	Energy barrier
τ_0	preexponential factor/relaxation time
pfbaH	4-fluorobenzoic acid
pclbaH	4-chlorobenzoic acid
pclbaH	4-cyanobenzoic acid
dfbaH	3,5-difluorobenzoic acid
dtbbaH	3,5-diterbutylbenzoic acid
ehimpH ₂	2-ethoxy-6-(((2-hydroxyphenyl)imino)methyl)phenol
pivH	Pivalic acid
hmmpH ₂	2-[(2-hydroxyethylimino)methyl]-6-methoxyphenol
mdeaH ₂	N-methyldiethanolamine
ampdH ₅	3-amino-3-methylpentane-1,5-diol
teaH ₃	Triethanolamine
Me-teaH ₃	<i>rac</i> -1-[<i>N,N</i> -bis-(2-hydroxyethyl)amino]-2-propanol
apadH ₄	2,2'-(3-aminopropylazanediyl)diethanol
H ₂ pmide	<i>N</i> -(2-pyridylmethyl)diethanolamine
DC	Direct current
AC	Alternating current
KD	Kramers' doublet

12.6 List of complexes

(1) $[\text{Dy}_3(3\text{-ethoxysalicyl})_3(\mu_3\text{-OH})_2(\text{H}_2\text{O})_4\text{Cl}_2]\text{Cl}_2 \cdot 5\text{H}_2\text{O} \cdot 3\text{MeOH}$	153
(2) $[\text{Dy}_3(3\text{-ethoxysalicyl})_3(\mu_3\text{-OH})_2(\text{H}_2\text{O})_2(\text{CH}_3\text{OH})\text{Cl}_3]\text{Cl} \cdot 2\text{H}_2\text{O} \cdot 2\text{CH}_3\text{OH}$	153
(3) $[\text{Eu}_3(3\text{-ethoxysalicyl})_3(\mu_3\text{-OH})_2(\text{H}_2\text{O})_2(\text{CH}_3\text{OH})\text{Cl}_3]\text{Cl} \cdot 2\text{CH}_3\text{OH} \cdot 2\text{H}_2\text{O}$	153
(4) $[\text{Tb}_3(3\text{-ethoxysalicyl})_3(\mu_3\text{-OH})_2(\text{H}_2\text{O})_2(\text{CH}_3\text{OH})\text{Cl}_3]\text{Cl} \cdot 3\text{CH}_3\text{OH}$	154
(5) $[\text{Ho}_3(3\text{-ethoxysalicyl})_3(\mu_3\text{-OH})_2(\text{H}_2\text{O})_2(\text{CH}_3\text{OH})\text{Cl}_3]\text{Cl} \cdot 3\text{CH}_3\text{OH}$	154
(6) $[\text{Er}_3(3\text{-ethoxysalicyl})_3(\mu_3\text{-OH})_2(\text{H}_2\text{O})_2(\text{CH}_3\text{OH})\text{Cl}_3]\text{Cl} \cdot \text{H}_2\text{O} \cdot 2\text{CH}_3\text{OH}$	155
(7) $[\text{Cr}_2\text{Dy}_3(\text{pfba})_6(\mu_3\text{-OH})_6(\text{NO}_3)_3(\text{H}_2\text{O})_2(\text{C}_3\text{H}_7\text{OH})] \cdot \text{H}_2\text{O}$	155
(8) $[\text{Cr}_2\text{Dy}_3(\text{pfba})_9(\mu_3\text{-OH})_6(\text{C}_3\text{H}_7\text{OH})_3] \cdot 3\text{C}_3\text{H}_7\text{OH}$	155
(9) $[\text{Cr}_2\text{Dy}_3(\text{pclba})_9(\mu_3\text{-OH})_6(\text{C}_3\text{H}_7\text{OH})_3] \cdot \text{H}_2\text{O} \cdot \text{C}_3\text{H}_7\text{OH}$	156
(10) $[\text{Cr}_2\text{Dy}_3(\text{pcnba})_6(\mu_3\text{-OH})_6(\text{NO}_3)_3(\text{H}_2\text{O})_3]$	156
(11) $[\text{Cr}_2\text{Dy}_3(\text{dfba})_6(\mu_3\text{-OH})_6(\text{NO}_3)_3(\text{DMF})_3] \cdot \text{DMF}$	156
(12) $[\text{Cr}_2\text{Dy}_3(\text{dtbba})_9(\mu_3\text{-OH})_6(\text{C}_3\text{H}_7\text{OH})_3] \cdot 3\text{C}_3\text{H}_7\text{OH}$	157
(13) $[\text{Fe}_2\text{Dy}_3(\text{dtbba})_9(\mu_3\text{-OH})_6(\text{C}_3\text{H}_7\text{OH})_3] \cdot 3\text{C}_3\text{H}_7\text{OH}$	157
(14) $[\text{Al}_2\text{Dy}_3(\text{dtbba})_9(\mu_3\text{-OH})_6(\text{CH}_3\text{OH})_{0.75}(\text{H}_2\text{O})_{1.5}(\text{C}_3\text{H}_7\text{OH})_{0.75}] \cdot \text{CH}_3\text{H}_7\text{OH}$	157
(15) $[\text{Al}_2\text{Dy}_3(\text{dtbba})_7(\mu_3\text{-OH})_6(\text{NO}_3)_2(\text{C}_3\text{H}_7\text{OH})(\text{H}_2\text{O})_2] \cdot 3\text{H}_2\text{O}$	158
(16) $[\text{Co}_2\text{Dy}_3(\text{dtbba})_7(\mu_3\text{-OH})_6(\text{NO}_3)_2(\text{C}_3\text{H}_7\text{OH})_3] \cdot 3\text{C}_3\text{H}_7\text{OH} \cdot 3\text{CH}_3\text{CN}$	158
(17) $\text{Tb}_4(\text{OH})_2(\text{NO}_3)_2(\text{DMF})_2(\text{ehimp})_4$	158
(18) $\text{Dy}_4(\text{OH})_2(\text{NO}_3)_2(\text{DMF})_2(\text{ehimp})_4$	159
(19) $\text{Ho}_4(\text{OH})_2(\text{NO}_3)_2(\text{DMF})_2(\text{ehimp})_4$	159
(20) $\text{Er}_4(\text{OH})_2(\text{NO}_3)_2(\text{DMF})_2(\text{ehimp})_4$	160
(21) $\text{Yb}_4(\text{OH})_2(\text{NO}_3)_2(\text{DMF})_2(\text{ehimp})_4$	160
(22) $\text{Y}_4(\text{OH})_2(\text{NO}_3)_2(\text{DMF})_2(\text{ehimp})_4$	160
(23) $[\text{Dy}_6(\text{NO}_3)_6(\text{teaH})_6] \cdot 2\text{C}_2\text{H}_5\text{OH}$	161
(24) $[\text{Dy}_6(\text{NO}_3)_6(\text{apadH}_2)_6]$	161

12.7 List of tables

Table 3-1	Comparison of distances and angles of Dy3-1 , Dy3-2 , (1) and (2).	44
Table 3-2	Energies and <i>g</i> -values of the ground and first excited Kramers' doublets (KD1 and KD2) for (1), calculated by <i>ab initio</i> . The minimum reversal energy is calculated by MAGELLAN.	51
Table 3-3	Energies and <i>g</i> -values of the ground and first excited Kramers' doublets (KD1 and KD2) for (2), calculated by <i>ab initio</i> . The minimum reversal energy is calculated by MAGELLAN.	53
Table 3-4	Comparison of selected angles and lengths for (3) to (6).	63
Table 3-5	Energies and <i>g</i> -values of the ground and first excited doublets for (4).	65
Table 3-6	Energies and <i>g</i> -values of the ground and first excited doublets for (5).	66
Table 3-7	Energies and <i>g</i> -values of the Ground Kramers' doublets (KD1) and first excited Kramers' doublets (KD2) for (6).	68
Table 3-8	Comparison of selected angles and lengths for Dy3-1 , Dy3-2 , (1) and (2).	71
Table 4-1	Bond lengths, angles, space groups, coordination spheres and susceptibility measurements summarized of series-1 , containing different organic ligands but the same metal(III) ions M = Cr.	98
Table 4-2	Bond lengths, angles, space groups, coordination spheres and susceptibility measurements summarized of series-2 , containing the same organic ligand (dtbbaH). (12) is listed here again for the better comparison with different incorporated metal ions.	99
Table 5-1	Comparison of Ln-O and Ln-N bond lengths and Ln-O-Ln angles involving the bridging oxygens in (17) to (22).	105
Table 5-2	Comparison of the {Dy ₄ } systems in regard of distances, angles, donor sets and magnetic results.	123
Table 5-3	Comparison of the {Dy ₄ } systems in regard of their ligands and toroidicity.	123
Table 6-1	Comparison of the crystal structures of (23) and Dy6-1	129
Table 6-2	Comparison of (24) and Dy6-3	133
Table 6-3	Selected distances [Å] and angles [°] of Dy6-4	137
Table 6-4	Comparison of the Dy ₆ systems. The systems with the same colour are isostructural.	141
Table 9-1	Crystallographic data and structure refinement for (1) and (2).	162
Table 9-2	Crystallographic data and structure refinement for (3) and (4).	163
Table 9-3	Crystallographic data and structure refinement for (5) and (6).	164
Table 9-4	Crystallographic data and structure refinement for (7) and (8).	165
Table 9-5	Crystallographic data and structure refinement for (9) and (10).	166
Table 9-6	Crystallographic data and structure refinement for (11) and (12).	167
Table 9-7	Crystallographic data and structure refinement for (13) and (14).	168
Table 9-8	Crystallographic data and structure refinement for (15) and (16).	169
Table 9-9	Crystallographic data and structure refinement for (17) and (18).	170
Table 9-10	Crystallographic data and structure refinement for (19) and (20).	171
Table 9-11	Crystallographic data and structure refinement for (21) and (22).	172
Table 9-12	Crystallographic data and structure refinement for (23) and (24).	173

Table 12-1	Distances [Å] and angles [°] of (1).....	182
Table 12-2	Distances [Å] and angles [°] of (2).....	184
Table 12-3	Distances [Å] and angles [°] of (3).....	186
Table 12-4	Distances [Å] and angles [°] of (4).....	187
Table 12-5	Distances [Å] and angles [°] of (5).....	188
Table 12-6	Distances [Å] and angles [°] of (6).....	189
Table 12-7	Distances [Å] of (7).....	192
Table 12-8	Angles [°] of (7).	193
Table 12-9	Distances [Å] of (8).....	195
Table 12-10	Angles [°] of (8).	196
Table 12-11	Distances [Å] of (9).....	199
Table 12-12	Angles [°] of (9).	200
Table 12-13	Distances [Å] of (10).....	202
Table 12-14	Angles [°] of (10).	203
Table 12-15	Distances [Å] of (11).....	205
Table 12-16	Angles [°] of (11).	206
Table 12-17	Distances [Å] of (12).....	208
Table 12-18	Angles [°] of (12).	209
Table 12-19	Distances [Å] of (13).....	212
Table 12-20	Angles [°] of (13).	213
Table 12-21	Distances [Å] of (14).....	216
Table 12-22	Angles [°] of (14).	216
Table 12-23	Distances [Å] of (15).....	218
Table 12-24	Angles [°] of (15).	219
Table 12-25	Distances [Å] of (16).....	222
Table 12-26	Angles [°] of (16).	223
Table 12-27	Distances [Å] and angles [°] of Tb (17).	225
Table 12-28	Distances [Å] and angles [°] of Dy (18).	226
Table 12-29	Distances [Å] and angles [°] of Ho (19).	227
Table 12-30	Distances [Å] and angles [°] of Er (20).	228
Table 12-31	Distances [Å] and angles [°] of Yb (21)	229
Table 12-32	Distances [Å] and angles [°] of Y (22).	230

12.8 List of figures

Figure 1-1	Magnetic flux course in a diamagnetic and paramagnetic material under an applied field. Adapted from reference ^[25]	3
Figure 1-2	Spin alignment for the different types of magnetism.	5
Figure 1-3	χ vs T and χT vs T plots.	6
Figure 1-4	$1/\chi$ vs T plots with Weiss constant θ	6
Figure 1-5	Hysteresis for a ferromagnet with the new curve (red), saturation of magnetization M_{sat} , remanence M_R and coercivity H_c . The black arrows in the boxes represent the magnetic moments within the domains.	7
Figure 1-6	The bistability (a) is destroyed by applying a magnetic field and reduce the energy of the M_S states in field direction (b). By switching off the magnetic field (c), the relaxation of the spins is slowed down by an energy barrier U_{eff} . The yellow dots represent the spins.	11
Figure 1-7	Left: The arrows show the mechanisms of relaxation of magnetization. An ideal SMM corresponds to the suppression of all relaxation mechanisms except the Orbach process (red arrows). Adapted from reference ^[38] . Right: The blue lines indicate levels of the lattice and the red ones are crystal field levels of the lanthanide ion. The dotted lines are virtual states, involved only in the Raman processes. Reprinted with permission from reference ^[39]	11
Figure 1-8	Frequency-dependent in-phase (left) and frequency-dependent out-of-phase measurements (right).	12
Figure 1-9	The different relaxation processes in a plot of $\ln t$ vs T^{-1} . Only the Orbach process follows the Arrhenius law in a straight line (red line).	13
Figure 1-10	Cole-Cole plot at different temperatures with the distribution parameter α . Adapted with permission from reference ^[41] . Copyright 2020 Royal Society of Chemistry.	14
Figure 1-11	Hysteresis loops for a complex of the Mn_{12} family. Adapted with permission from reference ^[45] . Copyright 2005 American Chemical Society.	15
Figure 1-12	The M vs T plot shows time-independent slow relaxation of magnetization below 0.1 K. Adapted with permission from reference ^[44] . Copyright 2005 Wiley-VCH.	15
Figure 1-13	Electronic interactions for lanthanide ions and the usual energy quantities. Adapted with permission from reference ^[46] . Copyright 2016, Wiley-VCH Verlag.	17
Figure 1-14	Left: The electron density for oblate ions (Dy(III), Tb(III)) in the ground state is stabilised by an axial ligand field (yellow dots). The shapes from oblate to prolate in the different energy states (right) with $J = 6$ for Tb(III) and $J = 15/2$ for Dy(III). Adapted with permission from references ^[47,50]	18
Figure 1-15	Left: The electron density for prolate ions (Er(III), Tm(III)) in the ground state is stabilised by an equatorial ligand field (yellow dots). The shapes from prolate to oblate in the different energy states (right) with $J = 15/2$ for Er(III) and $J = 6$ for Tm(III). ^[47,50]	18

Figure 1-16	Ground state spin configuration of the co-linear Ising model on a triangle cluster. In the case of ferromagnetic interactions (left) between the spin centres (blue arrows), all interactions are favourable. With antiferromagnetic interactions between the spins (right), there is one bond (red cross) which is energetically unfavourable, and this leads to a manifold of degenerated ground states.20
Figure 1-17	Magnetic frustration within systems with the same antiferromagnetic interactions between all spin carriers, forming a triangle (left), a square (middle) and a tetrahedron (right). There are two spins in each system (blue arrows) which align antiparallel, but the remaining spins are frustrated.....20
Figure 1-18	Frustrated 2D lattices with edge and corner-sharing triangular units (left) and Kagomé lattice (middle). The 3-D pyrochlore lattice are formed by corner-sharing tetrahedrons (right). The circles in the Kagomé lattice show the different spin arrangements within the lattice. Adapted from reference ^[54] . Copyright 2010, Springer Nature.21
Figure 1-19	Degenerated ground states with the vortex-like arrangement of non-collinear spins (blue) in a triangle (top left), in a square (top right) and in a hexagon (bottom) with spins arranged either all clockwise or all anticlockwise.22
Figure 1-20	The illustration of a toroidal moment T created by an enclosed magnetic field m which are induced by circular currents I on the surface of a torus (left). The toroidal moment T can also be described as the head-to-tail arrangement of Spins S with the radius r from the origin of the molecule (right). Adapted from reference ^[57]23
Figure 1-21	The combination of a toroidal magnetic dipole and an electric dipole leads to an anapole moment. The anapole moment does not emit any radiation because the radiation of the two dipoles cancel each other out (left). ^[61] The smallest known anapole moment in an atomic nuclei (right). The nuclear currents (red) enclose a closed loop of magnetic field (green). ^[57]24
Figure 1-22	The demonstration of the three multipoles: Electric dipole moment P , magnetic dipole moment M and the toroidal moment which can be divided into the polar magnetic toroidal dipole moment T and the axial electric toroidal moment G . Images adapted by permission from reference ^[64] . Copyright 2019, Springer Nature. The table implies the transformation properties of the multipoles under time and space inversion with inversion (-1) and no inversion (+1).25
Figure 1-23	The ferroic orders under the parity of space and time. Adapted with permission from reference ^[65] . Copyright 2007 Nature Publishing Group.....26
Figure 1-24	The often-observed S-shaped curve of the magnetization in a toroidal system at low temperatures, here at 1.8 K (top left). The graphical determination of the magnetic field where the steep rise of magnetization occurs in the dM/dH plot (top right). The determination of level-crossing from the toroidal (nearly non-magnetic) ground state and the first excited state, supported by

	<i>ab initio</i> calculations. (bottom left). The lines represent the energies of the system with different spin directions. Single crystal micro-SQUID measurements at very low temperatures (down to 30 mK) for a better determination of the desired magnetic field (bottom right). Adapted from reference ^[69] and reference ^[70] . Copyright 2009 Royal Society of Chemistry.....28
Figure 1-25	Toroidal arrangement in a {Dy ₃ } -triangle and corresponding ligand (top) with antiferromagnetic interactions (bottom left) between the spin centres, typical S-shaped curve of the magnetization (inset) and steps in the hysteresis (bottom right). Adapted with permission from reference ^[9] . Copyright 2012 Royal Society of Chemistry.....29
Figure 1-26	Toroidal arrangement in two coupled {Dy ₃ } -triangles and corresponding ligand (top) with dominant antiferromagnetic interactions (bottom left inset) in the system which can overcome by an applied magnetic field and leads to ferromagnetic alignment of the magnetic moments. The pronounced S-shaped curve of the magnetization (bottom left) and steps in the hysteresis (bottom right) show the toroidal moment in the ground state. Adapted with permission from reference ^[19] . Copyright 2012 John Wiley & Sons Ltd.30
Figure 1-27	Toroidal arrangement in a {Cr ^{III} Dy ^{III} }_6 system and corresponding ligand (top) with dominant antiferromagnetic interactions (middle left), typical S-shaped curve of the magnetization (inset) and steps in the hysteresis (middle right). The anisotropy axes of the analogues, {Cr ^{III} Tb ^{III} }_6 and {Cr ^{III} Er ^{III} }_6 also suggest a toroidal moment in the ground state (bottom). Adapted with permission from reference ^[20] and reference ^[21] . Copyright 2017 Nature Publishing Group and 2018 Wiley-VCH.....31
Figure 1-28	The structure of {Fe ₈ Dy ₈ } with a toroidal arrangement and corresponding ligand (top), The typical S-shaped curve is seen in the <i>M</i> vs <i>H</i> plot (bottom left). <i>Ab initio</i> calculations (bottom right) with lines representing the energies of the system with different spin directions. The red arrow indicates the level-crossing from the toroidal ground state to the excited state. Adapted with permission from reference ^[4] . Copyright 2020 Elsevier Inc.32
Figure 1-29	The structure of a {Fe ₁₈ Dy ₆ } SMT with corresponding ligand (top), the anisotropy axes forming a wheel (middle), susceptibility (bottom left), bulk magnetization (inset) and single crystal micro-SQUID measurements (bottom right). Adapted with permission from reference ^[23] . Copyright 2020 American Chemical Society.33
Figure 1-30	Partial charges assigned to the formally charged ligands in this thesis.....36
Figure 3-1	Molecular structure of Dy3-1 with two chlorides on the Dy(3) site (left) and molecular structure of Dy3-2 with a 50:50 disorder of chloride and water on the Dy(3) site (right). For the disorder, water is chosen to be illustrated.....39
Figure 3-2	Molecular structure of the very first SMT (Dy3-1) with anisotropy axes represented by the dashed lines and the direction of the magnetic moments (blue arrows). Reprinted with permission from ^[3] and ^[84] . Copyright 2009 and 2019 Royal Society of Chemistry.40

Figure 3-3	Anisotropy axes calculated using MAGELLAN for Dy3-1 with two chlorides at the Dy(3) site (left) and one water and one chloride at the Dy(3) site (right). As comparison the anisotropy axes of the Dy(III) ions for Dy3-2 are shown at the bottom.	41
Figure 3-4	The ligand <i>ortho</i> -vanillin which was used for the originals {Dy ₃ } compounds (Dy3-1 and Dy3-2) and the ligand 3-ethoxysalicylaldehyde used in this work for (1) and (2).....	42
Figure 3-5	The molecular structures of [Dy ₃ (L) ₃ (μ ₃ -OH) ₂ (H ₂ O) ₄ Cl ₂]Cl ₂ (1) (left) and [Dy ₃ (L) ₃ (μ ₃ -OH) ₂ (H ₂ O) ₂ (CH ₃ OH)Cl ₃]Cl (2) (right).....	43
Figure 3-6	Binding mode of the organic ligands in (1), (2) (left) and Dy3-1 and Dy3-2 (right).....	43
Figure 3-7	The perfect geometries of the coordination spheres for a donor set with eight atoms, here with an example of an O ₈ donor set.	45
Figure 3-8	Coordination spheres of the Dy(III) ions in the molecule. Here as representative, complex (1) is chosen.....	47
Figure 3-9	Packing of (1) and the chain of {Dy ₃ }- triangles linked via lattice chlorides. The dashed lines represent hydrogen bonding.....	48
Figure 3-10	Packing of (2) and the chain of {Dy ₃ }-triangles linked via coordinated chlorides. The dashed lines represent hydrogen bonding.	48
Figure 3-11	The comparison factors of the anisotropy axes of the Dy(III) ions are the tilting angle θ of the anisotropy axes with the tangential direction (red line) (left). The tilting angle of the anisotropy axes out of the Dy ₃ plane, the out-of-plane angle, is identified by φ (right). .	49
Figure 3-12	Anisotropy axes and angles of (1) from <i>ab initio</i> calculations (left) and MAGELLAN calculations (right), viewed from the top and the side.	50
Figure 3-13	Anisotropy axes and angles of (2) from <i>ab initio</i> calculations (left) and MAGELLAN calculations (right), viewing from the top and the side.	52
Figure 3-14	Plots of χT vs T for Dy3-1 (□) and Dy3-2 (•) (left). The solid line represents the calculated value for three uncorrelated Dy(III) ions. Adapted from reference ^[6] . Plots of χT vs T for (1) (right, blue) and (2) (right, green).	56
Figure 3-15	Plots of M vs H of Dy3-1 (□) and Dy3-2 (•) (top) at 1.8 K and the complexes (1) (bottom left) and (2) (bottom right) at different temperatures. The insets show the enlarged magnetization for 2 K to make the S-shaped curve visible.	56
Figure 3-16	The first derivatives of the magnetizations at 2 K show peaks at 0.9 T for both complexes (1) (left) and (2) (right).	57
Figure 3-17	Frequency dependent in-phase (left) and out-of-phase (right) measurements on (1) at 2 K under different DC fields.	57
Figure 3-18	Frequency dependent out-of-phase measurements on (1) (left) and on (2) (right) under an applied field of 0.5 T.	58
Figure 3-19	Relaxation time of the magnetization versus inverse temperature for Dy3-1 (□) and Dy3-2 (•). Adapted from reference ^[6]	58
Figure 3-20	The relaxation times are following the Arrhenius law in the high temperature region (red curve) for (1) (left) and (2) (right).	59
Figure 3-21	Parameters of the relaxation processes of (1), indicating additional Direct processes (Parameter A) and QTM (Parameter B).....	59

Figure 3-22	Arrhenius and Cole-Cole plots of (1) (left) and of (2) (right).	60
Figure 3-23	Single crystal measurements on Dy3-2 with applied field in the plane (light) and perpendicular to the plane (bold) of the Dy(III) ions (top). Adapted from reference ^[6] . Single crystal measurements on (1) (middle). The first derivative shows a steep rise of magnetization at ± 0.73 and ± 0.8 T and zero field (bottom).	61
Figure 3-24	At zero applied field, the toroidal arrangement is intact. Due to the different Dy(III) ions, the values of H where one of the spin flips is different.	62
Figure 3-25	Anisotropy axes and tilting angles θ and φ of (4) from <i>ab initio</i> calculations.	64
Figure 3-26	Anisotropy axes and tilting angles θ and φ of (5) from <i>ab initio</i> calculations.	66
Figure 3-27	Anisotropy axes and tilting angles θ and φ of (6) from <i>ab initio</i> calculations.	67
Figure 4-1	The general scheme of the M_2Dy_3 systems with the Dy (lavender), forming a plane and the metal ions M (green) in the axial positions. The μ_3 -OH ⁻ bridges in white and the additional bridging oxygens from the benzoate ligands (O _L). R stands for the different rest of the used ligands displayed below.	72
Figure 4-2	Coordination spheres with their perfect geometry around the metal ions for an O ₉ and O ₈ donor set for Dy(III) ions (lavender) and with an O ₆ donor set for the M(III) ions (green).	73
Figure 4-3	The different benzoic acid derivates, used for (7) to (16)	74
Figure 4-4	Structures with six (left), seven (middle) and nine (right) benzoate derivates as ligands. Cr(III) in dark green, Al(III) in light yellow.	75
Figure 4-5	The additional coordinated ligands on the Dy(III) ions of (7) to (12) . The {Cr ₂ (μ_3 -OH) ₆ Dy ₃ } core is highlighted with orange bonds. The bridging benzoate derivates are omitted for clarity. In (7) hydrogen atoms are omitted.	76
Figure 4-6	The additional coordinated ligands on the Dy(III) ions of (13) to (16) . The {M ₂ (μ_3 -OH) ₆ Dy ₃ } core is highlighted with orange bonds. The bridging benzoate derivates are omitted for clarity. In (14) for the disorder on Dy(1), water is chosen to be displayed, and hydrogen atoms are omitted.	78
Figure 4-7	χT vs T plots from 0-50 K (left) and from 0-300 K (right) for the complexes (7) - (12) with the same {Cr ₂ Dy ₃ } core but different organic ligands at 0.1 T.	80
Figure 4-8	M vs H plots (left) and the first derivative at 2 K (right) of (7)	81
Figure 4-9	M vs H plots (left) and the first derivative at 2 K (right) of (8)	81
Figure 4-10	M vs H plots (left) and the first derivative at 2 K (right) of (9)	82
Figure 4-11	M vs H plots (left) and the first derivative at 2 K (right) of (10)	82
Figure 4-12	M vs H plots (left) and the first derivative at 2 K (right) of (11)	82
Figure 4-13	M vs H plots (left) and the first derivative at 2 K (right) of (12)	83
Figure 4-14	Out-of-phase susceptibility measurements (top left), Arrhenius plot (top right) and Cole-Cole plot (bottom) of (7)	84
Figure 4-15	Out-of-phase susceptibility measurements (top left), Arrhenius plot (top right) and Cole-Cole plot (bottom) of (9)	85
Figure 4-16	χT vs T plots at 0.1 T for the complexes (13) , (14) and (15) with the same ligand but with different metal ions M in the {M ₂ Dy ₃ } core. ...	86

Figure 4-17	M vs H plots (left) and the first derivative at 2 K (right) of (13)	87
Figure 4-18	M vs H plots (left) and the first derivative at 2 K (right) of (14)	87
Figure 4-19	M vs H plots (left) and the first derivative at 2 K (right) of (15)	88
Figure 4-20	Out-of-phase susceptibility measurements (top left), Arrhenius plot (top right) and Cole-Cole plot (bottom) of (15)	89
Figure 4-21	Single crystal measurements of (15) (top) and the derivative of the magnetization (bottom). The peaks in the derivatives indicate possible QTM and/or level-crossing.	90
Figure 4-22	The deviation of the anisotropy axes out of the plane is identified by the angle φ (left). The tilting of the anisotropy axes from the tangential direction (red line) is identified by the angle θ (right).	91
Figure 4-23	MAGELLAN calculations of the anisotropy axes from the side view (left) and down the pseudo 3-fold axis (right) of (8) with corresponding out-of-plane angles (φ) and deviation θ of the tangential direction.	91
Figure 4-24	MAGELLAN calculations of the anisotropy axes from the side view (left) and down the pseudo 3-fold axis (right) of (9) with corresponding out-of-plane angles (φ) and deviation θ of the tangential direction.	92
Figure 4-25	MAGELLAN calculations of the anisotropy axes from the side view of (10) (left) and of (11) (right) with corresponding out-of-plane angles (φ).	92
Figure 4-26	MAGELLAN calculations of the anisotropy axes from the side view (left) and down the pseudo 3-fold axis (right) of (12) with corresponding out-of-plane angles (φ) and deviation θ of the tangential direction.	93
Figure 4-27	MAGELLAN calculations of the anisotropy axes from the side view (left) and down the pseudo 3-fold axis (right) of (13) with corresponding out-of-plane angles (φ) and deviation θ of the tangential direction.	93
Figure 4-28	MAGELLAN calculations of the anisotropy axes from the side view (left) and down the pseudo 3-fold axis (right) of (14) with corresponding out-of-plane angles (φ) and deviation θ of the tangential direction.	94
Figure 4-29	MAGELLAN calculations of the anisotropy axes from the side view of (15) (left) and of (16) (right) with corresponding out-of-plane angles (φ) and deviation θ of the tangential direction.	94
Figure 4-30	Reaction schemes of series-1 with the complexes (7) to (12)	96
Figure 4-31	Reaction schemes series-2 of (13) to (16) without (12)	96
Figure 4-32	Scheme of the defined angles of the core structures from series-1 and series-2 . M stands either for Cr(III), Fe(III), Al(III) or Co(III). The black dummy atom in the middle of the Dy ₃ triangle is for the determination of the M-Dy-DyPlane angle (red). The Dy-Dy-Dy angle is not shown here.	97
Figure 5-1	Molecular structure of the first reported {Dy ₄ } SMT with ligand and coordination spheres around the Dy(III) ions (top) and the χT vs T plot (bottom, left) and the M vs H plots (inlet). The level crossing at about 0.25 T is indicated by <i>ab initio</i> calculations (bottom right). The dashed lines in the molecular structure represent the anisotropy axes and the green arrows the direction of the magnetic moments.	

	Reprinted with permission from reference ^[12] . Copyright 2012 American Chemical Society.	100
Figure 5-2	Single-ion anisotropy axes of the literature known Dy4-1 , coordination spheres and deviations from the perfect geometry. Calculations of the anisotropy axes from MAGELLAN.	101
Figure 5-3	In situ reaction of 3-ethoxysalicy aldehyde and 2-aminophenol, leading to the Schiff base ehimpH ₂	102
Figure 5-4	Molecular structure of (17) to (22) with Ln = Tb, Dy, Ho, Er, Yb, Y. Primed-atoms at 1-x, 1-y, 1-z.	103
Figure 5-5	Binding mode of the organic ligands in (17) to (22).	103
Figure 5-6	Coordination spheres around the Dy(III) ions of (18) and the deviations from the perfect geometries (in %).	104
Figure 5-7	Powder patterns of (17) to (22) compared to the simulated one in red (out of the Dy-analogue).	104
Figure 5-8	Anisotropy axes of (18) calculated using MAGELLAN.	105
Figure 5-9	χT vs T plots for Dy (18) (left) and Er (20) (right) at 0.1 T.	107
Figure 5-10	M vs H plot for Dy (18) (left) and Er (20) (right). The inset is the enlarged M vs H plot for 2 K.	107
Figure 5-11	The first derivatives of the magnetizations at 2 K shows a peak at 0.2 T for Dy ₄ (18) (left) but no peak is observed for the first derivative for Er ₄ (20) (right).	107
Figure 5-12	In-phase and out-of-phase susceptibility measurements on (18) at the top. Cole-Cole plot and Arrhenius plot at the bottom. The lines in the susceptibility measurements and in the Cole-Cole plot represent the best fit with the Debye model.	108
Figure 5-13	Single crystal micro-SQUID measurements of Dy ₄ (OH) ₂ (NO ₃) ₂ (DMF) ₂ (ehimp) ₄ (18) (top) and the derivative of the magnetization (bottom). The red arrows indicate the possible level-crossing from the ground to first excited state.	109
Figure 5-14	Scheme of the possible flipping of the spins if a field H is applied parallel to the Dy ₄ plane. The toroidal arrangement of the spins at zero field ($H = 0$) (a), one flipped spin by increasing the field ($H = 0 - 0.17$ T) (b) and a second flipped spin at further increasing field ($H = 0.17 - 0.33$ T) (c).	110
Figure 5-15	The core of the {Dy ₄ } complexes with different number of μ_2 -O ⁻ bridging oxygens.	111
Figure 5-16	Molecular structure of Dy4-2 ^[92] with anisotropy axes calculated using MAGELLAN, corresponding ligand, binding mode and coordination spheres. The χT vs T and M vs H plots are taken from reference ^[92] . The first derivative is for the magnetization at 1.8 K.	113
Figure 5-17	Molecular structure of Dy4-3 ^[92] with anisotropy axes calculated by MAGELLAN, corresponding ligand, binding mode and coordination spheres. The χT vs T and M vs H plots are taken from reference ^[92] . The first derivative is for the magnetization at 1.8 K.	114
Figure 5-18	Molecular structure of Dy4-4 ^[93] with anisotropy axes calculated by MAGELLAN, corresponding ligand, binding mode and coordination spheres. The M vs H plot is taken are taken from reference ^[93] . The first derivative is for the magnetization at 1.8 K.	116

Figure 5-19	Molecular structure of Dy4-5 ^[93] with anisotropy axes calculated by MAGELLAN, corresponding ligand, binding mode and coordination spheres. The M vs H plots (bottom, left) are taken from reference ^[94] . The first derivative is for the magnetization at 2 K (bottom, right).....	118
Figure 5-20	Molecular structure of Dy4-6 ^[93,96] with anisotropy axes calculated by MAGELLAN, corresponding ligand, binding mode and coordination spheres. The χT vs T and M vs H plots (bottom left) are taken from reference ^[96] . The first derivative is for the magnetization at 2 K (bottom right).....	120
Figure 6-1	The used ligands for the {Dy ₆ } systems in the literature.....	124
Figure 6-2	First derivatives of the magnetization at 2 K for [Dy ₆ (Me-teaH) ₆ (NO ₃) ₆]·6MeCN (Dy6-2) in blue and for [Dy ₆ (apadH ₂) ₆ (NO ₃) ₆]·2THF (Dy6-3) in red. The lines represent the fit. Adapted from reference ^[83]	125
Figure 6-3	Structure of [Dy ₆ (teaH) ₆ (NO ₃) ₆]·8MeOH (Dy6-1) with the anisotropy axes (dotted lines) and the direction of the magnetic moments (green arrows). The dot and the dotted line in the middle of the molecule indicate the S ₆ symmetry of the molecule. ^[16]	125
Figure 6-4	The χT vs T plot shows antiferromagnetic interactions (left), the M vs H plots out of bulk magnetization measurements show a S-Shaped curve (middle) and the level-crossing from the toroidal ground state to the first excited state gives a value of $H = 0.65$ T from <i>ab initio</i> calculations (right). Adapted with permission from reference ^[16] . Copyright 2012 American Chemical Society.....	125
Figure 6-5	Angle θ between the S ₆ symmetry axis (blue dotted line) and the anisotropy axes (turquoise lines).	126
Figure 6-6	Anisotropy axes of [Dy ₆ (teaH) ₆ (NO ₃) ₆] (Dy6-1) calculated with MAGELLAN. The dot in the middle of the molecule and the dotted line both indicate the S ₆ symmetry axis.....	126
Figure 6-7	Anisotropy axes of [Dy ₆ (Me-teaH) ₆ (NO ₃) ₆] (Dy6-2) calculated with MAGELLAN. The dot in the middle of the molecule and the dotted line both indicate the S ₆ symmetry axis.....	127
Figure 6-8	Anisotropy axes of [Dy ₆ (apadH ₂) ₆ (NO ₃) ₆] (Dy6-3) calculated with MAGELLAN. The dot in the middle of the molecule and the dotted line both indicate the S ₆ symmetry axis.....	127
Figure 6-9	Molecular structure of (23) with selected distances [Å] and angles [°]. Primed atoms at 1/3+y, 2/3-x+y, 2/3-z; double-primed atoms at 1/3+x-y, -1/3+x, 2/3-z.	129
Figure 6-10	Anisotropy axes of [Dy ₆ (NO ₃) ₆ (teaH) ₆]·2C ₂ H ₅ OH (23) calculated with MAGELLAN. The dot in the middle of the molecule and the dotted line both indicate the S ₆ symmetry axis.....	130
Figure 6-11	Coordination spheres around the Dy(III) ions in (23) (left) and in Dy6-1 (middle) with the deviations from the perfect geometry. The ligand and the binding scheme (right) are the same in both structures.	130
Figure 6-12	Single crystal micro-SQUID measurements of [Dy ₆ (NO ₃) ₆ (teaH) ₆]·2C ₂ H ₅ OH (23) (top) and the first derivatives of the magnetization (bottom).	131

Figure 6-13	Molecular structure of (23) with selected distances [Å] and angles [°]. Primed atoms at $-1/3+y$, $1/3-x+y$, $4/3-z$; double-primed atoms at $2/3+x-y$, $1/3+x$, $4/3-z$	132
Figure 6-14	Anisotropy axes of $[\text{Dy}_6(\text{NO}_3)_6(\text{teaH})_6] \cdot 2\text{C}_2\text{H}_5\text{OH}$ (23) calculated with MAGELLAN. The dot in the middle of the molecule and the dotted line both indicate the S_6 symmetry axis.....	133
Figure 6-15	Coordination spheres around the Dy(III) ions in (24) (left) and in Dy6-1 (middle) with the deviations from the perfect geometry. The ligand and the ligand scheme (right) are the same in both structures.	134
Figure 6-16	Single crystal micro-SQUID measurements of $[\text{Dy}_6(\text{apadH}_2)_6(\text{NO}_3)_6]$ (24) (top) and the derivative of the magnetization (bottom).....	135
Figure 6-17	Molecular structure of Dy6-4 . Primed atoms at $1-x$, $1-y$, $1-z$	136
Figure 6-18	Anisotropy axes of $[\text{Dy}_6(\text{NO}_3)_6(\text{teaH})_6] \cdot 2\text{C}_2\text{H}_5\text{OH}$ (23) calculated with MAGELLAN. The dot in the middle of the molecule and the dotted line both indicate the pseudo S_6 symmetry axis.	138
Figure 6-19	Coordination spheres around the Dy(III) ions in Dy6-4 (top) with the deviations from the perfect geometry. The ligand and the ligand scheme are illustrated at the bottom.	138
Figure 6-20	Single crystal micro-SQUID measurements of $[\text{Dy}_6(\text{NO}_3)_3(\text{pmide})_6]$ (Dy6-4) (top) and the derivatives of the magnetization (bottom). .	139
Figure 12-1	Molecular structure of $[\text{Dy}_3(\text{L})_3(\mu_3\text{-OH})_2(\text{H}_2\text{O})_4\text{Cl}_2]\text{Cl}_2 \cdot 5\text{H}_2\text{O} \cdot 3\text{MeOH}$ (1).....	182
Figure 12-2	Molecular structure of $[\text{Dy}_3(\text{L})_3(\mu_3\text{-OH})_2(\text{H}_2\text{O})_2(\text{CH}_3\text{OH})\text{Cl}_3]\text{Cl} \cdot 2\text{H}_2\text{O} \cdot 2\text{CH}_3\text{OH}$ (2).	184
Figure 12-3	Molecular structure of (3) to (6) with Ln = Eu in (3) , Tb in (4) , Ho in (5) and Er in (6)	186
Figure 12-4	Molecular structure of $[\text{Cr}_2\text{Dy}_3(\text{pfba})_6(\mu_3\text{-OH})_6(\text{NO}_3)_3(\text{H}_2\text{O})_2(\text{C}_3\text{H}_7\text{OH})] \cdot \text{H}_2\text{O}$ (7) from the side view (left) and down the pseudo 3-fold axis (right). Primed atoms at x , $1-y$, z	191
Figure 12-5	Coordination spheres around the Dy(III) ions with deviations from the perfect geometries in %.	191
Figure 12-6	Coordination spheres around the Cr(III) ions with deviations from the perfect geometry.	192
Figure 12-7	Packing of (7) from different viewing directions. Coordination spheres of the Dy(III) ions in lavender and of the Cr(III) ions in dark green.....	192
Figure 12-8	Molecular structure of $[\text{Cr}_2\text{Dy}_3(\text{pfba})_9(\mu_3\text{-OH})_6(\text{C}_3\text{H}_7\text{OH})_3] \cdot 3\text{C}_3\text{H}_7\text{OH}$ (8) from the side view (left) and down the pseudo 3-fold axis (right).	194
Figure 12-9	Coordination spheres around the Dy(III) ions with deviations from the perfect geometries in %.	194
Figure 12-10	Coordination spheres around the Cr(III) ions with deviations from the perfect geometry.	194
Figure 12-11	Packing of (8) from different viewing directions. Coordination spheres of the Dy(III) ions in lavender and of the Cr(III) ions in dark green.....	195
Figure 12-12	Molecular structure of $[\text{Cr}_2\text{Dy}_3(\text{pclba})_9(\mu_3\text{-OH})_6(\text{C}_3\text{H}_7\text{OH})_3] \cdot \text{H}_2\text{O} \cdot \text{C}_3\text{H}_7\text{OH}$ (9) from the side view (left) and	

	down the pseudo 3-fold axis (right). Primed atoms at 1-x, x-y, z; double-primed atoms at 1-x+y, 1-x.....	198
Figure 12-13	Coordination spheres around the Dy(III) and Cr(III) ions with deviations from the perfect geometries.	198
Figure 12-14	Packing of (9) from different viewing directions. Coordination spheres of the Dy(III) ions in lavender and of the Cr(III) ions in dark green.....	199
Figure 12-15	Molecular structure of $[\text{Cr}_2\text{Dy}_3(\text{pcnba})_6(\mu_3\text{-OH})_6(\text{NO}_3)_3(\text{H}_2\text{O})_3]$ (10) from the side view (left) and down the pseudo 3-fold axis (right). Primed atoms at 1-y, x-y, z; double-primed atoms at 1-x+y, 1-x.	201
Figure 12-16	Coordination spheres around the Dy(III) and Cr(III) ions with deviations from the perfect geometries.	201
Figure 12-17	Packing of (10) from different viewing directions. Coordination spheres of the Dy(III) ions in lavender and of the Cr(III) ions in dark green.....	202
Figure 12-18	Molecular structure of $[\text{Cr}_2\text{Dy}_3(\text{dfba})_6(\mu_3\text{-OH})_6(\text{NO}_3)_3(\text{DMF})_3] \cdot \text{DMF}$ (11) from the side view (left) and down the pseudo 3-fold axis (right). Primed atoms at -x+y, 1-x, z; double-primed atoms at 1-y, 1+x-y, z.	204
Figure 12-19	Coordination spheres around the Dy(III) and Cr(III) ions with deviations from the perfect geometries.	204
Figure 12-20	Packing of (11) from different viewing directions. Coordination spheres of the Dy(III) ions in lavender and of the Cr(III) ions in dark green.....	205
Figure 12-21	Molecular structure of $[\text{Cr}_2\text{Dy}_3(\text{dtbba})_9(\mu_3\text{-OH})_6(\text{C}_3\text{H}_7\text{OH})_3] \cdot 3\text{C}_3\text{H}_7\text{OH}$ (12) from the side view (left) and down the pseudo 3-fold axis (right).....	207
Figure 12-22	Coordination spheres around the Dy(III) ions with deviations from the perfect geometries in %.	207
Figure 12-23	Coordination spheres around the Cr(III) ions with deviations from the perfect geometry.	207
Figure 12-24	Packing of (12) from different viewing directions. Coordination spheres of the Dy(III) ions in lavender and of the Cr(III) ions in dark green.....	208
Figure 12-25	Molecular structure of $[\text{Fe}_2\text{Dy}_3(\text{dtbba})_9(\mu_3\text{-OH})_6(\text{C}_3\text{H}_7\text{OH})_3] \cdot 3\text{C}_3\text{H}_7\text{OH}$ (13) from the side view (left) and down the pseudo 3-fold axis (right).....	211
Figure 12-26	Coordination spheres around the Dy(III) ions with deviations from the perfect geometries in %.	211
Figure 12-27	Coordination spheres around the Cr(III) ions with deviations from the perfect geometry.	211
Figure 12-28	Packing of (13) from different viewing directions. Coordination spheres of the Dy(III) ions in lavender and of the Fe(III) ions in green.....	212
Figure 12-29	Molecular structure of $[\text{Al}_2\text{Dy}_3(\text{dtbba})_9(\mu_3\text{-OH})_6(\text{CH}_3\text{OH})_{0.75}(\text{H}_2\text{O})_{1.5}(\text{C}_3\text{H}_7\text{OH})_{0.75}] \cdot \text{CH}_3\text{H}_7\text{OH}$ (14) from the side view (left) and down the pseudo 3-fold axis (right). Hydrogens are omitted for clarity. For the disorder at the Dy(III) ions, water is chosen to be displayed. Primed atoms at x, y, 3/2-z; double-primed	

	atoms at 1-y, 1+x-y, z; triple-primed atoms at 1-y, 1+x-y, 3/2-z, ^{IV} -primed atoms at -x+y, 1-x, z; ^V -primed atoms at -x+y, 1-x, 3/2-z..	215
Figure 12-30	Coordination spheres around the Dy(III) and Al(III) ions with deviations from the perfect geometries.	215
Figure 12-31	Packing of (14) from different viewing directions. Coordination spheres of the Dy(III) ions in lavender and of the Al(III) ions in light green.....	216
Figure 12-32	Molecular structure of [Al ₂ Dy ₃ (dtbba) ₇ (μ ₃ -OH) ₆ (NO ₃) ₂ (C ₃ H ₇ OH)(H ₂ O) ₂].3H ₂ O (15) from the side view (left) and down the pseudo 3-fold axis (right).	217
Figure 12-33	Coordination spheres around the Dy(III) ions with deviations from the perfect geometries in %.	217
Figure 12-34	Coordination spheres around the Al(III) ions with deviations from the perfect geometry.	217
Figure 12-35	Packing of (15) from different viewing directions. Coordination spheres of the Dy(III) ions in lavender and of the Al(III) ions in light green.....	218
Figure 12-36	Molecular structure of [Co ₂ Dy ₃ (dtbba) ₇ (μ ₃ -OH) ₆ (NO ₃) ₂ (C ₃ H ₇ OH) ₃].3C ₃ H ₇ OH.3CH ₃ CN (16) from the side view (left) and down the pseudo 3-fold axis (right).	221
Figure 12-37	Coordination spheres around the Dy(III) with deviations from the perfect geometries in %.	221
Figure 12-38	Coordination spheres around the Co(III) with deviations from the perfect geometry.	221
Figure 12-39	Packing of (16) from different viewing directions. Coordination spheres of the Dy(III) ions in lavender and of the Co(III) ions in dark blue.	222
Figure 12-40	Molecular structure of (17) to (22) with Ln = Tb, Dy, Ho, Er, Yb, Y. Primed-atoms at 1-x, 1-y, 1-z.....	225